Title
PHOTODISSOCIATION OF NO[SUB]2 -X (X = C10, NO[SUB]3 , C1) MOLECULES

Permalink
https://escholarship.org/uc/item/65t2t2f7

Author
Oh, B.Y.

Publication Date
1989-03-03

LBL-26462

Lawrence Berkeley Laboratory
UNIVERSITY OF CALIFORNIA

Materials & Chemical Sciences Division

Photodissociation of NO_2-X
(X = ClO, NO_3, Cl) Molecules

B.Y. Oh
(Ph.D. Thesis)

December 1988

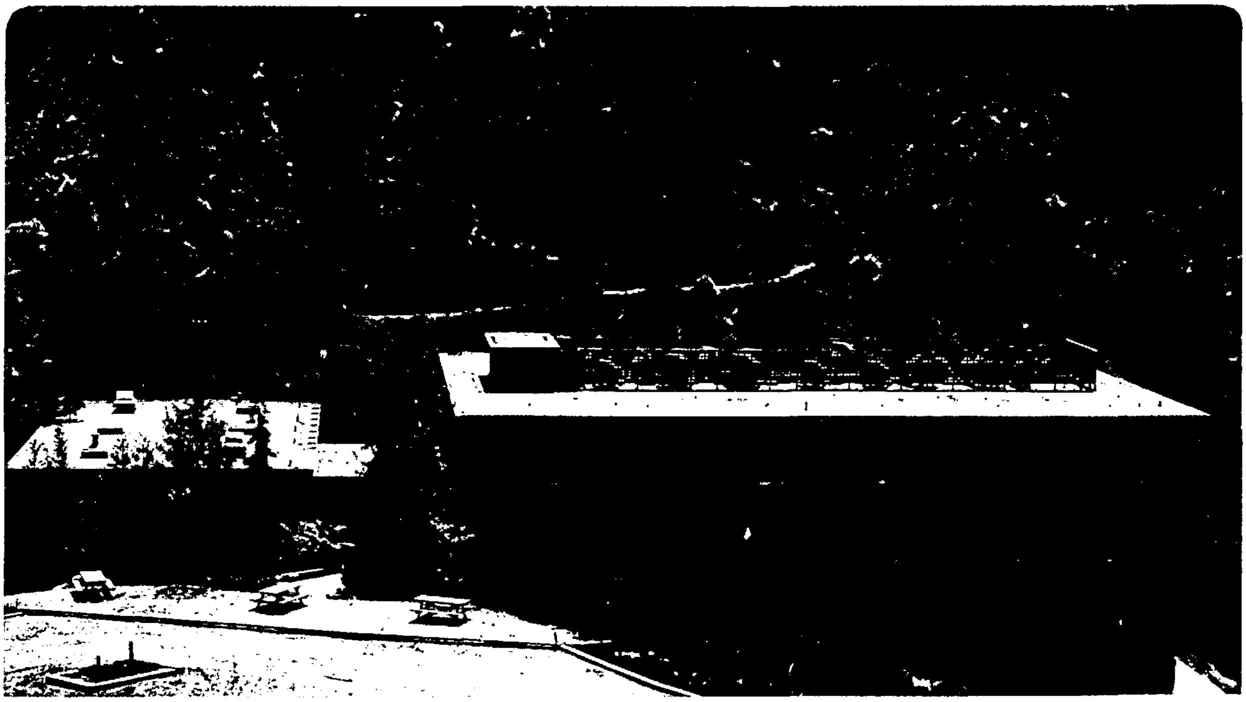

Prepared for the U.S. Department of Energy under Contract Number DE-AC03-76SF00098.

Photodissociation of NO_2-X (X = ClO, NO_3, Cl) molecules

Baek Yul Oh

Department of Chemistry
University of California

and

Materials and Chemical Sciences Division
Lawrence Berkeley Laboratory
1 Cyclotron Road
Berkeley, CA 94720

ABSTRACT

Studies of the photodissociation of NO_2-X molecules, where X = ClO, NO_3, and Cl, are reported here.

Chlorine nitrate ($ClONO_2$) is photolyzed at 248 nm, and the product nitrate radical (NO_3) is detected by time-resolved resonance absorption. The primary quantum yield of NO_3 is found to be $0.99\pm0.16(2\sigma)$, and the secondary quantum yield is $0.91\pm0.26(2\sigma)$. The initial NO_3 fragments are vibrationally excited, and collisional deactivation from X(v>0) levels of NO_3 into X(0,0,0,0) is observed to have a quenching rate constant of $4.2\pm0.2(2\sigma) \times 10^{-13}$ cm^3 $molecule^{-1}$ s^{-1} for both N_2 and O_2. The sum of the primary and secondary NO_3 quantum yields is $1.7\pm0.28(2\sigma)$, as measured from analysis of the time-resolved absorption profile at NO_3 X(0,0,0,1).

The Photolysis Induced Fluorescence (PIF) method, which represents the NO_2^* emission spectrum as a linear combination of monoenergetically prepared NO_2 Laser Induced Fluorescence spectra, is derived. This method estimates the internal energy distribution ($P(E_{int})$) of NO_2^* from photolysis over the range of observations, which is limited to the visible spectrum, from 400 to 800 nm or 25,000 to 12,500 cm^{-1}.

The PIF spectra of nitrogen dioxide (N_2O_5) are studied at 248 and 193 nm. Upon N_2O_5 photolysis at 248 nm, the internal energy of the NO_2 product is spread almost uniformly from 25,000 to 12,500 cm^{-1} with a weak maximum value around 20,000 cm^{-1}. Upon photolysis of N_2O_5 at the much higher energy of 193 nm radiation, there is an order of magnitude less photolysis induced fluorescence and much more NO_2 dissociation; and the inferred internal energy of NO_2 molecules that fluoresce appears to be maximum at 25,000 cm^{-1} and to fall off slowly to and below 12,500 cm^{-1}.

The PIF spectra of nitryl chloride (NO_2Cl) are studied at 266, 248 and 193 nm. This investigation demonstrates how the internal energy distribution of the reaction products changes with the energy of the photolysis laser. The average NO_2^* internal energies from 266, 248 and 193 nm are estimated to be 17,000 cm^{-1}, 21,000 cm^{-1} and 21,000 cm^{-1}. The emission yields of NO_2^* at these photolysis energies are estimated to be 0.9 ± 0.5, 0.7 ± 0.2 and 0.03 ± 0.03. This study also demonstrates the change in the nascent $P(E_{int})$ profile as the NO_2^* molecule undergoes a controlled number of collisions.

Time-of-Flight / Mass Spectrometry (TOF/MS) study of the photochemical reactions of NO_2Cl, performed in collaboration with Y.T. Lee group, is reported. This method gives the distribution of translational energies ($P(E_{Trans})$) of the product molecules, which is complimentary to the $P(E_{int})$ from the PIF method.

By combining the experimental results from both studies, the following photolytic channels are identified at 248 nm photolysis.

	PIF	TOF/MS
NO_2Cl + 248 --> $NO_2(X) + Cl$		observed
$NO_2^*(A,B) + Cl$	observed	observed
$NO + O + Cl$	inferred	inferred
$NOCl + O$		observed

Based on the experimental evidence observed from two complimentary experiments, it is thought that UV photodissociation of NO_2Cl involves highly localized initial excitation in the NO_2 group, followed by predissociation of the Cl-N bond where much of the excess energy remains in the NO_2 fragment. This is manifested by NO_2^* emission, and the inferred dissociation into NO + O when sufficient excess energy exists.

Comparison of $P(E_{Trans})$ from TOF/MS analysis and the $P(E_{int})$ from PIF analysis at 248 nm results in fair matching of the distribution profiles within the uncertainties of each method.

This thesis is dedicated to;
my parents who had raised me with love and understanding,
and to my wife Christine who show love and understanding
even when I am neither lovable nor understandable.

ACKNOWLEDGEMENTS

I wish to thank those who have made this thesis possible.

First of all, my deep felt gratitude goes to Professor Harold Johnston for his guidence and patience throughout the research and especially during the last phase of completing this thesis. He took many hours from his much needed weekends to correct and to polish the text. Thanks goes to Professor C.Bradley Moore for many helpful advises during the development phase of the PIF methods. I also wish to acknowledge the supports and encouragements by Professor Y.T. Lee in performing complimentary experiments in his laboratory. It was a great privilege to be able to collaborate with him and his students. Mike Covinsky and Floyd Davis were two of the Professor Lee's graduate students who performed most of the experiments, analyzed the data, and taught me how to analyze the data myself. Their help and hard work is greatly appreciated.

The assistance and encouragement of my coworkers was greatly appreciated. Postdoctoral researcher Dr. Anthony Young provided much needed day to day guidences and encouragements, especially when things were not going as well as one wished. His friendship and valuable advises during the "session" in his office will be cherished by me. Dr. Diane Swanson Waterman introduced me to the lab and helped me to set up and run the first experiment. I wish her well. Wade Sisk has been a coworker in the literal sense of the word. His contribution in the development and application of the PIF method has been substantial and most valuable. His indefatigable sense of humor (albeit somewhat on the uncollimated side) and enthusiasm for science made some of the more difficult days bearable. Also, his help and hospitality during the final phase of completing the thesis is appreciated. I wish him good luck on his molecular beam experiments. Doug Kinnison has provided friendship and valuable assistance with computer programming. (Next time I play racquet ball with him, I know I will beat him in straight sets). I also wish him good luck in his work with Cray computer in simulating atmospheric chemistry. Help and support in various forms from Phil Hunter, Ken Patten, Bong Soo Kim, Charles Miller and Joel Burley are greatfully acknowledged.

Thanks also goes to Drs. Andy Kung and Tim Ling in San Fransisco Laser Center (which, unfortunately no longer exists) for loaning a laser system during the initial phase of PIF experiment.

Most of all, love and support provided by my family members are acknowledged. My wife Christine and our daughter Allison patiently waited for the completion of this thesis during which I have been less than available and bearable. Much love and abundant support came from Christine before and during the writing of thesis. Her love and understanding made this thesis possible, and her support is greatfully acknowledged. My parents and my sisters, my parents-in-laws and my brothers-in laws and sister-in law all believed in my dream to offer supports in various forms. Their love and support is much appreciated.

Thanks are also due for the support of the work performed in University of California at Berkeley and Lawrence Berkeley Laboratory by the Director, Office of Energy Research, Office of Basic Energy Sciences, Chemical Sciences Division of the U.S. Department of Energy under Contract No. DE-AC03-76SF00098.

TABLE OF CONTENTS

CHAPTER 1. Photodissociation of the Chlorine Nitrate ($ClONO_2$) at 248 nm.

ABSTRACT

Quantum yields of primary NO_3 and Cl fragments from chlorine nitrate ($ClONO_2$) photolysis at 248 nm were measured by resonance absorption of NO_3 A(0,0,0,0) ← X(0,0,0,0) at 661.9nm by a method that does not depend on the ultraviolet cross-section of $ClONO_2$. Nascent NO_3 was formed in excited vibrational state, $NO_3(v>0)$, and it was observed after collisional deactivation by carrier gas into the NO_3 X(0,0,0,0) level. The product of primary quantum yield Φ_1 and optical absorption cross-section σ at 661.9 nm is $1.88\pm0.30 \times 10^{-17}$ cm^2 $molecule^{-1}$. The average secondary quantum yield (from reaction of primary Cl with $ClONO_2$) is obtained from $\Phi_2\ \sigma = 1.73\pm0.49 \times 10^{-17}$ cm^2 $molecule^{-1}$, but this value approached 1.9×10^{-17} at high carrier gas pressure. Using our preferred cross section (1.9×10^{-17} cm^2), the average quantum yields are: $\Phi_1 = 0.99\pm0.16$ and $\Phi_2 = 0.91\pm0.26$. The quenching rate constant for collisional deactivation is $4.2\pm0.2 \times 10^{-13}$ cm^3 $molecule^{-1}$ s^{-1} for both N_2 and O_2. The average primary plus secondary NO_3 quantum yield of 1.7±0.28 (approaching 2.0 at high gas carrier gas pressure) was measured from the analysis of the hot band absorption profile at 679.0 nm. The error estimates are twice the standard deviation.

INTRODUCTION

This work was undertaken in order to (1) determine the quantum yields of primary NO_3 and secondary NO_3 (from Cl plus reactant) upon $ClONO_2$ photolysis at 248 nm, and (2) obtain information about the vibrational population distribution in the primary NO_3 fragments.

The photochemistry of chlorine nitrate has been studied previously [1-3]. These studies sought to identify the photolytic channels that are involved and to assess the extent of photodissociation through each channel by quantum yield measurement of each photofragment. Listed below are possible photolytic channels available for chlorine nitrate along with the estimated threshold wavelengths.

$ClONO_2 + h\nu \to$	$ClO + NO_2$	< 1072 nm	(Eq.1.1)
	$Cl + NO_3$	< 705	(Eq.1.2)
	$Cl + NO + O_2$	< 652	(Eq.1.3)
	$ClONO + O(^3P)$	< 394	(Eq.1.4)
	$Cl + NO_2 + O(^3P)$	< 318	(Eq.1.5)
	$ClO + NO + O(^3P)$	< 291	(Eq.1.6)

Of these channels, (4) is forbidden under spin conservation rules.

Among the studies where primary photofragments were directly detected, two [2,3] show appreciable differences in the quantum yields and the possible photolytic channels involved. In this laboratory, Marinelli et al. [2] photolyzed chlorine nitrate at 248 nm with an excimer laser equipped with unstable resonator optics, and detected NO_3 by resonance absorption at 661.9 nm which is primarily the transition, $A(0,0,0,0) \leftarrow X(0,0,0,0)$ [4]. With Ar or Ar/CH_4 as a carrier gas between 20 and 100 torr, the primary NO_3 quantum yield was reported to be 0.55 ± 0.2. They observed a slower, secondary rise in the NO_3

absorption, and with added methane the peak of this rise amounted to secondary NO_3 quantum yield of 0.1 to 0.2. They concluded that major channel is Eq.1.2.

Margitan [3] photolyzed chlorine nitrate at 266 and 355 nm with 4th and 3rd harmonic outputs from Nd:YAG lasers, and detected Cl and O atoms with atomic resonance fluorescence. The Cl and O atom quantum yields were found to be 0.9 and 0.1, respectively. This led him to conclude that channel shown in Eq.1.2 is the dominant step, in agreement with Marinelli et al.'s conclusion on the dominant channel.

Whereas the major photolysis channel was agreed to be one shown in Eq.1.2 by these two groups, there is substantial disagreement in the reported primary quantum yields. We were able to decouple the NO_3 absorption profile into a primary and secondary rise under the time scale of 100 ns/channel. We followed the NO_3 X(0,0,0,0) level by the time-resolved absorption at 661.9 nm, which is assigned to be A(0,0,0,0) ← X(0,0,0,0). We also studied the pressure dependence of the formation rate of primary NO_3 X(0,0,0,0).

The NO_3 X(0,0,0,0) level was followed with 679.0 nm absorption, which is assigned to be A(0,0,0,0) ← X(0,0,0,1) transition. The NO_3 X(0,0,0,1) level has a quantum of vibrational excitation in the doubly degenerate bending mode ($\nu_4 = 380\ \mathrm{cm}^{-1}$) of NO3 under D_{3h} symmetry [4-6]. The total NO_3 quantum yield from $ClONO_2$ photolysis was studied at this level and compared to the 661.9 nm result.

These identifications of X(0,0,0,0) and X(0,0,0,1) must be modified by the following considerations. Cantrell et al. [16] found no change in the NO_3 cross section at 661.9 nm over a wide temperature range. Over this range of temperature there is a large change in the equilibrium population of $NO_3(0,0,0,1)$, and at high temperatures more than a quarter of the molecules are in this excited vibrational state. This invariance of cross section with temperature implies that the two transitions

$$\begin{aligned} &A(0,0,0,1) \leftarrow X(0,0,0,1) \qquad\qquad \text{(Eq.1.7)} \\ &A(0,0,0,0) \leftarrow X(0,0,0,0) \end{aligned}$$

have the same cross section, which implies the same Frank-Condon factors and further implies that the X and A states have very nearly the same structure. In the discussions below, the absorption at 661.9 nm is interpreted as giving the total amount of NO_3, since there is equal absorption from states X(0,0,0,0) and X(0,0,0,x), where x is certainly 1 and maybe 2,3, or more.

EXPERIMENTAL

The block diagram of the experimental apparatus is shown in Figure 1.1, which is similar in basic design to the one described before [2,7]. Photolysis pulses from an excimer laser (Lumonics TE-860T), operating with KrF at 248 nm, were passed through apertures and a cylindrical / spherical lens assembly in order to eliminate beam divergence. They were sent through a 128 cm photolysis cell, colinerly with the output from an Ar^+ pimped dye laser, which was tuned either to the NO_3 A(0,0,0,0) ← X(0,0,0,0) transition at 661.9 nm or to A(0,0,0,0) ← X(0,0,0,1) hot band transition at 679.0 nm. After exiting the cell, the two beams were separated by a prism. The dye laser beam was incident upon an integrated photodiode-preamplifier detector (EG&G HFD-1100), which monitored the beam intensity. The photodiode response time was estimated to be about 50 ns when a small portion of excimer laser was directed to the detector. The time-resolved absorption profile was recorded with a transient digitizer (Biomation 8100) and stored in a microcomputer. Data could also be sent to CDC 7600 main frame computer for analysis. A beam splitter sent a portion of the dye laser beam to a 1 meter monochromator equipped with an Optical Multichannel Analyzer for wavelength monitoring. A Ne pilot lamp provided emission lines for the calibration of monochromator/OMA unit with accuracy 0.8Å. A pyroelectric joulemeter (Gen-Tec), which had been calibrated with ClNO actinometery and checked against a factory calibrated joulemeter, measured the excimer pulse energies.

For the 661.9 nm absorption experiment, energies of 20 pulses each were measured (1) through the empty cell (E_o) and (2) while $ClONO_2$ sample was flowing through the cell (E). Then, 128 shots were averaged at 1 Hz repetition rate and recorded with the time resolution of 100 ns/ch for 2048 channels. The excimer laser was triggered after the digitizer trigger to measure the baseline of the absorption profile. After each run was completed, sample flow was stopped to record the empty cell UV absorbance (for $ClONO_2$ monitoring) and the E_o fro the next run. Carrier gas pressures were varied from run to run foe quenching rate determination.

For the runs involving 679.0 nm absorption, similar experimental procedures were adopted. Due to lower absorbance, the $ClONO_2$ concentration was increased by about a factor of 5 relative to the 661.9 nm study. The time resolution of the transient digitizer was reduced to 50 ns/ch in an effort to resolve the build up of population into the NO_3 X(0,0,0,1) level.

The experimental conditions involved in these runs are shown in Tables 1.1(a) and 1.1(b) for 661.9 nm and 679.0 nm absorption, respectively. For convenient comparison, the concentration of reactant and the number of photons absorbed per unit volume are given in the same units in the tables.

Chlorine nitrate was prepared by the method of Schmeisser [8], where Cl_2O was reacted with excess N_2O_5

$$Cl_2O \quad + \quad N_2O_5 \quad -> \quad 2ClONO_2 \qquad \text{(Eq.1.8)}$$

The trap containing reactants was placed in a 200 K bath and was allowed to warm up to 273 K during which the reaction occurred. The chlorine nitrate was collected by distillation from a trap held at 175 k into a trap at 157 k, leaving behind N_2O_5, HNO_3, or NO_2. After the volatile product had been collected in the trap immersed in 157 k bath, it was pumped on to remove volatile impurities like Cl_2O, OClO, and Cl_2. In order to check the purity of the distilled $ClONO_2$ sample, a known pressure of chlorine nitrate vapor was introduced into a 10 cm cell and the UV absorption was taken. The measurement agreed with the recommended value [9,10] within a few percent. Upper limits of various possible impurity concentrations are estimated to be: Cl_2O, 0.4%; NO_2, 0.8%; OClO, 0.07%; Cl_2, 4.2%; N_2O_5, 0.2%. The carrier gases, N_2 (>99.99%) and O_2 (>99.99%), were supplied from Lawrence Berkeley Laboratories and used without further purification.

The $ClONO_2$, held at 200 k, was picked up in a flowing stream of N_2 or O_2 carrier gas. The cell residence time of the sample was about 10 seconds at 20 torr total pressure. The pressure was measured with a capacitance manometer (MKS Baratron). $ClONO_2$ concentration was determined after the photolysis cell with an UV absorption cell at 250 nm, where HNO_3 and NO_2 absorptions are low.

Before the experiment began, both the photolysis cell and the UV absorption cell were baked with heating tape and pumped on overnight. Also, the entire flow system was pre-treated with $ClONO_2$ by flowing the sample for about 20 minutes. These steps were taken to minimize the interferences from impurities adsorbed on the wall of the cell.

RESULTS

1. NO_3 absorption at 661.9 nm

Nineteen chlorine nitrate photolyses at 248 nm were carried out with reactant concentrations varying from 0.34 to 3.01×10^{15} molecules cm^{-3}, and with laser energy of about 20 mj/pulse, Table 1.1(a). The dimensions and volume of the photolysis beam in the reaction cell and optical absorption cross sections are given in Table 1.2.

(a) The primary and secondary production of NO_3.

A typical NO_3 optical density profile as a function of time, measured at 661.9 nm upon $ClONO_2$ photolysis, is shown in Figure 1.2. The profile shows two different, time-resolved rises in NO_3 optical density. The initial fast rise, which was observed to be pressure dependent, started from the baseline indicating no nascent population in NO_3 X(0,0,0,0) upon photolysis. There followed a slower, secondary rise and finally a slow decay. These features were used to set up a system of simultaneous first order equations:

(i) The fast, initial rise of NO_3 observed at this wavelength comes from collisional deactivation of internally excited nascent NO_3 by the carrier gas (N_2 or O_2).

$$NO_3\ X(v>0) + M \rightarrow NO_3\ X(0,0,0,0) + M \quad k_1 \qquad (Eq.1.9)$$

The associated rate constant including [M] is written as $\alpha = k_1[M]$. The above step should obey pseudo first order kinetics, since $[M] >> [NO_3]$ under our experimental condition.

(ii) The slower, secondary rise of NO_3 is assumed to come from primary photofragment Cl reacting with $ClONO_2$ to yield NO_3 and Cl_2.

$$Cl + ClONO_2 \rightarrow Cl_2 + NO_3 \quad k_2 \qquad (Eq.1.10)$$

where $k_2(298K) = 1.04E-11$ [3] and $\beta = k_2[ClONO_2]$.

(iii) The decay is assumed to come from various sources such as loss of NO_3 due to reaction and diffusion out of probing region. This loss is described with the exponential term, Γ.

The solution to these simultaneous first order equations for the observed optical density D of NO_3 at 661.9 nm was based on the trial function:

$$D = - C_1\exp(-\alpha t) - C_2\exp(-\beta t) + (C_1+C_2)\exp(-\Gamma t) \qquad (Eq.1.11)$$

which yields the following expressions for the pre-exponential terms C_1 and C_2:

$$C_1 = D_1 \alpha / (\alpha - \Gamma) \qquad \text{(Eq.1.12)}$$

$$C_2 = D_2 \beta / (\beta - \Gamma) \qquad \text{(Eq.1.13)}$$

where D_1 is the maximum primary NO_3 optical density and D_2 is the maximum secondary optical density.

The fitting of each optical density profile based on 661.9 nm absorption was done by a non-linear least square routine, where C_1, C_2, α, and Γ were varied for optimum fit. The pseudo first order rate constant β was assigned its room temperature value. We were able to achieve good fits as can be seen from Figure 1.2. The results of these fittings are compiled in Table 1.2. The expressions for the fitting parameters are inverted to give

$$k_1 = \alpha / [M],\ D_1 = C_1 (\alpha - \Gamma) / \alpha,\ D_2 = C_2 (\beta - \Gamma) / \beta \qquad \text{(Eq.1.14)}$$

(b) Quantum Yields.

This section examines what is actually measured in the laboratory to give what is interpreted as the quantum yield, Φ. The meaning of quantum yield in this experiment is

$$\Phi = \frac{\text{molecules of } NO_3 \text{ produced in the cell per pulse}}{\text{photons absorbed in the cell by } ClONO_2 \text{ per pulse}} \qquad \text{(Eq.1.15)}$$

Quantities measured were pulse energy transmitted through the empty cell E_o, pulse energy transmitted through the cell with $ClONO_2$ E (Table 1.1), cross-sectional area (Table 1.2) of the laser beam (by means of apertures and of spherical and cylindrical lenses, the uniformity of the beam down the length of the reaction cell was established), the optical density of NO_3 produced by the laser pulse (D_N), the optical density of $ClONO_2$ in the external cell (D_A), and the lengths of the photolysis and analytical cells (L_N and L_A). By means of geometrical considerations and corrections for photon loss due to window absorption and reflection, the measured energies per pulse E were translated into energy intensities per area per pulse I, which are quantities convenient for Beer's law

$$D = \ln (I_o / I) = \sigma [X] L \qquad \text{(Eq.1.16)}$$

Using N to identify NO_3 and A to identify $ClONO_2$ and by expressing Eq.1.15 in terms of quantities per unit area, the quantum yield expression becomes

$$\Phi = \frac{(D_N / \sigma_N L_N) L_N}{I_o - I} \qquad \text{(Eq.1.17)}$$

The quantity measured is the product of quantum yield and NO_3 cross section, and Eq.1.17 can be rewritten

$$\Phi \sigma_N = \frac{D_N}{I_o - I} \qquad \text{(Method I)} \qquad \text{(Eq.1.18)}$$

From data in Tables 1.1(a) and 1.2, the denominator may be directly obtained.

A second method of finding the quantum yield is to use Beer's law to evaluate the denominator of Eq.1.18

$$I_o - I = I_o [1 - \exp^{-(\sigma_A N_A L_N)}] \qquad \text{(Eq.1.19)}$$

The concentration of reactant N_A was measured by optical absorption at 250 nm in the external cell

$$N_A = D_A / \sigma_A (250 \text{ nm}) L_A \qquad \text{(Eq.1.20)}$$

in series with the reaction cell where absorption occurred at 248 nm. The ratio σ_A (248 nm) L_N / σ_A (250 nm) L_A = 1.493 so that the expression for quantum yield times cross section is

$$\Phi\, \sigma_N = \frac{D_N}{(1 - \exp^{-(1.493 D_A)}) I_o} \quad \text{(Method II)} \qquad \text{(Eq.1.21)}$$

where numerical values of chlorine nitrate cross section at 248 and 250 nm and the lengths of the reaction cell and the analysis cell (Table 1.2) are combined. In Method II. also, the cross section for chlorine nitrate cancels, except for the ratio between 248 and 250 nm.

Combining Eq.1.14, 1.18 and 1.21 we get the final expressions for the primary and secondary NO3 quantum yields as obtained by Method I and II:

Method I $\quad \Phi_1\sigma = C_1(\alpha - \Gamma) / [\alpha (I_o - I)]$ (Eq.1.22)

$\Phi_2\sigma = C_2(\beta - \Gamma) / [\beta (I_o - I)]$ (Eq.1.23)

Method II $\quad \Phi_1\sigma = C_1(\alpha - \Gamma) / [1.493\, \alpha\, D_A\, I_o]$ (Eq.1.24)

$\Phi_2\sigma = C_2(\beta - \Gamma) / [1.493\, \beta\, D_A\, I_o]$ (Eq.1.25)

Therefore, two sets of quantum yields are obtained for both primary and secondary NO_3. These values are shown in Table 1.4, as well as the average values. The average primary NO_3 quantum yield multiplied by the NO_3 cross section, $\Phi_1\sigma$ and twice the standard deviation of the observed values are

Method I $\quad \Phi_1\sigma = (1.90 \pm 0.34) \times 10^{-17}$ (Eq.1.26)

Method II $\quad \Phi_1\sigma = (1.88 \pm 0.23) \times 10^{-17}$

and the two averages of the secondary NO3 quantum yield times the cross section, $\Phi_2\sigma$, are

Method I $\quad \Phi_2\sigma = (1.73 \pm 0.53) \times 10^{-17}$ (Eq.1.27)

Method II $\quad \Phi_2\sigma = (1.71 \pm 0.42) \times 10^{-17}$

If the cross section is taken to be 1.9 x 10^{-17} cm^2 [11,12], the quantum yields are

$$\begin{array}{lll} \text{Method I} & \Phi_1 = 1.00 \pm 0.18 & \text{(Eq.1.28)} \\ \text{Method II} & \Phi_1 = 0.99 \pm 0.12 & \\ \text{Method I} & \Phi_2 = 0.91 \pm 0.28 & \\ \text{Method II} & \Phi_2 = 0.90 \pm 0.22 & \end{array}$$

as given in detail in Table 1.4. Using 1.9 x 10^{-17} cm^2 as cross section, Figure 1.3 shows plots of the primary NO_3 quantum yield against the carrier gas pressure from Method I and II. There is no noticeable dependence on the primary quantum yield from either method.

Similarly, Figure 1.4 shows the secondary NO_3 quantum yield from Method I and II plotted against the carrier gas pressures. The secondary quantum yield has an increasing trend, tending toward 1.0 as the carrier gas pressure increases to 100 torr.

The value of α, which is the pseudo first order rate constant of $NO_3(v>0)$ quenching into NO_3 X(0,0,0,0) level, is plotted against the carrier gas pressure in Figure 1.5 for N_2 and O_2, and the expected increase of with pressure is observed. The slope of the line gives the second-order, vibrational quenching rate constant, k_2, which for N_2 carrier gas is

$$k_2(N_2) = (4.22 \pm 0.22) \times 10^{-13}\ \text{cm}^3\ \text{molecule}^{-1}\ \text{s}^{-1}, \quad \text{(Eq.1.29)}$$

and for O_2 carrier gas is

$$k_2(O_2) = (4.11 \pm 0.08) \times 10^{-13}\ \text{cm}^3\ \text{molecule}^{-1}\ \text{s}^{-1}. \quad \text{(Eq.1.30)}$$

The values of Γ are much less than those of α and β and are listed in Table 1.2.

2. NO_3 detection at 679 nm A(0,0,0,0) ← X(0,0,0,1)

With the monitoring wavelength set to the first vibrational hot band at 679.0 nm, twelve chlorine nitrate photolyses at 248 nm were carried out with reactant concentration at 1.0×10^{16} molecule cm^{-3}, and with laser energies of 14 to 19 mj/pulse, Table 1.1(b). Unlike the study at 661.9 nm, there was strong absorption of the photolysis beam; about 2/3 the original pulse was absorbed along the 128 nm cell. The integrated form of Beer's law was used in these calculations.

An example of the optical density produced by the transition NO_3 A(0,0,0,0) ← X(0,0,0,1) as a function of time after photolysis is shown in Figure 1.6. Due to lower absorbance compared to 661.9 nm, a poorer signal level is evident in the absorption profile. The optical density can be related to concentration in the vibrationally excited state on the basis of Graham's [12] absorption spectrum and consideration of the equilibrium concentration of excited vibrational states at his temperature. The ν_4 mode of D_{3h} NO_3 is assigned as the doubly degenerate bending mode with 380 cm^{-1} vibrational frequency. At room temperature, this level has about 23% of the total population

$$N(0,0,0,1) / \Sigma N = 2\exp^{(-h\nu/kT)} \; / \; \{1-\exp^{(-h\nu/kT)}\}^{-2} \qquad \text{(Eq.1.31)}$$

So, dividing the room temperature bulk absorption cross section 5.9E-19 cm^2 by 0.23 gives 2.56E-18 cm^2 as the state-specific absorption cross section for the molecules actually in NO_3 X(0,0,0,1).

Unlike the 661.9 nm absorption profile, there are no distinct primary and secondary rises in this profile. The rise-time half way to the maximum concentration is about 1.6 μs, compared to about 4 μs primary rise at 661.9 nm. The secondary rise at 661.9 nm is about 200 μs, while the maximum is reached in 679 nm after about 15 μs, and the signal level stays relatively constant or decays slightly. In making these comparisons, it should be remembered that the experiments at 679 nm involves about five times as much reactant as that used at 661.9 nm.

We attempted to fit the growth curve of NO_3 absorption at 679 nm with a model involving primary and secondary formation in excited states higher than X(0,0,0,1), deactivation into X(0,0,0,1), and further deactivation into activation back out of state X(0,0,0,0). Fitting such a model to the observations led to parameters that contradict the physics of the kinetic model; the data are too noisy to support fitting so many parameters. However, examination of the quantities involved indicates that the leveling of the absorption after about 15 μs in Figure 1.6 corresponds to the vibrational state X(0,0,0,1) attaining thermal equilibrium with the other states of NO_3.

Assuming that the absorbing species in Figure 1.6 is at equilibrium with the ground state after 15 μs, the optical density observed after 15 μs is the quantity D_N needed in Eq.1.18 for Method I and in Eq.1.21 for the Method II to give the primary plus secondary quantum yield of NO_3 times the empirical bulk cross section at 679 nm.

For each run, Table 1.5 gives: the maximum optical density observed through the 128 cm tube, D, at times typically about 15 microseconds; $\Delta E = E_o - E$ photons cm^{-2} absorbed per pulse (see Table 1.1(b)); $\Phi\,\sigma = D / \Delta E$ cm^2; the total quantum yield for primary and secondary NO_3 according to Method I and Method II is found by dividing $\Phi\,\sigma$ by Graham's value for σ at 679 nm; the concentration of total NO_3 produced is found from D, the path length of the cell, and Graham's σ ; and the concentration of vibrationally excited NO_3 (0,0,0,1) is found from the Boltzmann factor (Eq.1.31). Figure 1.7 shows the total NO_3 quantum yield obtained from 679.0 nm observation with Method I and II, respectively, as a function of carrier gas pressure. The averaged total NO_3 quantum yield is

Method I = 1.7 ± 0.2

Method II = 1.8 ± 0.2

Combining all values gives the average of 1.7 ± 0.2. The plots of all pressure vs. quantum yield shows that the total NO_3 quantum yield approaches 2.0 at about 100 torr (Fig.1.7).

The adiabetic temperature rises in the photolysis volume were calculated, where the maximum such temperature rise was 7K, and the temperature rise for the case shown in Figure 1.6 was 4.5K.

DISCUSSION

1. Quantum Yield

Equation 1.18 shows the quantities used to measure NO_3 quantum yield to be : (i) the observed optical density of the NO_3 produced, (ii) the change of photons per square centimeter over the length of the tube in which chlorine nitrate absorbed ultraviolet radiation, and (iii) the NO_3 cross section. Possible systematic and other errors associated with each of these quantities is discussed below. The uncertainty of $ClONO_2$ absorption cross section is removed in this study by directly measuring the laser energy with and without reactant in the system.

The numerator of Equation 1.18 and 1.21 concerns the probe beam. At 661.9 nm the maximum observed optical density D_N is 0.3 (Figure 1.2), which is in the optimum region for an absorption measurement. This measurement is used by both Methods I and II. At 679.0 nm the maximum observed optical density is about 0.03 (Figure 1.6 and Table 1.5), and there is higher experimental error in making these measurements. The optical densities D_N (Eq.1.18,1.21) should not introduce a large systematic error, since they involve ratios of intensities in which much systematic errors should cancel.

The denominators of Equations 1.18 and 1.21 concern the number of ultraviolet photons absorbed per flash, and two methods are used to measure this quantity. Method I (Eq.1.18) makes two absolute photon intensity measurements, takes the difference of these two measurements, the differences are typically 15 % of the initial value for runs at 661.9 nm, and the differences are 60 - 65 % for runs at 679.0 nm. This method makes no use of the absorption cross section of chlorine nitrate, and so avoids uncertainty associated with that value. Method II measures one absolute photon intensity and the optical density of chlorine nitrate in a cell in series with the reaction cell. This method would be preferred if the fractional absorption of the photolysis beam is small. However, in these runs the degree of absorption is substantial, and the Method I is regarded as the more direct and better of the two. For studies at 661.9 nm, Method I gives 2% more photons absorbed than Method II; at 679 nm Method I gives 8 % more photons absorbed than Method II. The reasons for these differences is not known. The method of making absolute measurements of photons per laser pulse is given in the Experimental Section. Any systematic error in calibration of the Gen-Tec Pyroelectric joulemeter translates inversely into a systematic error in quantum yield for both methods.

Methods I and II implicitly require that the probe beam be contained inside the photolysis beam and that the photolysis beam is uniform. The quantity D_N in the numerator of Equations 1.18 and 1.21 is the optical density measured along the probe beam, which sweeps out a smaller volume than the photolysis beam. If the photolysis beam diverges, converges, or has non-uniform cross sectional area, properties of the gas photolyzed may differ significantly from those of the gas probed. This problem was recognized in the design of this experiment, and care was taken to make the photolysis beam uniform and parallel.

The quantum yield of NO_3 from $ClONO_2$ photolysis previously measured in this laboratory [2] is in disagreement with that obtained here. The other study gave the primary NO_3 quantum yield as 0.55 ± 0.2, whereas the values found here are 1.0 ± 0.2. The previous study used Method II [2], and the experimental conditions were not far from those used here. The major recognized differences concern the geometry of the photolysis beam. In this experiment the photolysis cell is 1.28 m long and in the other cell it was 1.9 m long.

The earlier experiment used a Lumonics laser beam with the unstable resonator. A purpose in using the unstable resonator is that it gives a beam of relatively low divergence. However, the beam is highly non-uniform over its cross sectional area; the most intense part has a hole in the middle. It is now felt that the absolute intensity of the photolysis beam was non-uniform, that the probe beam sampled a volume that was non-representative of the average photolysis volume, and that this non-uniformity led to a large systematic error in the earlier experiment.

The primary and secondary NO_3 quantum yields as measured here are inversely proportional to the literature value we used for the absorption cross section of NO_3. There have been a number of reports [13-16] addressing the room temperature absorption cross section of NO_3 at 661.9 nm, as well as its temperature dependence. There remain large uncertainties in its value. We prefer a value in the range of 1.9×10^{-17} cm^2 molecule^{-1} [11,12] up to $2.08 \pm 0.38 \times 10^{-17}$ cm^2 molecule^{-1}, Cantrell et al. [17]. Only Graham reports a cross section at 679.0 nm, and its value appears to be more uncertain than that at 661.9 nm.

The results of this study and our choice of NO_3 absorption cross section indicate that the primary process is Eq.1.1 with unit quantum yield, followed by the secondary process Eq.1.10 for which the NO_3 quantum yield approaches unity at high pressures of carrier gas. The statistical errors are such that other primary processes could occur at about ten percent level. If one uses higher NO_3 cross sections reported [15,16], all quantum yields reported here are reduced proportionally.

2. Nascent vibrational population in NO_3

Upon photolysis of chlorine nitrate at 248 nm, these appears to be no nascent population at NO_3 X(0,0,0,0), Figure 1.2, nor at X(0,0,0,1), Figure 1.6. At 248 nm photolysis, the excess energy after Cl-O bond dissociation in $ClONO_2$ is 26000 cm^{-1}. The Cl atom, with 881 cm^{-1} spin-orbit energy difference in $^2P_{1/2}$ - $^2P_{3/2}$, would carry only a small amount of internal energy. Since the NO_3 product does not further fragment based on our quantum yield results, this excess energy is partitioned between relative translational energy and internal excitation of NO_3. If all of the excess energy went into NO_3 internal excitation, it would amount to 25 vibrational quanta of excitation (using 1000 cm^{-1} as the average vibrational frequency of NO_3). It is concluded that upon photolysis of $ClONO_2$ the nascent population is vibrationally excited, possibly highly excited, and there is no significant population in X(0,0,0,0) or X(0,0,0,1).

3. Kinetic parameters.

The observed similarity in quenching constant of NO_3 X(v>0) by N_2 and O_2 can be understood based on the similarity of shape (diatomic molecule) and the mass of the colliding M gases, and the intermolecular potential in what is essentially V -> T energy transfer. The quenching constant of $4.2 \pm 0.2 \times 10^{-13}$ cm^3 $molecule^{-1}$ s^{-1} deduced from this work for the step

$$NO_3(v>0) + M \rightarrow NO_3\ X(0,0,0,0) + M\ (M= N_2, O_2),$$

is 2.6 times larger than the quenching constant reported for the NO_3 (v>0) produced from N_2O_5 photolysis at 248 nm [7]. This difference may be the reflection of differences in the internal population distribution of NO_3 from each photodissociation.

ACKNOWLEDGEMENTS

This work at the University of California and the Lawrence Berkeley Laboratory was supported by the Director, Office of Energy Research, Office of Basic Energy Sciences, Chemical Sciences Division of the U.S. Department of Energy under Contract No. DE-AC03-76SF00098.

REFERENCES

1. F.S. Rowland, J.E. Spencer and M.J. Molina, J.Phys.Chem. 80 (1976) 2711; 80 (1976) 2713.
2. W.J. Marinelli and H.S. Johnston, Chem. Phys. Lett., 93 (1982) 127 and references therein.
3. J.J. Margitan, J. Phys. Chem., 87 (1083) 674 and references therein.
4. H.H. Nelson, L. Pasternack and J.R. McDonald, J. Phys. Chem., 87 (1983) 1286.
5. T. Ishiwata, I. Fujiwara, Y. Naruge, K. Obi and I. Tanaka, J. Phys. Chem., 87 (1983) 1349.
6. T. Ishiwata, I. Tanaka, K. Kawaguchi and E. Hirota, J. Chem. Phys., 82 (1985) 2196.
7. D. Swanson, B. Kan and H.S. Johnston, J. Phys. Chem., 88 (1984) 3115.
8. M. Schmeisser, Inorg. Syn., 9 (1967) 127.
9. NASA PAnel for Data Evaluation , "Chemical Kinetics and Photochemical Data for USe in Stratospheric Modelling, Evalution No.7", JPL Publication 85-87, Jet Propulsion Laboratory, 1985.
10. L.T. Molina and M.J. Molina, J. Photochem., 11 (1979) 139.
11. W.J. Marinelli, D.M. Swanson and H.S. Johnston, J. Chem. Phys., 76 (1982) 2864.
12. R.A. Graham, Ph.D. Thesis, University of California, Berkeley, 1975.
13. A.R. Ravishankara and P.H. Wine, Chem. Phys. Lett., 101 (1983) 73.
14. J.P. Burrows, G.S. Tyndall and G.K. Moortgat, J. Phys. Chem., 89 (1985) 4848.
15. S.P. Snader, J. Phys. Chem., 90 (1986) 4135.
16. C.A. Cantrell, J.A. Davidson, R.E. Shetter, B.A. Andersonand J.G. Calvert, J. Phys. Chem., 91 (1987) 5858.

Table 1.1(a): Experimental conditions for NO_3 observation at 661.9 nm.

Carrier gas			$[ClONO_2] / 10^{13}$	E_0	E	ΔE	Photons abs./10^{13} cm^3	
Run #	torr		mole. cm-3		mj/pulse		Method I	Method II
1	20.5	N_2	240	19.1	15.7	3.4	6.63	7.22
2	20.6	N_2	258	19.4	15.1	4.3	8.38	7.82
3	20.6	N_2	181	19.2	16.4	2.8	5.46	3.75
4	11.6	N_2	182	18.5	15.5	3.0	5.85	5.44
5	27.8	N_2	182	18.9	15.6	3.3	6.43	5.55
6	38.8	N_2	182	18.9	16.2	2.7	5.26	5.55
7	45.4	N_2	185	23.3	19.6	3.7	7.21	6.95
8	54.9	N_2	180	22.8	19.6	3.2	6.24	6.63
9	44.5	N_2	181	22.9	19.6	3.3	6.43	6.69
10	36.5	N_2	181	22.7	19.6	3.1	6.04	6.64
11	26.5	N_2	182	22.6	19.5	3.1	6.04	6.64
12	16.7	N_2	183	22.0	19.1	2.9	5.65	6.50
13	95.2	O_2	182	18.0	15.3	2.7	5.26	5.29
14	74.2	O_2	180	17.2	14.8	2.4	4.68	5.00
15	50.7	O_2	180	17.7	14.8	2.9	5.65	5.15
16	34.8	O_2	181	16.9	14.4	2.5	4.87	4.94
17	17.3	O_2	181	17.2	14.2	3.0	5.85	5.03
18	20.1	O_2	34	17.9	17.4	0.5	0.98	1.05
19	20.4	O_2	301	17.5	12.9	4.6	8.97	8.08

Runs are recorded with 100 ns/channel time resolution.

Table 1.1(b): Experimental conditions for NO_3 X(0,0,0,1) observation at 679.0 nm.

Carrier gas			[$ClONO_2$] / 10^{13}	E_0	E	ΔE	Photons abs./10^{13} cm^3	
run	#		molec.cm^{-3}		mj/pulse		Method I	Method II
1	10.6	N_2	1010	18.7	6.7	12.0	23.4	21.6
2	20.0	N_2	1010	18.7	6.5	12.2	23.8	21.6
3	30.0	N_2	1010	18.5	6.6	11.9	23.2	21.4
4	40.6	N_2	1010	18.4	6.4	12.0	23.4	21.4
5	50.5	N_2	1020	18.4	6.3	12.1	23.6	21.5
6	60.2	N_2	1020	18.0	6.2	11.8	23.0	21.1
7	76.4	N_2	1020	18.1	6.4	11.7	22.8	21.2
8	97.3	N_2	1020	18.0	6.3	11.7	22.8	21.1
9	5.1	N_2	1010	15.0	5.3	9.7	18.5	17.4
10	15.2	N_2	1010	14.2	5.2	9.0	17.6	16.5
11	25.0	N_2	1010	13.7	5.1	8.6	16.8	15.9
12	45.4	N_2	1010	13.8	5.1	8.7	17.0	16.0

Runs were recorded with 50 ns/channel time resolution.

Table 1.2: Parameters used for analysis of data.

1) Photolysis Volume = 0.50 cm^2 x 128 cm = 64 cm^3

2) Absorption Cross Sections (298 K)

$ClONO_2$	248 nm	7.0 E-19 cm^2	(Photolysis wavelength) [10]
	250 nm	6.0 E-19 cm^2	(UV monitoring wavelength) [10]
NO_3	661.9 nm	1.90 E-17 cm^2	(NO_3 X(0,0,0,0) probe) [11]
	679.0 nm	5.9 E-17 cm^2	(NO_3 X(0,0,0,1) probe) [12]

The bulk NO_3 room temperature absorption cross section at 679.0 nm is corrected for the Boltzmann factor for the first excited vibrational level, (5.9 E-19) / (0.23) = 2.56 E-18 cm^2, to give the state specific cross section (v = 1, 380 cm-1, doubly degenerate ν_4 mode, see Eq.1.31).

Table 1.3: Fitted parameters from non-linear least squares analysis of NO_3 absorption profiles as a function of time at 661.9 nm.

	First order k /s^{-1}			Pre-exp factors		Ratios	
Run	$\alpha/10^5$	$\Gamma/10^2$	$\beta/10^4$	C_1	C_2	$\alpha / (\alpha - \Gamma)$	$\beta^* / (\beta^* - \Gamma)$
1	3.100	3.628	2.50	0.191	0.143	1.001	1.015
2	2.762	2.386	2.68	0.203	0.151	1.001	1.009
3	2.902	2.673	1.88	0.139	0.110	1.001	1.014
4	1.499	4.377	1.89	0.152	0.109	1.003	1.024
5	3.979	3.959	1.89	0.138	0.133	1.001	1.021
6	5.010	3.418	1.89	0.133	0.132	1.001	1.018
7	6.153	3.341	1.92	0.156	0.148	1.001	1.018
8	7.504	3.566	1.87	0.155	0.150	1.000	1.019
9	6.377	3.773	1.87	0.157	0.147	1.001	1.020
10	4.961	3.380	1.88	0.154	0.142	1.001	1.018
11	3.544	3.326	1.89	0.148	0.134	1.001	1.018
12	2.179	4.204	1.90	0.153	0.128	1.002	1.023
13	13.19	4.048	1.89	0.134	0.134	1.000	1.022
14	9.550	4.722	1.87	0.199	0.123	1.000	1.026
15	6.715	3.748	1.87	0.124	0.120	1.000	1.020
16	4.628	4.552	1.88	0.122	0.118	1.001	1.025
17	2.403	6.670	1.88	0.125	0.117	1.003	1.037
18	3.126	7.000	0.35	0.023	0.039	1.002	1.246
19	3.043	3.593	3.13	0.177	0.164	1.001	1.012

* β was calculated with k_2 literature value (for $Cl + ClONO_2 \rightarrow Cl_2 + NO_3$) of 1.04 E-11 $cm^3\ s^{-1}$. This value was fixed during the fitting.

Table 1.4: Primary and secondary NO_3 Quantum Yields from 661.9 nm absorption od NO_3 using = 1.9E-17 cm^2 for NO_3 cross section [11,12]. (See Eq.1.22-1.28)

	Primary NO_3 Quantum Yield		Secondary NO_3 Quantum Yield	
Run#	Method I	Method II	Method I	Method II
1	1.19	1.09	0.88	0.80
2	1.00	1.06	0.73	0.79
3	1.04	1.02	0.82	0.80
4	1.06	1.14	0.75	0.80
5	0.88	1.02	0.83	0.96
6	1.03	0.98	1.02	0.97
7	0.89	0.92	0.83	0.86
8	1.02	0.96	0.97	0.91
9	1.00	0.96	0.92	0.88
10	1.05	0.95	0.96	0.88
11	1.00	0.91	0.90	0.82
12	1.11	0.97	0.91	0.79
13	1.05	1.05	1.03	1.02
14	1.05	0.98	1.05	0.98
15	0.90	0.95	0.86	0.94
16	1.03	1.01	0.97	0.96
17	0.88	1.02	0.80	0.93
18	0.95	0.89	1.35	1.25
19	0.81	0.90	0.74	0.83
Avg±2σ	1.00±0.18	0.99±0.12	0.91±0.28	0.90±0.22

Table 1.5: Fitted parameters and Total Quantum Yield of NO_3 based on absorption at 679.0 nm. Φ (total) is sum of primary and secondary quantum yield. Third and fourth columns are for Method I.

Run#	D(max)	$\Delta E/cm^{-2}$	$\Phi\sigma/cm^2$	Φ(total)		$[NO_3]/10^{13}$ cm^{-3}	
	10^{-2}	10^{16} photons	10^{-19}	I	II	v=1	total
1	2.64	3.00	8.81	1.5	1.6	8.1	35
2	2.93	3.05	9.62	1.6	1.8	9.0	39
3	2.85	2.97	9.60	1.6	1.8	8.7	38
4	2.85	3.00	9.50	1.6	1.8	8.7	38
5	3.15	3.02	10.4	1.8	2.0	9.6	42
6	3.15	2.94	10.7	1.8	2.0	9.6	42
7	3.08	2.92	10.6	1.8	1.9	9.4	41
8	3.08	2.92	10.6	1.8	1.9	9.4	41
9	2.18	2.37	9.21	1.6	1.7	6.7	29
10	2.03	2.25	9.01	1.5	1.6	6.2	27
11	2.10	2.15	9.77	1.7	1.8	6.4	28
12	2.18	2.18	10.0	1.7	1.8	6.7	29

Figure Captions

Fig. 1.1: The block diagram of experimental apparatus.

Fig.1.2: Time resolved absorption profile of NO_3 at 661.9 nm upon photolysis. Two distinct rises with different time constants are evident. The curves obtained from non-linear least square fitting with the expression described in Results is shown along with the experimental profile. This spectrum corresponds to Run # 9 in Table 1.1(a).

Fig.1.3: Primary NO_3 quantum yield estimated with Method I and II plotted against the carrier gas pressure. Circles represent N_2 carrier gas, and the triangles the O_2 carrier gas. The linear least square fitting through the points yielded the solid line where error bar represent one standard deviation.

Fig.1.4: Secondary NO_3 quantum yield, which was the reaction product of Cl + $ClONO_2$. Compare Figure 1.3. The linear least square fit through the points resulted in the solid lines, which shows the slight increasing trend as the pressure of carrier gas increases.

Fig.1.5: Primary NO_3 reciprocal rise-time, obtained from non-linear least square fitting of 661.9 nm absorption profile, plotted against the carrier gas pressure. The solid line was from the linear least square fit through the data points, where slope yielded the quenching rate constant of $NO_3(v>0)$ + M -> NO_3 X(0,0,0,0) + M as (4.22 ± 0.22) E-13 cm^3 $molecules^{-1}$ s^{-1} for N_2 and for O_2 it is (4.11 ± 0.08)E-13 cm^3 $molecules^{-1}$ s^{-1}.

Fig.1.6: Observed optical density of NO_3 at 679.0 nm as produced by photolysis of chlorine nitrate with radiation at 248 nm. The maximum optical density, which appears to be reached 15 μs after the photolysis, is entered as D in Table 1.5. This figure corresponds to Run # 1 in Table 1.1(b).

Fig.1.7: Total NO_3 quantum yield estimated with Method I and II, observed from 679.0 nm absorption profile against the N_2 carrier gas pressure. The solid line is the linear least square fit through the data points, which approaches 2.0 at higher pressure.

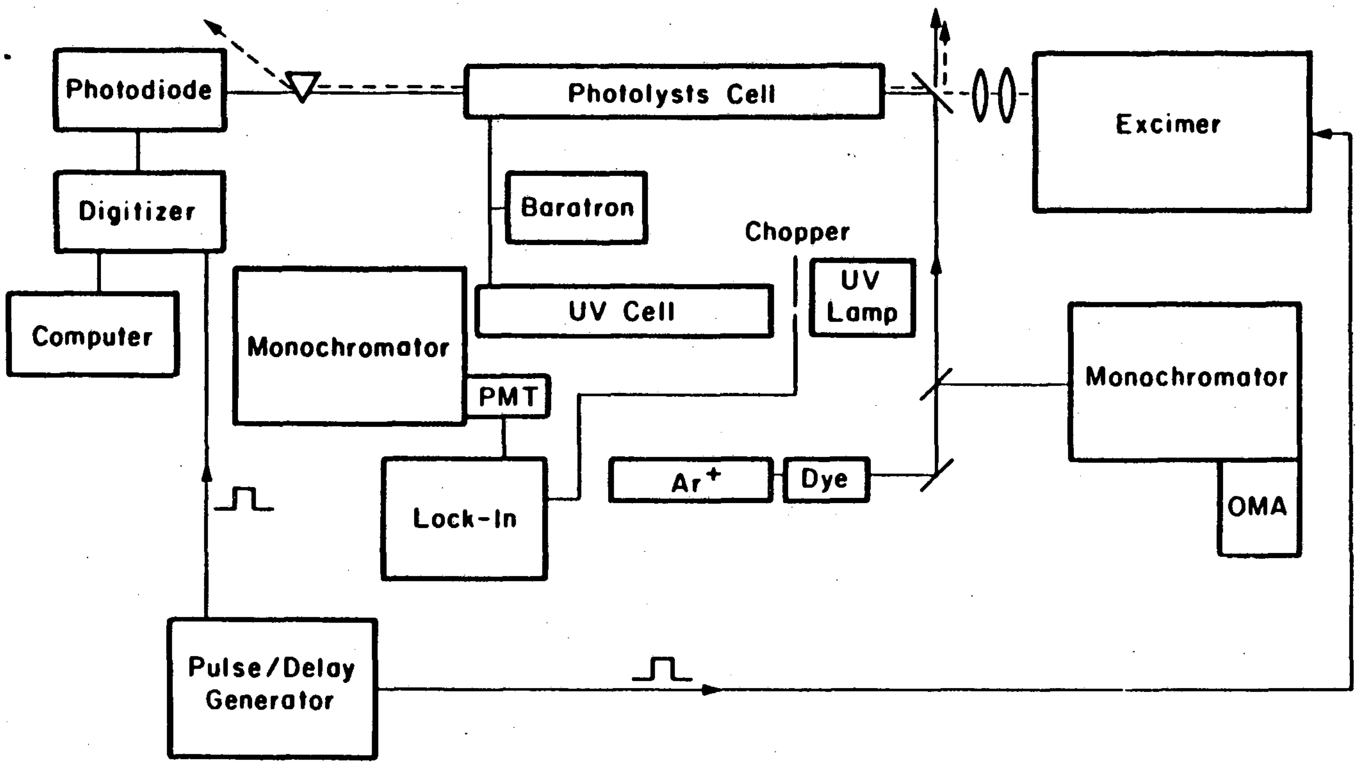
Photodiode
Photolysts Cell
Excimer
Digitizer
Baratron
Chopper
UV Lamp
Computer
Monochromator
UV Cell
Monochromator
PMT
Lock-In
Ar^+
Dye
OMA
Pulse/Delay Generator

Figure 1.1

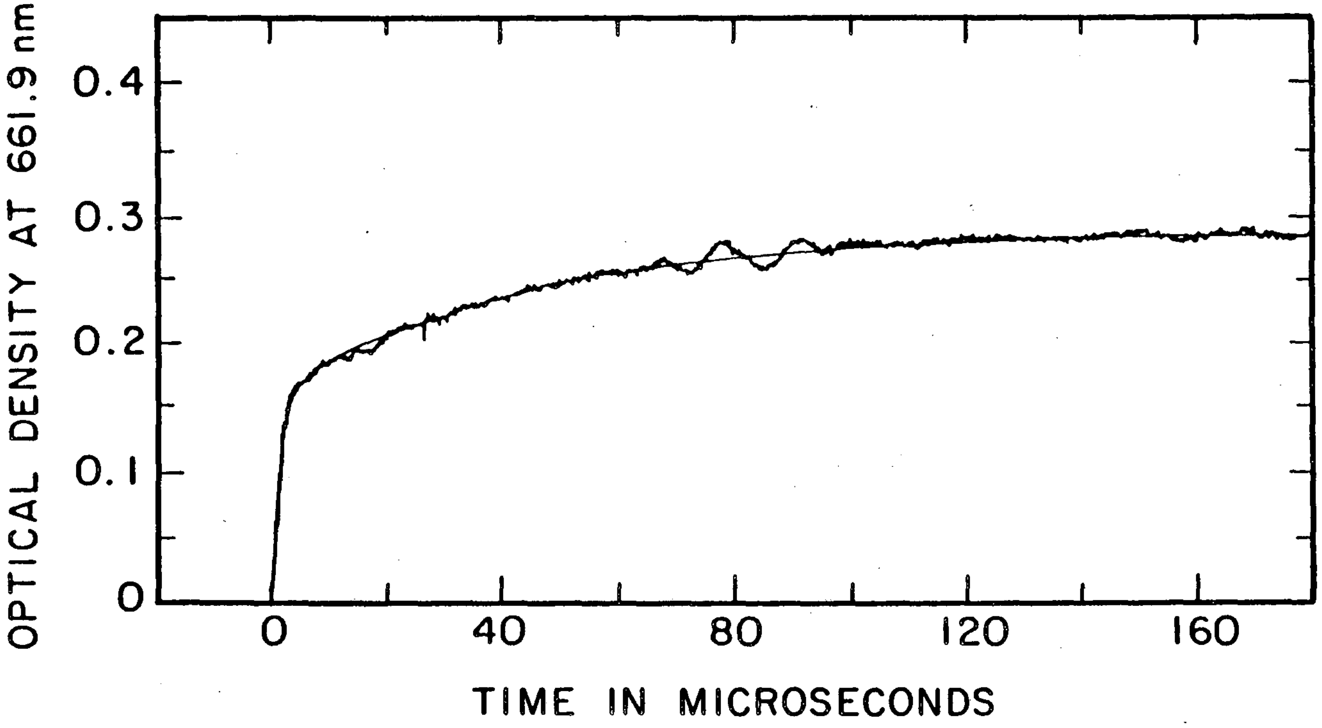
OPTICAL DENSITY AT 661.9 nm
0.4
0.3
0.2
0.1
0
0
40
80
120
160
TIME IN MICROSECONDS

Figure 1.2

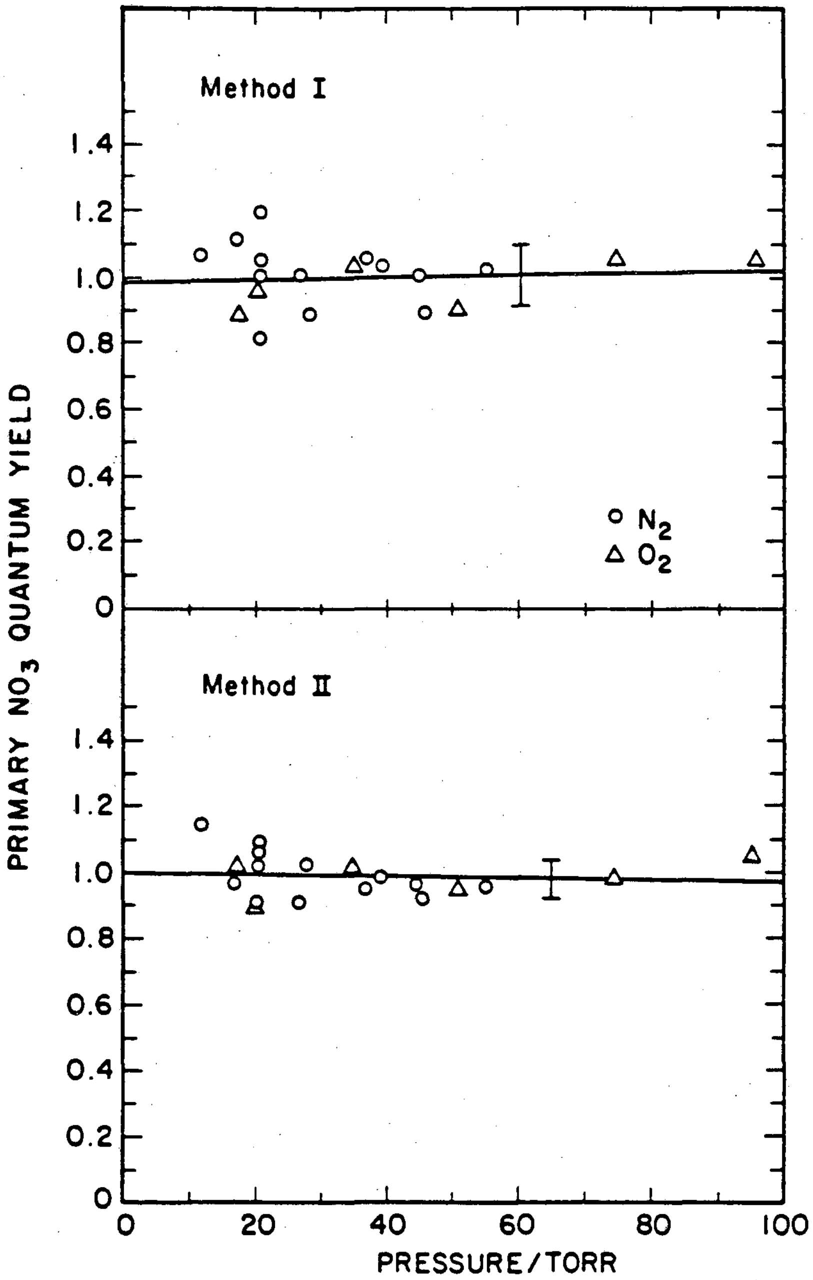
Method I
Method II
PRIMARY NO_3 QUANTUM YIELD
PRESSURE/TORR
○ N_2
△ O_2
0
0.2
0.4
0.6
0.8
1.0
1.2
1.4
0
20
40
60
80
100

Figure 1.3

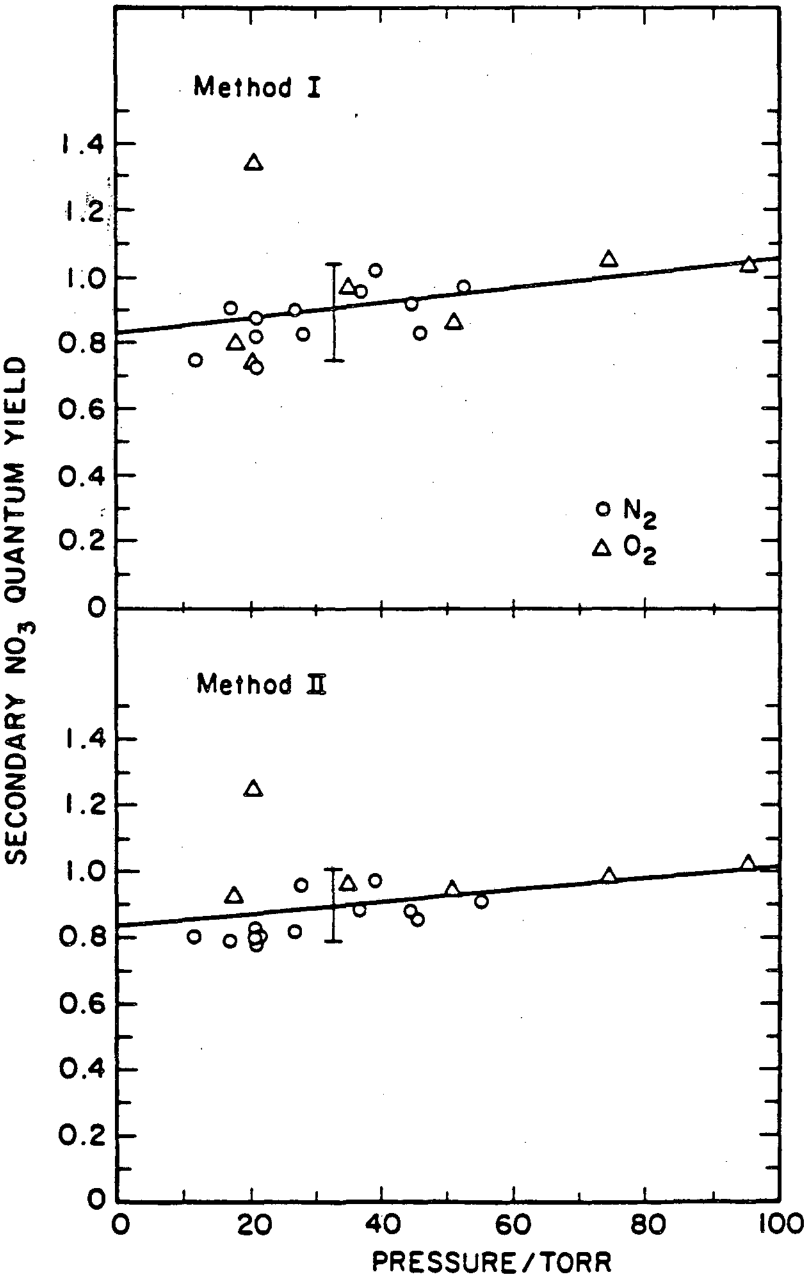
Method I
Method II
SECONDARY NO_3 QUANTUM YIELD
PRESSURE / TORR
○ N_2
△ O_2
0
0.2
0.4
0.6
0.8
1.0
1.2
1.4
0
20
40
60
80
100

Figure 1.4

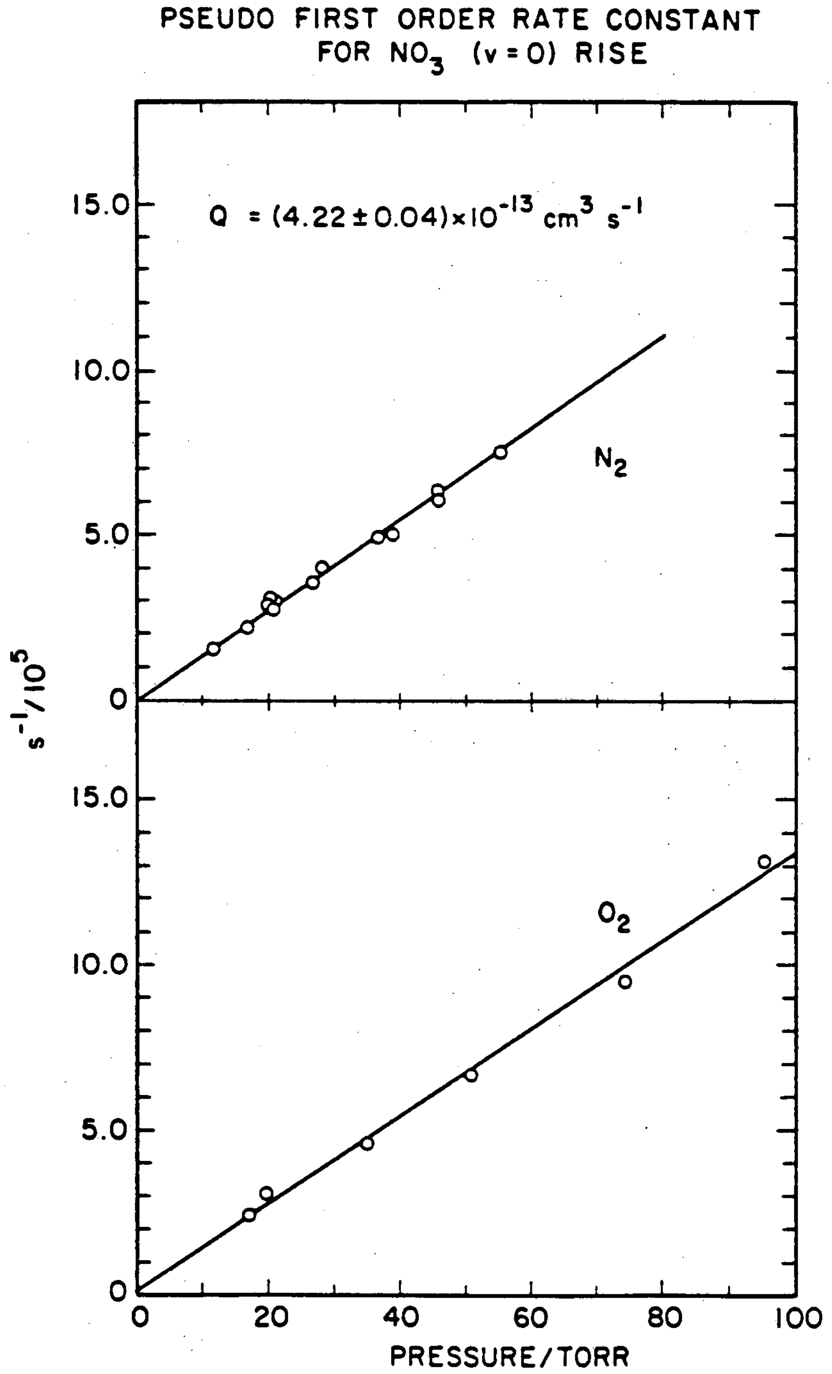
PSEUDO FIRST ORDER RATE CONSTANT FOR NO_3 (v = 0) RISE
Q = $(4.22 \pm 0.04) \times 10^{-13}$ cm^3 s^{-1}
N_2
O_2
$s^{-1}/10^5$
15.0
10.0
5.0
0
0
20
40
60
80
100
PRESSURE/TORR

Figure 1.5

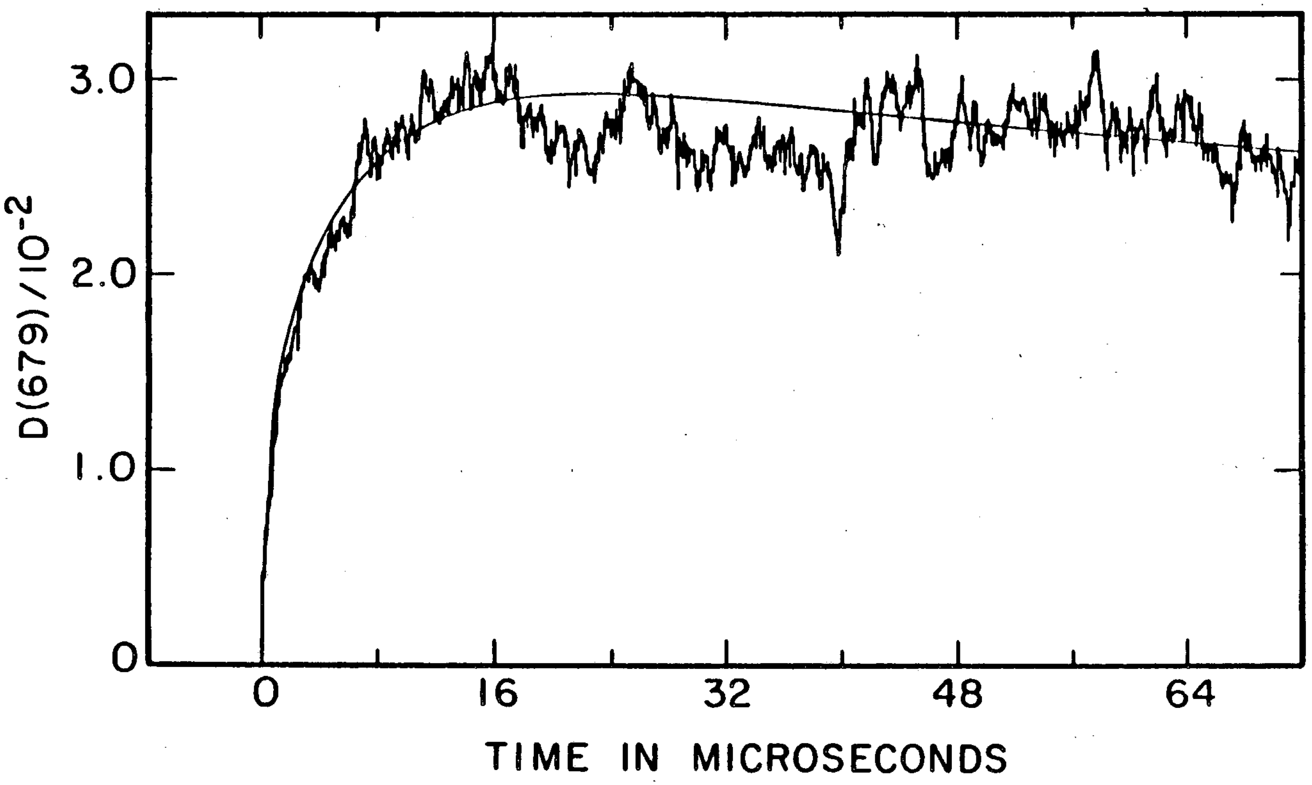

Figure 1.6

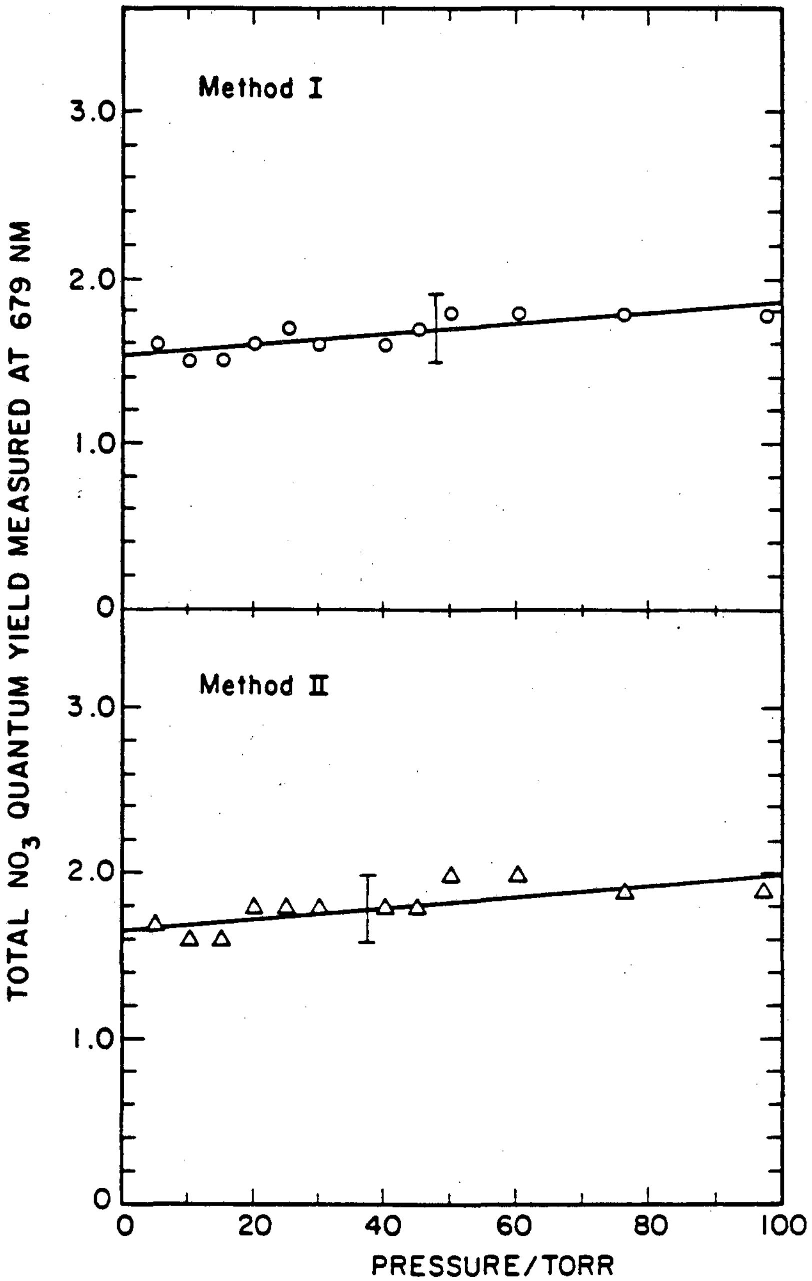
Method I
Method II
TOTAL NO_3 QUANTUM YIELD MEASURED AT 679 NM
3.0
2.0
1.0
0
0
20
40
60
80
100
PRESSURE/TORR

Figure 1.7

CHAPTER 2. Study of Dinitrogen Pentoxide (N_2O_5) photodissociation at 248 and 193 nm via NO_2^* PIF technique.

ABSTRACT

The Photolysis Induced Fluorescence (PIF) method is derived which incorporates many improvements over the first report [1]. By representing the NO_2^* emission spectrum as a linear combination of monoenergetically prepared NO_2 Laser Induced Fluorescence spectra, it provides the internal energy distribution ($P(E_{int})$) of NO_2^* from photolysis. The PIF analysis is applied to NO_2^*emission spectra from 193 and 248 nm photolysis of N_2O_5. From this work and with the report on $O(^3P)$ quantum yields from another group[2], the following conclusions were drawn.

1) At 248 nm photolysis, these two channels appear to account for the majority of photolysis.

$$N_2O_5 + h\nu \dashrightarrow \quad NO_3(X) + NO_2^*(A,B) \qquad \text{Yield} = 0.3$$

$$NO_3(X) + NO(X) + O(^3P) \qquad \text{Yield} = 0.7$$

2) At 193 nm photolysis, the channel producing $NO(X) + O(^3P)$ products appears to be even more extensive than at 248 nm. These findings are consistent with our tentative assignments of $\pi \to \pi^*$ and $n \to \pi^*$ at 193 nm and 248 nm absorption of N_2O_5, which suggest highly localized initial excitation in NO_2^* group in the parent molecule followed by predissociation into NO_3 and NO_2 fragments with much of the excess energy in the NO_2 fragment. The possible utility of the PIF method to measure collision induced energy transfer was qualitatively demonstrated. NO^* emission was observed readily at 193 nm and under high laser fluence at 248 nm.

INTRODUCTION

The importance of studying N_2O_5 photodissociation stems, in part, from its role as a reservoir molecule of NO_x species in the atmosphere [3]. In order to properly assess the importance of the N_2O_5 molecule in atmospheric chemistry, accurate information on the photolysis channels and quantum yields of each photofragment are essential. The energy content of each photofragment and the pattern of excess energy partitioning into different degrees of freedom (translational, rotational and vibrational) provide clues in deducing photodissociation dynamics.

In Figure 2.1, the UV absorption spectrum of room temperature N_2O_5 [4] and the HNO_3 absorption spectrum [5] are depicted in log scale. The absorption spectrum of N_2O_5 is smooth and continuous, decreasing in magnitude as the wavelength of absorption increases. The HNO_3 absorption profile shows two absorption peaks, a strong absorption near 190 nm (assigned to be $\pi \rightarrow \pi^*$) and a weaker absorption near 270 nm (assigned to be $n \rightarrow \pi^*$) [6,7]. The nature of the electronic states involving N_2O_5 photodissociation at 193 nm and 248 nm is not known. The tentative assignments are made based on theoretical calculations on HNO_3 and other NO_2-X systems [6,7], where 193 nm absorption of N_2O_5 involves $\pi \rightarrow \pi^*$ transition while $n \rightarrow \pi^*$ transition is involved in 248 nm absorption.

The structure of N_2O_5 has been studied by McClelland et al.[8] by electron diffraction on a gas phase sample. The deduced structure consists of two NO_2 groups joined non-linearly to the central O atom, with each NO_2 subgroup undergoing free rotations along the central N-O bond. The most stable structure corresponds to the two NO_2 group staggered with dihedral angles of 30^o each, with respect to the plane of central N-O-N bond. This is depicted in Figure 2.2.

In order to positively identify the photolysis channels accessed and to measure quantum yields of primary photoproducts, direct detection of each nascent photofragment under well characterized conditions is necessary. Previous studies of N_2O_5

photodissociation employing direct detection of primary fragments began to appear only recently [2,9-11]. With the advent of these reports, however, an interesting contradiction began to emerge.

It has been experimentally shown that the primary NO_3 quantum yield is nearly unity between 248 and 351 nm photolysis [2,9-10]. There has also been a number of primary $O(^3P)$ atom quantum yield measurements reported. Margitan [11] reported $O(^3P)$ atom yield of 0.35±0.15 when N_2O_5 was photodissociated N_2O_5 at 266 nm. Barker et al. [10] reported $O(^3P)$ atom production of less than 0.1 when it was photodissociated at 290 nm. Ravishankara et al. [2] reported wavelength dependence in $O(^3P)$ atom yield of 0.72, 0.38, 0.21, 0.15, and 0.0 at 248, 266, 287, 289, and above 307 nm respectively. All these studies suggest the following photolytic channels;

$$N_2O_5 + hv \text{ --> } NO_2(X) + NO_3(X) \quad \text{(Eq. 2.1)}$$

$$NO(X) + O(^3P) + NO_3(X) \quad \text{(Eq. 2.2)}$$

These photolytic channels imply that the stronger N-O bond in NO_2 (E(N-O) = 72 kcal mole^{-1}) breaks instead of the weaker one in NO_3 (E(N-O) = 49 kcal mole^{-1}), which would appear to be a highly non-statistical localization of energy.

The study of N_2O_5 photodissociation was initiated with an attempt to find any evidence of electronically excited NO_3 fragments upon UV photolysis. Instead, a continuous emission spectrum starting from ~ 400 nm extending well into the near infrared was observed upon UV photolysis of N_2O_5. This emission has since been identified as NO_2^* fluorescence [1].

There is a well appreciated difficulty in applying quantum state resolved spectroscopy to the NO_2 molecule. These difficulties have been summarized by Zare et al. [13], who show the core of the difficulties. As an introduction to the scope of the problem, a small space is devoted here. In Figure 2.3(a), a low resolution room temperature NO_2 absorption spectrum is reproduced. There are number of sharp absorption features, some of which can be identified as various vibrational progressions. Upon closer inspection under much higher resolution, one finds a wealth of absorption features that must be the delight of any spectroscopists. A portion of the assigned spectral region by Zare et.al.is adopted from their work [13] and is shown as Fig.2.3(b). However, such spectral assignments which provide spectroscopic constants of rovibrational states in the ground and excited electronic states cannot be used to assign and to predict the spectral features observed in another part of the spectral region. In fact, of ~ 18000 absorption features observed by Zare et. al. [13] between 550 and 650 nm, only a small fraction could be positively assigned. The NO_2 seeded in the molecular beam, which exhibits considerable cooling of vibration and in rotation, was studied with LIF excitation by Smalley et.al. [14]. Their work resulted in assigning more than 140 vibrational origins of NO_2 between 17700 and 14900 cm^{-1}. Sub-Doppler spectroscopic technique was employed by Demtroder et.al. [15] in their study of rotational features. These and many other works (as discussed in Zare et al. review [13]) showed how complex and difficult traditional quantum state resolved spectroscopic assignments can be on NO_2 molecule. In fact, there is a growing body of reports that question the validity of quantum numbers [16] that are used for spectral assignments.

The source of these difficulties have been identified to originate from interaction among low lying electronic states and the corresponding energy region of high vibrational ground electronic state, also known as Douglas effect [17]. The Figure 2.4 shows the electronic states of NO_2 calculated by Gillispie et.al. with ab initio method [18]. In addition to the ground electronic state ($^1A_1$), three other electronic states ($^2B_2$,$^2B_1$, and $^2A_2$) are energetically accessible with less than 2 eV of energy. Through mainly vibronic [13,19] interactions, these states are coupled to give rise to intractable quantum states.

These complexities prevent the deduction of the nascent quantum state distribution of NO_2^*. A new method of analyzing the fluorescence emission profile was devised, which could provide the distribution profile of internal energy, $P(E_{int})$. This technique was reported before [1], where NO_2^* from N_2O_5 photolysis at 266 nm to 304.5 nm was observed under conditions involving about one hard sphere collision. An additional photolysis channel was suggested to explain the observation of NO_2^*emission.

N_2O_5 + hv --->

$NO_3(X) + NO_2(X)$	$> 7458\ cm^{-1}$	from	(Eq. 2.1)
$NO_3(X) + NO(X) + O(^3P)$	$> 32570\ cm^{-1}$	from	(Eq. 2.2)
$NO_3(X) + NO_2^*(A,B)$	$> 17208, 22288\ cm^{-1}$		(Eq. 2.3)

A number of refinements have been made on the experimental apparatus since the first report [1]. The sensitivity of the detection system was increased by improving the optical arrangement of the fluorescence detection, which allowed NO_2^* PIF (Photolysis Induced Fluorescence) detection to be collision-free. Far more complete coverage of excitation wavelengths in NO_2 LIF emission curves to provide a more thorough experimental coverage of X_L, improvement in the analysis of NO_2 LIF spectra which includes all emission features (discreet as well as continuum), and better characterization of instrument response over the spectral range are some of the improvements that have been added. By quantifying the NO_2^* emission yield from photolysis, the relative importance of NO_2^* production channel (Eq.2.3) became possible.

In this chapter, the derivation of Photolysis Induced Fluorescence (PIF) method is presented followed by results of PIF analysis on NO_2^* emission from N_2O_5 photolysis at 193 nm and 248 nm. The uncertainties involved in the PIF method and resulting $P(E_{int})$ distributions are discussed. The obtained $P(E_{int})$ profiles of NO_2^* are then utilized to deduce the photodissociation dynamics in UV photolysis of N_2O_5.

EXPERIMENTAL

The experimental arrangement is shown in Fig.2.5 as a block diagram. An excimer laser (Lumonics Model TE 861M-2), operating on ArF (193 nm) and KrF (248 nm), was used as the photolysis source. For NO_2 LIF experiments, an excimer pumped dye laser (Lumonics Model EPD-330) with output ranging from 399.8 nm to 672.6 nm was used. The line width of the dye laser, estimated from the observed linewidth of the NO two photon LIF spectrum, was ~0.8 cm^{-1}. These outputs were collimated with an iris before the fluorescence cell, and the beam diameter was kept at about 3 mm in diameter. Laser power was measured with a power meter (Scientech 360001), calibrated against the factory calibrated power meter. Shot to shot variations of the laser pulse energy were measured by monitoring laser scatter off the input window with a photodiode (EG&G GPD100) and fed to a boxcar averager (SRS 250). The sample pressure was measured with a capacitance manometer (Baratron model 310AHS-10) at each observation point and stored in a computer.

The NO_2^* fluorescence emission was collected with a f/2 quartz lens, and focused onto the input slit of a 1 meter monochromator (Interactive Technology Model CT-103) which had a 1200 lines/mm grating blazed at 500 nm and quartz slit lenses. At 2 mm input and output slit widths, the monochromator resolution was about 1.6 nm in the visible (8.1A/mm reciprocal linear dispersion at 200 nm). The dispersed fluorescence was focused onto a PMT (RCA 31034), which was kept cold at -30 degree C. The signal from the PMT was amplified by a home assembled amplifier (Avantek GPD 461,462 & 463) and sent to a gated integrater/boxcar averager (SRS 250) for time resolved signal detection.

For the nascent fluorescence observation, gate delay of 10 to 30 ns and the gate width of 30 ns were typically used. Sample pressure was typically 5 mtorr for nascent fluorescence detection, resulting in ~0.3% of the molecules undergoing a hard sphere collision. For time delayed observation, the gate width was kept at 30ns while the gate delay was varied. The experimental conditions are compiled and shown in Tables 2.3 and 2.7 for NO_2 LIF and N_2O_5 PIF runs, respectively. The processed fluorescence signal from the boxcar was sent to a computer (IBM/AT) equipped with an A/D board (Data Translation 2800). The ASYST [23] software installed in the computer controlled A/D board for data acquisition, analysis of the data, and the plotting. Sample pressure and laser power were monitored throughout the entire scan and stored for normalizing each spectrum.

At each wavelength of observation, 100 shots were averaged at 10 Hz repetition rate. Then, the monochromator was advanced by 2 nm to the next observation wavelength and the signal averaging resumed. Each spectrum was taken 30 to 50 nm before the onset of fluorescence emission in order to establish the baseline and covered beyond 800 nm where the PMT response began to fall off rapidly.

The spectral response curve of the detection arrangement (i.e. convolution of PMT spectral response, monochromator spectral sensitivity, transmittance of optics, etc.) was obtained by dispersing and detecting the emission profile from a tungsten lamp. The emitting surface temperature of tungsten strip was measured with an optical pyrometer. Knowing the temperature of the emitting surface and the tungsten emissivity profile at that temperature [24], the instrument response function was generated and shown in Fig.2.6. The dotted line at 398 nm corresponds to the predissociation limit of NO_2, below which wavelength no NO_2^* emission is detected. Each spectrum was subjected to the spectral response correction with this curve. The scattered laser light in each NO_2 LIF spectrum was subtracted from the observed emission spectrum by an empty cell emission spectrum at each wavelength of excitation.

The N_2O_5 was prepared by the method of Schott and Davidson [25]. The O_2 was passed through a heated copper tube and a P_2O_5 drying column to remove moisture and hydrocarbon impurities before it entered the ozonizer (Ozone Research & Equipment Corporation). A small portion of purified O_2 was bubbled through a pyrex bubbler containing NO_2, and the NO_2 reacted with the O_3 from the ozonizer at the T-joint. The

N_2O_5 was collected in a trap held at -77 ^oC with an isopropyl alcohol/dry ice slush bath. Each batch of N_2O_5 was pumped on while held in CCl_4 slush bath (-29^{o}C) before each experiment. The purity of the sample was checked with Cary spectrometer by measuring UV absorption profile of N_2O_5 [4] in a 10 cm quartz gas cell. The main impurity was believed to be HNO_3 formed from the reaction between N_2O_5 and the residual moisture on the wall of the trap. About 10% - 15% HNO_3 was estimated in each batch of freshly prepared N_2O_5, but no further attempts were made to purify the sample because purification did not yield reduction of HNO_3 impurity level. The absorption cross section of HNO_3 [5] is smaller than N_2O_5 [4] by about a factor of 10 in 248 nm, and any interference from photolysis of HNO_3 is considered small. At 193 nm, however, HNO_3 absorption cross section is slightly larger than N_2O_5 and the interference from HNO_3 can be appreciable. Given the level of HNO_3 impurity in N_2O_5, however, interference is not thought be too serious . The NO_2 was not a detectable impurity because it had reacted in the presence of excess O_3.

The NO_2 sample, used in the LIF experiments, was taken out of the tank. The freeze-pump-thaw procedure was performed to remove possible NO impurity. The purified NO_2 was stored in either the darkened bulb or kept in the liquid nitrogen trap until ready to use.

RESULTS AND ANALYSIS

(A) NO_2 LIF Analysis

It was found that NO_2 LIF emission spectra could be approximated [1], on the average, by a simple analytical function

$$L(X_L, X) = C Z^2 \exp^{-Z} \qquad \text{(Eq. 2.4)}$$

where X = Energy of observed fluorescence in cm^{-1},

X_L = Excitation laser energy for LIF in cm^{-1},

$L(X_L, X) = 0$ when $X \geq X_L + \Delta$,

$Z = (X_L + \Delta - X) / a (X_L + \Delta)$,

$X_L + \Delta$ = Threshold energy of fluorescence emission in cm^{-1},

Δ = Thermal rotational – vibrational energy of room temperature NO_2 molecule in cm^{-1},

$\underline{a}$ = Dimensionless parameter.

The Figure 2.7 illustrates an example of NO_2 LIF emission spectrum fitted with the Eq.2.4, along with the quantities used in the equation. Because of the spectral features rising above the congested continuum, it is difficult to judge how well Equation 2.4 fits the observed data.

An alternative method was devised which utilizes all of the data and evaluates the parameters $\underline{a}$, Δ and C in Equation 2.4 using a non-linear least squares procedure. Integrating Eq.2.4 with respect to parameter Z between the range of 0 and Z_i and leaving out the constant C for now,

$$\int_{0}^{Z_i} Z^2 \exp^{-Z} dZ = 2 - (2 + 2Z_i + Z_i^2) \exp^{-Z_i} \qquad \text{(Eq. 2.5)}$$

where $Z = (X_L + \Delta - X) / \underline{a} (X_L + \Delta)$ as defined in Eq.2.4,

Z_i = upper bound of integration in Z variable.

Changing the variable in terms of X,

$dZ = -dX / B\underline{a}$,

where $B = X_L + \Delta$ = threshold energy of fluorescence emission in cm^{-1},

and when $Z = 0$, $X = B$

when $Z = Z_i$, $X_i = B - Ba\ Z' = B(1 - aZ')$,

and Z' = same as Z except X replaced by X',

and X' = end point of cumulative sum of the observed emission energy,

and emission intensity is 0 when $X > B$.

The calculated cumulative sum of NO_2 LIF emission spectrum, excited at X_L and integrated to the lower limit of observation X_i, is

$$I_{Calculated}(X_L,X_i) = C \int_{X=25102cm^{-1}}^{X_i} Z^2 \exp^{-Z} dX = C\,[\,0\Big|_{25102}^{B} + \int_{B}^{X_i} Z^2 \exp^{-Z} dX]$$

$$= C\,[\,0\Big|_{25102}^{B} - Ba \int_{0}^{Z(X_i)} Z^2 \exp^{-Z} dZ\,] \qquad \text{(Eq.2.6)}$$

The range of integration is divided into two parts; 1) from x = 25102 cm^{-1} (NO_2 dissociation threshold) to x = B, where no fluorescence emission is possible because of excitation laser energy X_L, and 2) from B to X_i where B = maximum fluorescence threshold energy and X_i is the lower bound of observation energy.

The integrated experimental NO_2 LIF emission spectrum, excited at X_L and observed to the low energy limit of X_i, is

$$I_{Observed}(X_L,X_i) = \sum_{25102\,cm^{-1}}^{X_i} (NO_2 \text{ LIF emission spectrum}) \qquad \text{(Eq.2.7)}$$

The NO_2 laser induced fluorescence emission spectra (= $L(X_L,X)$), excited at 16 different excitation wavelengths (X_L = 399.8 nm - 672.6 nm) and observed from 25102 cm^{-1} (dissociation limit) to 12500 cm^{-1} (detector sensitivity limit), are shown on the left panel of Figures 2.8(a-p). These are normalized for the experimental variables (such as laser fluence and sample pressure) and corrected for the instrument response. The scattered laser light was estimated by taking the empty cell emission profile and then subtracted from the spectra. On the right panel of these Figures are the integrated running sum profiles ($I(X_L,X)$) of the observed emission spectra from left.

In Eq. 2.4, Δ was defined as the thermal rotational-vibrational energy of room temperature NO_2 molecule. It was also related to the observed fluorescence emission threshold energy ($X_L + \Delta$) in observed NO_2 LIF emission spectra. However, experimental observation and determination of emission threshold depend on the signal to noise ratio of observed spectra. Using the method of Pitts et.al. [26], the rovibrational energy of NO_2 at 293 ^oK was calculated, including rotational quantum number K from 1 to 12. The resulting superposition of the various rotational K curves was well represented by the normalized Boltzmann distribution expression;

$$\text{Boltz}(E_{VR})\, dE_{VR} = (E_{VR} / kT)\, \exp^{-E_{VR}/kT}\, d(E_{VR}/kT) \qquad \text{(Eq. 2.8)}$$

This is also shown in Figure 2.9, where the expected range of Δ is 1000 cm^{-1} to 1400 cm^{-1} . In order to determine the optimum value of Δ, nonlinear least square fits of calculated cumulative sum profiles (Eq.2.6) to the integrated experimental NO_2 LIF spectra (Eq.2.7) were performed with Δ fixed at 1000, 1200 and 1400 cm^{-1} while varying a and C independently. The results are compiled in Table 2.4, and obtained a values from each Δ are plotted against the laser excitation energy in Figures 2.10(1-c) and 2.11. The parameter a was observed to have minimum variance at $\Delta = 1000\ \text{cm}^{-1}$, and this is fixed for the rest of analysis.

The a values from the fit with $\Delta = 1000\ \text{cm}^{-1}$, tabulated as a function of X_L, were fitted by a second order polynomial. The fit, shown in Figure 2.12, has the following form;

$$a = a_o + a_1 X_L + a_2 X_L^2 \qquad \text{(Eq. 2.9)}$$

where $a_o = 5.8737\text{E-}1$
$a_1 = -1.8252\text{E-}3$
$a_2 = 1.6910\text{E-}6$
and X_L = laser wavelength of excitation in nm.

With Δ and a parameters fixed as above, the calculated cumulative sum profile was fitted against the experimental integrated emission spectra with C (constant) as the only variable are shown on the right panel of Fig.2.8(a-p). In many instances, the very good fit resulted in the appearance of a single curve in the right panel. When a difference can be noted (for example, Fig.2.8(l) to 2.8(p)), the irregular profile corresponds to the experimental cumulative sum (I_{Observed}) and the smooth curve to the calculated profile ($I_{\text{Calculated}}$). At lower energy of excitation, irregularities in the experimental integrated profile took on the shape of a series of step functions due to mostly sharp features in the emission spectra.

The NO_2 LIF emission spectrum $L(X_L,X)$ in Eq. 2.4 was normalized as follows, in order to establish a comparable intensity scale among LIF spectra:

$$L_D(X_L,X) = L(X_L,X) / \int_0^B L(X_L,X)\, dX \qquad \text{(Eq. 2.10(a))}$$

where $L_D(X_L,X)$ = normalized NO_2 LIF emission spectrum,
excited at X_L and observed at X,
and $B = X_L + \Delta X$ = fluorescence emission threshold energy.

Since no fluorescence emission was observed above the predissociation limit of 25102 cm^{-1}, the upper limit of integration was fixed to the predissociation limit rather than B for the integration for the X_L between 25102 cm^{-1} and (25102 - Δ) cm^{-1}. The expression obtained was

$$L_D(X_L,X)\, dX = \frac{Z^2 \exp^{-Z}\, dX}{Ba\,[\,2 - (2 + (2/a) + (1/a)^2)\exp^{-1/a}]} \qquad \text{(Eq. 2.10(b))}$$

where all the variables have been defined before.

In this analysis, it was found that cumulative sum profile of experimental NO_2 LIF emission spectra was well fitted by an integral of Eq. 2.4 with fitting parameters <u>a</u> and C.

(B) NO_2^* PIF Analysis

An example of NO_2^* emission spectrum from N_2O_5 photolysis at 248 nm is shown in Figure 2.13(a). The motivation of this analysis is how to represent the observed NO_2^* PIF emission spectrum as a linear combination of $L_D(X_L,X)$, the <u>calculated</u> NO_2 LIF emission profiles. Figure 2.13(b) illustrates this point with a diagram of idealized NO_2^*

emission spectrum like the one in Fig. 2.13(a). The observed PIF emission between X and X+ ΔX is shown as a column, divided into several blocks with different shades representing amount of contributions from various X_L, which is indicated by the origin of each arrow. This is expressed analytically as follows. Assume that there exists a distribution of X_L expressed as $W(X_L)$, which can represent the observed PIF as

$$\mathrm{PIF}(X) = \int_{X_L=X-\Delta}^{25102\,\mathrm{cm}^{-1}} L_D(X_L,X)\, W(X_L)\, dX_L \qquad \text{(Eq. 2.11)}$$

If the distribution of X_L weighing factors ($W(X_L)$) is normalized, it take the form

$$\mathrm{PIF}(X) = N \int_{X_L=X-\Delta}^{25102\,\mathrm{cm}^{-1}} L_D(X_L,X)\, F(X_L)\, dX_L \qquad \text{(Eq. 2.12)}$$

where N includes laser fluences, UV absorption cross sections, detection geometric factors and efficiency, emission yields, etc,

and $F(X_L)$ = coefficient distribution of X_L.

The coefficient distribution of X_L, $F(X_L)$, was assumed to be well represented by two different types of expressions. The first one has the shape of Boltzmann distribution with energy scale reversed, with two adjustable and one fixed parameters. Called Expression A, it has the following form;

$$\text{Expression A} = (M - X)^{\nu} \exp^{(-(M - X)/\rho)} \qquad \text{(Eq. 2.13)}$$

ν = adjustable parameter,

ρ = adjustable parameter,

M = Maximum allowed internal energy in NO_2, and fixed at each photolysis wavelength.

The M in this distribution, calculated from E_{Total}(photolysis) - $E_{Dissociation}$ ($N_2O_5 \rightarrow NO_2 + NO_3$), confined the overall distribution coefficients to the energy region accessible in the experiment. In the PIF analysis, only the distribution corresponding to the observed energy region was utilized.

The other was a Gaussian distribution function with two adjustable parameters, which was called Expression B;

$$\text{Expression B} = \frac{\exp^{-(\mu - X_L)^2/2\sigma^2}}{(2\pi\sigma^2)^{1/2}} \qquad \text{(Eq. 2.14)}$$

μ = adjustable parameter (mean of the coefficient distribution),

σ = adjustable parameter (width of the distribution).

With Expression B, the overall coefficient distribution could include energetically inaccessible regime although only experimentally relevant portion of the distribution was utilized.

The nonlinear least squares fit of ν and ρ in expression A and μ and σ in B to the PIF(X) in terms of $L_D(X_L,X)$ was performed by fitting the experimental cumulative sum profile with calculated cumulative sum profile until the optimum fit was achieved. Both coefficient distribution expressions (A and B) were used in the PIF analysis. The results of the PIF analysis are shown in Figures 2.14-25.

In Figures 2.14(a) and 2.15(a), PIF analysis with Expression A and B on NO_2^* nascent emission from 193 nm photolysis of N_2O_5 are shown. In each of these Figures, the right side depicts experimental cumulative sum profile (in solid line) fitted by a calculated cumulative sum profile (in dotted line) while left side shows the experimental emission spectrum (in noisy solid line) overlapped by the calculated emission spectrum (in smooth solid line) which was from the calculated cumulative sum profile fitted on right side.The fits achieved using coefficient expression A and B are both good, judging from almost no disagreement between experimental and calculated cumulative sum profiles. The overlap in the emission profiles (both calculated and experimental) confirms the good fit.

The corresponding coefficient distributions from Expression A and B are shown in Figures 2.14(b) and 2.15(b). In each coefficient distribution, there are two vertical lines marking the upper and lower limits of observation. As mentioned earlier, the high energy limit of observation was NO_2 predissociation limit of 25102 cm^{-1}, while the lower limit of 12500 $cm^{-1}$was due to the instrument sensitivity. Only the coefficients between these two limits were used for analysis also. Parameters used to generate these distributions are depicted in the earlier Figures which showed the PIF analysis results. The upper limit of overall distribution for expression A, which is M = 4.435E4 cm-1, is out of scale and not shown in Figure 2.14(b). The region of distribution utilized appears to be well situated in the decaying part of the curve. The utilized region of distribution from expression B, on the other hand, is located from top to the half way down with somewhat different curvature.

The result of PIF analysis on nascent NO_2^* emission from 248 nm photolysis of N_2O_5 is shown in Figures 2.17(a) and 2.18(a). On the right side of each Figure, the experimental cumulative sum curve (solid line) fitted by the calculated cumulative sum profile (dotted line) are overlapped and shown as before. The experimental and calculated emission spectra are overlapped and displayed on the left. There are some emission features near 26000 cm^{-1}, which is identified as NO* emission. There is an appearance of mismatch especially in the cumulative sum profile because of this extra emission, but good matching is shown in the NO_2^* emission curves on the left if the NO^* peaks are ignored. The fitting achieved with expression A and B are comparable.

Figures 2.17(b) and 2.18(b) show the coefficient distributions generated with expression A and B, where the region of distribution used to calculate the cumulative sum emission profile is marked with two vertical lines as before. No discernable difference between the two profiles is noted in the shape of coefficient distribution within the marked range of distribution. However, the maximum energy of distribution from expression A is bound by M = 3.278E4 cm^{-1} while maximum energy of distribution from expression B is out of range and not shown.

The delayed observation of NO_2^* emission from 248 nm photolysis are shown in Figures 2.20(a) and 2.21(a), and Figures 2.23(a) and 2.24(a) for the PIF analysis with coefficient expression A and B for 2.0 and 19.8 collisions, respectively (See Table 2.7 for collision number estimate). Shown in Figures 2.20(b) and 2.21(b), and in Figures 2.23(b) and 2.24(b) are the respective coefficient distributions. The fits between experimental and calculated cumulative sum profiles are quite acceptable, and the coefficient distributions generated with expression A and B also show similar profiles.

It has been shown that there exists a distribution of X_L that can represent observed PIF(X) as a linear combination of calculated $L_D(X_L,L)$. Two different expressions called A and B were used to generate the distribution of X_L, which resulted in equally acceptable fit of calculated cumulative sum profile to the experimental cumulative sum profile. The fits achieved in cumulative sum profile was further checked by overlapping calculated and experimental emission spectrum together. The overall shape of coefficient distributions generated with expression A and B are quite different, but only a slight difference at most is noted between the two within the region of distribution utilized in fitting. The resulting parameters from PIF analysis of NO_2^* from N_2O_5 at each wavelength of photolysis and delay are assembled in Table 2.8.

The coefficient distribution of NO_2 LIF laser excitation energy, $F(X_L)$, does not yield the internal energy distribution of NO_2^*, $P(E_{int})$, for two reasons: (1) The internal energy spread (E_{VR}) in room temperature NO_2 (Figure 2.8) associated in each LIF excitation at X_L, which was used to find the value Δ, and (2) variation of NO_2^* fluorescence lifetime as a function of laser excitation energy X_L. In order to incorporate these additional factors in extracting $P(E_{int})$ of NO_2^*, following axiom is adopted from statistics. Given two independent events a and b with separate probabilities (P_a,P_b),

P_a *and* $P_b = P_a \times P_b$ which leads to Π operator for numerous events,

P_a *or* P_b = Pa + Pb which leads to Σ and $\int$ for numerous events.

The internal energy E of interest is composed of E_{VR} from 0 to 1000 cm^{-1} (equivalent to or), and of laser excitation energy $X_L = E - E_{VR}$. Therefore, probability $P(E_{VR})$ should be multiplied by the probability of $X_L = E - E_{VR}$ for every value of E_{VR}, and then integrated over all values of E_{VR} (0 to 1000 cm-1) in order to extract the probability at energy E, the P(E). Rewriting this as an equation,

$$P(E) = \int_{R=0}^{1000cm^{-1}} [\, F(X_L{=}E-R) * P(E_{VR}{=}R)]\, dR \qquad \text{(Eq. 2.15)}$$

where $R = E_{VR}$, and used as an integration variable,

and $F(X_L = E-R)$ = probability at laser excitation energy (X_L), which is from coefficient distribution profile.

The PIF(E), which is observed fluorescence emission intensity at energy E and proportional to P(E), can be related to the NO_2 fluorescence lifetimes as follows.

$$PIF(E) = k(E)\, N(E)^* = 1/\tau(E)\, N(E)^* \propto P(E) \qquad \text{(Eq.2.16)}$$

where PIF(E) = Observed emission intensity at energy E,
k(E) = radiative decay rate constant at energy E,
$N(E)^*$ = excitated state population at E,
$1/\tau(E)$ = inverse of fluorescence lifetime at E,
P(E) = probability at energy E from Eq. 2.15.

Rewriting Eq. 2.16,

$$N(E)^* = \tau\,(E)\, PIF(E),$$

and proportional to τ (E) P(E).

Substituting Eq. 2.15 with P(E), the probability of population at E, the NO_2^* internal (= electronic + rovibrational) energy, is

$$P(E_{int}) \propto \tau(E) \int_{R=0}^{1000cm^{-1}} [F(X_L=E-R) * P(E_{VR}=R)]\, dR \qquad \text{(Eq. 2.17)}$$

where $R = E_{VR}$, and used as an integration variable,

$F(X_L= E-R)$ = probability at laser excitation energy (X_L),

which is from coefficient distribution profil,

$P(E_{VR}=R)$ = probability at rovibrational energy E_{VR},

which is from Boltzmann distribution in Eq. 2.8,

$\tau(E)$ = NO_2 fluorescence lifetime E,

and $P(E_{int})$ = Probability of population at NO_2 internal energy E,

where $E_{int}=E_{electronic} + E_{VR}$.

These steps were incorporated in the data analysis routine written in ASYST [23], and analysis was carried out to extract P(Eint) from NO_2 LIF excitation energy coefficient distribution obtained earlier.

The reported fluorescence lifetimes of NO_2^* vary widely [27-30] depending on the linewidths of the lasers used, and the energy of the excitation. This is to be expected since congested spectral features of NO_2 are believed [13] to originate from complicated, strong coupling of low lying excited electronic states with high vibrational states of ground state [13,17], and high resolution (i.e. sub-Doppler resolution) excitation would tend to resolve these states resulting in widely varying fluorescence lifetimes[29-30]. However, for the purpose of NO_2^* PIF emission analysis, selection of reported lifetimes was made based on the similarity of the experimental conditions of reported works to the present study. These criteria resulted in the following two reports: Donnelly et.al. [27] and Uselman et.al. [28]. From Donnelly paper, both short and the long decay fluorescence lifetimes were adopted as lower and upper limits. From Uselman et.al., all of their values were adopted. These were combined and tabulated for a linear least square fit. The obtained fit has the form of

$$\tau(\mu sec) = 251.35 -(7.277E-3)X_L \qquad \text{(Eq. 2.18)}$$

The assembled data points and the least square fitted line are shown in Figure 2.26(a). This also served as an extrapolation of lifetimes in the energy region below 15000 cm^{-1}, where no reported values exist yet. The error in extrapolating fluorescence lifetime is estimated with upper and lower limits of extrapolations, shown with dotted lines in Fig.2.26(a)

Going back to Figures 2.14 - 25, which showed the PIF analysis results under different experimental conditions, the obtained $P(E_{int})$ distribution profiles from analysis are plotted (in solid line with maximum = 0.5) on the left side of Figures with suffix of (a). For contrast and comparison, $P(E_{int})$ distribution profiles from analysis with expression A and B are overlapped and shown in Figures 2.16,19,22 and 25. There are small differences in the $P(E_{int})$ profile from expression A and B, which is taken as a measure of uncertainty in $P(E_{int})$ obtained from PIF analysis.

The uncertainty in $P(E_{int})$ profile of NO_2^* introduced by extrapolating NO_2 fluorescence lifetimes was estimated with upper and lower limits of extrapolation expressions presented in Fig.2.26(a). In Fig.2.26(b), nascent NO_2^* $P(E_{int})$ profile from 248 nm photolysis analyzed with expression B is presented. The middle trace in the Figure2.26(b) corresponds to the $P(Ei_{int})$ profile obtained with linear least squares fitted lifetime equation, which is identical to $P(E_{int})$ profile shown in Fig.2.18(a). The upper and lower $P(E_{int})$ traces are obtained with upper and lower limits of lifetime extrapolations. The variation observed indicates the range of uncertainty introduced into $P(E_{int})$ profile by two extreme extrapolations of NO_2 fluorescence lifetimes.

The NO_2^* $P(E_{int})$ profiles from 248 nm photolysis of N_2O_5 observed at three different collision conditions (shown in Figures 2.19, 2.22 and 2.25) are overlapped in Figure 2.27. The small mismatch between the profile from expression A and B are shown as darkened area. Although limited by upper and lower limits of observation, shifting of $P(E_{int})$ profile to lower energy is graphically illustrated as a function of collision. More quantitative information, i.e. average energy removed per collision, needs additional considerations: (1) Contribution of radiative loss to the observed overall loss needs to be estimated and then subtracted because different delay settings were used from one run to the next; and (2) better means of estimating average NO_2^* energy is needed given the limits of observation range of energy.

The emission yield of NO_2^* was estimated by comparing NO_2 LIF intensity to that from N_2O_5 PIF. These emission profiles (both LIF and PIF) were normalized for the variables such as sample pressure, laser fluence, instrument settings, and absorption cross sections [31] already. By normalizing laser energy to the variation in the energy per photon (because of different energy of excitations for LIF and PIF) in each spectrum and measuring the area under each emission profile, we can estimate the NO_2^* emission intensity (both LIF and PIF) proportional to the intensity per photon absorbed. Furthermore, if we assume that NO_2^* emission yields prepared from LIF at 410.29, 415.76 and 421.0 nm are unity, then the ratio of PIF to LIF intensity yields an estimate of NO_2^* yields from photodissociation of N_2O_5.

This is an approximate method in that (1) extent of emission below the detectable energy range is not characterized, and emission spectra may be different in this unobservable region between PIF and LIF, and (2) normalization of NO_2^* emission profiles involve a number of experimental variables with associated uncertainties. In Table 2.9, NO_2^* PIF yields from 193 and 248 nm photolysis of N_2O_5 were estimated to be $0.05\pm0.01(2\sigma)$ and $0.3\pm0.1(2\sigma)$ of NO_2 LIF emission, respectively, while NO_2 LIF emission was set to be 1.0 with 0.6(2σ) reflecting normalization uncertainty from run to run.

In Fig.2.28, $P(E_{int})$ profiles of NO_2^* scaled to the estimated emission yields from 193 nm and 248 nm photolysis are overlapped for comparison. The darkened area represents the disagreement observed from analysis with X_L coefficient expression A and B. The shape of $P(E_{int})$ distributions, with its area scaled to the NO_2^* emission yields, indicates the shift toward dissociation as the photolysis energy increased from 248 nm to 193 nm. Further discussion is made in connection with the dissociation mechanism below.

(D) NO* emission

The NO* emission was observed with short delay of boxcar gate from both the 248 nm and 193 nm photolysis of N_2O_5. Most of these emission features could be filtered out with an UV cut-off filter (CS 0-52), but some features near 26000 cm^{-1} could be seen even with the filter. In Figures 2.29(a) and (b), emissions from 193 nm photolysis of N_2O_5 at two different delay settings are observed. We note the disappearance of NO^* emission features near 26000 cm^{-1} after 500 ns delay in Figure 2.29(b) while the rest of the NO_2^* emission profile has changed very little when compared to Figure 2.29(a).

Although no detailed power dependence was carried out, large enhancement of NO^* emission was observed when the laser beam was focused inside the photolysis cell. This is shown in Figure 2.29(c) where a progression of banded features is observed in second order from 193 nm photolysis of N_2O_5. A preliminary analysis of NO^* vibrational band assignment was attempted, but uncertainty in assignment due to low spectral resolution (~2 nm) and broad overlapping features kept us from assigning NO* vibrational states involved. Based on the range of emission energy and qualitative comparison of emission spectra with other reports [32], these NO^* emissions from N_2O_5 photolysis (both 193 nm and 248 nm) appear to correspond to A -> X (γ-band) and B -> X (β-band) transitions .

DISCUSSION

(A) NO_2 LIF analysis

In expressing NO_2 LIF spectra with Eq. 2.4, Δ and a were two parameters which had been deduced from the LIF analysis. The derived value of $\Delta = 1000\ cm^{-1}$ was based on the room temperature Boltzmann distribution of NO_2 and the lowest variance observed from nonlinear least squares fit in NO_2 LIF cumulative sum profiles. The obtained value of Δ is physically reasonable, as evidenced from Fig.2.9. Furthermore, any small change in Δ is observed to be corrected by a parameters. In Figure 2.11, corresponding shift in overall average a values can be observed as Δ increases from 1000 to 1400 cm^{-1}.

The obtained a values were derived from fitting a second order polynomial to individual a values obtained from LIF analysis with Δ fixed at 1000 cm^{-1}, as shown in Fig. 2.12. This amounts to averaging the scattered a values. Judging from the scatter of individual data points in Fig. 2.12, this is also believed to be a good approximation of a.

Finally, achieved fits between experimental and calculated cumulative sum profiles in Fig. 2.8(a-p) confirm the validity of the adopted parameters.

(B) NO_2^* PIF analysis

In PIF analysis, NO_2 LIF excitation energy coefficients $F(X_L)$ were represented by two types of expressions A and B (See Eq. 2.13 and 2.14). As shown in corresponding Figures 2.14-25, the fits achieved with the two expressions were comparable and good. The resulting $P(E_{int})$ distributions from expression A and B had small disagreements from one another as shown in Figures 2.16, 2.19, 2.22 and 2.25. These small differences can be traced back to differences in the curvatures of coefficient distribution profiles. Although additional fixed parameter M exists in expression A, both distribution expressions contain two independent variables. It is possible that more than two adjustable parameters are necessary to arrive at the optimum fit. On the other hand, increasing the number of parameters to fit also increases the difficulty of achieving the optimum fit. It was believed that two adjustable parameters are a good compromise, in that good fits are achieved relatively easily with least-squares impartiality.

The merit of expression A over B may be in the fixed parameter M of expression A, which sets the maximum allowed energy in NO_2 to that of the experimentally allowed level and keeps the distribution within physically reasonable bounds. The expression B does not. The two parameters are independently varied with no restriction at all until optimum fit is achieved. If, however, the criterion of judging the acceptable distribution expression is confined to how good the achieved fit is within the observable range of energy, there is no reason to prefer expression A over B. Within the confines of the observable energy region, both distributions yield equally acceptable fits with somewhat different $P(E_{int})$ distribution from one another. The only possible instance when the expression A is to be preferred over B might be when one is to attempt to discern initial distribution profile of NO_2^* in the predissociating region (between $M < \text{Energy} < 25102\ cm^{-1}$) which had undergone predissociation. Therefore, within the observed energy range, expression A and B yield an equally acceptable fit with small disagreements in the $P(E_{int})$ distributions derived.

One uncertainty in PIF analysis stems from the lower limits of observation. Unable to discern the shape of $P(E_{int})$ distribution below 12500 cm^{-1} (due mainly to the drop in the PMT sensitivity), it is difficult to discuss either the average energy or energy removed per collision in NO_2^*. Improved sensitivity with either IR sensitive PMT or IR detector may be necessary to discern the $P(E_{int})$ distribution in this unobserved emission energy region.

Another source of uncertainty comes from NO_2 fluorescence lifetimes. The widely varying reported lifetimes [27-30], single vs.multi-exponential decay lifetimes [27-30], extreme dependence of fluorescence lifetime on the region of excitation under high resolution laser excitation [29-30] both illuminate and force us to confront the complexity of NO_2 molecule. As was described in NO_2^* PIF Analysis, a selected number of literature lifetime values were adopted based on the similarity of experimental conditions. This amounted to averaging of widely varying fluorescence lifetimes reported in literature under very high resolution [29] by preparing NO_2 LIF emissions with a moderate linewidth (~0.8 cm^{-1}) laser. Furthermore, the lifetimes were extrapolated below the lowest reported literature values of 15000 cm^{-1} with a least square fitted line in Eq. 2.18 and shown in Fig. 2.26(a). The extrapolation increases uncertainty in the energy region from ~ 17500 cm^{-1} and below. The uncertainty introduced into the $P(E_{int})$ profile from fluorescence lifetime extrapolation, as estimated in Fig.2.26(b), is comparable in magnitude to the mismatch observed in $P(E_{int})$ profiles deduced from expression A and B.

However, the most convincing test of NO_2^* PIF method should come from a complimentary experiment which can be compared against $P(E_{int})$ of NO_2^*. Such complimentary experiment was performed on NO_2Cl, and the results are presented in the next chapter. We will discuss more on merits of PIF method there.

(C) N_2O_5 Photodissociation at 193 nm.

The UV excitation of N_2O_5 at 193 nm was tentatively assigned to be $\pi \rightarrow \pi^*$ transition in the Introduction, based on theoretical calculations of other NO_2-X molecules [6-7,33]. Although exact electronic states in N_2O_5 molecules have not been calculated, we draw from other NO_2-X work (namely X = OH [6-7], CH_3 [6-7,33], NO_2 [34]) that this transition is localized in NO_2 group, and that dissociation should proceed through predissociation by curve crossing of another electronic state[35].

There is no NO_3 or O product quantum yields reported at 193 nm photolysis as yet, and therefore other channels involving NO_3^* or fragmentation cannot be ruled out. The estimated $0.05 \pm 0.01(2\sigma)$ NO_2^* emission yield at 193 nm photolysis from this work would allow room for other channels such as

$$N_2O_5 + h\nu \rightarrow NO_3^* + NO_2(X) \quad < 22563\ \mathrm{cm}\text{-}1[12] \qquad (\mathrm{Eq.2.17})$$

$$2NO_2(X) + O(^3P) \quad < 25000\ \mathrm{cm}\text{-}1[12] \qquad (\mathrm{Eq.2.18})$$

in addition to Eq.2.1 - 3. With 51813 cm^{-1} energy available from 193 nm photolysis, these channels are accessible in terms of thermodynamic thresholds.

However, no traces of NO_3^* fluorescence was observed from dispersed emission detection, which should show strong banded emissions ~660 nm [36]. Instead of excitation of NO_3 , the drop in the NO_2^* emission yield of $0.3 \pm 0.1 (2\sigma)$ from 248 nm photolysis to $0.05 \pm 0.01 (2\sigma)$ at 193 nm supports the dissociation model of further increase in excess energy of photolysis results in more fragmentations of NO_2 into NO + O. This model is consistent with the observation of a highly skewed internal energy distribution of NO_2^* toward NO_2 dissociation limit as shown in Fig.2.16. With the majority of initial excitation localized in NO_2 group, as the $\pi \rightarrow \pi^*$ assignment suggests, the excess energy partitioned into NO_2 group would result in NO_2^* as well as further dissociation into NO and O fragments. As discussed further in the 248 nm results, other work [2] seems to support this model with the right trends of NO_3 and O quantum yields measurements. However, experimental verification of NO_3 and O quantum yields at 193 nm photolysis would strengthen this proposal greatly. In Fig.2.30, an energy level diagram is shown for 193 nm photolysis of N_2O_5 along with the NO_2^* yield scaled $P(E_{int})$. The average energy of NO_2^* is estimated to be about 19500 cm^{-1}, which leaves 24810 cm^{-1} for translational energy and the internal excitation of NO_3 for the channel producing NO_2^*.

The observation of NO* emission, due to multiphoton absorption of either parent N_2O_5 or any NOx initial fragments, cannot be translated into emission quantum yield because of lack of power dependence study. The one thing we may have learned from this observation is how easy it is to observe NO^* via multiphoton effect when N_2O_5 is photolyzed at 193 nm, even with relatively small laser fluence.

(D) N_2O_5 Photodissociation at 248 nm.

Although N_2O_5 absorption at 248 nm was tentatively assigned to be n -> π^* transition, it is less clear whether this should be σ -> π^* instead[6-7]. Again, parallel comparison is made to CH_3NO_2 electronic spectral assignments [33], where π -> π^* and n -> π^* were assigned to strong and weak absorption features in decreasing order of energy. Like the π -> π^* transition of 193 nm, n -> π^* transition involves localization of initial excitation in the NO_2 group which is followed by predissociation caused by a curve crossing of another state. Therefore, much localization of excess energy in NO_2 group resulting in NO_2^* as well as NO + O fragmentation is expected.

The highly skewed $P(E_{int})$ distribution was observed with the maximum of distribution toward the NO_2 dissociation limit in Fig. 2.19. Coupled with $0.3\pm0.1(2\sigma)$ NO_2^* emission yield, it is believed that $NO_2^*(A,B)$ from Eq.2.3 (namely, $NO_3 + NO_2^*$ product channel) constitutes one of the major photofragments. This is also consistent with Ravishankara's report on $O(^3P)$ quantum yield of 0.72 and NO_3 quantum yield of 0.96 at 248 nm [2]. This would suggest that, at 248 nm photolysis of N_2O_5,

$$\begin{array}{lllll} & & & \text{Yield} & \\ N_2O_5 + h\nu & \text{--->} & NO_3(X) + NO_2^*(A,B) & 0.3 & \text{(Eq. 2.3)} \\ & & NO_3(X) + NO + O(^3P) & 0.7 & \text{(Eq. 2.2)} \end{array}$$

these channels account for the most, if not all, of the photolytic products within experimental uncertainties (especially in estimating NO_2^* emission yield).

The dissociation model of NO_2 group retaining much of initial excess energy and undergoing further dissociation into NO + O is commensurate with the report by Ravishankara et al.[2] where $O(^3P)$ quantum yield increased from 0 below 307 nm to 0.72 at 248 nm. In Fig.2.31, an energy level diagram is shown for 248 nm photolysis of N_2O_5 along with the NO_2^* yield scaled $P(E_{int})$. The average energy of NO_2^* is estimated to be about 19000 cm^{-1}, which leaves 13740 cm^{-1} for translational energy and the internal excitation of NO_3 for the channel producing NO_2^*.

Observation of NO^* emission under the high laser fluence at 248 nm photolysis (for instance, Fig.2.15(a,c), which employed laser energy of 13 mj/pulse as opposed to more typical 0.4-0.5 mj/pulse) cannot be pursued further because no power dependence study was done. However, NO^* emission channel is thought to be a minor based on the discussion above and from observation only when high laser fluences are employed.

(E) Other uses of PIF method.

As shown in Fig.2.27, one of the applications may be the study of energy transfer between NO_2^* and colliding partner M. However, careful deconvolution of radiative loss is necessary from overall loss to estimate the energy transferred by collision. Also, extension of sensitivity below the current limit of 12500 cm^{-1} would yield a much better handle on average energy of NO_2^*. This may be applied to NO_2 LIF emission also. By varying LIF excitation energy, average energy transferred per collision as a function of excitation may be pursued. Currently, such study is in progress in our group.

CONCLUSION

An analysis method of NO_2^* emission spectrum, called PIF, was derived with improvements from the first report. By deconvolution of the emission spectrum with a linear combination of monoenergetically prepared NO_2 LIF spectra, an estimate of the internal energy distribution of NO_2^* was obtained. The N_2O_5 photolysis was studied with the PIF method by probing NO_2^* internal energy distribution from 193 nm and 248 nm photolysis. Based on the internal energy distribution profile, $P(E_{int})$, of NO_2^* normalized with emission yields, we found the following.

1) At 248 nm photolysis, the following channels seem to account for the most of the photolysis within experimental uncertainty.

$$\begin{aligned} N_2O_5 + h\nu \text{ --> } \quad & NO_3(X) + NO_2^*(A,B) \qquad && \text{Yield} = 0.3 \\ & NO_3(X) + NO + O(^3P) \qquad && \text{Yield} = 0.7 \end{aligned}$$

2) At 193 nm photolysis, the channel producing NO + O appears to be even more extensive than at 248 nm, based on the trend of $O(^3P)$ quantum measurement from another report and the decrease in NO_2^* emission yield.

NO^* emission was observed readily at 193 nm, and under high laser fluence at 248 nm. The number of photons involved was not established through power dependence.

ACKNOWLEDGEMENTS

This work at the University of California and the Lawrence Berkeley Laboratory was supported by the Director, Office of Energy Research, Office of Basic Energy Sciences, Chemical Sciences Division of the U.S. Department of Energy under Contract No. DE-AC03-76SF00098.

REFERENCES

1. D. Oh, W. Sisk, A. Young and H. Johnston, J. Chem. Phys. 85 (1986) 7146.
2. A. R. Ravishankara, P.H. Wine, C.A. Smith, P.E. Barbone and A.Torabi, J. Geophys. Res. 91 (1986) 5355.
3. H.S. Johnston, Science 173 (1971) 517.
4. F.Yao, I. Wilson and H. S. Johnston, J. Phys. Chem. 86 (1982) 3611.
5. L. T. Molina and M. J. Molina, J. Photochem. 15 (1981) 97.
6. D. A. Kleier and M. A. Lipton, J. Mol. Struct. (Theochem.) 109 (1984) 39.
7. L. E. Harris, J. Chem. Phys. 58 (1973) 5615.
8. B. W. McClelland, L. Hedberg, K. Hedberg abd K. Hagen, J. Am. Chem. Soc. 1983 (105) 3789.
9. D. M. Swanson, B. Kan and H.S. Johnston, J. Phys. Chem. 88 (1984) 3115.
10. J. R. Barker, L. Brouwer, R. Patrick, M. J. Rossi, P. L. Trevor and D. M. Golden, Int. J. Chem. Kinet. 17 (1986) 991.
11. J.J. Margitan, Presented at XVI Informal Photochemistry Conference, Harvard University, Aug. 20-24, 1984.
12. D.L. Baulch, R.A. Cox, R.F. Hampson Jr., J.A. Ken, J. Troe and R. T. Watson, J. Phys. Chem. Ref. Data 9 (1980) 295 - 471.
13. D. L. Hsu, D. L. Mounts and R. N. Zare, Spectral Atlas of Nitrogen Dioxide , (New York: Academic Press, 1978).
14. R. E. Smalley, L. Wharton and D. H. Levy, J. Chem. Phys. 63 (1975) 4977.
15. R. Schmiedl, I. R. Bonilla, F. Paech and W. Demtroder, J. Mol. Spect. 68 (1977) 236.
16. (a) S. L. Coy, K. K. Lehmann and F. C. DeLucia, J. Chem. Phys. 85 (1986) 4297; (b) K. K. Lehmann and S. L. Coy, J. Chem. Phys. 83 (1985) 3290.
17. A. E. Douglas, J. Chem. Phys. 45 (1966) 1007.

18. G. D. Gillispie, A. U. Khan, A. C. Wahl, R. P. Hosteny and M. Krauss, J. Chem. Phys. 63 (1975) 3425.
19. J. T. Hougen, "Interaction among Electronic, Vibrational, and Rotational Motions" in Physical Chemistry: An Advanced Treatise, Vol.IV, (New York: Academic Press, 1970).
20. K. E. J. Hallin and A. J. Merer, J. Mol. Spec. 65 (1977) 163.
21. J. C. D. Brand, K. J. Cross and A. R. Hoy, Can. J. Phys. 57 (1979) 428.
22. J. C. D. Brand and P. H. Chiu, J. Mol. Spec. 75 (1979) 1.
23. ASYST version 1.51, Macmillan Software Co., 1985.
24. J.C. DeVos, Physica XX (1954) 690.
25. G. Schott and N. Davidson, J.Am.Chem.Soc. 80 (1958) 1841.
26. J. N. Pitts, Jr., J. H. Sharp and S. I. Chen, J. Chem. Phys. 42 (1964) 3655.
27. (a) V. M. Donnelly and F. Kaufman, J. Chem. Phys. 66 (1977) 4100; (b) V. M. Donnelly and F. Kaufman, J. Chem. Phys. 69 (1978) 1456; (c) V. M. Donnelly, D. G. Keil and F. Kaufman, J. Chem. Phys. 71 (1979) 659.
28. W. M. Uselman and E. K. C. Lee, J. Chem. Phys. 64 (1976) 3457.
29. F. Paech, R. Schmiedl and W. Demtroder, J. Chem. Phys. 63 (1975) 4369.
30. O. Cheshnovsky and A. Amirav, Chem. Phys. Lett. 109 (1984) 368.
31. R.A. Graham, Ph.D. Thesis, University of California, Berkeley, 1975.]
32. H. Dunnwald, E. Siegel, W. Urban, J.W. Rich, G.F. Homicz and M.J. Williams, Chemical Physics 94 (1985) 195.
33. S. Nagakura, Mol. Phys. 3 (1960) 152.
34. M. Kaywasaki, K. Kasatani, H. Sato, H. Shinohara and N. Nishi, Chem. Phys. 78 (1983) 65.
35. L. J. Butler, D. Krajnovich, Y. T. Lee, G. Ondrey and R. Bershon, J. Chem. Phys.79 (1983) 1708.
36. W.J. Marinelli, Ph.D. Thesis, University of California, Berkeley, 1981.

37. A.W. Adamson, Physical Chemistry, 3rd ed. (Academic Press, 1986).

38. J.O. Hirschfelder, C.F. Curtiss and R.B. Bird, Molecular Theory of Gases and Liquids, corrected ed., (Wiley, New York, 1964).

TABLE 2.1. UV absorption cross section of N_2O_5 and HNO_3.

Wavelengths (nm)	N_2O_5(a)	HNO_3(b)
190	1.56e-17	
195	1.15e-17	
200	9.2e-18	6.61e-18
205	8.2e-18	2.93e-18
210	5.6e-18	1.05e-18
215	3.7e-18	3.56e-19
220	2.2e-18	1.51e-19
225	1.4e-18	8.62e-20
230	9.9e-19	5.65e-20
235	7.7e-19	3.72e-20
240	6.2e-19	2.57e-20
245	5.2e-19	2.10e-20
250	4.0e-19	1.91e-20
255	3.2e-19	1.90e-20
260	2.6e-19	1.88e-20
265	2.0e-19	1.71e-20
270	1.61e-19	1.59e-20
275	1.30e-19	1.35e-20
280	1.17e-19	1.10e-20
285	9.15e-20	8.48e-21
290	6.83e-20	6.07e-21
295	5.10e-20	4.09e-21
300	3.81e-20	2.41e-21
305	2.84e-20	1.46e-21
310	2.12e-20	7.1e-22
315	1.58e-20	3.2e-22
320	1.18e-20	1.2e-22
325	8.8e-21	5e-23
330	6.6e-21	2e-23
335	4.9e-21	
340	3.6e-21	
345	2.7e-21	
350	2.0e-21	
355	1.5e-21	
360	1.1e-21	
365	8.5e-22	
370	6.4e-22	
375	4.8e-22	
380	3.5e-22	

(a) The absorption cross section is from Yao et. al. [4]. For the wanelengths between 285nm and 380nm, following equation is used .

$$10^{20}\,\sigma = \exp\,[2.735 + (\,(\,4728.5 - 17.127\,\lambda\,)\,/\,T]$$

where σ / cm^2, λ / nm, T / °K.

(b) The absorption cross sections are from Molina et. al. [5].

TABLE 2.2 Instrument response profile of the fluorescence detection appratus.

Wavelength (nm)	Response (Maximum normalized to 1.0)
300	0*
320	0*
340	0*
360	0*
380	0.3
400#	0.52
420	0.62
440	0.86
460	0.93
480	0.955
500	0.88
520	0.98
540	1
560	0.99
580	0.96
600	0.94
620	0.915
640	0.87
660	0.815
680	0.775
700	0.72
720	0.685
740	0.625
760	0.58
780	0.53
800	0.495

* Values are truncated to zero when smaller than 0.1.

\# NO_2 LIF emission has the high energy threshold of 398nm. Below this wavelength, it undergoes predissociation and thus no fluorescence is observed [13].

TABLE 2.3. NO_2 LIF experimental conditions.

λ(nm)	File#[(a)]	P (mtorr)	E (mj)	PMT bias(V)	σ[(b)] (* 10^{-20} cm^2)	Gate Delay /width (ns)
399.8	DOD91YA	6	0.3	-1500	68.02	30/30
	DOD92WA	5	0.4	-1500		
	DOD92WC	5	0.4	-1500		
	DOD92WD	20	0.4	-1400		
402.9	DOD92YA	20	0.3	-1400	56.73	30/30
	DOD94WC	5	0.3	-1500		
	DOD94WD	5	0.5	-1500		
405.3	DOD87WA	6	0.8	-1400	67.35	30/30
	DOD87WC	5	0.9	-1400		
	DOD87WD	6	0.8	-1400		
407.38	DOD93WC	5	1.2	-1400	51.95	30/30
	DOD93YA	5	0.9	-1400		
	DOD93YB	5	0.7	-1400		
410.29	DOD88WB	5	1.0	-1400	63.35	30/30
	DOD88WC	5	0.9	-1400		
	DOD88WD	7	1.1	-1400		
415.76	DOD90YC	5	0.4	-1500	54.70	30/30
	DOD90YD	5	0.4	-1500		
	DOD91WA	5	0.5	-1500		
421.0	DOD90WA	5	0.5	-1400	64.34	30/30
	DOD90WC	5	0.5	-1400		
	DOD90WD	6	0.5	-1500		
	DOD90YA	5	0.5	-1500		
438.26	DOD97WA	5	0.3	-1600	41.12	30/30
	DOD96YA	5	0.2	-1600		
	DOD97WB	6	0.2	-1600		
449.9	DOD84YA	5	0.6	-1400	42.0	30/30
	DOD84YE	5	1.8	-1400		
	DOD85WB	5	1.6	-1400		
	DOD85YB	5	1.7	-1400		
501.63	DOE21C	5	1.3	-1400	17.83	30/30
	DOE22C	5	1.1	-1400		
	DOE22D	4	1.0	-1400		
	DOE23A	6	0.9	-1400		
522.26	DOE23B	5	2.0	-1400	14.04	30/30
	DOE24A	6	1.7	-1400		
	DOE24E	5	1.4	-1400		

552.79	DOE25B	5	0.7	-1400	9.98	30/30
	DOE26A	5	0.8	-1400		
	DOE26C	5	0.4	-1400		
	DOE27A	4	1.2	-1400		
591.06	DOE27C	10	0.1	-1400	5.87	30/30
	DOE28C	9	0.2	-1400		
	DOE28E	11	0.2	-1400		
626.54	DOE19A	19	0.5	-1500	1.0	30/30
	DOE19C	15	0.3	-1500		
	DOE20A	20	0.3	-1500		
	DOE20C	22	0.5	-1500		
	DOE20D	25	0.4	-1500		
646.91	DOE16B	20	0.3	-1500	0.9	30/30
	DOE16C	18	0.2	-1500		
	DOE17B	20	0.2	-1500		
672.61	DOD101YC	20	0.5	-1500	0.3	30/30
	DOE13A	20	0.5	-1500		
	DOE13B	21	0.5	-1500		
	DOE13C	20	0.5	-1500		
	DOE14A	20	0.5	-1500		

(a) The file # is the designation corresponding to the lab notebook page only.
(b) The room temperature absorption cross section of NO_2 was taken from Graham [31].

TABLE 2.4* NO_2 LIF emission profile fitting parameters from analysis.

λ	a	<a>	a	<a>	a	<a>
(nm)	Δ =1000cm^{-1})		(Δ =1200cm^{-1})			(Δ =1400cm^{-1})
399.8	0.128		0.133		0.138	
	0.122		0.127		0.131	
	0.115		0.119		0.123	
	0.122	0.122	0.127	0.126	0.132	0.131
402.9	0.124		0.129		0.134	
	0.133		0.139		0.144	
	0.119	0.125	0.123	0.130	0.128	0.135
405.3	0.120		0.125		0.130	
	0.131		0.137		0.142	
	0.123	0.125	0.128	0.130	0.132	0.135
407.4	0.144		0.150		0.156	
	0.142		0.148		0.154	
	0.124	0.137	0.129	0.142	0.134	0.148
410.2	0.156		0.163		0.170	
	0.178		0.187		0.196	
	0.182	0.172	0.191	0.180	0.200	0.189
415.8	0.130		0.136		0.141	
	0.107		0.111		0.115	
	0.118	0.118	0.123	0.123	0.128	0.128
421.0	0.136		0.142		0.148	
	0.140		0.147		0.141	
	0.128	0.133	0.134	0.139	0.140	0.145
438.3	0.131		0.137		0.144	
	0.132		0.138		0.145	
	0.128	0.130	0.134	0.137	0.141	0.143
449.9	0.111		0.116		0.122	
	0.111		0.116		0.122	
	0.090		0.094		0.098	
	0.108	0.105	0.113	0.110	0.118	0.115
501.6	0.090		0.096		0.100	
	0.091		0.097		0.104	
	0.101		0.108		0.115	
	0.107	0.097	0.114	0.104	0.123	0.109
522.3	0.102		0.110		0.119	
	0.100		0.108		0.117	
	0.095	0.099	0.103	0.107	0.111	0.116

552.8	0.083		0.090		0.098	
	0.093		0.101		0.111	
	0.066		0.072		0.078	
	0.095	0.084	0.104	0.092	0.113	0.100
591.1	0.124		0.144		0.131	
	0.118		0.136		0.157	
	0.090	0.111	0.100	0.127	0.113	0.134
626.5	0.079		0.091		0.105	
	0.072		0.082		0.093	
	0.088		0.103		0.120	
	0.083		0.096		0.112	
	0.116	0.088	0.139	0.102	0.170	0.120
646.9	0.073		0.086		0.101	
	0.090		0.108		0.130	
	0.171	0.112	0.181	0.125	0.209	0.147
672.6	0.160		0.214		0.293	
	0.066		0.078		0.093	
	0.124		0.114		0.232	
	0.119	0.117	0.156	0.141	0.215	0.208

* Although not specifically named, the order in which each entry appears correspond to the file # in the Table 2.3.

TABLE 2.5 NO_2 fluorescence lifetime data used for the data analysis.

Reference	Wavelength (nm)	τ(us)
Donnely et.el. Short decay [27]	472.81	88
	525.76	93
	530.50	103
	531.91	100
	556.17	120
	557.10	123
	561.80	120
	657.89	124
Donnely et.al. Long decay [27]	472.81	88
	525.76	98
	530.50	102
	531.91	106
	556.17	120
	557.10	123
	561.80	120
	657.89	200
Lee et.al. [28]	400	70
	400.48	60
	402.41	71
	403.88	71
	404.86	80
	405.68	68.5
	406.83	68
	408.16	68
	409	69
	409.84	69
	410.68	69
	411.52	69
	412.37	69
	413.22	69
	414.08	89
	414.94	89
	415.8	80
	416.67	80
	417.54	80
	419.29	80
	420.17	80
	425.53	102
	430.11	90
	435.73	87
	439.56	76
	445.43	102
	447.43	100
	449.44	100
	455.58	87
	459.77	102.5

TABLE 2.6. NO_2 Boltzmann distribution at room temperature*.

Energy(cm^{-1})	Rel. population (297 K)
0	0.0
50	0.53
100	0.82
150	0.96
200	1.0
250	0.97
300	0.91
350	0.83
400	0.74
450	0.64
500	0.56
550	0.48
600	0.41
650	0.34
700	0.29
750	0.24
800	0.20
850	0.16
900	0.14
950	0.11
1000	0.09
1050	0.07
1100	0.06
1150	0.05
1200	0.04
1250	0.03
1300	0.03
1350	0.02
1400	0.02

* The rovibrational Boltzmann distribution calculation follows the method of Pitts et. al [26]. The overall shape of the overlapped rovibrational distributions was fitted with the expression

$$D(E) = C(E/kT) \exp(1 - (E/kT)) \ [1].$$

Explanations for various symbols are be found in the Figure Captions.

TABLE 2.7. N_2O_5 PIF experimental conditions.

λ(nm)	File#	P (mtorr)	E (mj)	PMT bias(V)	$\sigma^{(a)}$ (* 10^{-20} cm^2)	Gate Delay /width (ns)	Collision number(b)
193	DOD77WA	5	0.8	-1400	1500	40/30	0.006
	DOD77WC	5	0.5	-1400		40/30	0.006
	DOD77YA	5	0.3	-1400		40/30	0.006
248	DOD38YA	5	0.4	-1600	40	10/30	0.003
	DOD38YB	10	0.5	-1600		10/30	0.006
	DOD38YC	10	0.5	-1600		10/30	0.006
	DOD38YD	10	0.5	-1600		10/30	0.006
	DOD42WA	5	13	-1450		10/30	0.003
	DOD42WC	5	13	-1450		10/30	0.003
	DOD42WD	5	13	-1450		10/30	0.003
	DOD39WA	50	0.3	-1450		2400/30	2.0
	DOD39WB	50	0.3	-1450		2400/30	2.0
	DOD43WC	50	6.9	-1300		2400/30	2.0
	DOD39YB	200	0.5	-1450		3000/30	9.8

(a) The absorption cross sections are from Yao et.al. [4]
(b) Collision number was calculated as follows.

For hard sphere model,

collision onto NO_2^* by N_2O_5 can be estimated by expression [37]

$$Z_1(2) = 2\sqrt{2}\,\sigma_{12}^2\,(\pi kT/\mu)^{1/2}\,n2$$

where $Z_1(2)$ = collision frequency experienced by 1 in the presence of 2,

$\sigma_{12} = (\sigma_1+\sigma_2)/2$ = average hard sphere diameter,

$\mu = (m_1 m_2 / m_1 + m_2)$ = reduced mass,

n_2 = concentration of 2.

With $1 = NO_2^*$ and $2 = N_2O_5$,

and estimated $\sigma_1 \cong 4Å$ and $\sigma_2 \cong 8Å$, and so $\sigma_{12} \cong 6Å$ [38]

an example of 200 mtorr N_2O_5 colliding with NO_2^* gives

3.08 E–7 second per collision, or 308 ns per collision.

TABLE 2.8(a). Fitting parameters from PIF analysis with expression A

λ(nm)	File#	$\nu^{(a)}$	$\rho^{(b)}$	$M^{(c)}$	# of collision
193	DOD77WA	1.0	7.5E3	4.435E4	0.006
	DOD77WC	1.0	7.5E3	4.435E4	0.006
	DOD77YA	1.0	7.5E3	4.435E4	0.006
248	DOD38YA	1.0	6.8E3	3.278E4	0.003
	DOD38YB	1.0	6.8E3	3.278E4	0.006
	DOD38YC	1.0	6.8E3	3.278E4	0.006
	DOD38YD	1.0	6.8E3	3.278E4	0.006
	DOD42WA	1.0	6.8E3	3.278E4	0.003
	DOD42WC	1.0	6.8E3	3.278E4	0.003
	DOD42WD	1.0	6.8E3	3.278E4	0.003
	DOD39WA	2.5	1.4E4	3.278E4	2.0
	DOD39WB	3.0	7.5E3	3.278E3	2.0
	DOD43WC	3.0	6.9E3	3.278E4	2.0
	DOD39YB	5.0	5.0E4	3.278E4	9.8

(a) The ν is a variable parameter.

(b) The ρ ia a variable parameter, in units of cm^{-1}.

(c) The M represents the maximum allowed excess energy in NO_2 fragment, which is fixed during the analysis .

TABLE 2.8(b). Fitting parameters from PIF analysis with expression B

λ(nm)	File#	μ[(a)]	σ[(b)]	# of collision[(c)]
193	DOD77WA	2.8E4	1.1E4	0.006
	DOD77WC	2.8E4	1.1E4	0.006
	DOD77YA	2.8E4	1.1E4	0.006
248	DOD38YA	2.5E4	9.0E3	0.003
	DOD38YB	2.5E4	9.0E3	0.006
	DOD38YC	2.5E4	9.0E3	0.006
	DOD38YD	2.5E4	9.0E3	0.006
	DOD42WA	2.5E4	9.0E3	0.003
	DOD42WC	2.5E4	9.0E3	0.003
	DOD42WD	2.5E4	9.0E3	0.003
	DOD39WA	1.0E4	1.0E4	2.0
	DOD39WB	1.0E4	1.0E4	2.0
	DOD43WC	1.0E4	1.0E4	2.0
	DOD39YB	6.0E3	6.0E3	9.8

(a) μ is a variable parameter (Mean of the Gaussian distribution).

(b) σ is a variable parameter (Standard deviation, or width of the Gaussian distribution).

(c) Collision number was estimated in Table 2.7.

TABLE 2.9. NO_2^* emission yields from NO_2 LIF and PIF

NO_2 LIF

λ(nm)	File #	Normalized Intensity* (arb.unit)	
410.29	DOD88WB	5.45E-3	
	DOD88WC	3.62E-3	
	DOD88WD	2.71E-3	
415.76	DOD90YC	7.97E-3	
	DOD90YD	4.14E-3	
	DOD91WA	7.16E-3	
421.0	DOD90WA	5.98E-3	
	DOD90WC	5.12E-3	
	DOD90WD	4.09E-3	
	DOD90YA	7.82E-3	Avg. = (5.4± 3.4)E-3 Ratio = 1±0.6**

N_2O_5 PIF

λ(nm)	File #	Normalized Intensity* (arb.unit)	
193	DOD77WA	3.24E-4	
	DOD77WC	2.73E-4	
	DOD77YA	2.73E-4	Avg. = (2.9±0.4)E-4 Ratio = 0.05±0.01
248	DOD42WA	1.38E-3	
	DOD42WC	1.29E-3	
	DOD42WD	1.27E-3	
	DOD43WC	1.94E-3	Avg. = (1.5±0.6)E-3 Ratio = 0.3±0.1

* Normalized for sample pressures, absorption cross scetions, instrument settings, and laser fluence normalized to the per photon basis.

** The error correspond to 2 standard deviations.

FIGURE CAPTIONS.

Fig. 2.1: UV absorption curve of N_2O_5 is smooth and continuous, with a few absorption features [4]. For the purpose of comparison, HNO_3 UV absorption curve [5] is also shown. In HNO_3, strong absorption at 190 nm is assigned to be $\pi \rightarrow \pi^*$ transition, while $n \rightarrow \pi^*$ transition is assigned to the weaker absorption feature in 270 nm [6,7]. By the parallel argument involving other NO_2-X compounds [6,7], we tentatively assign that 193 nm photolysis of N_2O_5 involves $\pi \rightarrow \pi^*$ transition while 248 nm photolysis involves $n \rightarrow \pi^*$ transition. See Table 2.1 for the numerical values of the absorption cross sections.

Fig. 2.2: The N_2O_5 gas phase structure is determined from an electron diffraction study [8]. The structure consists of two NO_2 groups bonded to central oxygen atom in bent shape. The NO_2 groups are thought to undergo a large amplitude torsional motion about a point of minimum energy corresponding to C_2 symmetry. The dihedral angles $\tau 1$ and $\tau 2$ between these two NO_2 groups and the N-O-N plane are thought to be about 30^o each. The N-O-N bond angle of 111.8^o and N-O bond length of 1.498Å for the central N-O bond, and O-N-O bond angle of 133.2^o and N-O bond length of 1.188Å for the NO_2 group are also estimated.

Fig. 2.3(a): Low resolution NO_2 absorption spectrum in the 3600Å - 6800Å region (9.70 torr, 7.5 cm path length, room temperature) is reproduced from Zare et. al. [13].

(b): High resolution NO_2 absorption spectrum of the 5933Å region along with the assigned transitions is reproduced from Zare et. al. [13]. The complexity of assignment and the interpretation of NO_2 spectrum is lucidly discussed in the above reference.

Fig. 2.4: The calculated NO_2 potential energy level diagram shown as a function of O-N-O bending angle, adopted from Gillispie et. al. [18]. Of the electronic states depicted, $^2A_1$, $^2B_2$, $^2B_1$, and $^2A_2$ states may be involved in NO_2* visible emission. It was Douglas [17] who suggested inter-electronic interactions as a possible source of "extra" vibrational bands as well as anomalously long fluorescence lifetimes in a small polyatomic molecule. The $^2A_1$ and $^2B_2$ state may vibrationally interact, while $^2A_1$ and $^2B_1$ states as well as $^2B_2$ and $^2A_2$ states may undergo Renner-Teller interaction [19]. In addition, spin-orbit interaction may couple high vibrational ground state A_1 levels with vibrational B_2 levels. All these interactions result in spectrum that is both difficult to assign as well as to predict. Spectral simplification was achieved in some degree by the use of supersonic jet expansion to cool the sample [14] and by sub-Doppler spectroscopic technique [29], but the state of understanding is far from satisfactory. For more in-depth discussion, refer to the excellent review by Zare et. al. [13].

Fig. 2.5: The experimental apparatus used for the study is depicted in block diagram. For more experimental detail, see the text.

Fig. 2.6: The instrument response profile obtained by placing a tungsten strip filament before the collection optic and dispersing through the monochromator and detecting with PMT. By measuring the temperature of the tungsten lamp and knowing the tungsten emissivity at that temperature [24], we can deduce what the instrument response is at a given wavelength

of observation. Our observation of NO_2* is further limited in the high energy end at 398.7 nm, the predissociation limit of NO_2. This response profile is used to correct the experimentally observed emission profile to the true emission profile.

Fig. 2.7: An experimental emission spectrum of NO2 LIF, approximated by an analytic expression $L(X_L,X) = C\,Z^2\,\exp^{-Z}$ (Eq. 2.4), least-squares fitted to the cumulative sum of the data.

Fig. 2.8(a-p): The NO_2 LIF emission spectra at the respective excitation wavelengths, corrected for the instrument response as well as normalized for experimental variables (i.e. laser power, sample pressure, etc). On the right side is cumulative sum profile of the LIF emission profile of the left, and the fit to an analytic expression with the fitting parameters. For more information, refer to the text. The fitting parameters are assembled in table 2. The wavelengths of excitation corresponding to the figures are; (a)399.8 nm, (b)402.9 nm, (c)405.3 nm, (d)407.38 nm, (e)410.29 nm, (f)415.76 nm, (g)421.0 nm, (h)438.26 nm, (i)449.9 nm, (j)501.6 nm, (k)522.26 nm, (l)552.8 nm, (m)591.1 nm, (n)626.54 nm, (o)646.9 nm, (p)672.6 nm.

Fig. 2.9 The room temperature Boltzmann distribution of NO_2 generated by Eq. 2.8 with the method of Pitts et. al.[26]. Three values of Δ, 1000 , 1200 and 1400 cm^{-1}, are depicted with arrows.

Fig. 2.10(a-c): One of the NO_2 LIF fitting parameters, a, is plotted against the NO_2 LIF excitation wavelengths at $\Delta = 1000\ cm^{-1}$, $\Delta = 1200\ cm^{-1}$ and $\Delta = 1400\ cm^{-1}$ for Fig. 2.10(a), 2.10(b) and 2.10(c) respectively. This was in an effort to formulate an analytical expression capable of reproducing NO_2 LIF emission profile with a minimum number of parameters. Note how the increase in Δ parameter,which represents the difference between laser excitation energy and the highest energy of fluorescence emission observed, also increase the magnitude and the spread of a parameters.

Fig. 2.11 Overlapped plots of <a>, average of a values at a given laser excitation wavelength, against the laser excitation wavelength at three different Δ values. We note that increases in Δ tends to increase the magnitude of a parameters at all excitation wavelengths, but the overall <a> parameter distributions at different Δ values appear to be quite similar to one another.

Fig. 2.12 In order to represent a parameters as a function of excitation wavelength, a least-squares fit with a quadratic equation was performed on Fig. 2.10(a). The $\Delta = 1000\ cm^{-1}$ data was chosen for the smallest variance of data to the quadratic fit, which was also based on room temperature Boltzmann distribution of rotational-vibrational energies shown in Fig.2.9.

Fig. 2.13(a) The experimental NO_2^* PIF emission spectrum from 248 nm photolysis of N_2O_5.

Fig. 2.13(b) Diagram depicting how the PIF(X) may be expressed as a linear combination of calculated $L_D(X_L,X)$.

Fig. 2.14(a) The result of PIF analysis on nascent NO_2^* emission from N_2O_5 photolysis at 193 nm with expression A. The left picture shows the experimentally observed emission profile of NO_2^* in solid line (——), superimposed by a dotted line (- - - -) which is the calculated emission profile based on the analysis. The picture on the right side shows the solid curve (——), which represent cumulative sum profile of NO_2^* emission spectrum of the left. Also shown is the dotted curve (- - - -), which represents the calculated cumulative sum profile based on the PIF analysis. Based on the distribution in Fig. 2.14(b), $P(E_{int})$ distribution of NO_2^* is also shown on the left side of the Figure. A small peak on 26000 cm^{-1} is the experimentally observed emission feature, which is thought to be from NO^* emission. An UV cut-off filter [CS 0-52] was used to block off most of the UV component, and the NO^* emission doesn't pose any interference in NO_2 PIF analysis.

Fig. 2.14(b) The NO_2 LIF coefficient distribution used for fitting experimental emission profiles in (a). Two vertical lines show the range of our observation limit, which is 12500 cm^{-1} and 25102 cm^{-1} for the lower and upper limit, respectively. This coefficient distribution was generated by expression A which has two adjustable and one fixed parameters.

Fig. 2.15(a) The result of PIF analysis on nascent NO_2^* emission from N_2O_5 photolysis at 193 nm with expression B. The left picture shows the experimentally observed emission profile of NO_2^* in solid line (——), superimposed by a dotted line (- - - -) which is the calculated emission profile based on the analysis. The picture on the right side shows the solid curve (——), which represent cumulative sum profile of NO_2^* emission spectrum of the left. Also shown is the dotted curve (- - - -), which represents the calculated cumulative sum profile based on the PIF analysis. Based on the distribution in Fig. 2.14(b), $P(E_{int})$ distribution of NO_2^* is also shown on the left side of the Figure.

Fig. 2.15(b) The NO_2 LIF coefficient distribution used for fitting experimental emission profiles in Fig.2.15(a). Two vertical lines show the range of our observation limit, which is 12500 cm^{-1} and 25102 cm^{-1} for the lower and upper limit, respectively. This coefficient distribution was generated by expression B, which has two adjustable parameters.

Fig. 2.16 The $P(E_{int})$ from expression A and B (from Fig. 2.14(a) and Fig.2.15(a)) are overlapped for easy comparison. The mismatch between the two is taken as a measure of uncertainty in $P(E_{int})$ obtained.

Fig. 2.17(a) The result of PIF analysis on nascent NO_2^* emission from N_2O_5 photolysis at 248 nm with expression A . All the curves represent similar quantities as in Fig. 2.14(a). There was some NO^* emission around 26000 cm^{-1}, where NO_2^* would predissociate rather than fluoresce[13], passing through the UV cut-off filter. The disagreement between experimental cumulative sum profile and the calculated cumulative sum on the right hand figure stems from the extra NO^* emission peak contributing to the experimental cumulative sum trace.

Fig. 2.17(b) The NO_2 LIF coefficient distribution, generated with expression B, which was used for the PIF analysis in Fig.2.17(a). Note that highest energy shown in the coefficient distribution is 32780 cm^{-1}, which represents the maximum excess energy (M) NO_2 fragment can be partitioned with. Of course, NO_2 fragments with internal energy in excess of 25102 cm^{-1} will predissociate and won't be detected via fluorescence emission.

Fig. 2.18(a) The result of PIF analysis on nascent NO_2^* emission from N_2O_5 photolysis at 248 nm with expression B . All the curves represent similar quantities as in Fig. 2.14(a). There was some NO^* emission around 26000 cm^{-1}, where NO_2^* would predissociate rather than fluoresce[13], passing through the UV cut-off filter. The disagreement between experimental cumulative sum profile and the calculated cumulative sum on the right hand figure stems from the extra NO^* emission peak contributing to the experimental cumulative sum trace.

Fig. 2.18(b) The NO_2 LIF coefficient distribution, generated with expression B, which was used for the PIF analysis in Fig.2.18(a).

Fig. 2.19 The $P(E_{int})$ from expression A and B (from Fig. 2.17(a) and Fig.2.18(a)) are overlapped for easy comparison. The mismatch between the two is taken as a measure of uncertainty in the $P(E_{int})$ obtained.

Fig. 2.20(a) The result of PIF analysis with expression A on NO_2^* emission from 248 nm photolysis of N_2O_5, observed after the fragments had undergone 2.0 hard sphere collisions on the average. Compare the shift of $P(E_{int})$ profile as well as the maximum of fluorescence emission intensity to the lower energy from the nascent condition in Fig. 2.17(a) as a result of collision.

Fig. 2.20(b) The NO_2 LIF coefficient distribution profile of Fig.2.20(a).

Fig. 2.21(a) The result of PIF analysis with expression B on NO_2^* emission from 248 nm photolysis of N_2O_5, observed after the fragments had undergone 2.0 hard sphere collisions on the average. Compare the shift of $P(E_{int})$ profile as well as the maximum of fluorescence emission intensity to the lower energy from the nascent condition in Fig. 2.18(a) as a result of collision.

Fig. 2.21(b) The NO_2 LIF coefficient distribution profile of Fig.2.21(a).

Fig. 2.22 The $P(E_{int})$ from expression A and B (from Fig. 2.20(a) and Fig.2.21(a)) are overlapped for easy comparison. The mismatch between the two is taken as a measure of uncertainty in $P(E_{int})$ obtained.

Fig. 2.23(a) The result of PIF analysis with expression A on NO_2^* emission observed after they had undergone 9.8 hard sphere collisions. The shift of $P(E_{int})$ and the fluorescence emission profile to the lower energy is extensive, but the estimate of average energy is difficult due to the limit of observation to 12500 cm^{-1}.

Fig. 2.23(b) The NO_2 LIF coefficient distribution profile used for the analysis in Fig.2.23(a).

Fig. 2.24(a) The result of PIF analysis with expression B on NO_2^* emission observed after they had undergone 9.8 hard sphere collisions. The shift of $P(E_{int})$ and the fluorescence emission profile to the lower energy is extensive, but no estimate of internal energy is given due to the reason in caption Fig.2.23(a).

Fig. 2.24(b) The NO_2 LIF coefficient distribution profile used for the analysis in Fig.2.24(a).

Fig. 2.25 The $P(E_{int})$ from expression A and B (from Fig. 2.23(a) and Fig.2.24(a)) are overlapped for easy comparison. The mismatch between the two is taken as a measure of uncertainty in $P(E_{int})$ obtained.

Fig. 2.26(a) The NO_2 fluorescence lifetimes from Donnelly et. al. [27] and Uselman et. al. [28] were combined and subjected to the least square fitting, which is shown as a solid line passing through the data points. The obtained expression was used to extrapolate the fluorescence lifetimes in the low excitation energy region where there are no reported values available. The dotted line above the solid line indicates an upper bound of fluorescence lifetime, and is extrapolated to lower energy of excitation. The dotted line below the solid line represents the lower bound of fluorescence lifetime data.

Fig. 2.26(b) The $P(E_{int})$ profile of nascent NO_2^* from photolysis at 248 nm, analyzed with expression B. The middle trace is identical to the $P(E_{int})$ in Fig.2.18(a), which uses linear least squares fitted and extrapolated fluorescence lifetimes (solid line in Fig.2.26(a)).

Fig. 2.27 Superimposed $P(E_{int})$ profiles of NO_2^* from 248 nm photolysis of N_2O_5 at nascent, 2.0 collision and 9.8 collisions. The maximum of each profile was scaled to 1.0.

Fig. 2.28 Comparison of nascent $P(E_{int})$ of NO_2^* from 193 nm and 248 nm N_2O_5 photolysis. The curves are normalized to the NO_2^* emission intensity (0.05 for 193 nm and 0.3 for 248 nm), and the darkened area corresponds to mismatches of $P(E_{int})$ from expression A and B. The sharp cut-off in both distributions at the high energy end suggest that part of NO_2^* fragments were produced with enough internal energy to undergo dissociation.

Fig. 2.29(a)	Observed NO_2^* emission profile from 193 nm photolysis of N_2O_5 at very short delay, with the UV cut-off filter installed. Again, we note the extra emission peaks around 26000 cm^{-1} region.
Fig. 2.29(b)	Same experimental condition as in (a), except the 500 ns delay on the observation. The sample pressure is low enough that collisional quenching is not significant. The extra emission features in the 26000 cm^{-1} region has disappeared, suggesting < 500 ns fluorescence lifetime for these emission features.
Fig. 2.29(c)	Experimental conditions are similar to (a), except (1) UV cut-off filter was removed, and (2) the photolysis laser fluorescence was increased by focusing the photolysis laser beam in the detection region with a short focusing optic. The observation of banded structure was in 2nd order, as evidenced from disappearance of almost all the banded structure when a UV cut-off filter was placed.
Fig. 2.30	Energy level diagram of N_2O_5 photolysis at 193 nm, along with photolysis channels discussed in the text.
Fig.2.31	Energy level diagram of N_2O_5 photolysis at 248 nm, along with the pertinent photolysis channels involved.

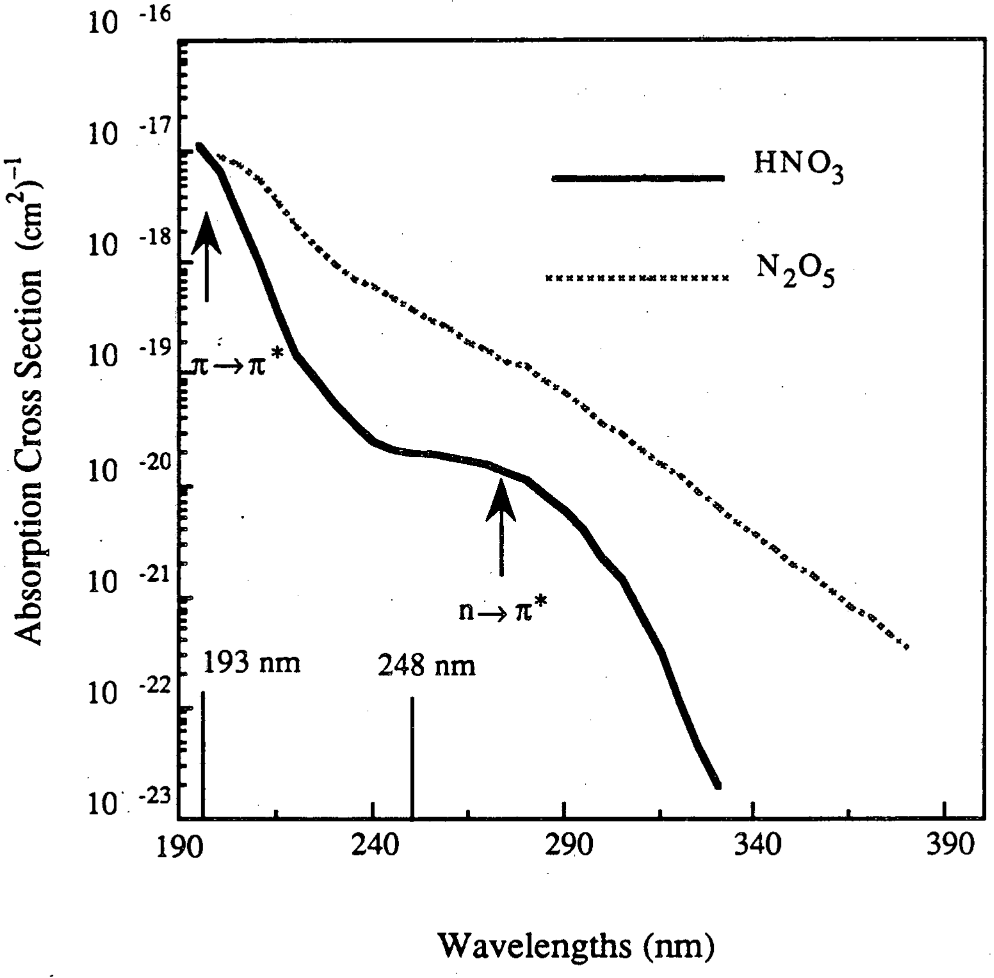
10 -16
10 -17
10 -18
10 -19
10 -20
10 -21
10 -22
10 -23
Absorption Cross Section (cm²)⁻¹
HNO3
N2O5
π→π*
n→π*
193 nm
248 nm
190
240
290
340
390
Wavelengths (nm)

Figure 2.1

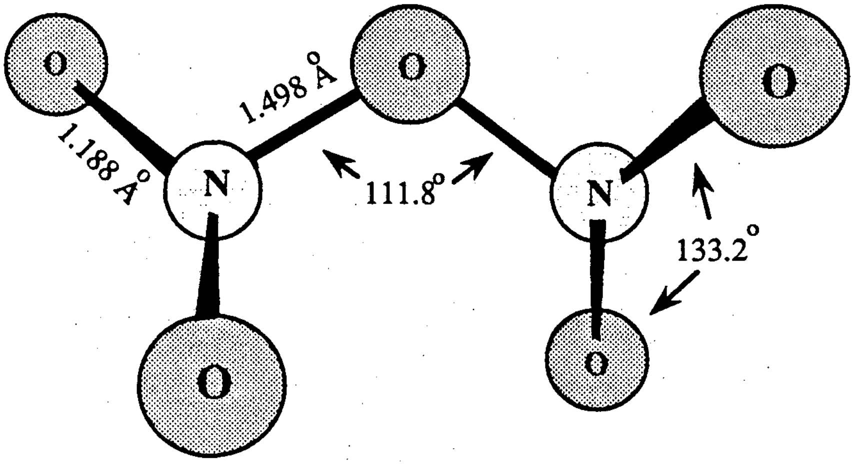

Figure 2.2

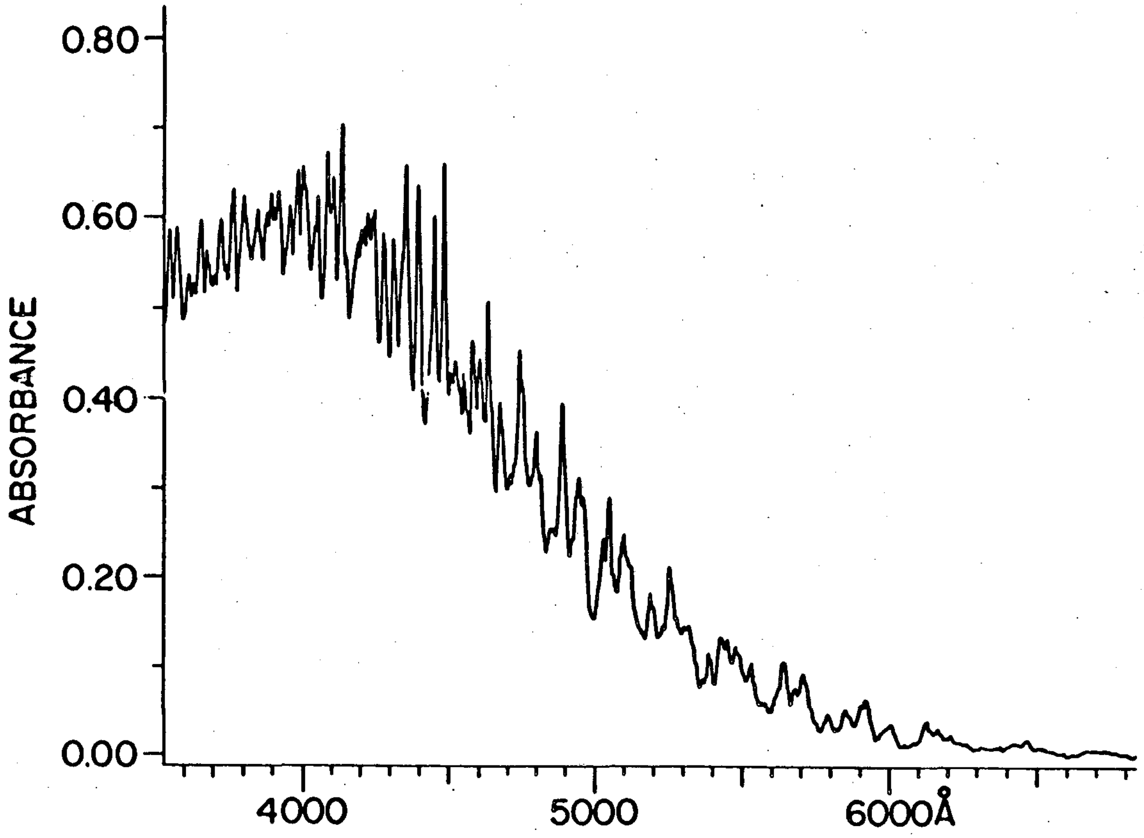

Figure 2.3(a)

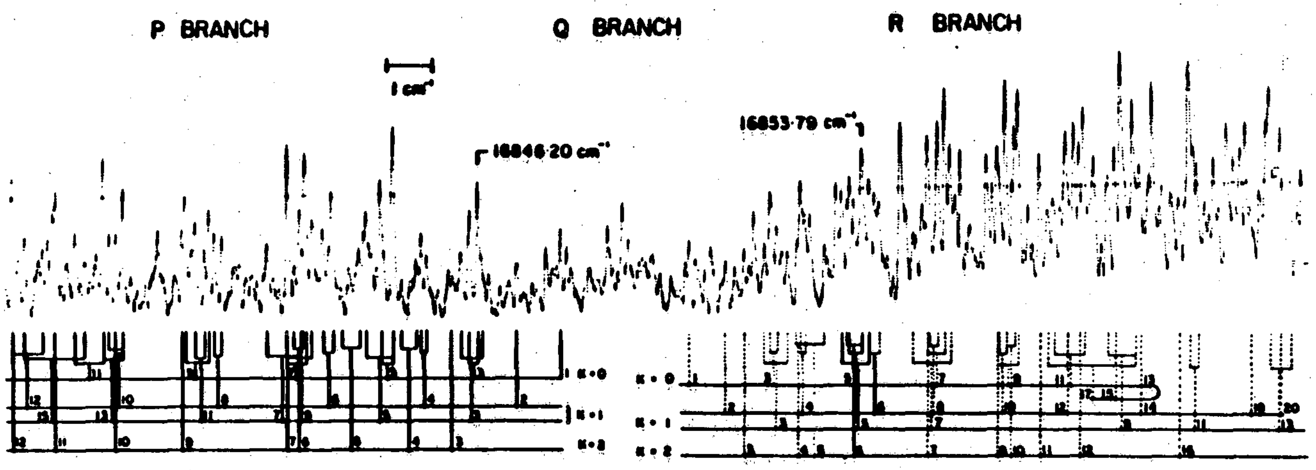
P BRANCH
Q BRANCH
R BRANCH
1 cm⁻¹
16846·20 cm⁻¹
16853·79 cm⁻¹
K = 0
K = 1
K = 2

Figure 2.3(b)

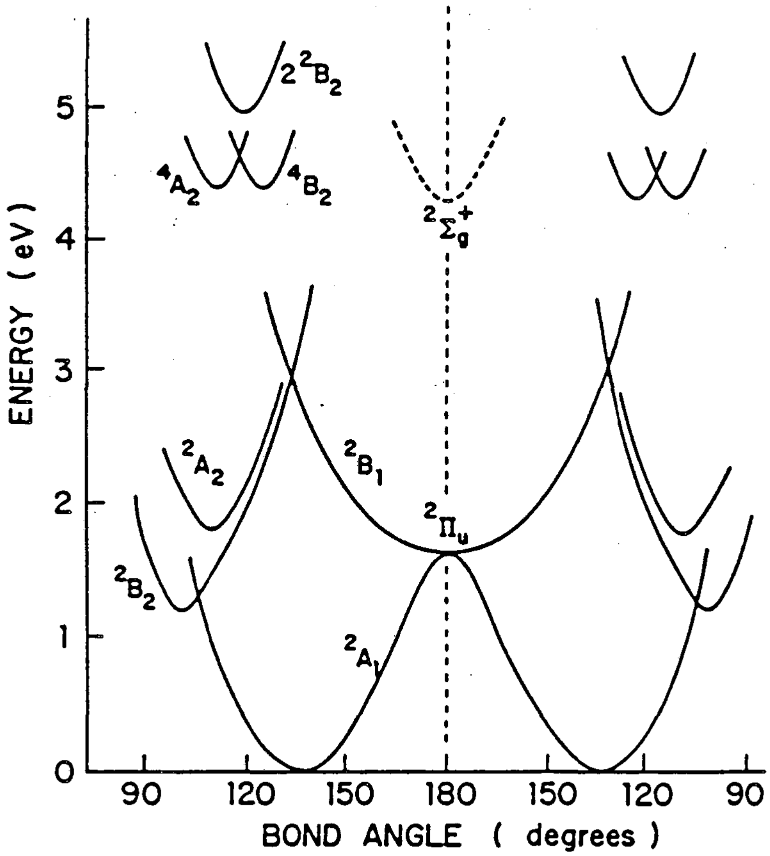
ENERGY (eV)
0
1
2
3
4
5
BOND ANGLE (degrees)
90
120
150
180
150
120
90
$2\,^2B_2$
$^4A_2$
$^4B_2$
$^2\Sigma_g^+$
$^2A_2$
$^2B_1$
$^2\Pi_u$
$^2B_2$
$^2A_1$

Figure 2.4

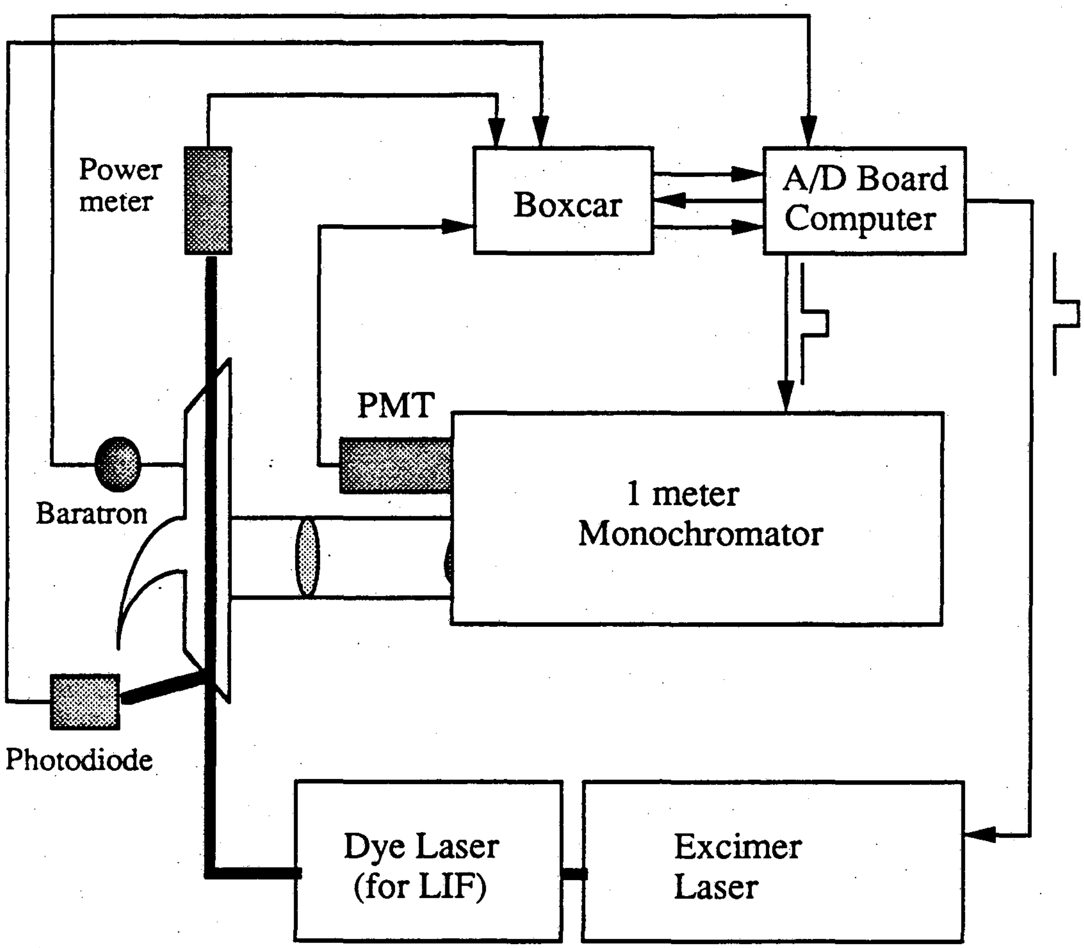
Power meter
Boxcar
A/D Board Computer
PMT
Baratron
1 meter Monochromator
Photodiode
Dye Laser (for LIF)
Excimer Laser

Figure 2.5

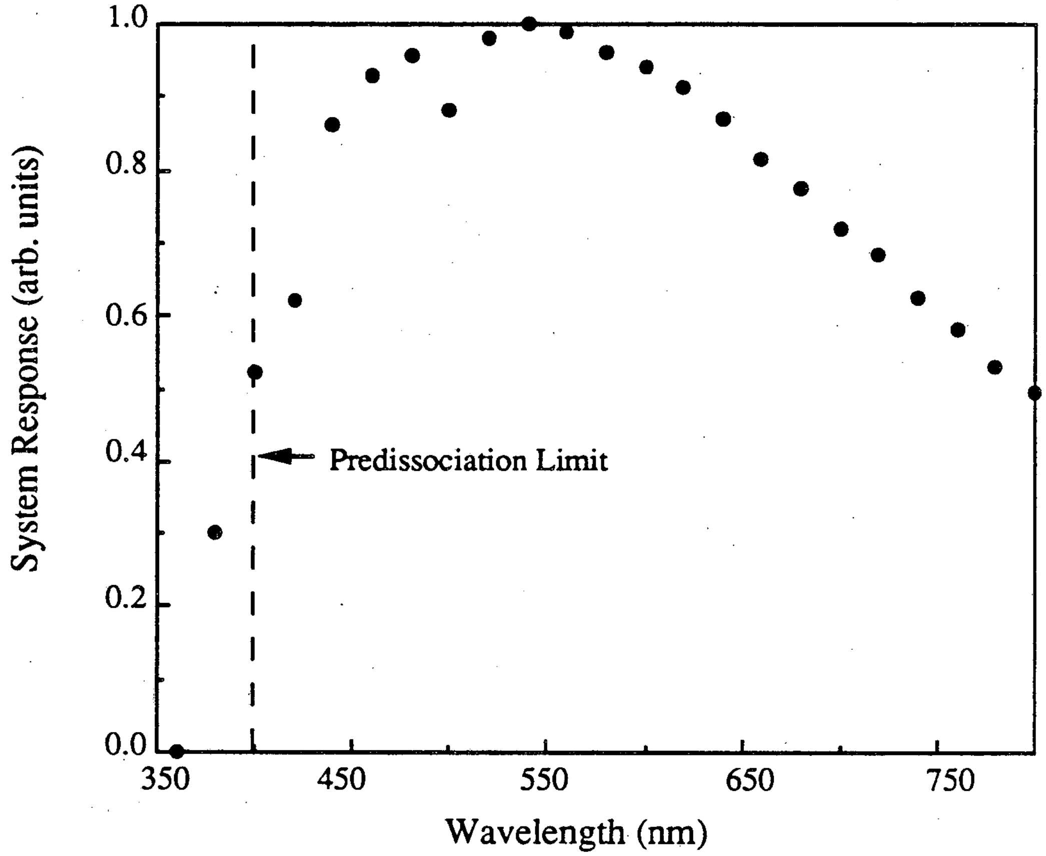
System Response (arb. units)
1.0
0.8
0.6
0.4
0.2
0.0
350
450
550
650
750
Wavelength (nm)
Predissociation Limit

Figure 2.6

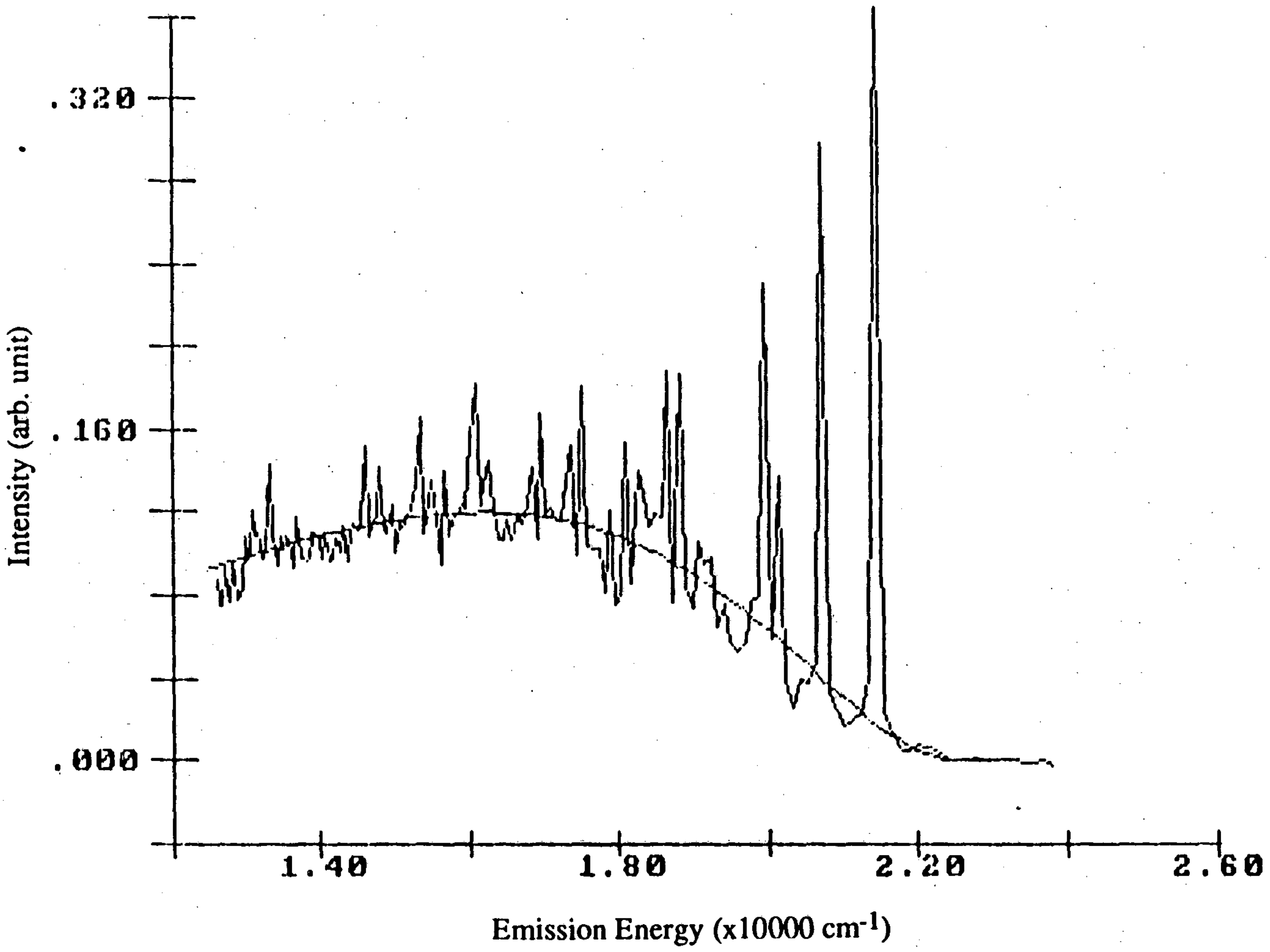
.320
.160
.000
Intensity (arb. unit)
1.40
1.80
2.20
2.60
Emission Energy (x10000 cm^{-1})

Figure 2.7

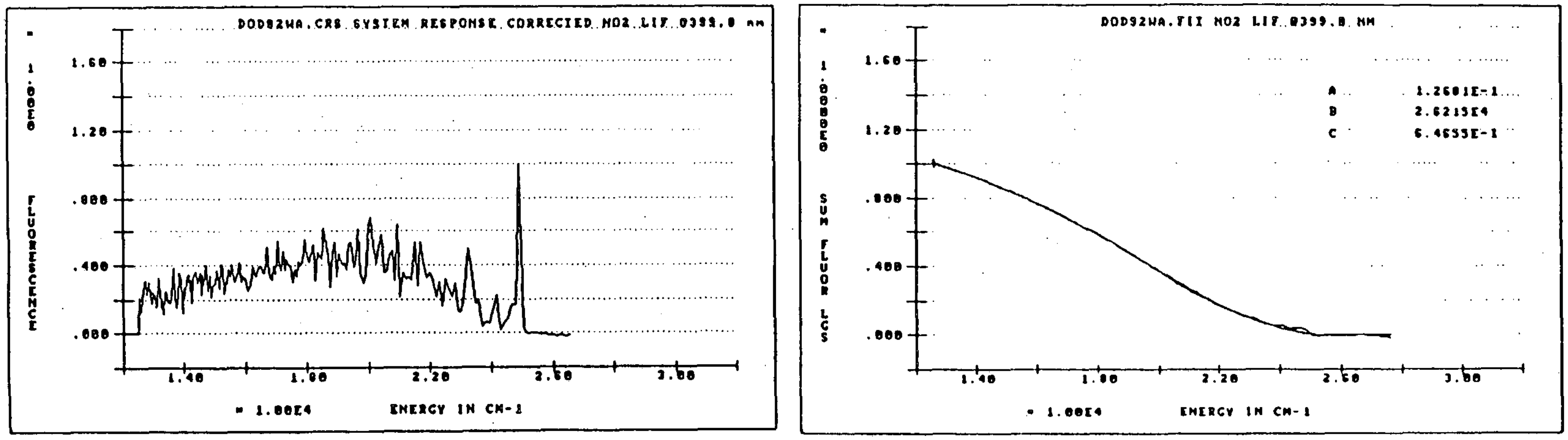

Figure 2.8(a)

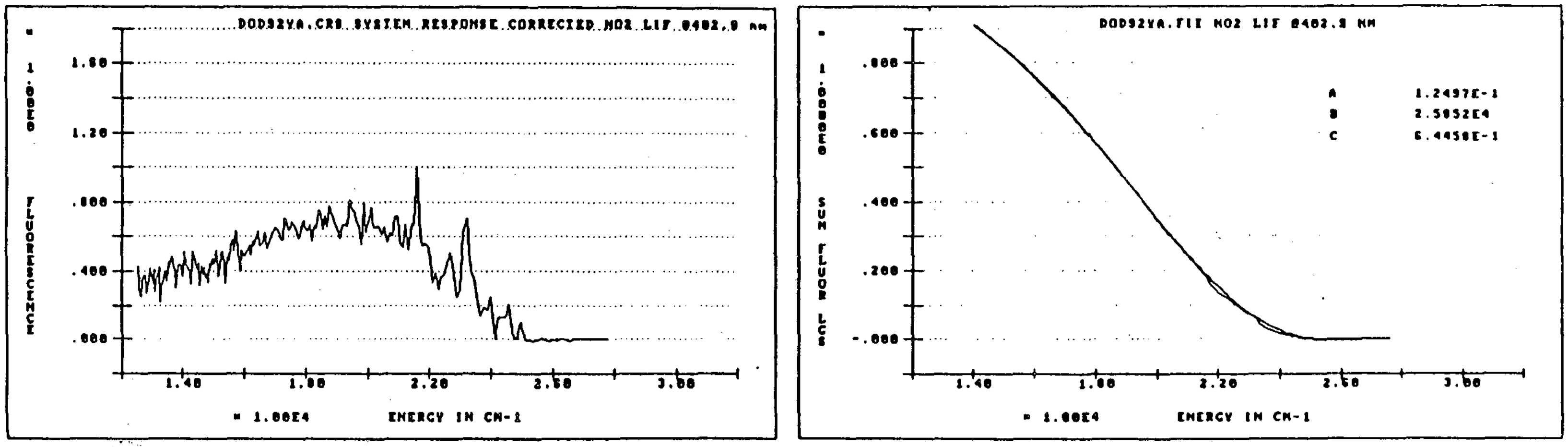

Figure 2.8(b)

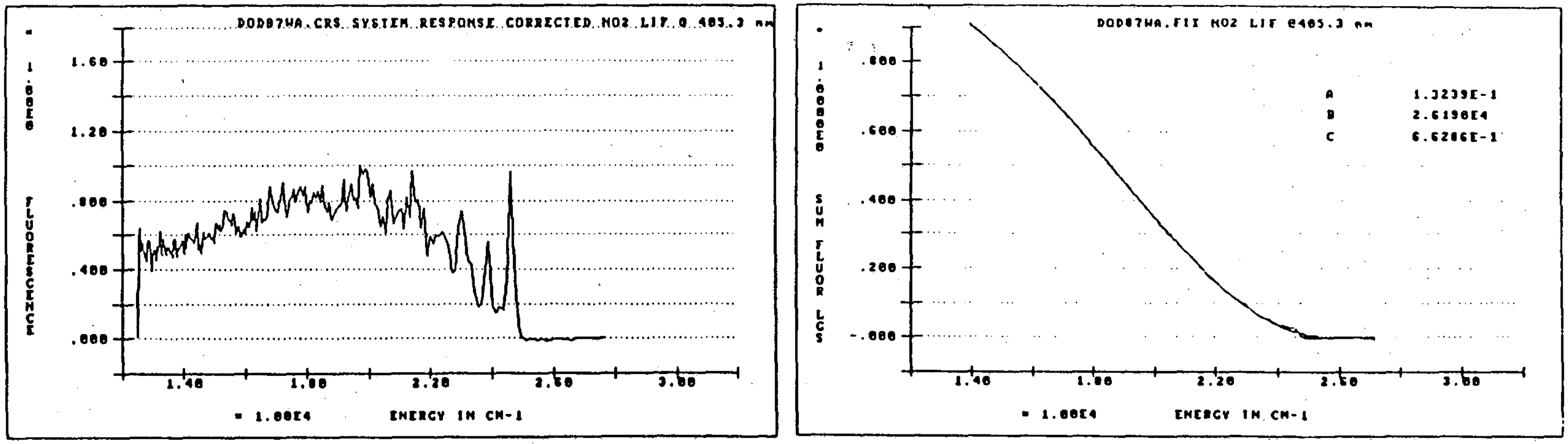

Figure 2.8(c)

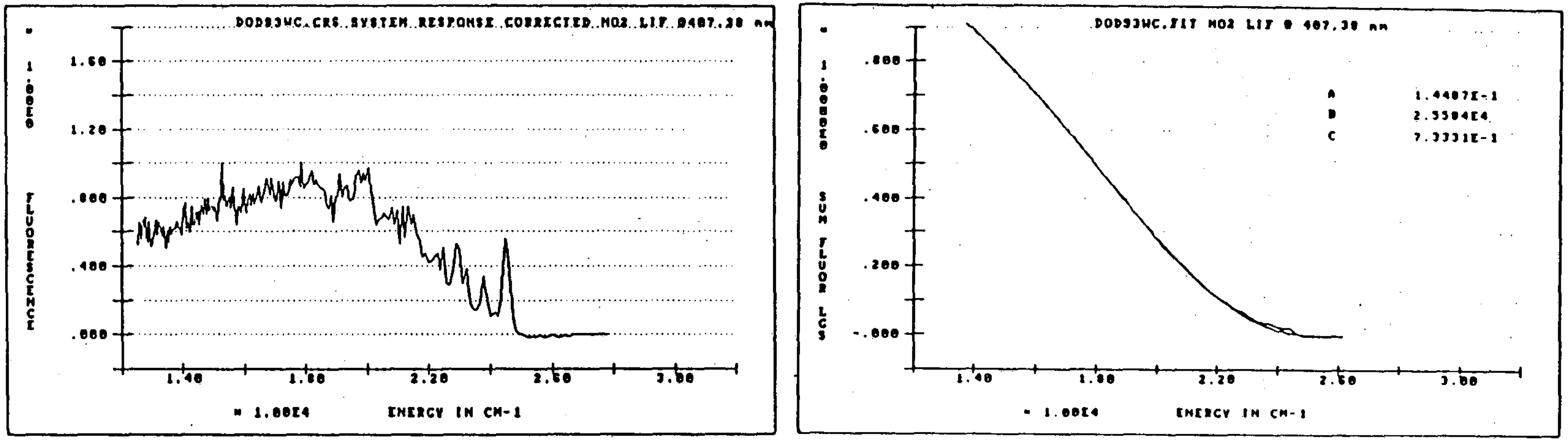

Figure 2.8(d)

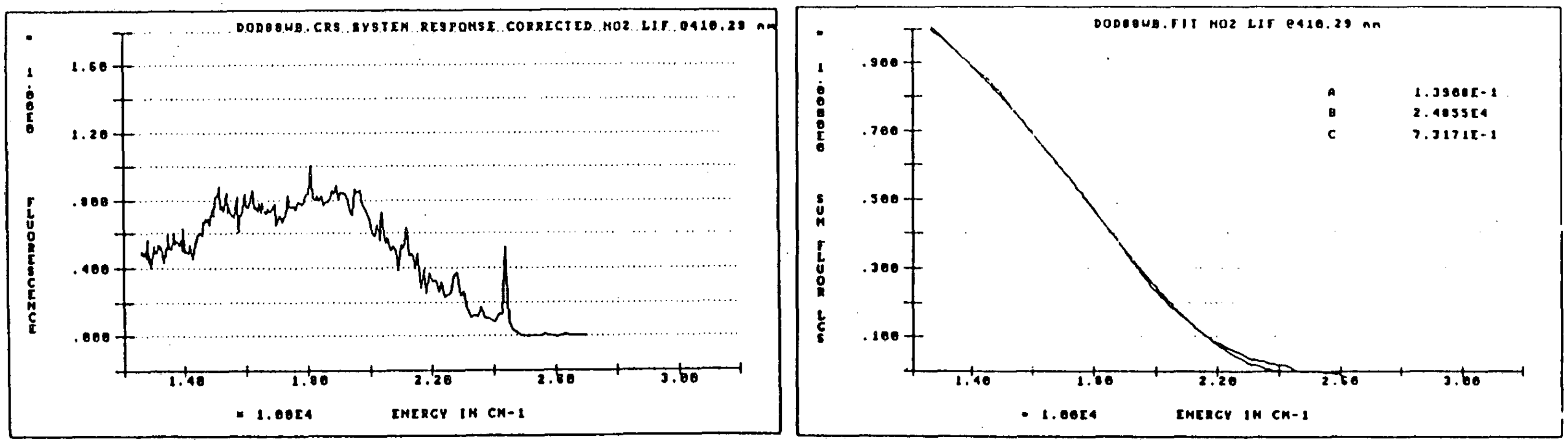

Figure 2.8(e)

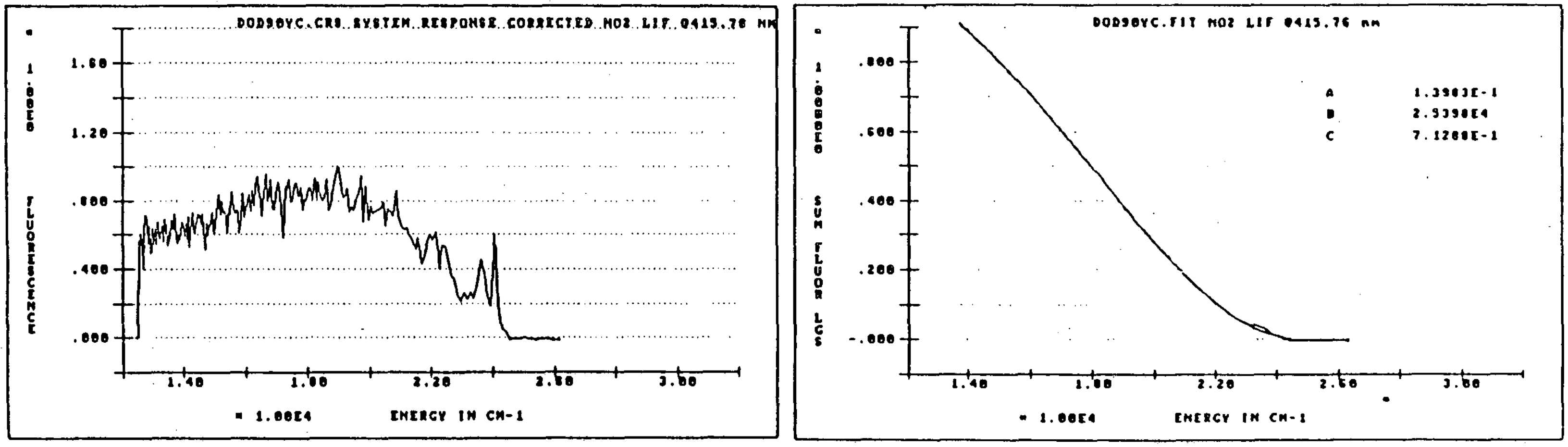

Figure 2.8(f)

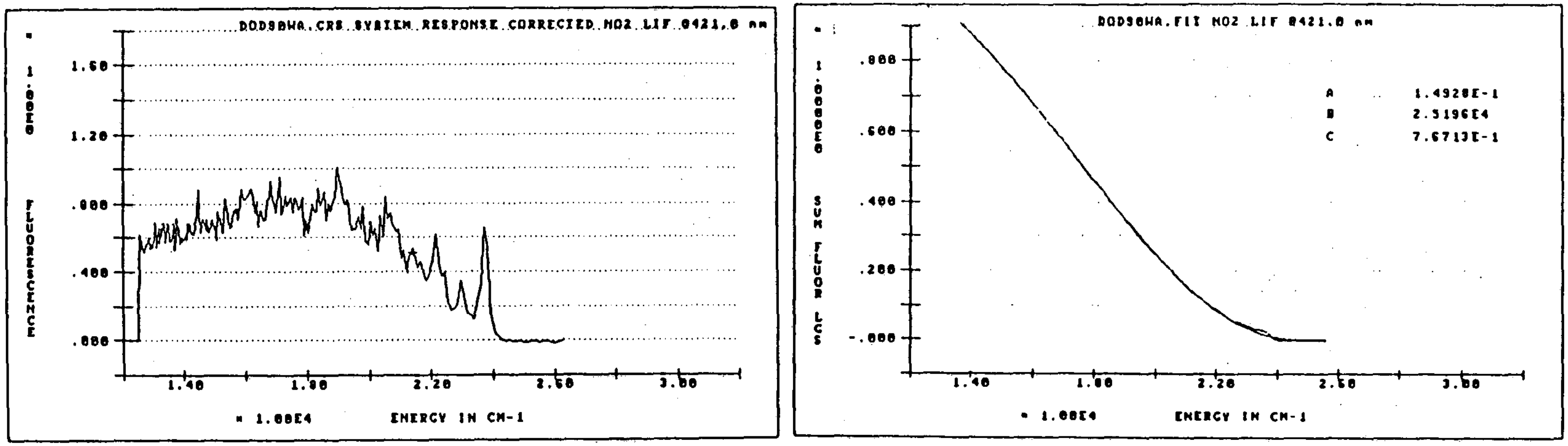

Figure 2.8(g)

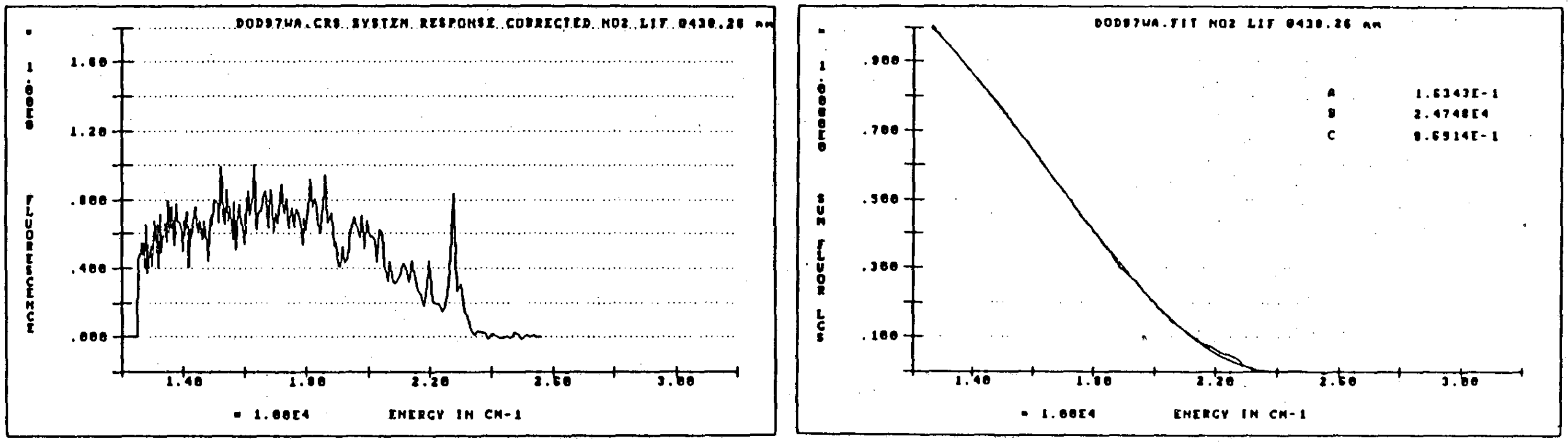

Figure 2.8(h)

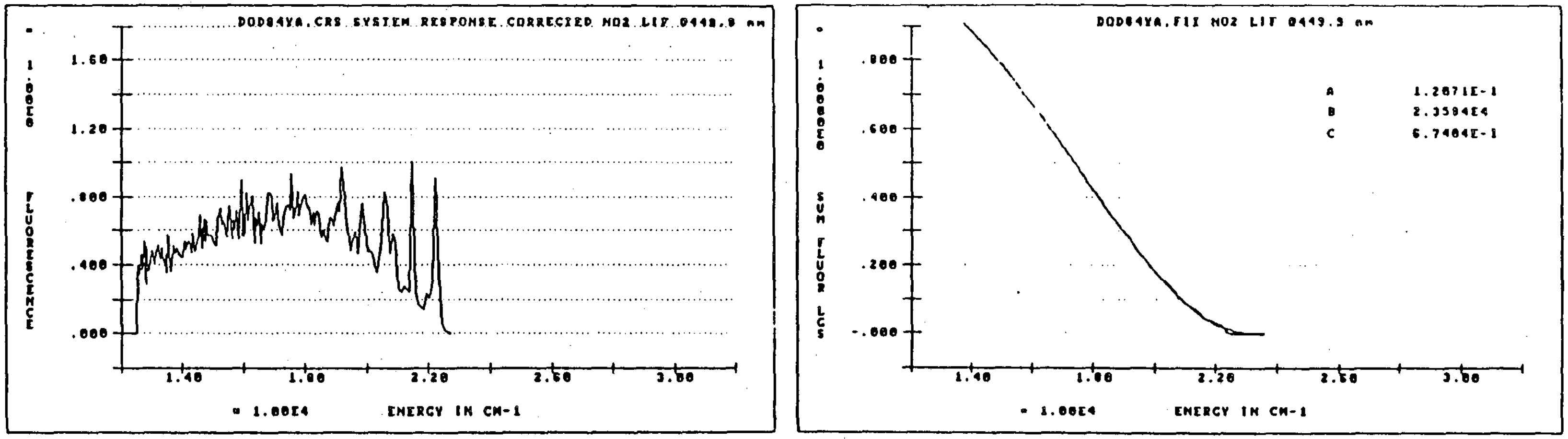

Figure 2.8(i)

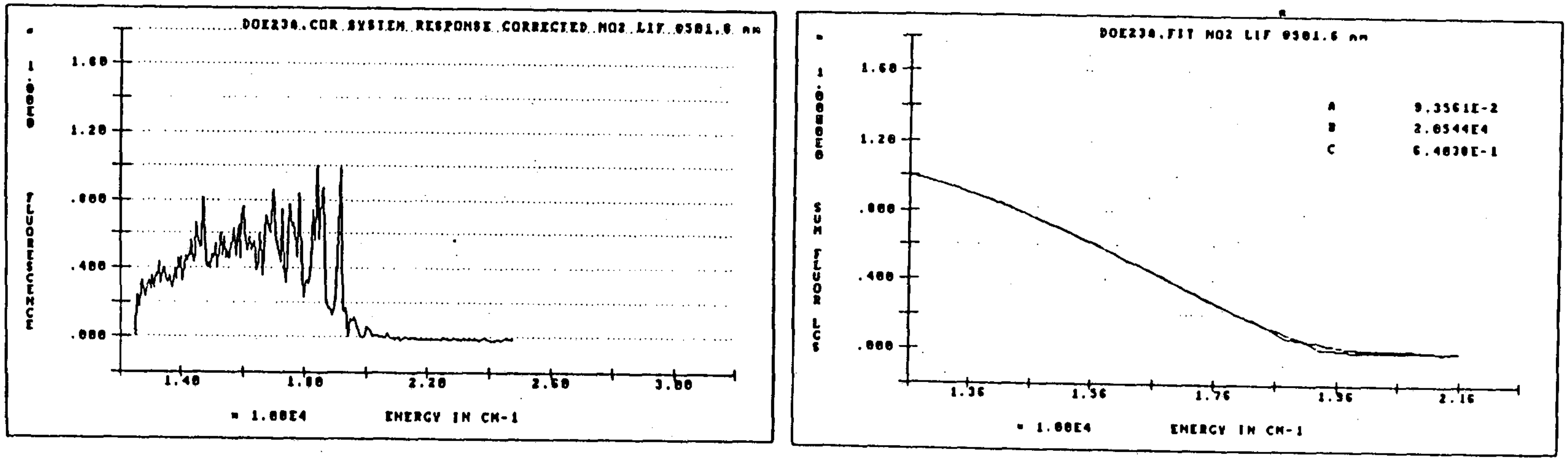

Figure 2.8(j)

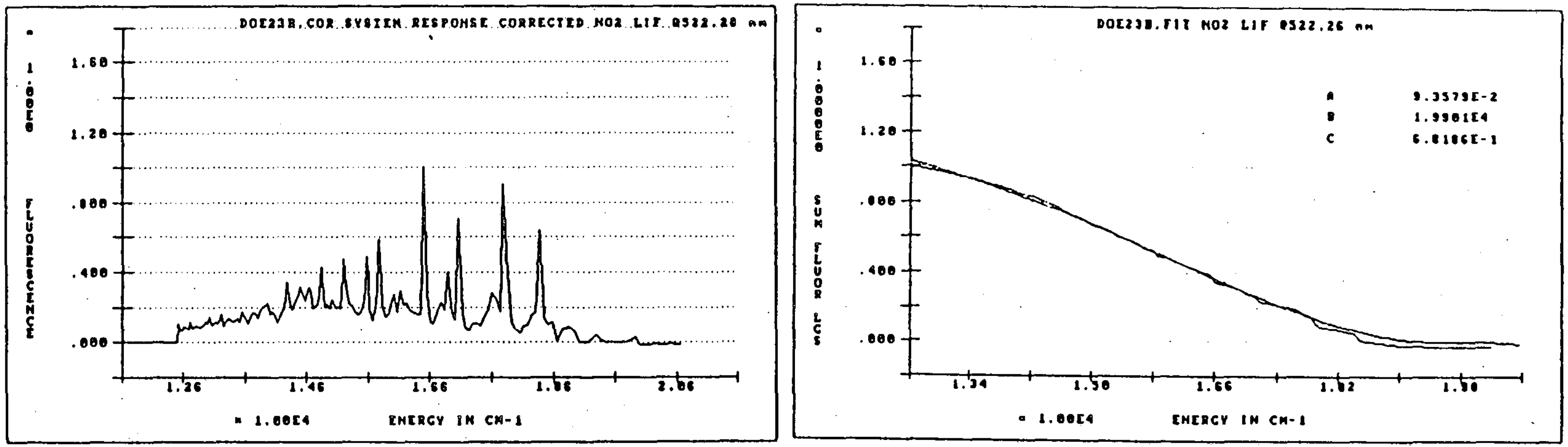

Figure 2.8(k)

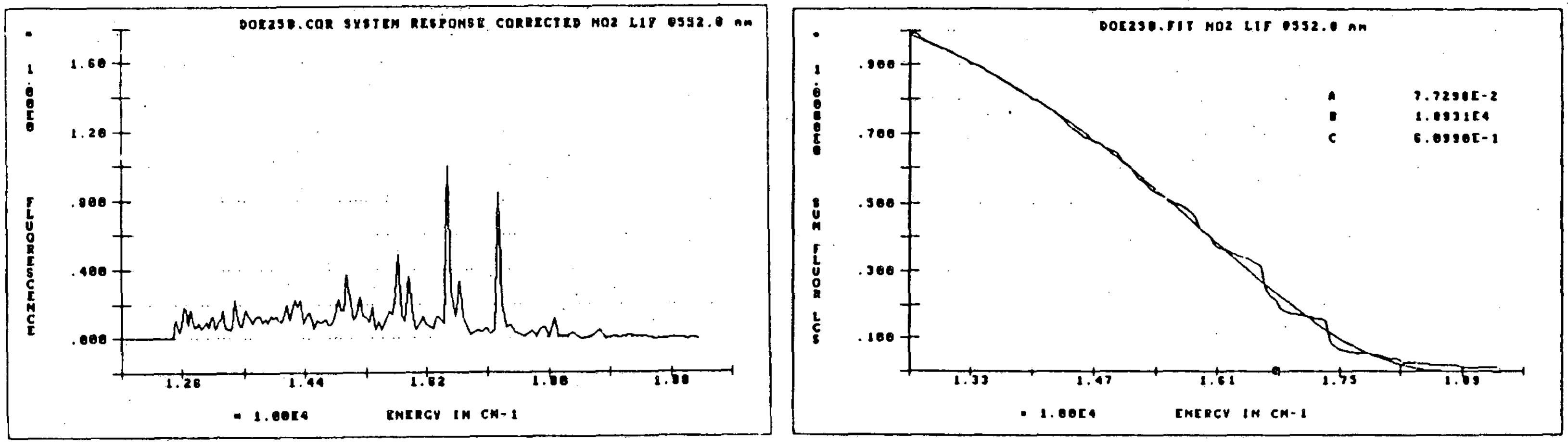

Figure 2.8(l)

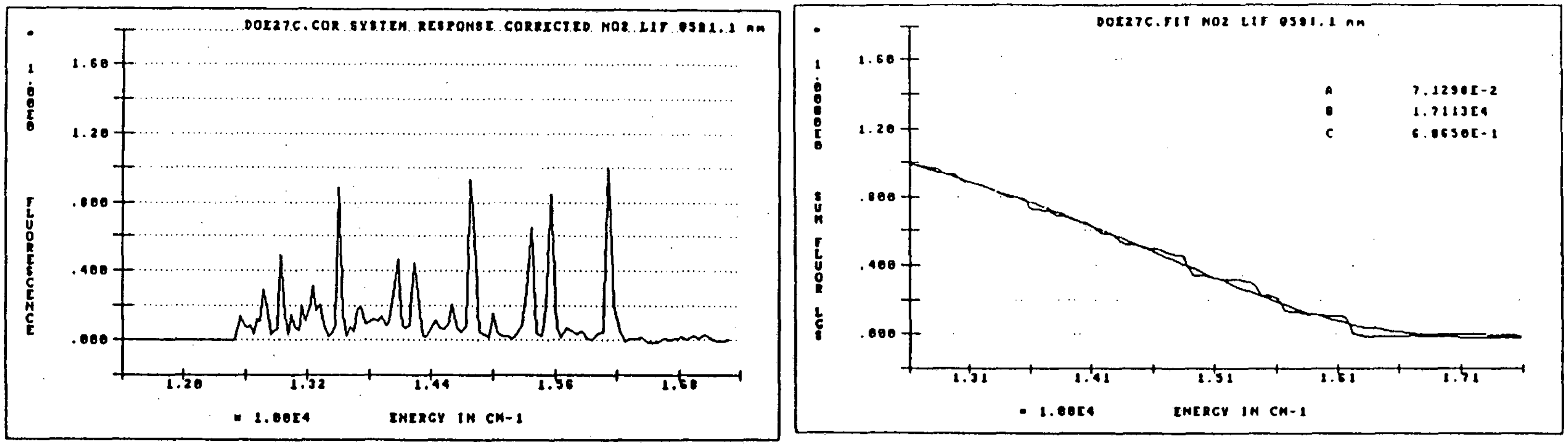

Figure 2.8(m)

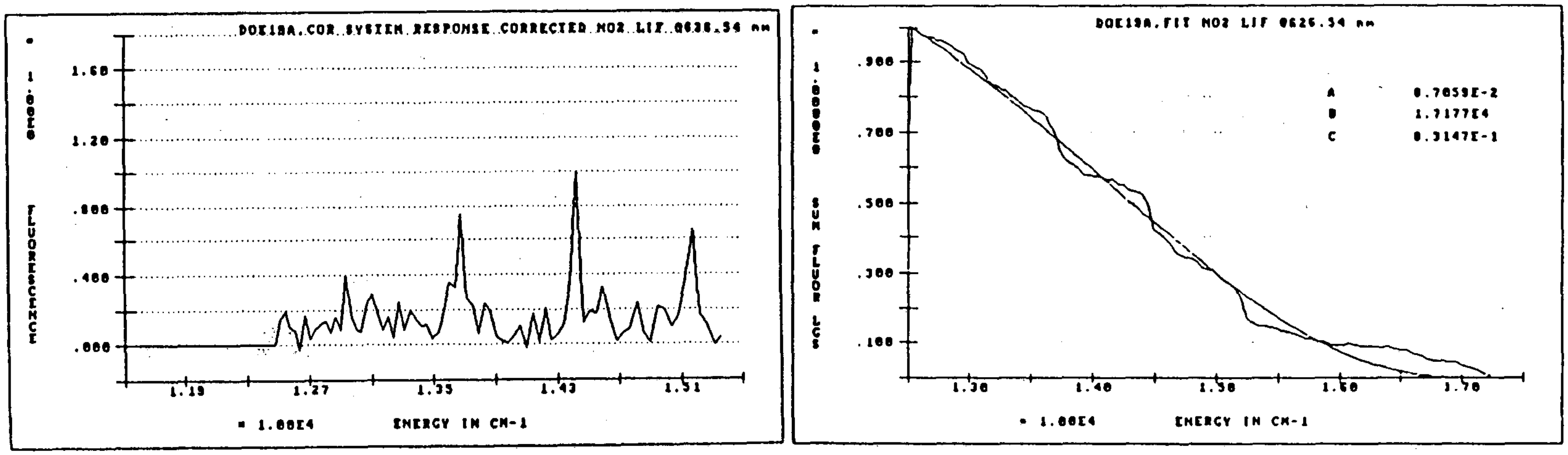

Figure 2.8(n)

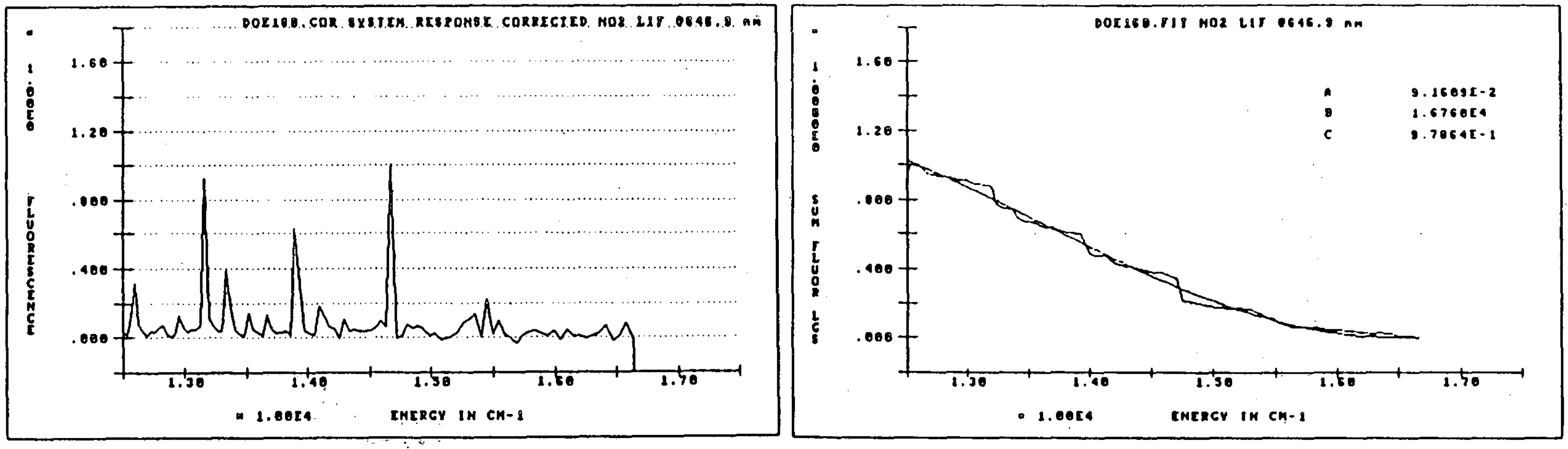

Figure 2.8(o)

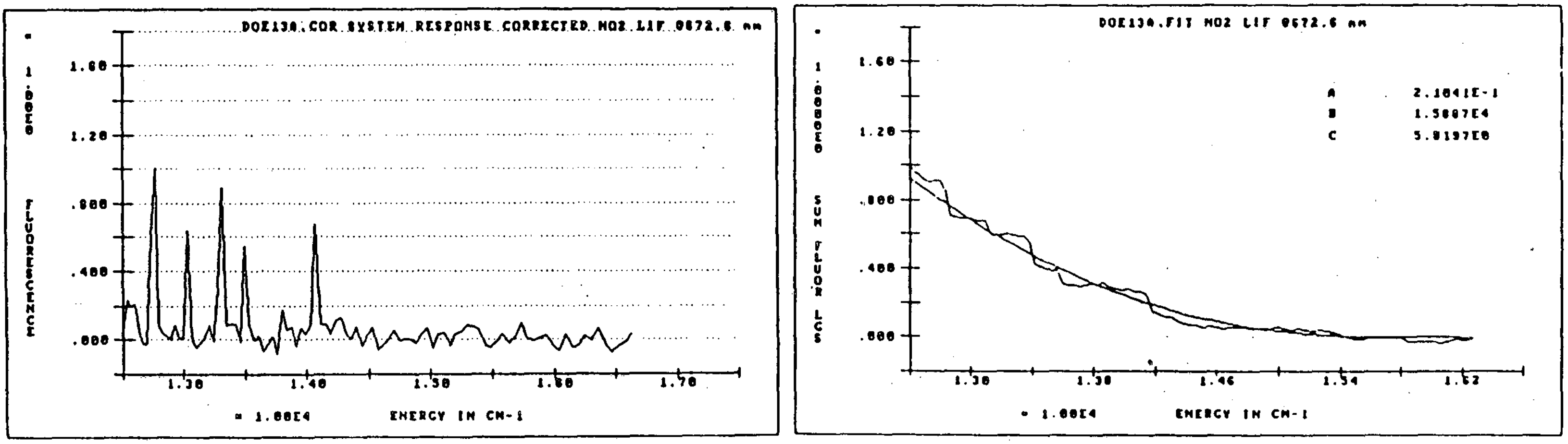

Figure 2.8(p)

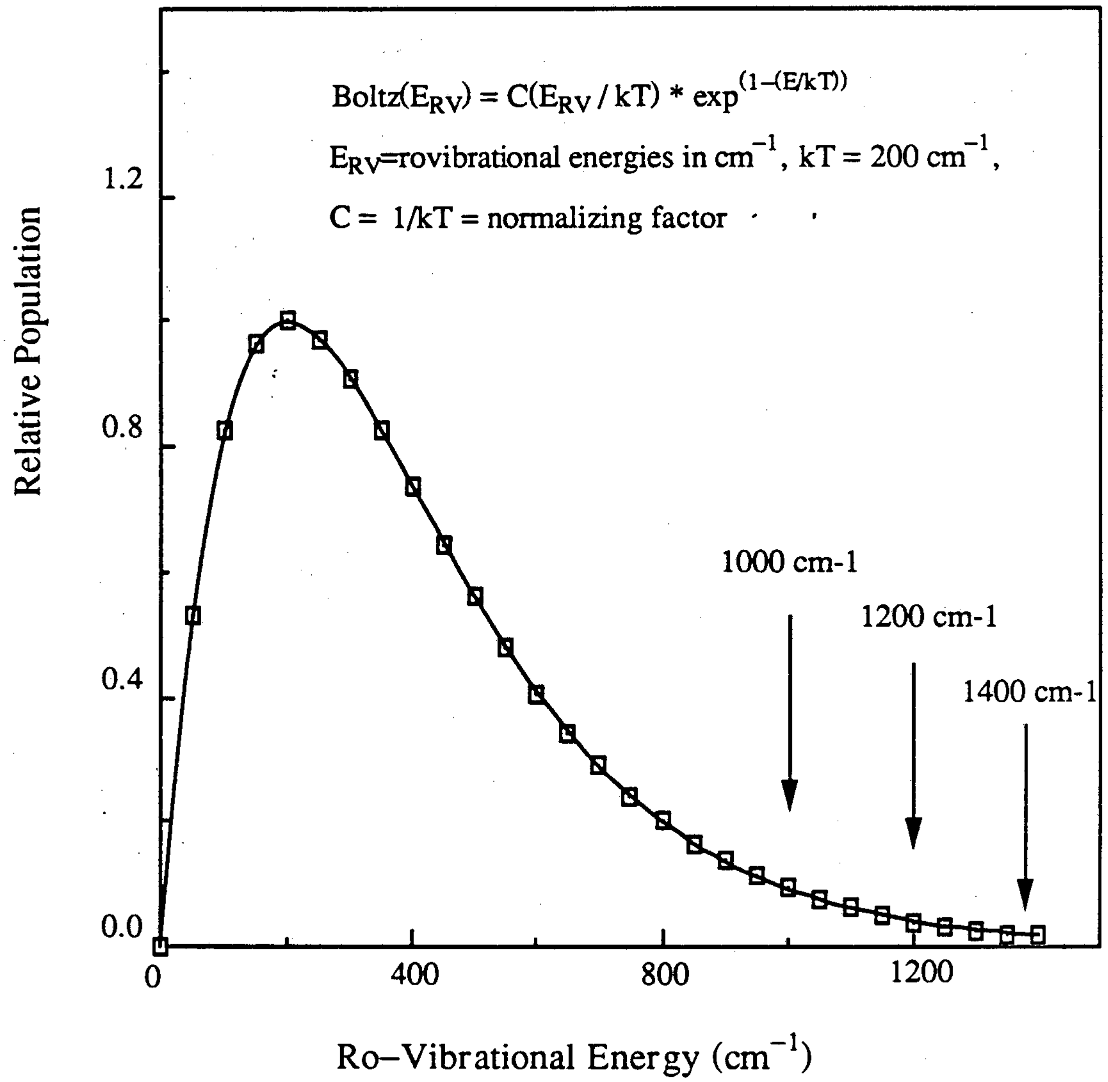
Boltz(E_RV) = C(E_RV / kT) * exp^(1−(E/kT))
E_RV=rovibrational energies in cm^−1, kT = 200 cm^−1,
C = 1/kT = normalizing factor
1000 cm-1
1200 cm-1
1400 cm-1
Relative Population
0.0
0.4
0.8
1.2
0
400
800
1200
Ro–Vibrational Energy (cm^−1)

Figure 2.9

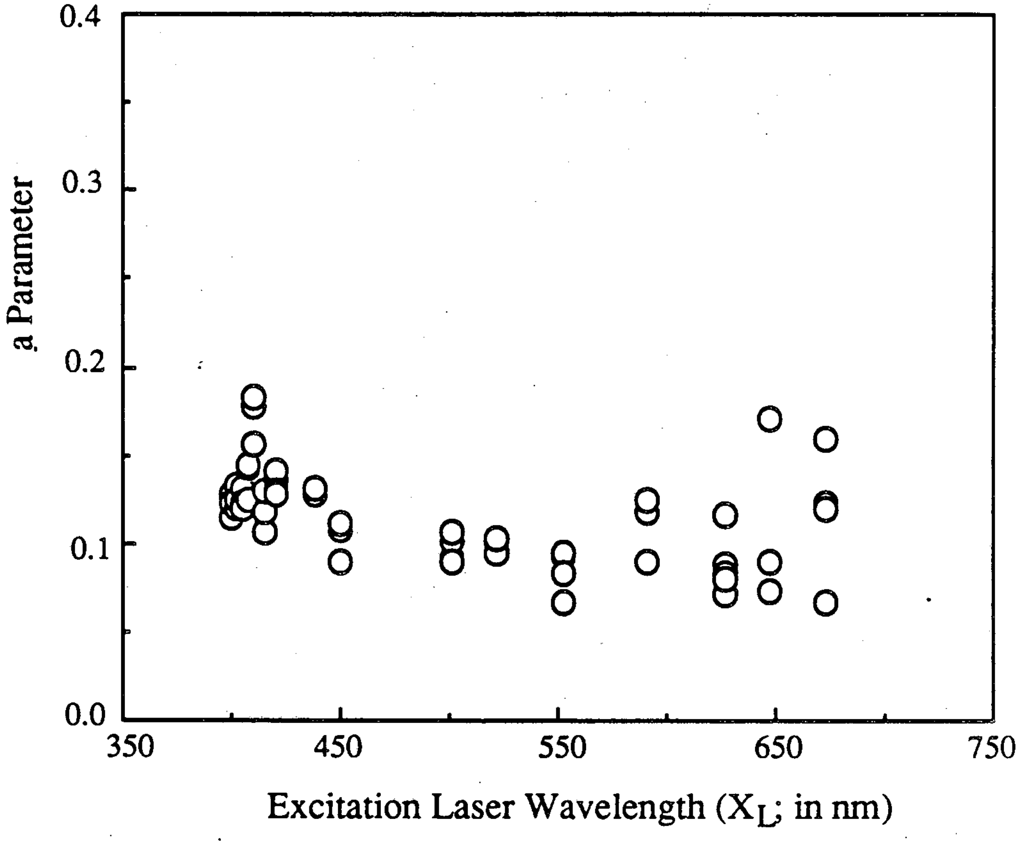
0.4
0.3
0.2
0.1
0.0
a Parameter
350
450
550
650
750
Excitation Laser Wavelength (X_L; in nm)

Figure 2.10(a)

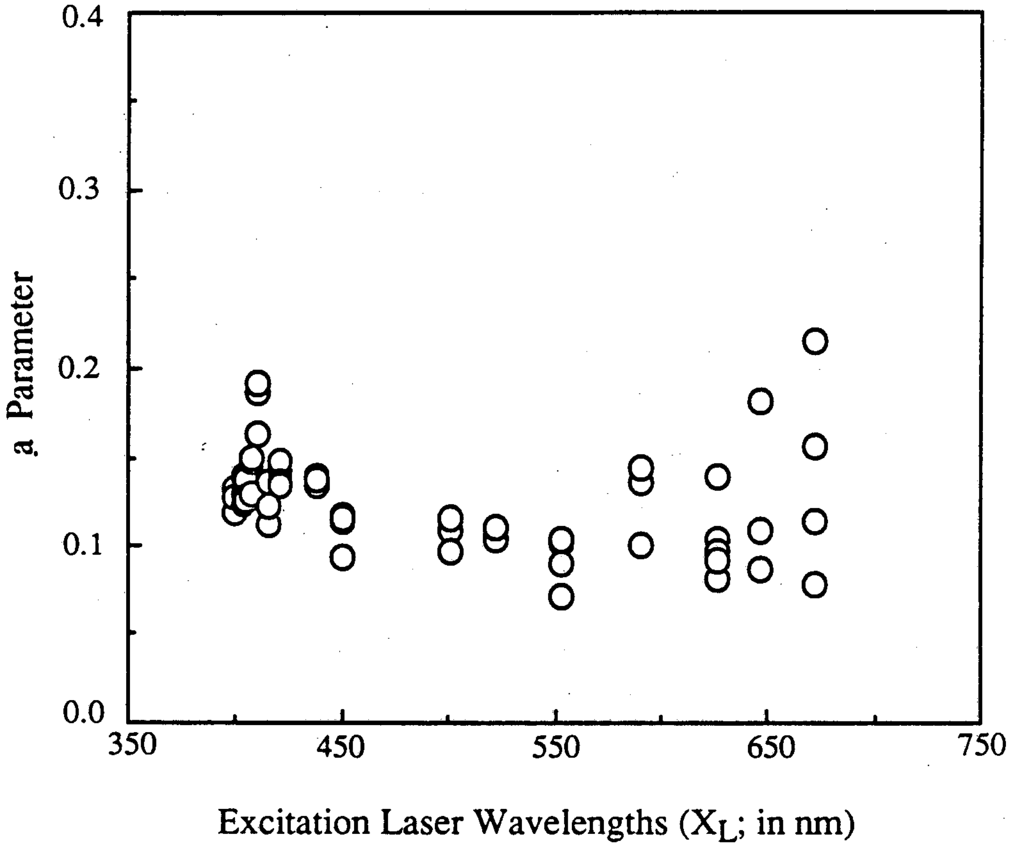
0.4
0.3
0.2
0.1
0.0
a Parameter
350
450
550
650
750
Excitation Laser Wavelengths (X$_L$; in nm)

Figure 2.10(b)

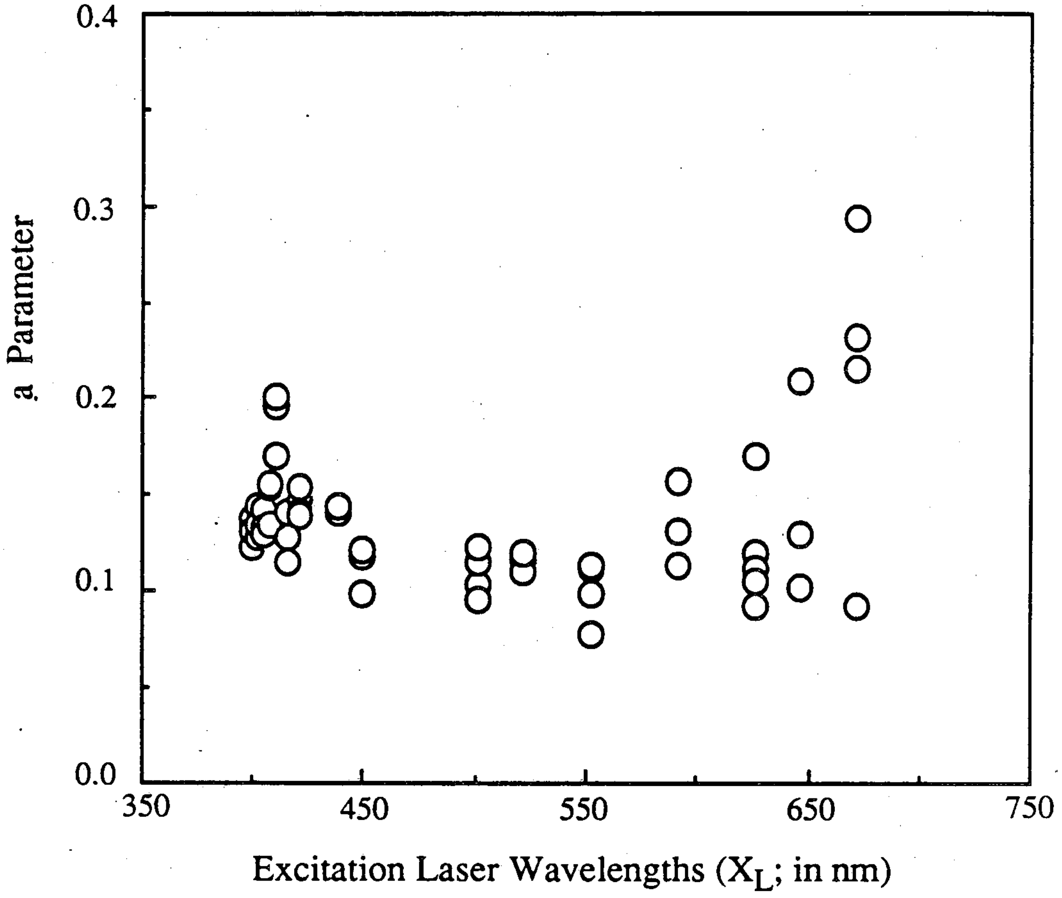
0.4
0.3
0.2
0.1
0.0
a Parameter
350
450
550
650
750
Excitation Laser Wavelengths (X$_L$; in nm)

Figure 2.10(c)

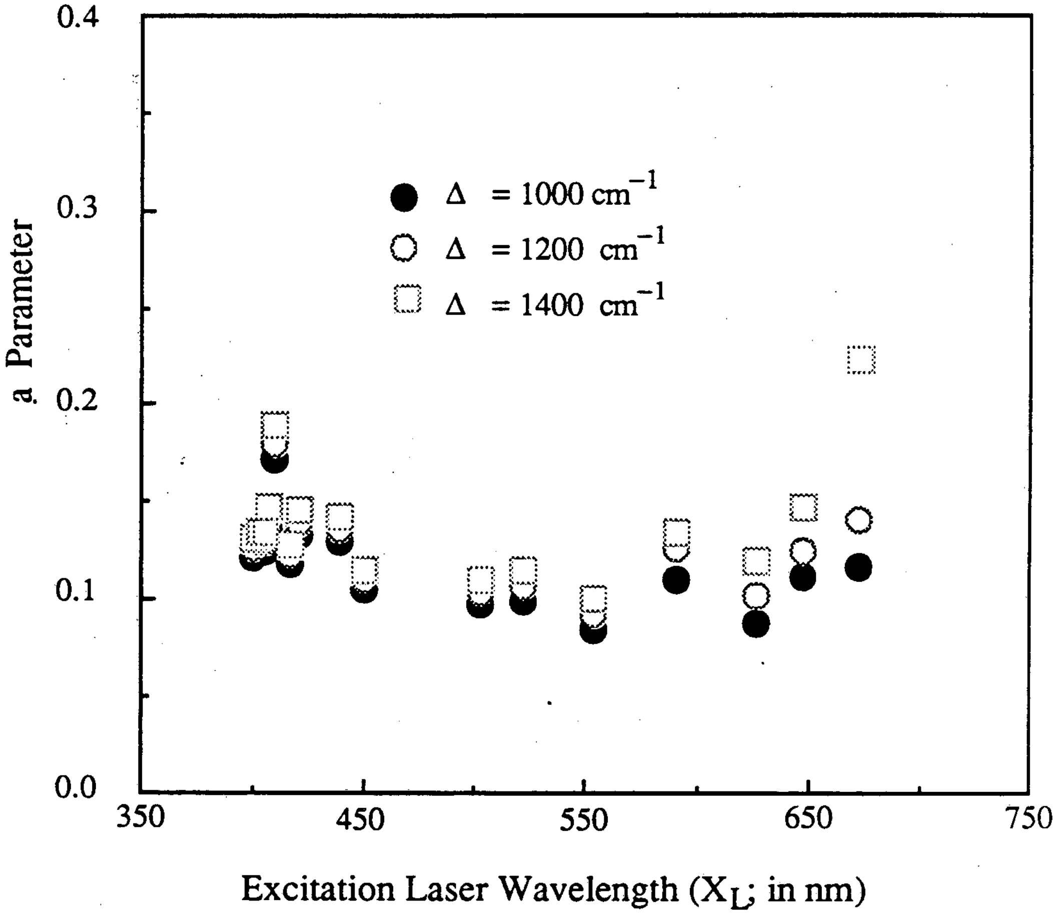
0.4
0.3
0.2
0.1
0.0
a Parameter
● Δ = 1000 cm⁻¹
○ Δ = 1200 cm⁻¹
□ Δ = 1400 cm⁻¹
350
450
550
650
750
Excitation Laser Wavelength (X_L; in nm)

Figure 2.11

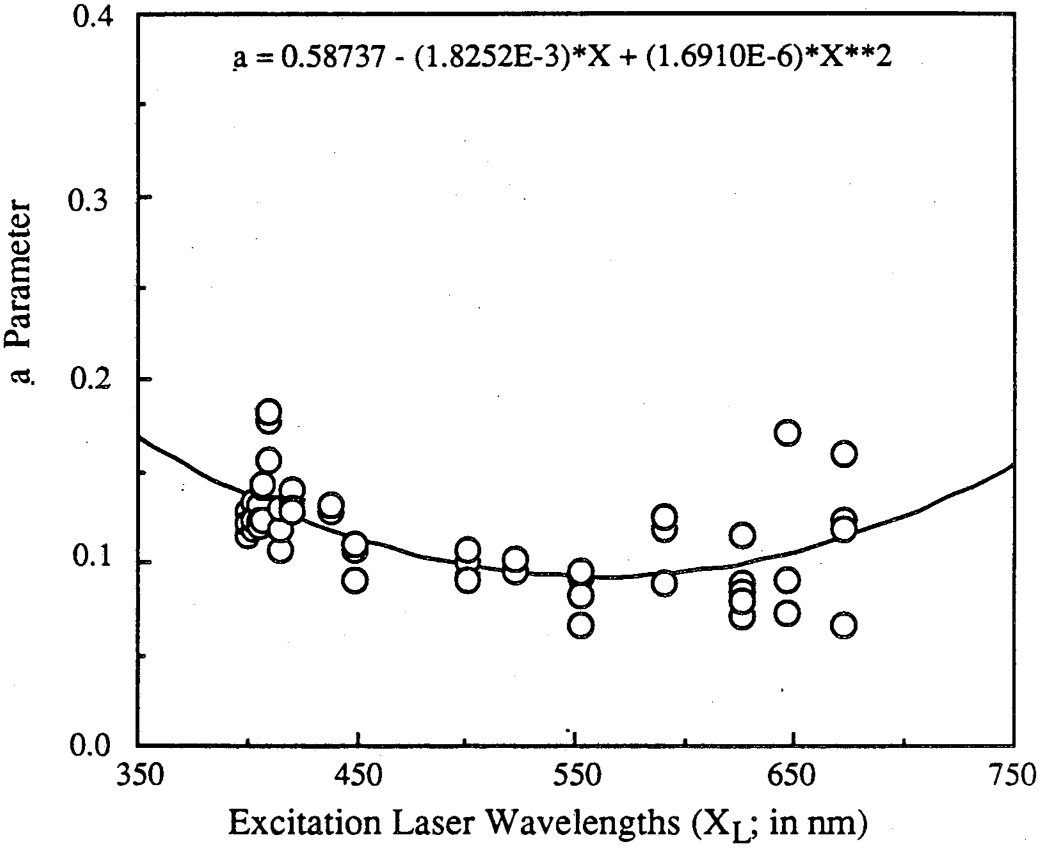
a = 0.58737 - (1.8252E-3)*X + (1.6910E-6)*X**2
a Parameter
0.4
0.3
0.2
0.1
0.0
350
450
550
650
750
Excitation Laser Wavelengths (X_L; in nm)

Figure 2.12

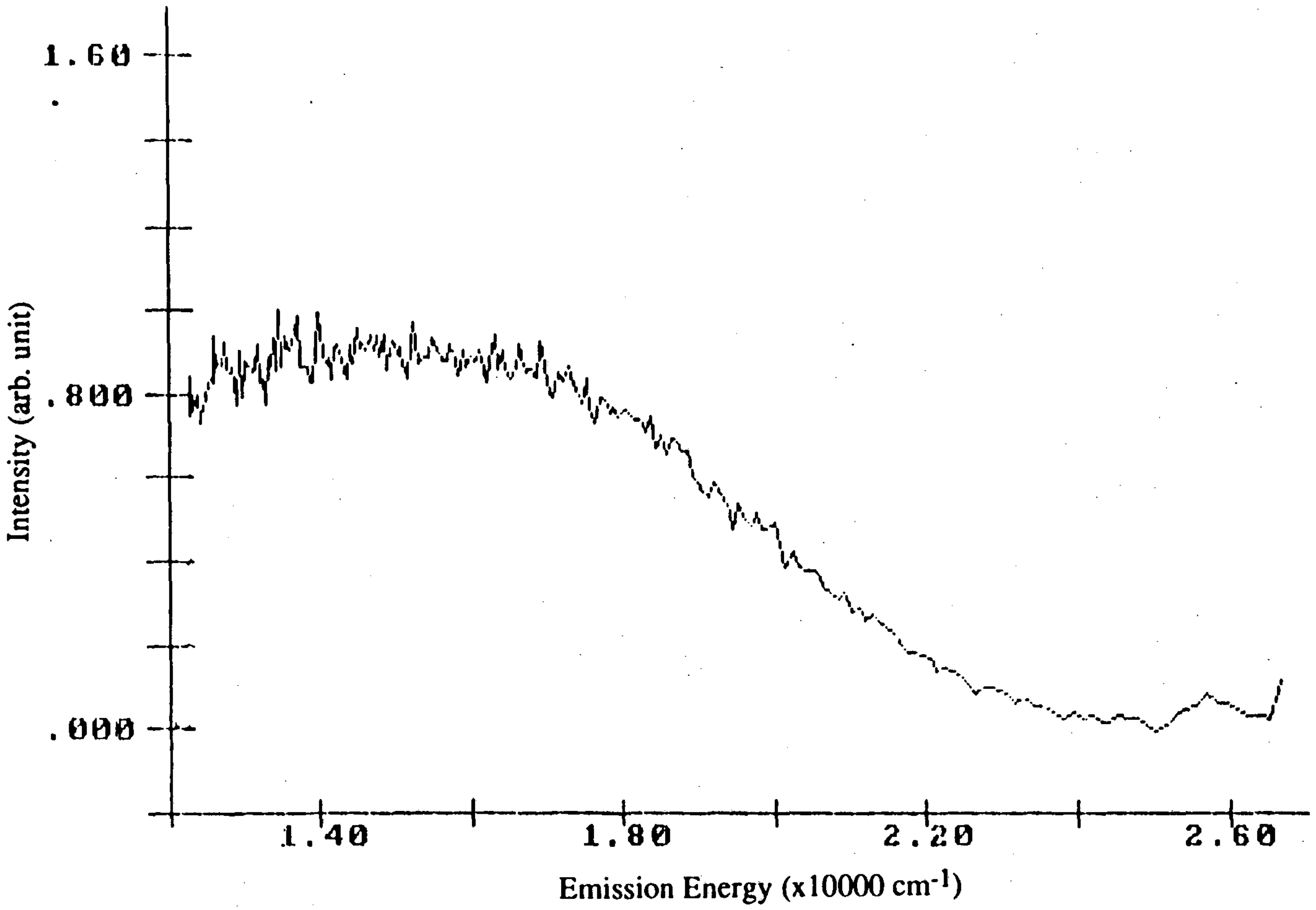
1.60
.800
.000
Intensity (arb. unit)
1.40
1.80
2.20
2.60
Emission Energy (x10000 cm^{-1})

Figure 2.13(a)

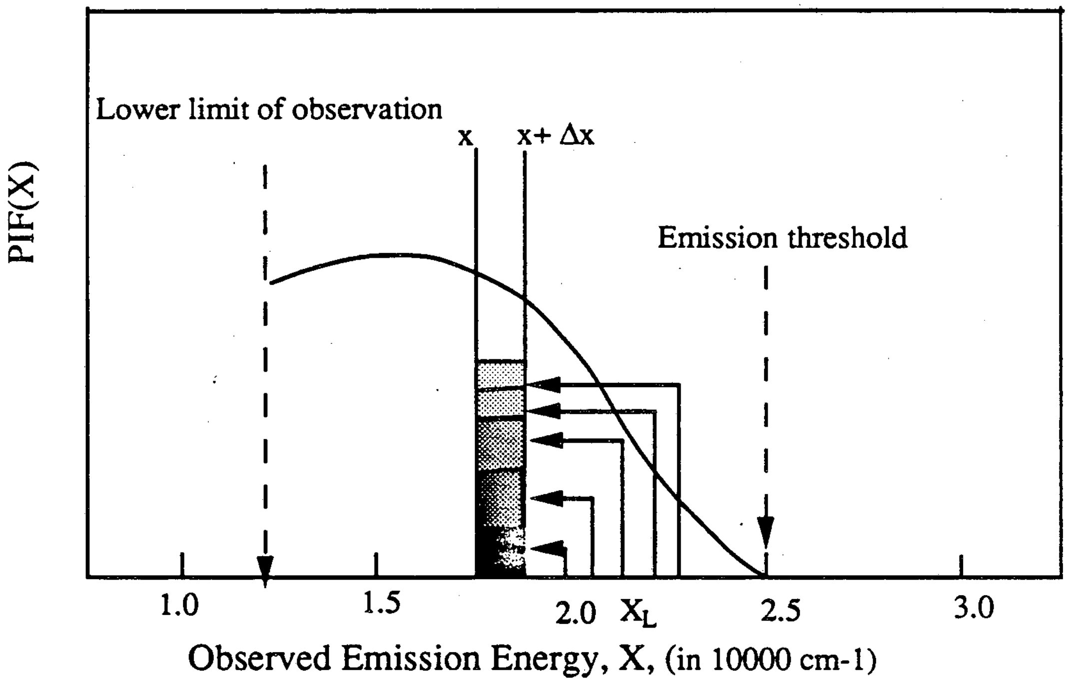
Lower limit of observation
x
x+ Δx
Emission threshold
PIF(X)
1.0
1.5
2.0
X_L
2.5
3.0
Observed Emission Energy, X, (in 10000 cm-1)

Figure 2.13(b)

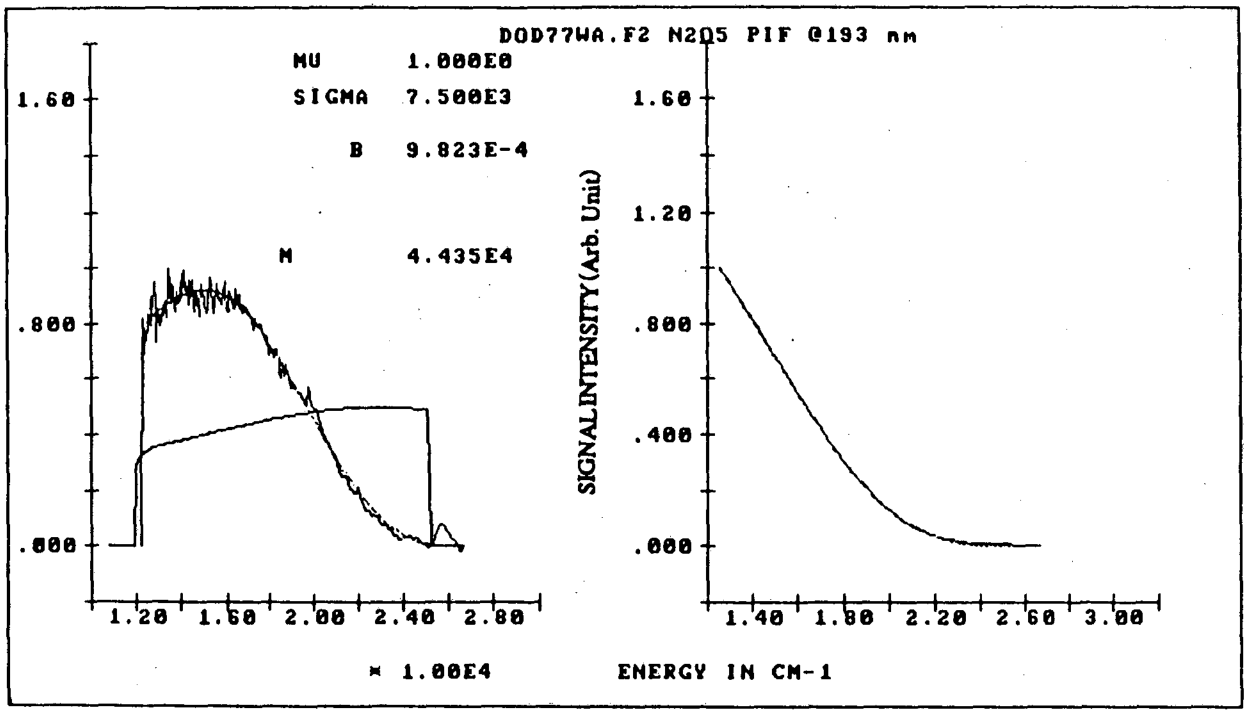
DOD77WA.F2 N2O5 PIF @193 nm
MU 1.000E0
SIGMA 7.500E3
B 9.823E-4
M 4.435E4
1.60
.800
.000
1.20
1.60
2.00
2.40
2.80
SIGNAL INTENSITY (Arb. Unit)
1.60
1.20
.800
.400
.000
1.40
1.80
2.20
2.60
3.00
* 1.00E4
ENERGY IN CM-1

Figure 2.14(a)

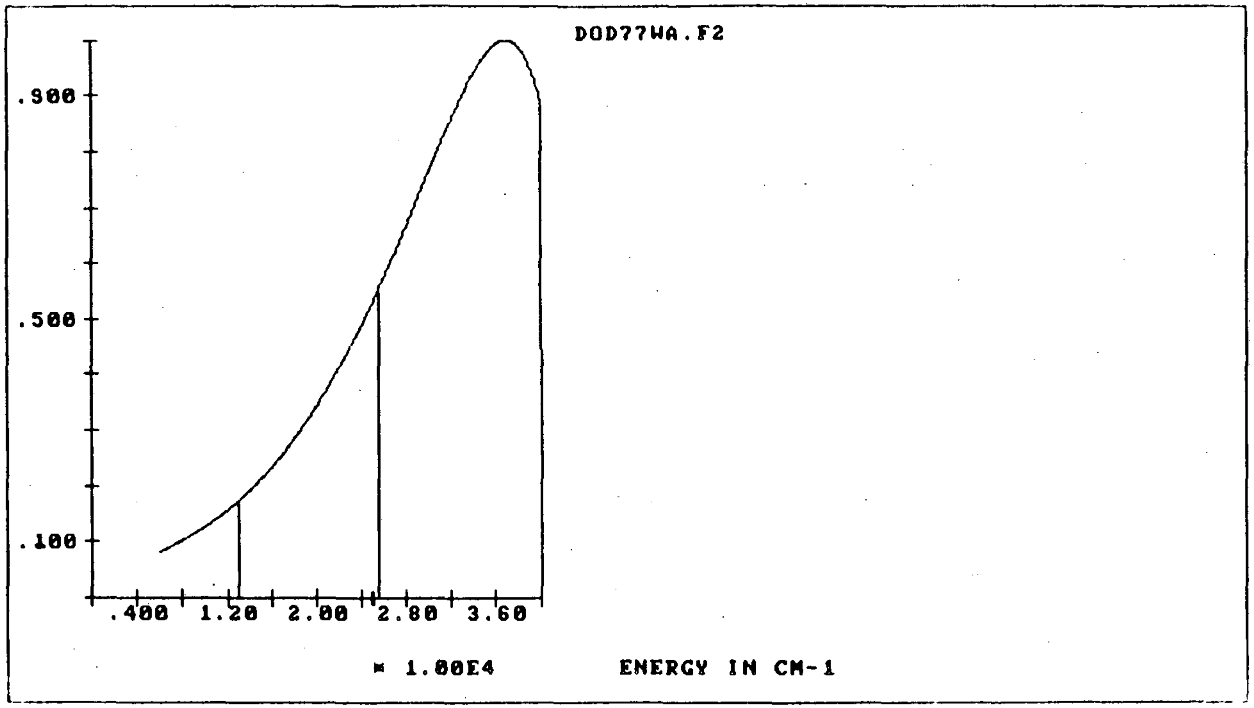

Figure 2.14(b)

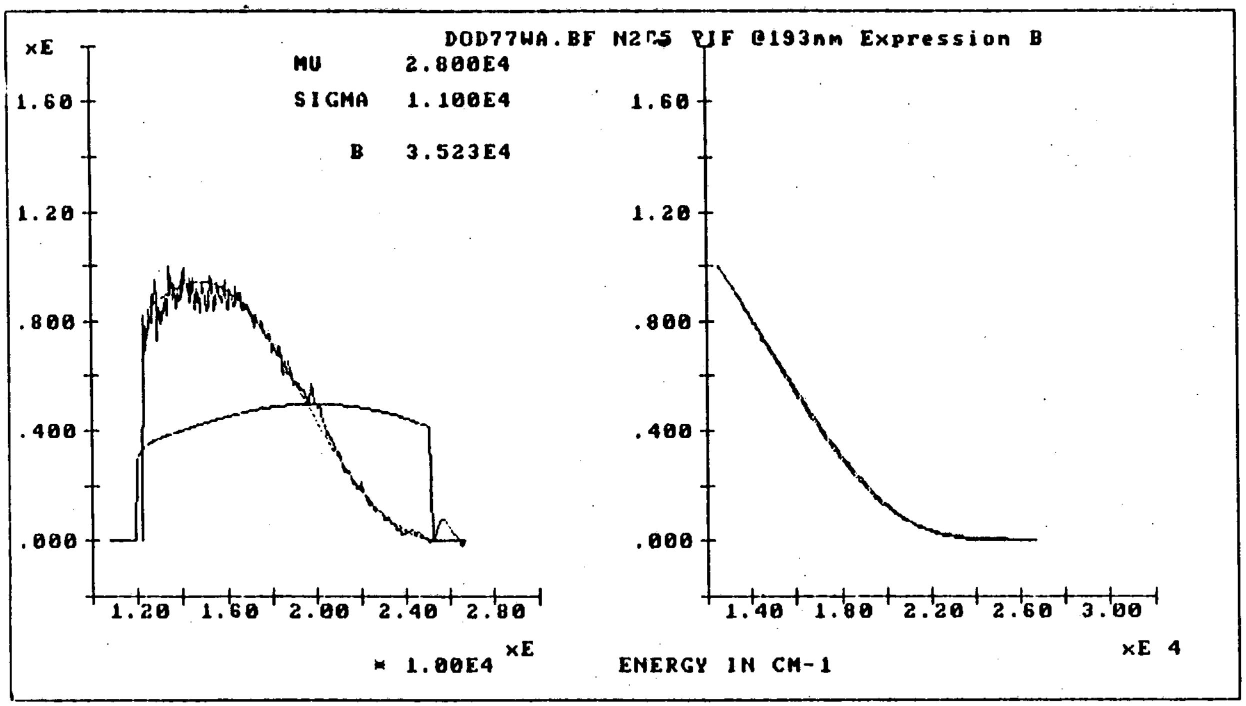
DOD77WA.BF N2O5 PIF @193nm Expression B
MU 2.800E4
SIGMA 1.100E4
B 3.523E4
xE
1.60
1.20
.800
.400
.000
1.20
1.60
2.00
2.40
2.80
* 1.00E4
xE
1.60
1.20
.800
.400
.000
1.40
1.80
2.20
2.60
3.00
xE 4
ENERGY IN CM-1

Figure 2.15(a)

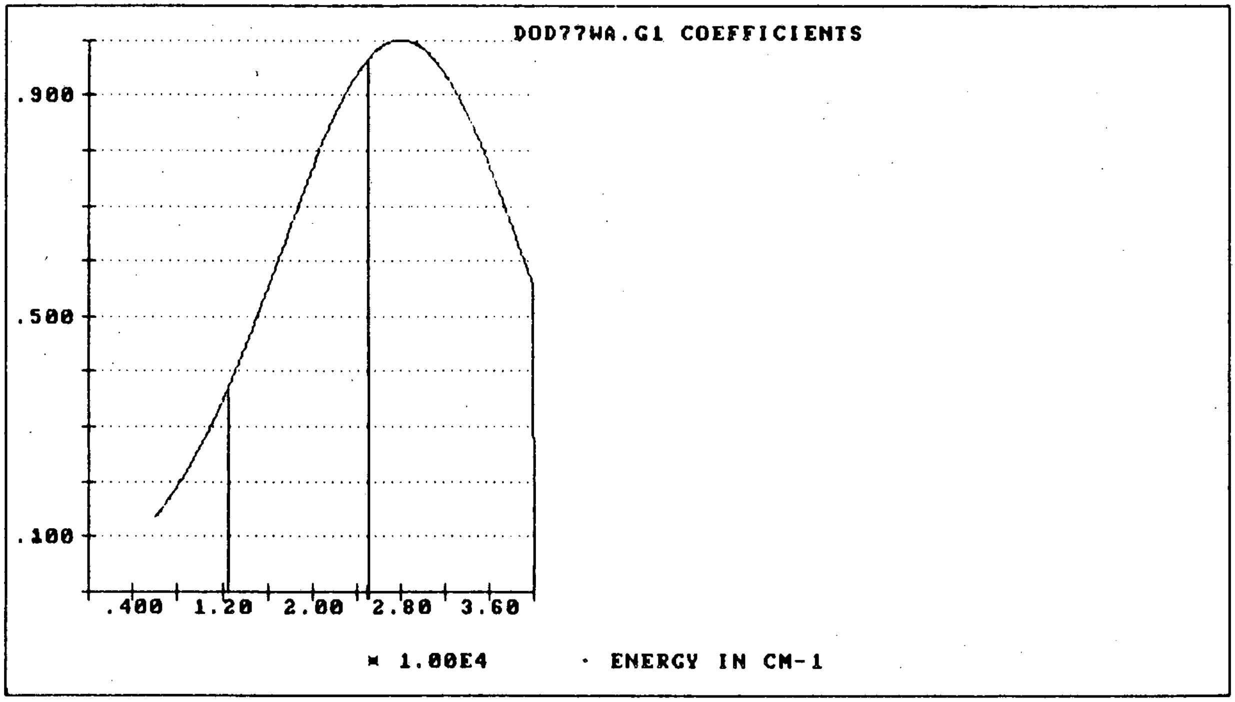
DOD77WA.G1 COEFFICIENTS
.900
.500
.100
.400
1.20
2.00
2.80
3.60
* 1.00E4
· ENERGY IN CM-1

Figure 2.15(b)

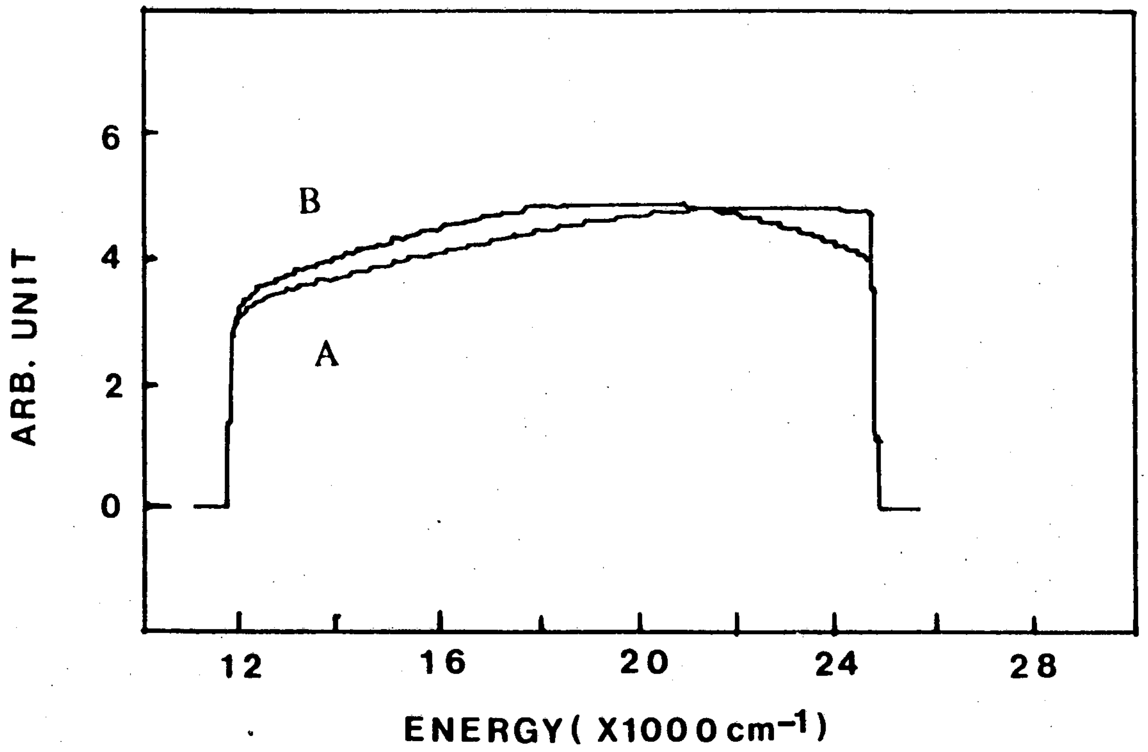

Figure 2.16

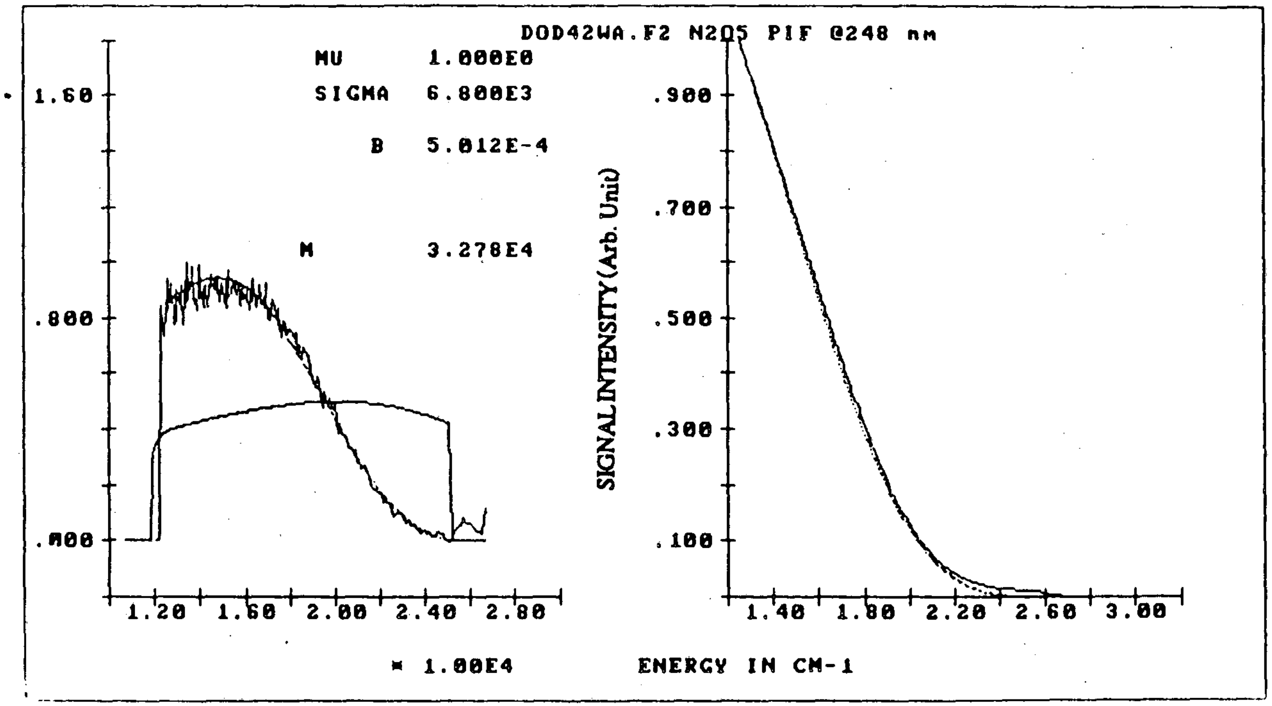
DOD42WA.F2 N2O5 PIF @248 nm
MU 1.000E0
SIGMA 6.800E3
B 5.012E-4
M 3.278E4
1.60
.800
.000
1.20
1.60
2.00
2.40
2.80
SIGNAL INTENSITY (Arb. Unit)
.900
.700
.500
.300
.100
1.40
1.80
2.20
2.60
3.00
* 1.00E4
ENERGY IN CM-1

Figure 2.17(a)

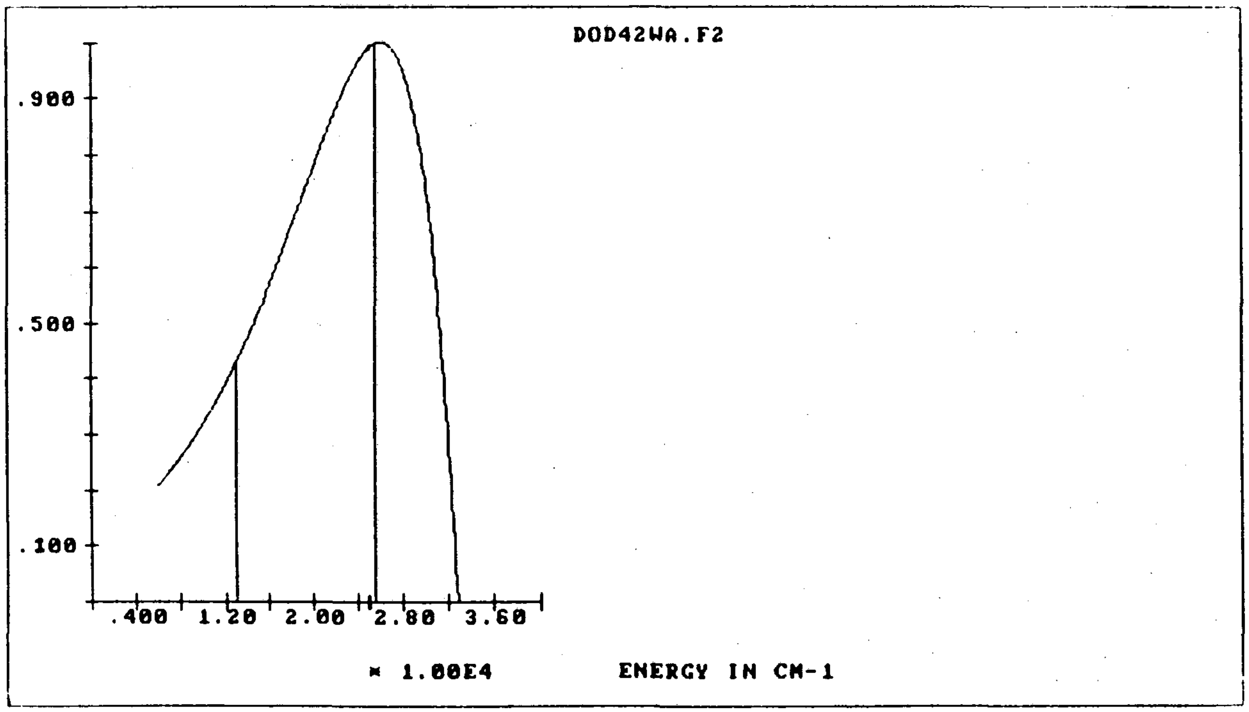

Figure 2.17(b)

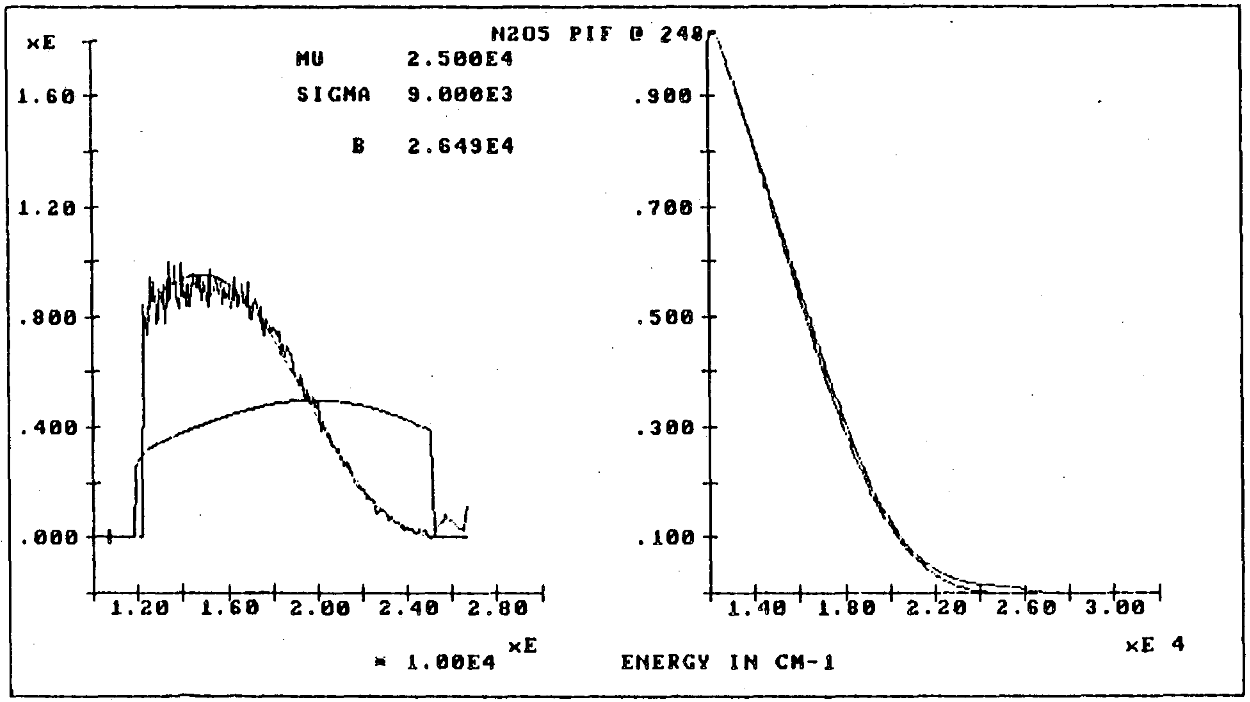
N2O5 PIF @ 248
MU 2.500E4
SIGMA 9.000E3
B 2.649E4
xE
1.60
1.20
.800
.400
.000
1.20
1.60
2.00
2.40
2.80
* 1.00E4
xE
.900
.700
.500
.300
.100
1.40
1.80
2.20
2.60
3.00
xE 4
ENERGY IN CM-1

Figure 2.18(a)

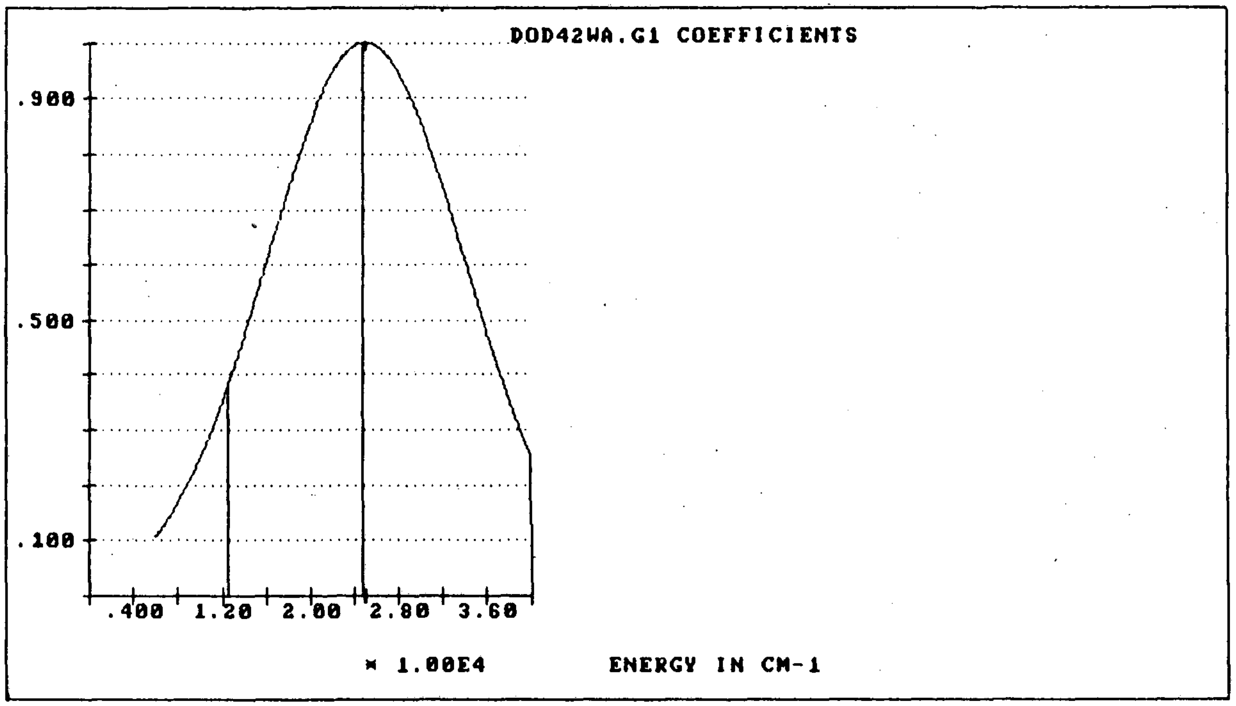
DOD42WA.G1 COEFFICIENTS
.900
.500
.100
.400
1.20
2.00
2.80
3.60
* 1.00E4
ENERGY IN CM-1

Figure 2.18(b)

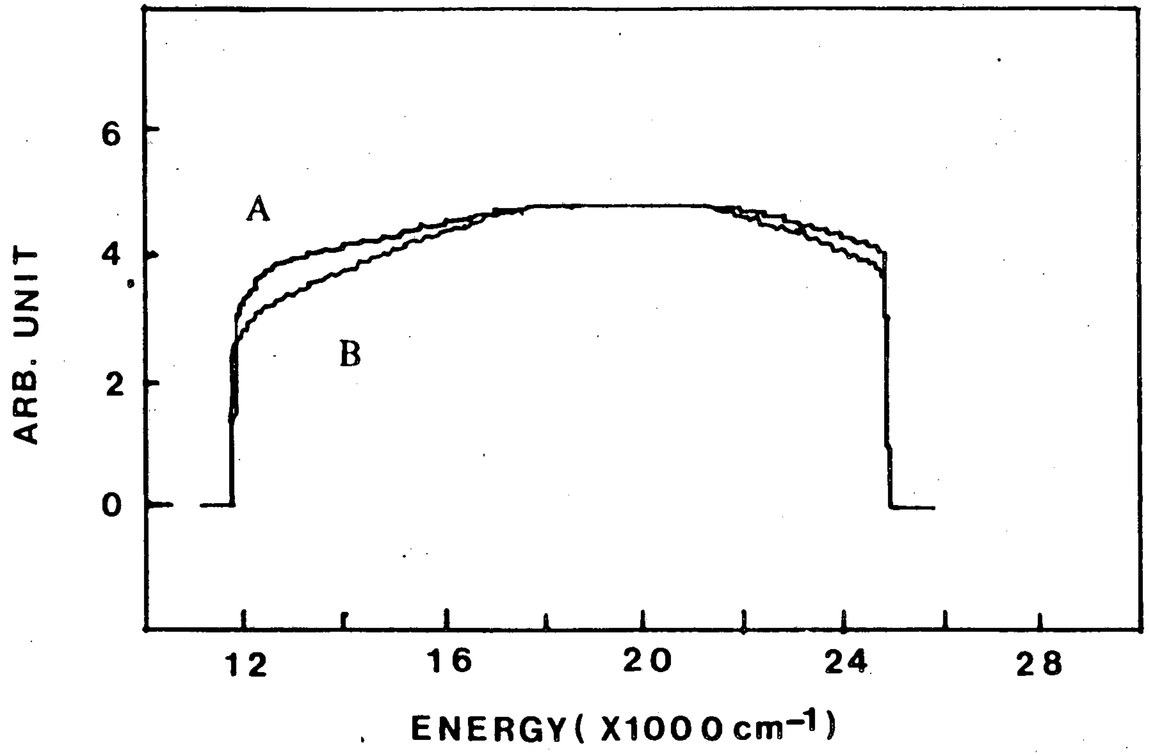

Figure 2.19

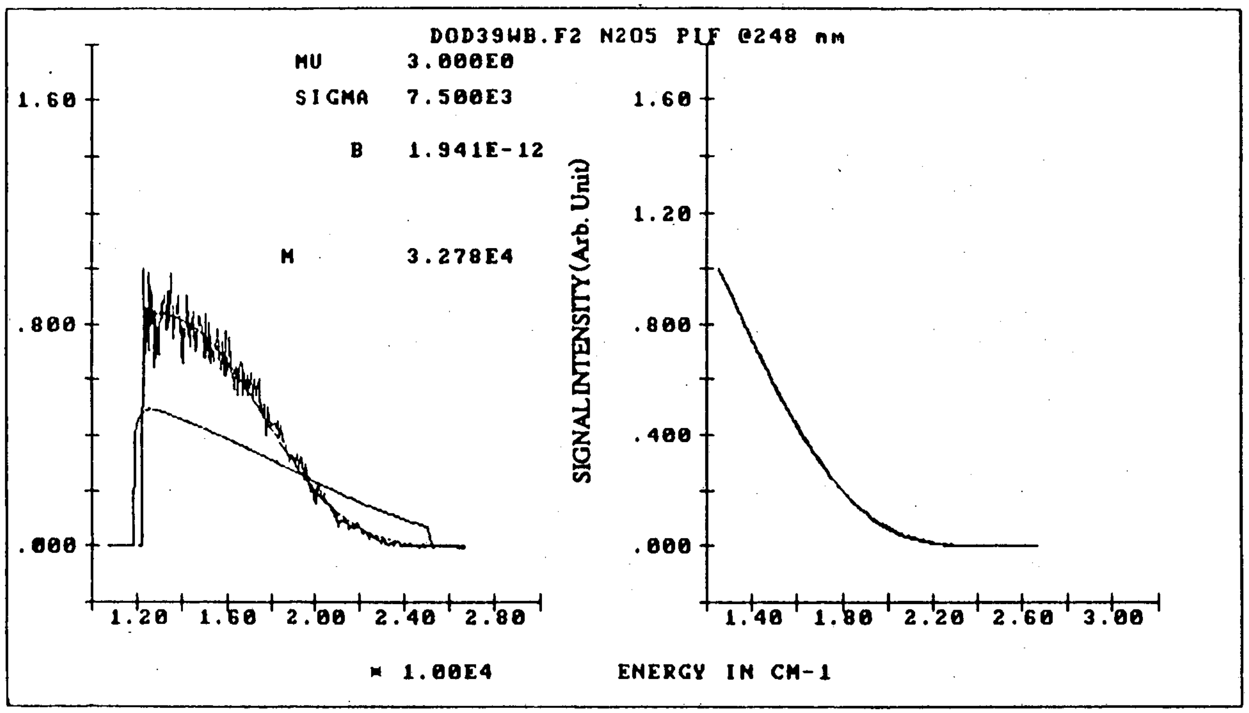
DOD39WB.F2 N2O5 PLF @248 nm
MU 3.000E0
SIGMA 7.500E3
B 1.941E-12
M 3.278E4
1.60
.800
.000
1.20
1.60
2.00
2.40
2.80
SIGNAL INTENSITY (Arb. Unit)
1.60
1.20
.800
.400
.000
1.40
1.80
2.20
2.60
3.00
* 1.00E4
ENERGY IN CM-1

Figure 2.20(a)

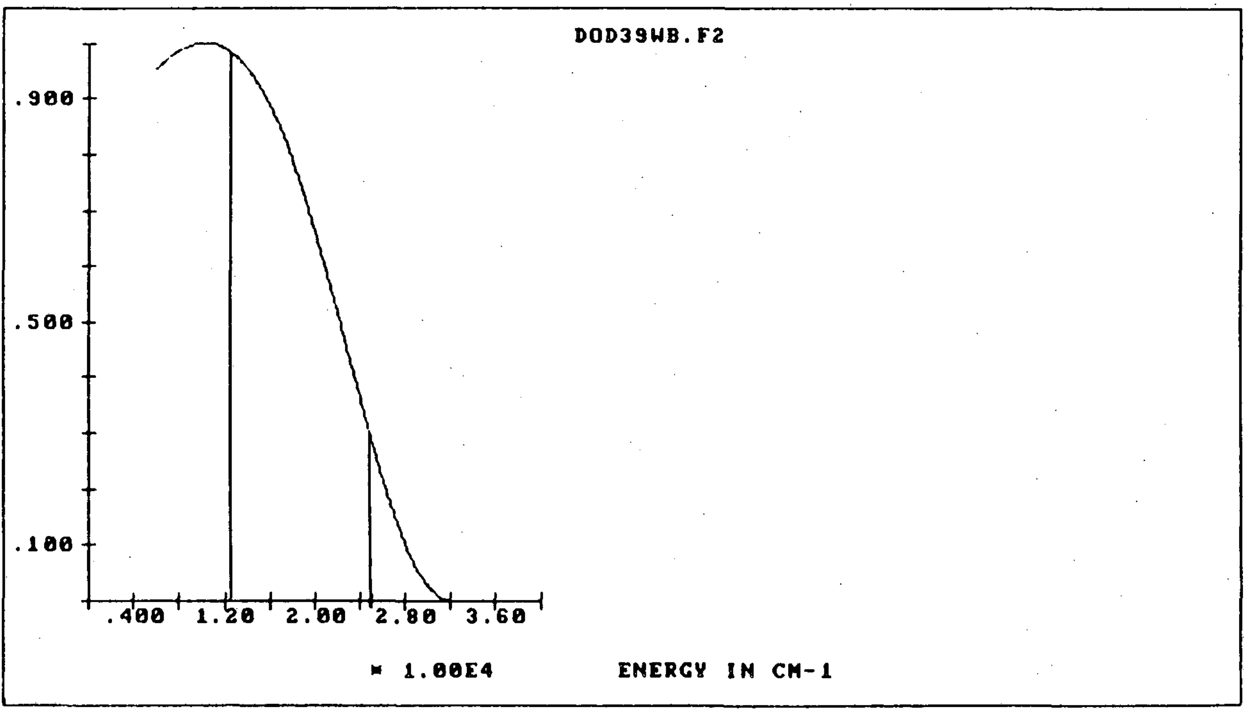

Figure 2.20(b)

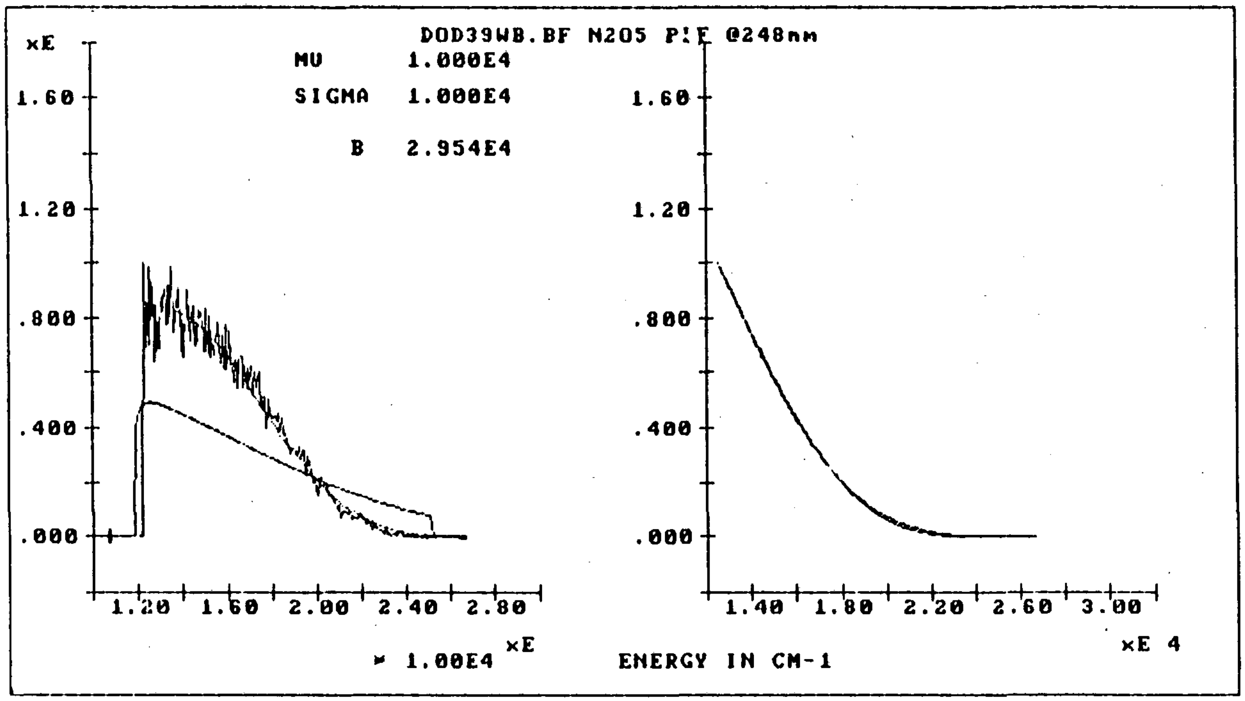
DOD39WB.BF N2O5 P:F @248nm
MU 1.000E4
SIGMA 1.000E4
B 2.954E4
xE
1.60
1.20
.800
.400
.000
1.20
1.60
2.00
2.40
2.80
xE
* 1.00E4
1.60
1.20
.800
.400
.000
1.40
1.80
2.20
2.60
3.00
xE 4
ENERGY IN CM-1

Figure 2.21(a)

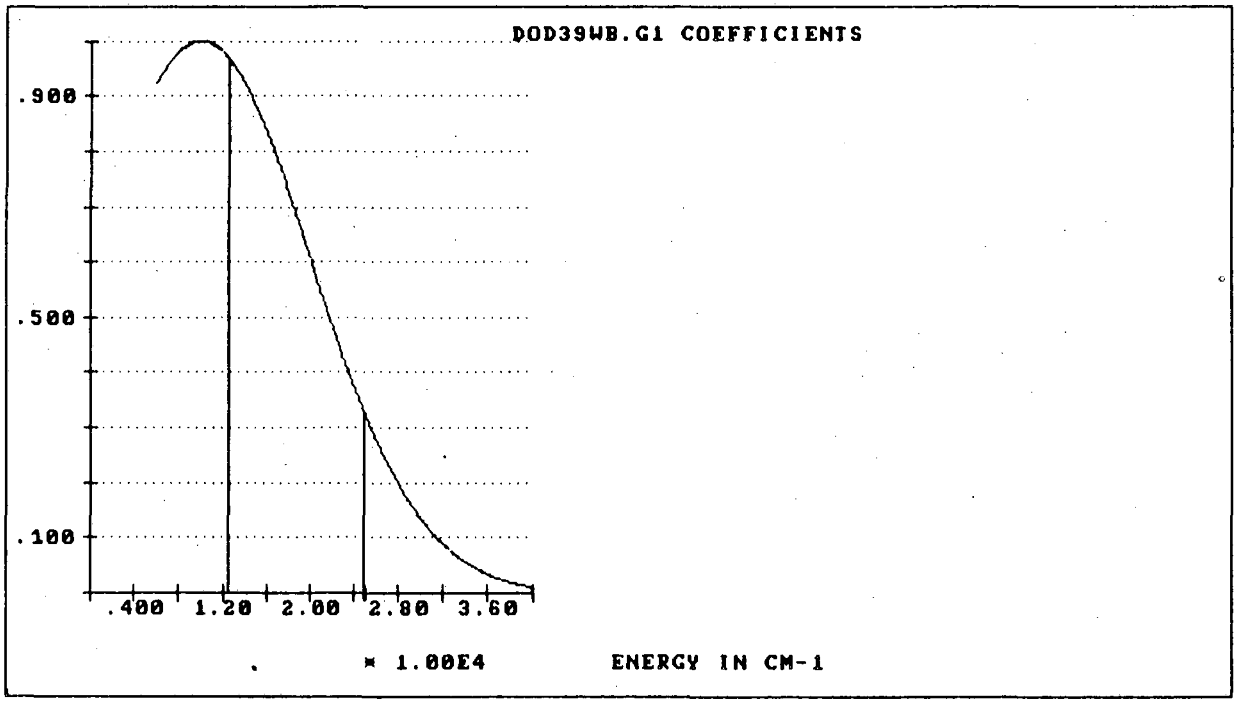
DOD39WB.G1 COEFFICIENTS
.900
.500
.100
.400
1.20
2.00
2.80
3.60
* 1.00E4
ENERGY IN CM-1

Figure 2.21(b)

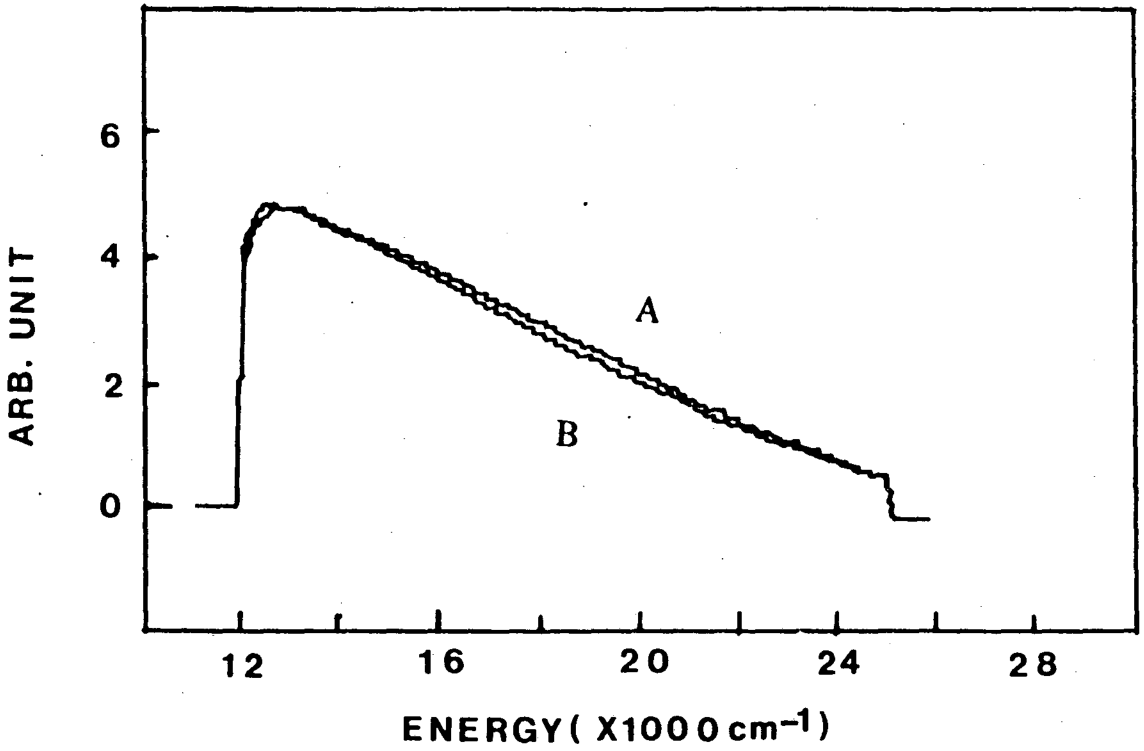

Figure 2.22

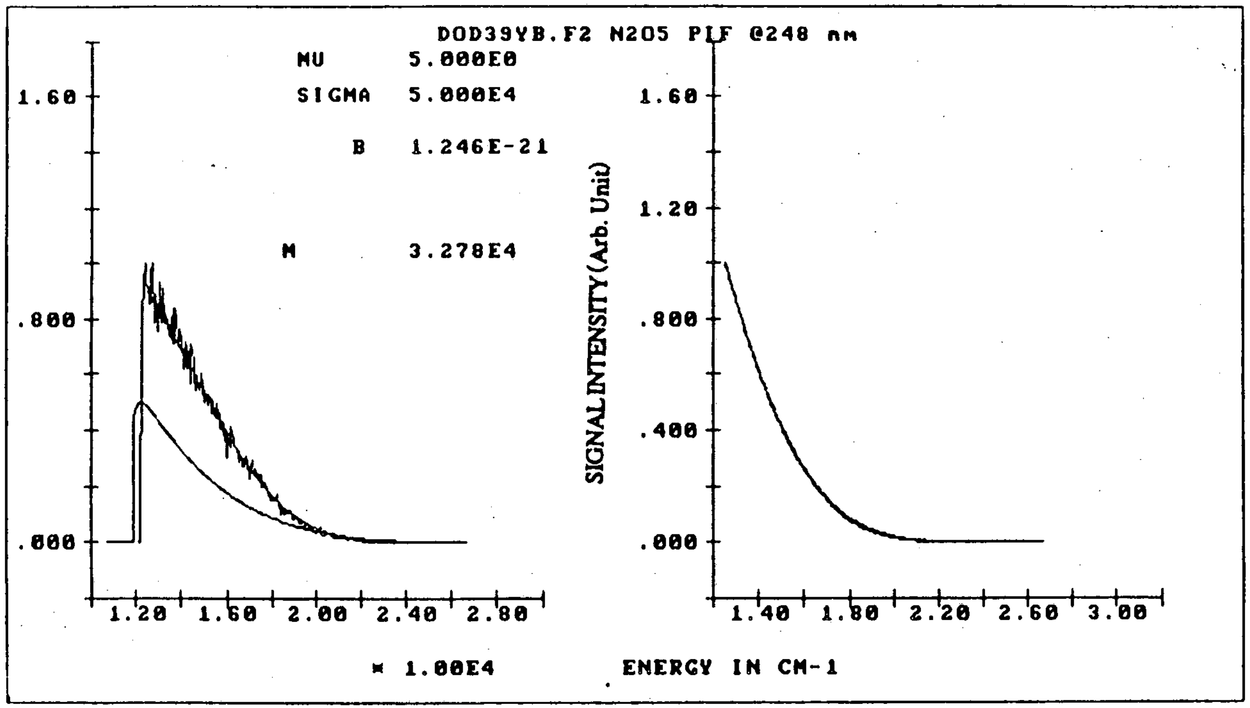
DOD39YB.F2 N2O5 PLF @248 nm
MU 5.000E0
SIGMA 5.000E4
B 1.246E-21
M 3.278E4
1.60
.800
.000
1.20
1.60
2.00
2.40
2.80
SIGNAL INTENSITY (Arb. Unit)
1.60
1.20
.800
.400
.000
1.40
1.80
2.20
2.60
3.00
* 1.00E4
ENERGY IN CM-1

Figure 2.23(a)

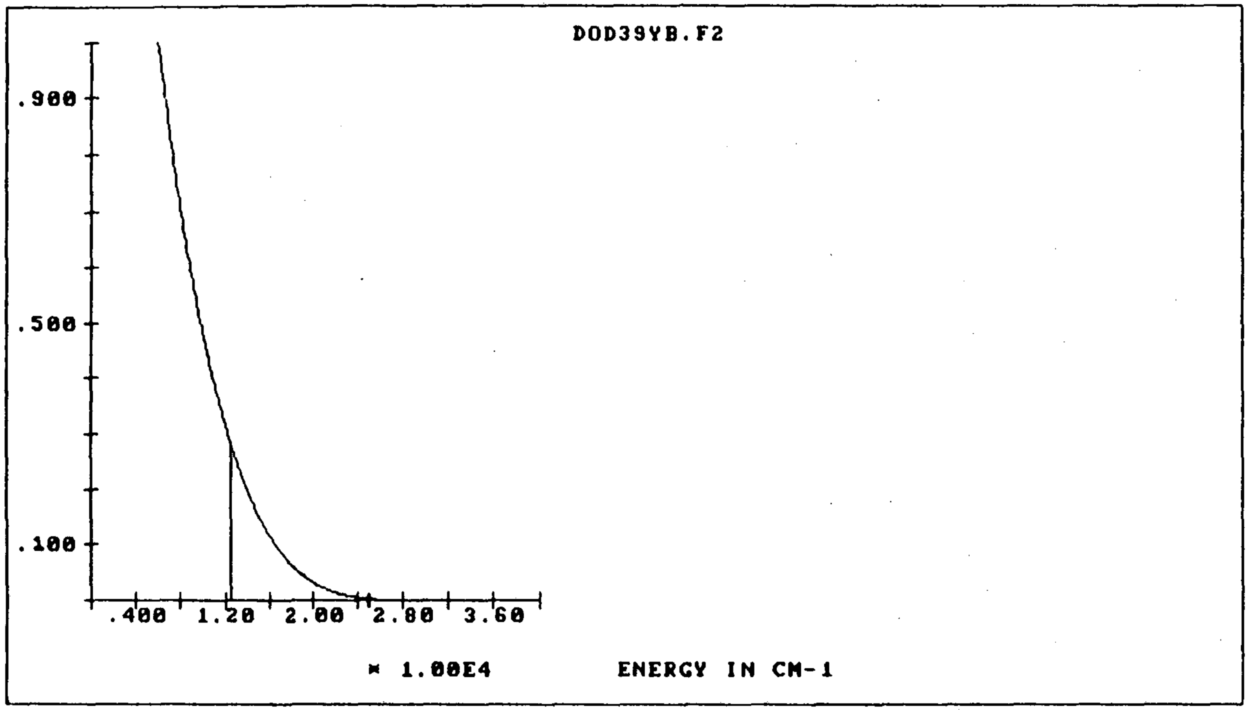

Figure 2.23(b)

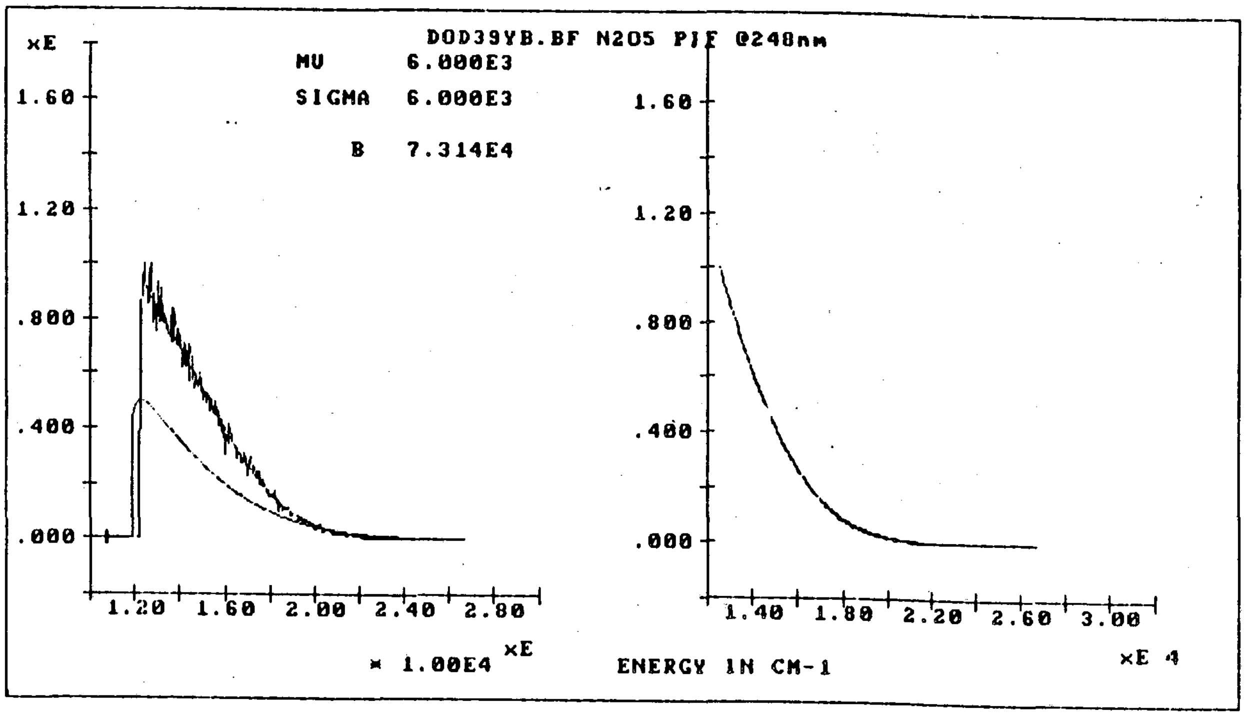
DOD39YB.BF N2O5 PJF @248nm
MU 6.000E3
SIGMA 6.000E3
B 7.314E4
×E
1.60
1.20
.800
.400
.000
1.20
1.60
2.00
2.40
2.80
× 1.00E4 ×E
1.60
1.20
.800
.400
.000
1.40
1.80
2.20
2.60
3.00
×E 4
ENERGY IN CM-1

Figure 2.24(a)

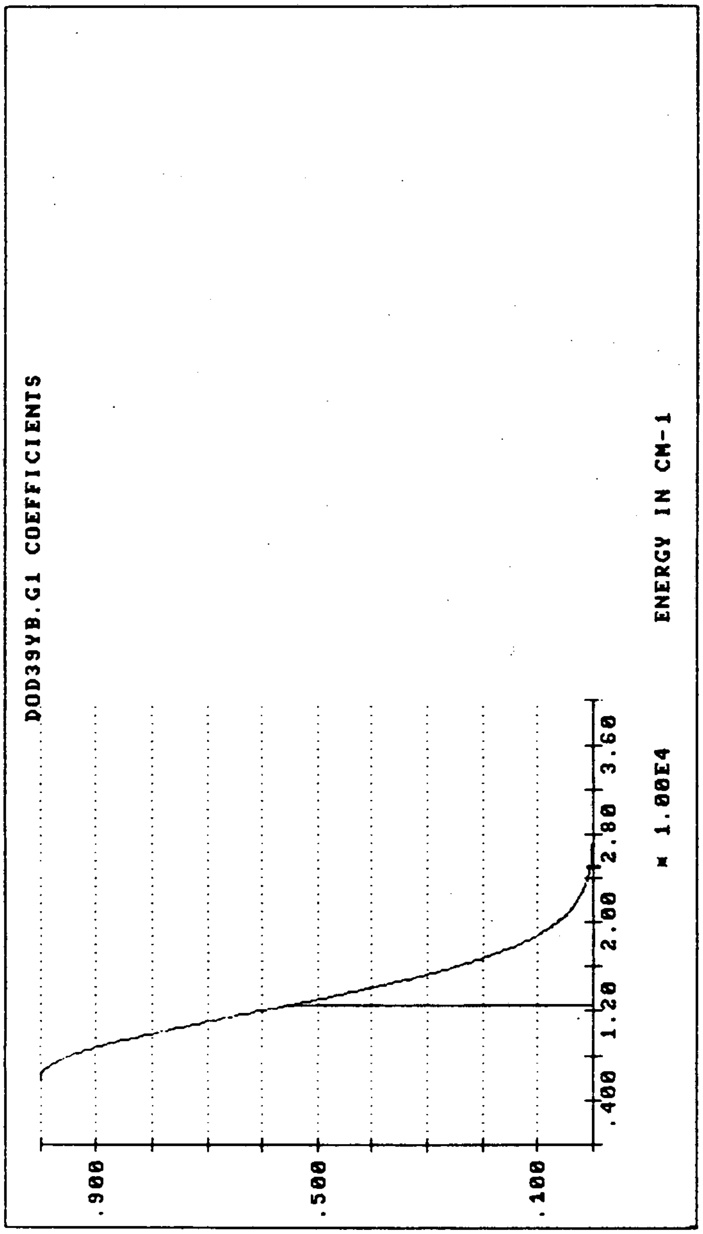
DOD39YB.G1 COEFFICIENTS
.900
.500
.100
.400
1.20
2.00
2.80
3.60
x 1.00E4
ENERGY IN CM-1

Figure 2.24(b)

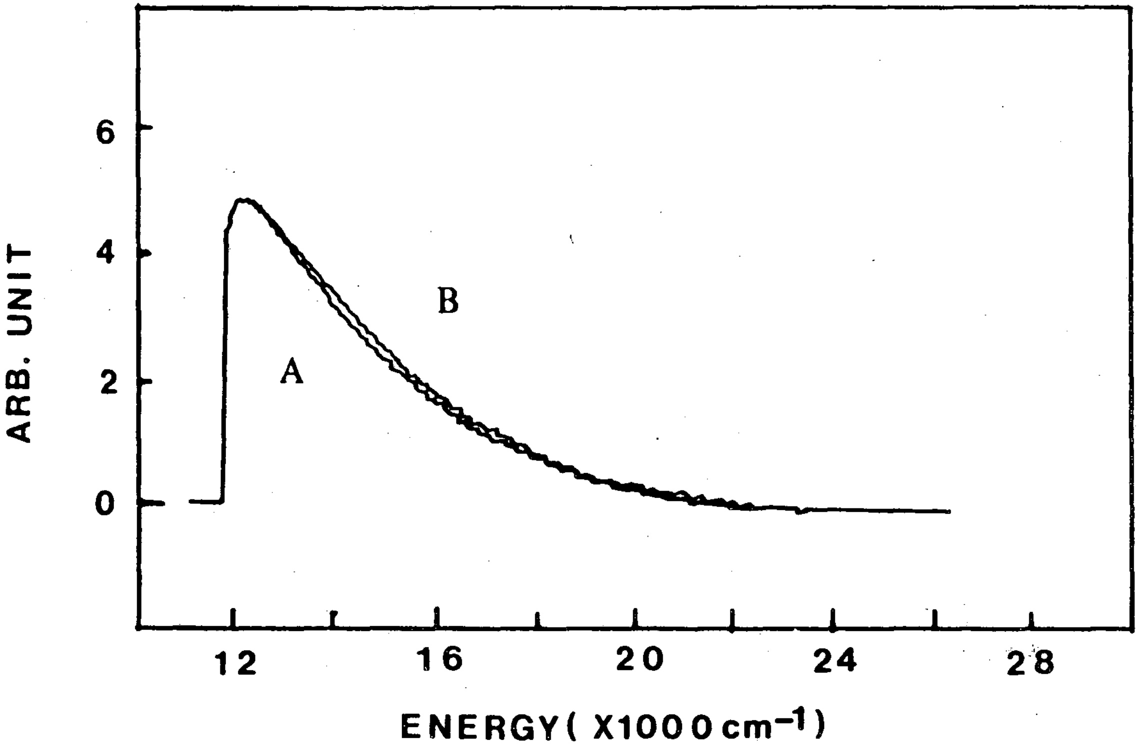

Figure 2.25

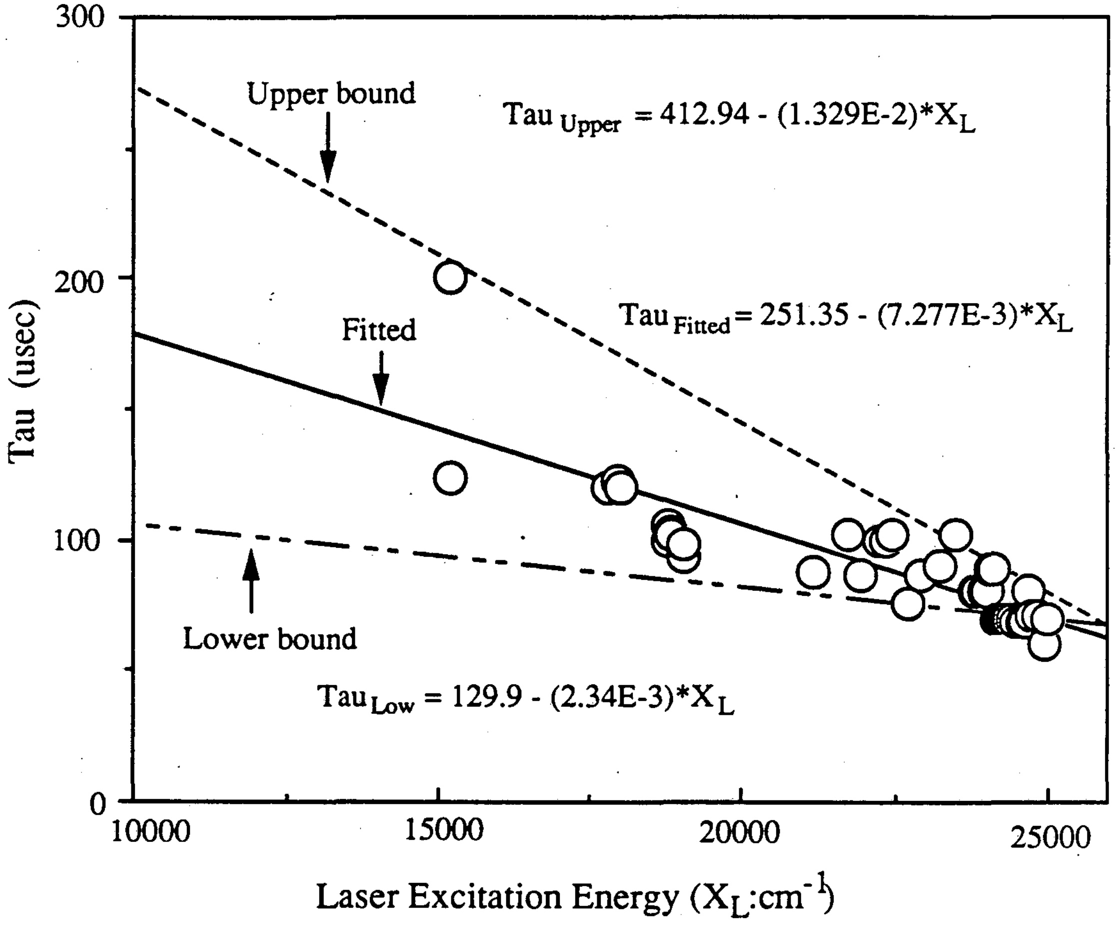
300
200
100
0
10000
15000
20000
25000
Tau (usec)
Laser Excitation Energy (X_L:cm^-1)
Upper bound
Tau Upper = 412.94 - (1.329E-2)*X_L
Fitted
Tau Fitted = 251.35 - (7.277E-3)*X_L
Lower bound
Tau Low = 129.9 - (2.34E-3)*X_L

Figure 2.26(a)

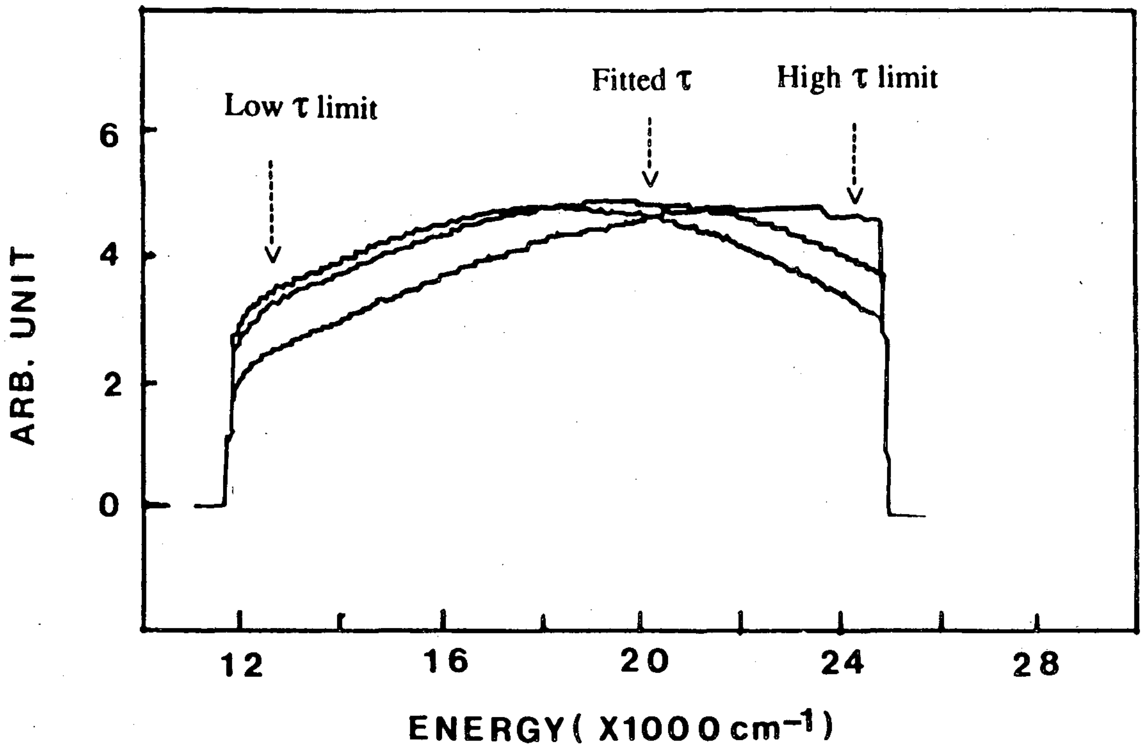
Low τ limit
Fitted τ
High τ limit
ARB. UNIT
0
2
4
6
12
16
20
24
28
ENERGY(X1000 cm^{-1})

Figure 2.26(b)

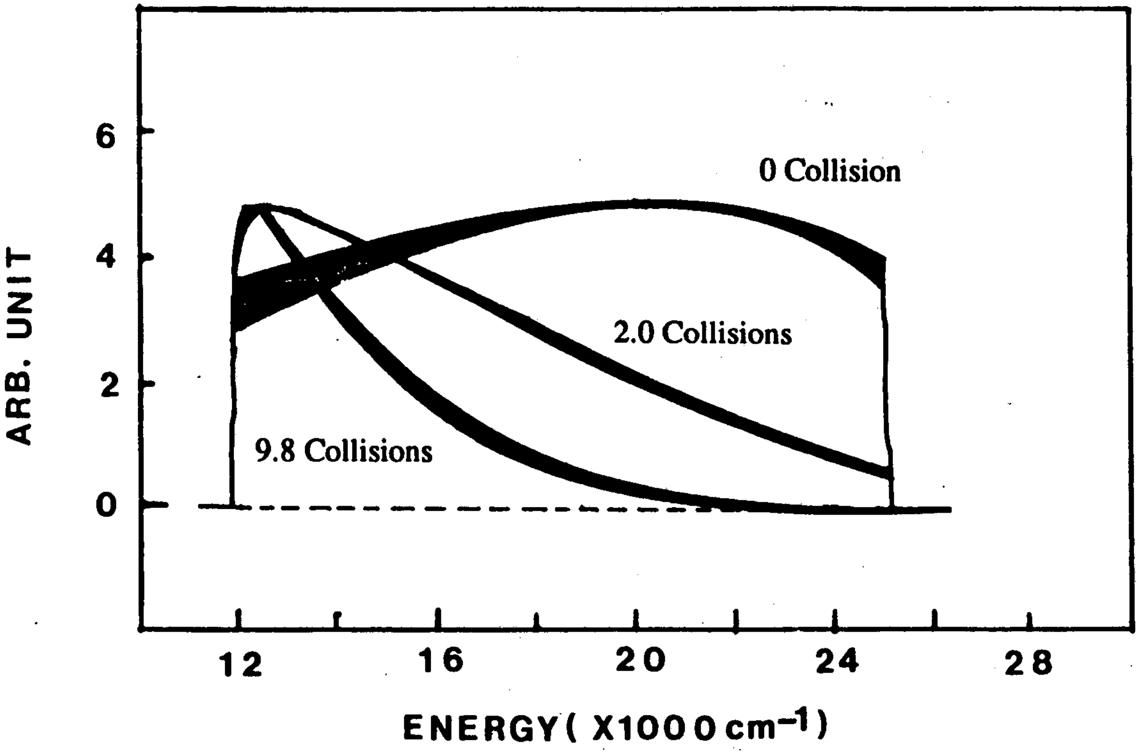
0 Collision
2.0 Collisions
9.8 Collisions
ARB. UNIT
0
2
4
6
12
16
20
24
28
ENERGY(X1000 cm⁻¹)

Figure 2.27

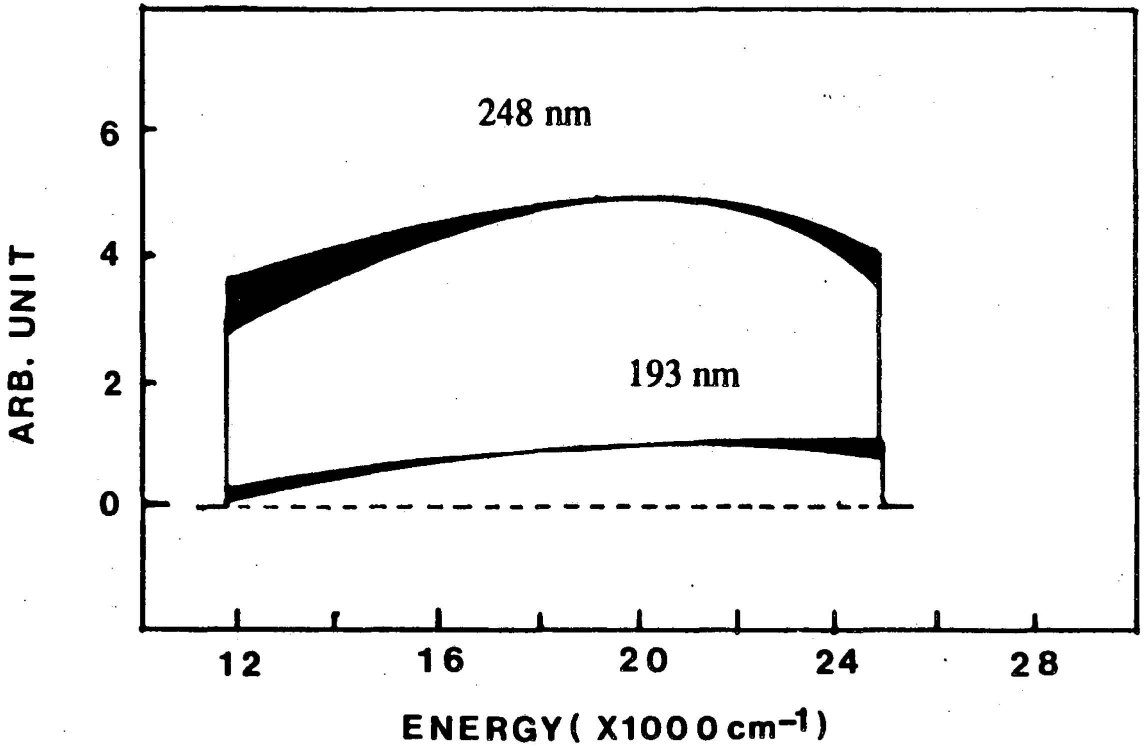

Figure 2.28

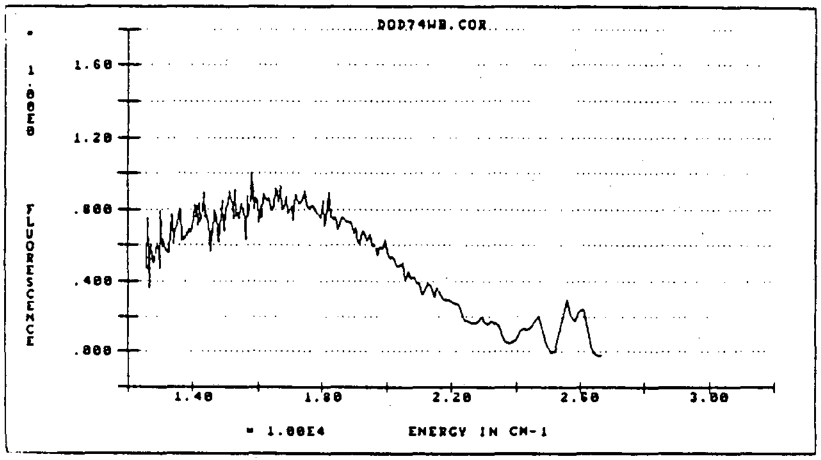

Figure 2.29(a)

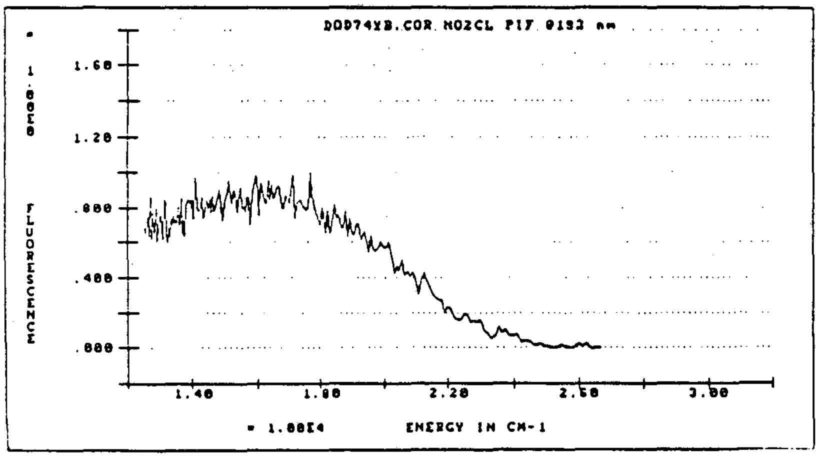

Figure 2.29(b)

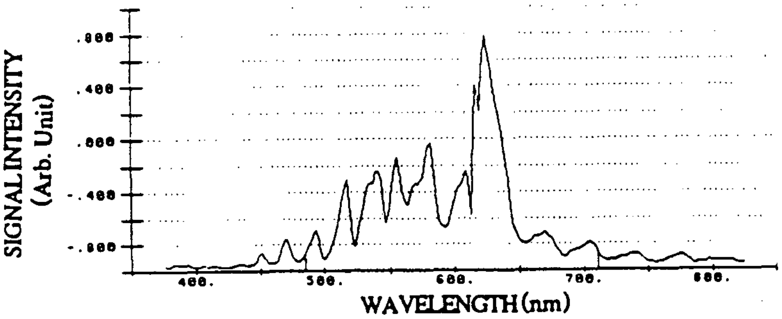

Figure 2.29(c)

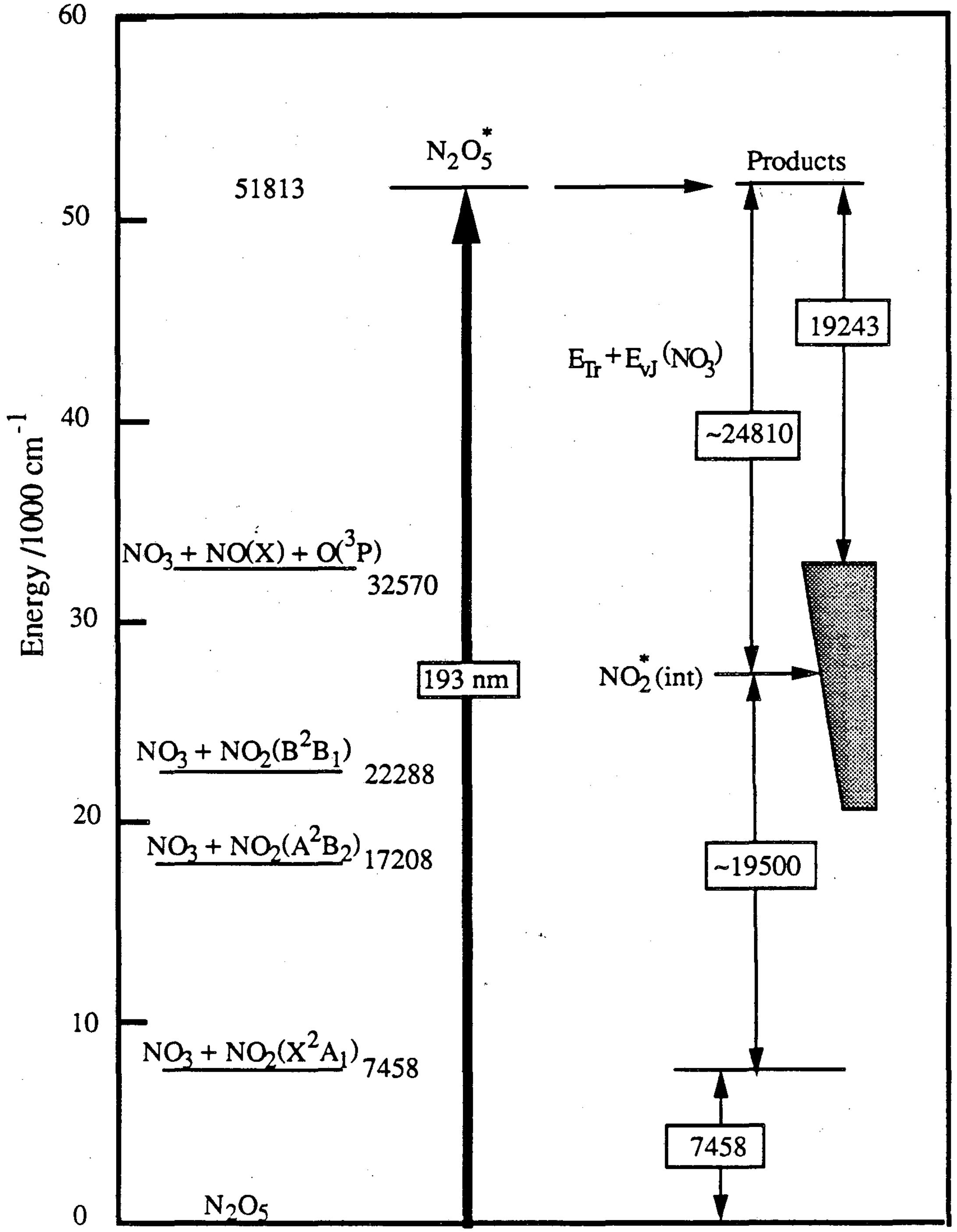
60
50
40
30
20
10
0
Energy /1000 cm-1
N2O5*
51813
Products
19243
ETr + EvJ (NO3)
~24810
NO3 + NO(X) + O(3P)
32570
193 nm
NO2*(int)
NO3 + NO2(B2B1)
22288
NO3 + NO2(A2B2) 17208
~19500
NO3 + NO2(X2A1) 7458
7458
N2O5

Figure 2.30

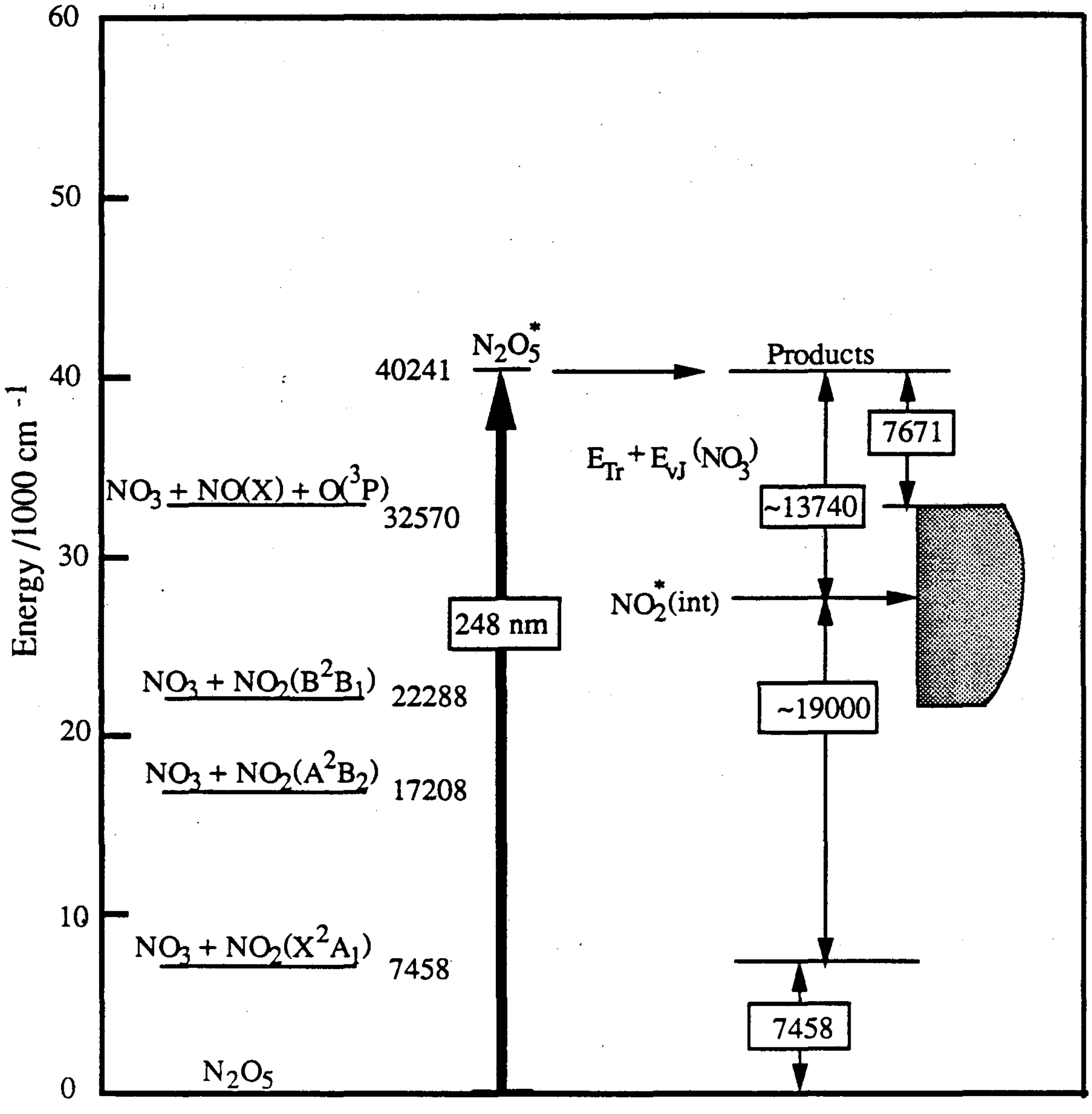
60
50
40
30
20
10
0
Energy /1000 cm -1
40241
$N_2O_5^*$
Products
$NO_3 + NO(X) + O(^3P)$
32570
$NO_3 + NO_2(B^2B_1)$
22288
$NO_3 + NO_2(A^2B_2)$
17208
$NO_3 + NO_2(X^2A_1)$
7458
N_2O_5
248 nm
$E_{Tr} + E_{vJ}(NO_3)$
7671
~13740
NO_2^*(int)
~19000
7458

Figure 2.31

CHAPTER 3.Study of Nitryl Chloride (NO_2CL) photodissociation at 266, 248 and 193 nm via NO_2^* PIF method and Molecular Beam Photofragment Translational Energy Release Spectroscopy at 248 nm.

ABSTRACT

The Photolysis Induced Fluorescence (PIF) of nitryl chloride (NO_2Cl) was studied at 266, 248 and 193 nm. This method gives an estimate of the distribution of internal energy in the product NO_2 fragments which fluoresce, $P(E_{int})$; and this investigation demonstrates how the internal energy distribution of reaction products changes with the energy of photolysis laser. This study also demonstrates the change in the nascent $P(E_{int})$ profile as the NO_2^* fragment undergoes a controlled number of collisions.

Time-of-Flight / Mass Spectrometry (TOF/MS) of the photochemical reaction was performed in the Y.T. Lee group's molecular beam machine. This method gives the distribution of translational energies of the product molecules, and it is complimentary to the PIF method.

Combining the experimental results from both studies, the following photolytic channels were identified.

		PIF	TOF/MS
NO_2Cl + 248 -->	$NO_2(X) + Cl$		observed
	$NO_2^*(A,B) + Cl$	observed	observed
	$NO + O + Cl$	inferred	inferred
	$NOCl + O$		observed

From PIF study, average NO_2^* internal energy from 266, 248 and 193 nm is estimated to be 17000 cm^{-1}, 21000 cm^{-1} and 21000 cm^{-1}. The emission yield of NO_2^* at these photolysis energies is estimated to be 0.9±0.5, 0.7±0.2 and 0.03±0.03.

Comparison of $P(E_{Trans})$ distribution from TOF/MS analysis and $P(E_{int})$ from PIF analysis at 248 nm result in fair matching of the distribution profiles within the uncertainties of each method. With refinements in the fluorescence lifetime of NO_2 for PIF analysis, and addition of low kinetic energyg release channel in the TOF/MS analysis, even better matching between the two profiles is expected. The estimated average internal energy of NO_2^* from PIF is well matched by estimated average translational energy of NO_2^* fragment from TOF/MS analysis.

Based on the experimental evidence observed from two complimentary experiments, it is thought that UV photodissociation of NO_2Cl involves highly localized initial excitation in NO_2 group, followed by predissociation of Cl-N bond where much of the excess energy remain in the NO_2 fragment. This is manifested by NO_2^* emission, and the inferred dissociation into NO + O when sufficient excess energy exists.

INTRODUCTION

The Photolysis Induced Fluorescence (PIF) method is introduced in Chapter 2. The technique yields the internal energy distribution of NO_2^*, $P(E_{int})$, and it was used to interpret the photodissociation of N_2O_5.

Application of the PIF method to a small NO_2-X molecule is desirable. A molecule with little or no internal degrees of freedom in the X group partitions its excess energy between translational energy and the NO_2 internal energy in the $NO_2\text{-X} + h\nu \rightarrow NO_2 + X$ product channel. The PIF analysis on NO_2^* emission provides $P(E_{int})$ of NO_2^*, which is the distribution of NO_2^* internal excitation. A complimentary experiment which probes translational energy release from NO_2-X photolysis provides the translational energy distribution ($P(E_{Trans})$) of each detectable photofragment including NO_2^*. The $P(E_{Trans})$ of NO_2^* is compared to the $P(E_{int})$ from PIF analysis.

The Nitryl Chloride (NO_2Cl) has a strong Ultra Violet (UV) absorption cross sections (10^{-17} cm^2 at 200 nm, and 10^{-18} cm^2 at 250nm [1,2]; see Figure 3.1), and it is photolyzed by this radiation to give NO_2 + Cl channel. The Cl atom has the low lying spin-orbit excited electronic state ($^2P_{1/2}$), which is 881 cm^{-1} above the ground state ($^2P_{3/2}$) [3].

No assignment has been made on UV absorption features of NO_2Cl to date. The tentative assignment is given with HNO_3 UV absorption assignments [4] and the theoretical calculations on other X-NO_2 molecules [4,5] as a guide. The strong absorption feature near 190 nm is assigned to $\pi \rightarrow \pi^*$, a weaker feature near 220 nm to $n \rightarrow \pi^*$, and another weak absorption feature near 310 nm to $\sigma \rightarrow \pi^*$ transition.

The geometry of ground state NO_2Cl was determined by Endo[6] with microwave spectroscopy. The N-Cl bond distance of 1.843Å, N-O bond distance of 1.198Å and the O-N-O bond angle of 130.9^o were deduced. This is shown in Figure 3.2, and listed in Table 3.2.

As for the previous studies on UV photolysis of NO_2Cl which address the question of possible photolytic channels, the report by H.Nelson [2] is the only one to date. From the laser flash photolysis of NO_2Cl at 351 nm, Cl atom quantum yield of 0.95 and O atom quantum yield of less than 0.05 were measured by atomic resonance fluorescence detection. Within experimental uncertainty, the only channel involved at photolysis wavelength of 351 nm was believed to be

$$NO_2Cl + 351\text{ nm} \rightarrow NO_2 + Cl \qquad \text{(Equation 3.1).}$$

This result, however, does not necessarily hold at other wavelengths of photolysis. Also, it is not clear whether electronically excited products are produced (i.e. NO_2^*).

Listed below are some of the the possible (in terms of heat of formation) photolytic channels involved in the UV photolysis. For simplicity, only the ground state $Cl(^2P_{3/2})$ is listed but spin-orbit excited state of $Cl(^2P_{1/2})$ channel can be estimated by adding 881 cm^{-1}.

	Thresholds[7]		
	nm	cm^{-1}	
$NO_2Cl + h\nu \rightarrow NO_2(X^2A_1) + Cl(^2P_{3/2})$	835	11970	(Eq.3.2)
$NO(X^2\Pi) + ClO(X)$	665	15030	(Eq.3.3)
$NO_2(A^2B_2) + Cl(^2P_{3/2})$	462	21630	(Eq.3.4)
$NOCl(X) + O(^3P)$	415	24110	(Eq.3.5)
$NO_2(B^2B_1) + Cl(^2P_{3/2})$	376	26620	(Eq.3.6)
$NO(X^2\Pi) + O(^3P) + Cl(^2P_{3/2})$	270	36980	(Eq.3.7)

In this chapter, the study NO_2Cl photodissociation with complimentary techniques is presented. The NO_2Cl dissociation was initiated by 266, 248 and 193 nm photolysis laser pulses, probed with the time-resolved nascent NO_2^* emission, and analyzed by the NO_2^* PIF method. The complimentary method of molecular beam photofragment translational energy spectroscopy [8] was performed in collaboration with Y.T. Lee group. The photolysis of NO_2Cl at 248 nm is analyzed and presented here. The resulting $P(E_{Trans})$ from this complimentary experiment is compared against the $P(E_{int})$ of NO_2^*, and the agreement with the PIF method is discussed. The results from both experiments are used to deduce the photolytic channels involved and the photodissociation dynamics of NO_2Cl at the wavelengths of photolysis employed.

EXPERIMENTAL

The experimental apparatus for NO_2^* PIF study was described in Chapter 2 (See Fig.2.5), and no further description is given here. For 266 nm photodissociation of NO_2Cl, 4th harmonic output of Nd:YAG laser (Quanta-Ray DCL-II) was used. Typical energy after collimation (2.5 mm diameter) in the cell was about 0.5 mJ/pulse. For 248 and 193 nm photolyses, an excimer laser (Lumonics TE 861M-2) operating with KrF and ArF gas mixtures was used. The divergence of the excimer laser pulses was corrected with a set of cylindrical and spherical convex lenses (CaF_2). In 248 nm photodissociation study, pulse energies between 0.3 ~ 10 mJ/pulse were used, while ~ 0.3 mJ/pulse was used in 193 nm experiment.

The NO_2^* emission spectra were taken at 10 Hz repetition rate, and each observation point consisted of the average of 100 shots. For the nascent NO_2^* emission observation from 248 nm photolysis of NO_2Cl, 5 mtorr of sample pressure and 30 ns each of gate delay and the gate width were used in a typical run, which corresponds to ~ 0.2 % of the molecules undergoing one hard sphere (4 Å diameter for NO_2, and 6 Å diameter for

NO_2Cl; See Table 3.3) collision on the average. At 266 nm photolysis, typically 10 mtorr of sample pressure and 30 ns gate delay coupled with 60 ns gate width were used for taking nascent emission spectrum. This increase in the sample presssure and the gate width, which was to compensate for the lower NO_2Cl absorption cross section at the photolysis wavelength, resulted in 1.4 % of the sample undergoing a collision at the end of the detection. At 193 nm photolysis, 20 mtorr of NO_2Cl and 30 ns each of the gate delay and the gate width were used for nascent NO_2^* emission spectra. This corresponded to 1.1% of the sample undergoing a collision on the average. For the collisionally relaxed NO_2^* emission spectra, appropriate combination of sample pressures and the boxcar gate delays were chosen. The experimental conditions at each photolysis wavelength are listed in Table 3.3.

In addition to the NO_2^* fluorescence, NO^* fluorescence emission was detected from 193 nm photolysis of NO_2Cl when a short delay of the detection gate was employed. The NO^* emission spectrum was dispersed through the monochromator and detected in second order. For the NO_2^* PIF observation at 193 nm, however, the NO^* emission was blocked with a UV cut-off filter (CS O-52).

The Time-of-Flight (TOF) mass spectrum of each photofragment was measured in a molecular beam apparatus in collaboration with Y.T. Lee group. The detailed specifications of the apparatus has been published elsewhere [9]. The block diagram of the experimental arrangement is shown in Fig.3.3. The molecular beam was formed by bubbling helium through nitryl chloride stored in -63 °C cold trap and expanding the mixture through 0.005 inch stainless steel nozzle at a total stagnation pressure of 325 torr (10 % NO_2Cl, 90 % He). The nozzle was heated to 105 °C to eliminate NO_2Cl cluster formation in the beam. The velocity of NO_2Cl seeded beam was measured by first chopping the molecular beam with a mechanical chopper, and then measuring the flight time of NO_2Cl via Time-of-Flight measurement of ion signals from parent molecule. The beam had a peak velocity of 1100 m/s with the full width at half maximum (FWHM) of the distribution being 18%. The beam was collimated by two skimmers, where two 6-inch diffusion pumps differentially pumped each stage before the main chamber. The molecular beam was then crossed at right angle by the photolysis laser beam. The 248 nm photolysis source was an excimer laser (Lambda Physik EMG 201 MSC) operating with KrF mixture. Typically, 100 mj/pulse at 150 hz was obtained and operated throughout the experiment. The laser beam was focused with quartz optics to a 1 mm by 1 mm spot at the interaction region. The dissociation products were detected in the plane of the laser and molecular beam by a rotatable ultra high vacuum mass spectrometer consisting of an electron bombardment ionizer, quadrupole mass filter, and a particle counter. The flight path from the interaction region and the ionizer was 20.8 cm. The TOF distributions were measured in the usual way [8,10].

The NO_2Cl sample was prepared with the method of Volpe et al. [11]. Anhydrous hydrogen chloride (Matheson Gas Company, 99%) was further dried by passing through a cold trap maintained at 196 K. Then, the HCl was bubbled through a fritted glass tube into a solution containing 25 ml 90% nitric acid, 60 ml 95% sulfuric acid, and 70 ml 30% fuming sulfuric acid. The product was collected with a trap, held in 196 K slush bath, which had a calcium chloride drying column attached to the outlet to keep the moisture in the air from entering the system. The reaction was stopped well before the half way point in order to minimize the chance of collecting NOCl impurity [11]. The collected product was typically about 25 ml in volume, about 70% NO_2Cl and 30% Cl_2 in composition. The product was distilled from 175 K to 77 K, to remove the volatile Cl_2 impurity. The most volatile fraction, which was believed to contain mostly Cl_2, and the least volatile fraction, possibly containing some NO_2 impurity, were discarded. The purity of the saved middle fraction was checked with a UV spectrophotometer (Cary 14). One torr of sample was introduced into a 10 cm quartz gas cell, and the UV absorption profile was taken between 200 and 360 nm [1,2]. Comparison to the absorption cross section reported by Illies and Takacs [1] (shown in Fig. 3.1 and the Table 3.1) showed the sample to be about 98% pure NO_2Cl. The sample was kept in liquid Nitrogen trap until ready to use.

RESULTS

(A) NO_2^* Fluorescence from NO_2Cl Photolysis.

The results of NO_2Cl photolysis are presented here in terms of the PIF (Photolysis Induced Fluorescence) method as described in Chapter 2. The nascent NO_2^* emission from 266, 248 and 193 nm photolysis of NO_2Cl was analyzed with the PIF method using two LIF excitation energy (X_L) coefficient distributions, Expression A (Ch.2, Eq. 2.13) and Expression B (Ch.2, Eq. 2.14).

For each experimental condition, the experimental results and their analysis are given by 6 curves on two Figures (a) and (b). Figure (a) has two panels with five curves; figure (b) has one panel with one curve. The 6 curves and their locations are as follows:

(1). The left hand panel of (a) in each case shows the observed PIF emission spectrum. Although the spectrum shows some structure, it is much less structured than individual NO_2 LIF emission spectrum (see Ch. 2, Fig. 2.8(a-p)).

(2). The right hand panel of (a) shows the running sum of the observed PIF spectrum (Ch. 2, Eq.2.11). This running sum was fit by non-linear least squares to the corresponding integral with variable end points (Ch.2, Eq. 2.12) for each of two LIF excitation energy (X_L) coefficient distributions (Expression A (Ch.2, Eq.2.13) and Expression B(Ch.2, Eq.2.14)).

(3). The least squares line based on the fitted parameters is also plotted on the right-hand panel of (a). Where only one line is visible on the right-hand panel, the fitted line is in agreeement with the observed running sum line within the width of the line that is shown. Where two lines are discernable, the fit is less good.

(4). The parameters taken from this fitting procedures were used to calculate the emission spectrum (Ch. 2, Eq. 2.12), and this can be seen as the solid line through the observed PIF spectrum in the left panel of (a).

(5). The X_L (LIF excitation energy) coefficient distribution that fits the PIF data is given in figure (b). The vertical lines on the figure mark the region of observations (400 - 800 nm; 25000 - 12500 cm^{-1}). Expression A is a non-symmetrical function (Eq. 2.13), which is capable of being symmetric or skewed to either high energy or low energies relative to its maximum energy. The figures report its adjusted parameters as μ and σ, but these should be read as ν and ρ as defined in Chapter 2, Eq. 2.13. Expression B is a Gaussian function (Eq. 2.14) which is symmetric with mean (and maximum) value occuring at energy μ; the standard deviation (width of distribution) is given by the parameter σ.

(6). The third curve in the left-hand panel of (a) is the profile of internal energy of NO_2^*, which is either nascent or relaxed (collisionally and radiatively) fragments from photolysis. This $P(E_{int})$ is based on the lifetime function (Eq. 2.18), Boltzmann distribution of room temperature NO_2 (Eq. 2.8) and X_L coefficient profile from either expression A or expression B, as shown in Eq. 2.17 of Chapter 2.

Nascent PIF analysis of 266 nm photolysis:

The nascent NO_2^* emission from 266 nm photolysis of NO_2Cl is analyzed with PIF method, using X_L coefficient distribution expression A in Fig. 3.4(a-b). The overlap between observed and the fitted cumulative sum profile is excellent. The agreement between experimental and calculated emission spectrum is also good. The parameters MU and SIGMA in the figure corresponds to ν and σ in the text as indicated above, and are varied for optimum fit in the cumulative sum profile. The M value, which indicates the maximum allowed energy in the NO_2 fragment, fixes the maximum of X_L coefficient distribution in (b). The coefficient distribution shows a skewed distribution, with the high energy side showing more rapid decay. The $P(E_{int})$ profile in (a) shows distribution of NO_2^* internal energy skewed toward low energy side.

The same NO_2^* emission spectrum is analyzed with X_L coefficient distribution expression B, and shown in Fig. 3.5(a-b). Some disagreements between experimental and fitted cumulative sum profiles near 18000 cm^{-1} region is seen, but the overlap in the emission spectrum between experimental and calculated profile is good. The overall coefficient distribution in (b) is symmetric, but the portion used for fitting indicates a skewed profile toward low energy. The resulting $P(E_{int})$ is symmetric within the upper and lower limits of observation.

The $P(E_{int})$ profiles from expression A (Fig. 3.4(a)) and B (Fig. 3.5(a)) are overlapped in Fig. 3.6 for comparison, with A and B indicating the coefficient expressions used for analysis. The A curve is slightly more skewed toward lower energy than B, with some observed differences in the curvature of $P(E_{int})$ profiles.

Nascent PIF analysis of 248 nm photolysis:

The nascent NO_2^* from 248 nm photolysis of NO_2Cl is analyzed with expression A and shown in Fig. 3.7(a-b), while analysis on same data with expression B is shown in Fig. 3.8(a-b). The agreement between experimental and fitted cumulative sum profiles is excellent for both expression A (Fig. 3.7(a)) and B (Fig. 3.8(a)). Agreement is also observed between experimental and calculated emission spectrum from analysis with expression A (Fig. 3.7(a)) and expression B(Fig. 3.8(a)). Coefficient distributions generated from analysis with expression A (Fig. 3.7(b)) and expression B (Fig. 3.8(b)) both show skewed distribution curves toward the high energy limit of observation, which is the predissociation limit of NO_2. The resulting $P(E_{int})$ profile of NO_2^* from expression A (Fig. 3.7(a)) and from expression B (Fig. 3.8(a)) both show highly skewed distribution toward high energy limit of observation, and these two estimates of $P(E_{int})$ are in good agreement (Fig.3.9).

Nascent PIF analysis of 193 nm photolysis:

The nascent NO_2^* from 193 nm photolysis of NO_2Cl is analyzed by PIF method with coefficient expression A (Fig. 3.10(a-b)) and B (Fig. 3.11(a-b)). There are some emission peaks near 26000 cm^{-1}, which are identified as NO^* emission peaks that pass through the UV cut-off filter (CS 0 - 52). These extra features contribute to the experimental cumulative sum profile (in solid line), and results in the appearance of poor fittings by the calculated cumulative sum curves (in broken line) in the analysis with expression A (Fig. 3.10(a)) and B (Fig. 3.11(a)). However, calculated emission curves are well overlapped with experimental emission spectra by tracing the baseline of NO^* emission features in both cases of analysis with expression A (Fig. 3.10(a)) and B (Fig. 3.11(a)).

The coefficient distribution from expression A appears as a tail end of low energy side being used for analysis in Fig. 3.10(b). The coefficient distribution from expression B, however, indicates nearly half of the overall distribution curve being used for analysis in Fig. 3.11(b). Over the range of observations, 12500 - 25102 cm^{-1}, these two coefficient distributions are similar, but the expressions above the dissociation limit of NO_2 and above the range of observation are strongly different. The resulting $P(E_{int})$ profiles from expression A (Fig. 3.10(a)) and from B (Fig. 3.11(a)) are overlapped in Fig. 3.12 for comparison. Both distributions are highly skewed toward the predissociation limit, with the distribution from expression B showing more rapid decrease toward low energy than the distribution from A.

Delayed PIF (1.4 collision) analysis of 248 nm photolysis:

The analysis of NO_2^* emission at 248 nm photolysis of NO_2Cl, observed under experimental condition which correspond to NO_2^* undergoing 1.4 hard sphere collision on the average, is analyzed by PIF method with coefficient expression A (Fig. 3.13(a-b)) and B (Fig. 3.14(a-b)). In both analyses with expression A and B, good fits are observed in cumulative sum profiles and emission profiles between experimental and fitted profiles. The coefficient distribution generated with expression A (Fig. 3.13(b)) is similar in shape with the distribution from expression B (Fig. 3.14(b)). The resulting $P(E_{int})$ distributions from expression A (Fig. 3.13(a)) and B (Fig. 3.14(a)), which are overlapped in Fig. 3.15, show similar distribution, with the distribution from A slightly departing from B in the lower energy region. The distributions (A and B) in Fig. 3.15 also show clear shift toward lower energy when compared to nascent NO_2^* $P(E_{int})$ in Fig. 3.9, indicating a loss of energy.

Delayed PIF (14.2 collisions) analysis of 248 nm photolysis:

The analysis of NO_2^* emission at 248 nm photolysis of NO_2Cl, observed under experimental condition which correspond to NO_2^* undergoing 14.2 hard sphere collisions before observation, is shown with expression A (Fig. 3.16(a-b)) and B (Fig. 3.17(a-b)). The shift in experimental emission spectrum toward lower energy limit of observation is evident compared to 1.4 collision condition (Fig. 3.13(a), 3.14(a)) or nascent condition (Fig. 3.7(a), 3.8(a)).

The agreement between experimental and fitted cumulative sum profiles are good in both cases of analysis with expression A (Fig. 3.16(a)) and expression B (Fig. 3.17(a)). The coefficient distributions from analysis with expression A (Fig. 3.16(b)) and with expression B (Fig.3.17(b)), as well as $P(E_{int})$ profiles from analysis with expression A (Fig.3.16(a)) and from expression B (Fig. 3.17(a)) all show highly skewed profiles toward low energy. The resulting P(Eint) from analysis with expression A and B are overlapped in Fig. 3.18, which show very close match between the two.

NO_2* emission yields

The emission quantum yields were estimated for PIF at each wavelength of photolysis by comparing the normalized emission from NO_2 LIF. The NO_2 LIF excited at 410.29, 415.76 and 421.0 nm were normalized and set as a unit emission yield, which is 1.0 ± 0.63 (2σ). The NO_2^* yields from 266, 248 and 193 nm photolysis were estimated to be 0.9±0.5(2σ), 0.7±0.2(2σ) and 0.03±0.03(2σ) from the comparison, where 2σ corresponds to 2 standard deviations (See Table 3.6).

NO^* Emission

The NO^* emission, observed from 193 nm photolysis of NO_2Cl, is shown in Figure.3.19. The emission was observed in second order through the monochromator, with 10 ns gate delay and 30 ns gate width for observation. No quantitative assignments on the observed emission features were made due to uncertainty in line positions under the 2 nm per point resolution. However, the observed NO^* fluorescence can be attributed to A -> X (γ - band) and B -> X (β - band) transitions [12,13] based on the range of emission wavelengths and the intensity profiles. No quantitative power dependence of NO^* emission was attempted, but increased laser fluence by the focusing of 193 nm laser increased the signal many fold compared to the unfocused condition. There was no detectable NO^* emission at the 248 nm photodissociation of NO_2Cl, even under the high laser fluence condition.

(B) Time-of-Flight / Mass Spectrometry

Upon 248 nm photolysis of NO_2Cl in the molecular beam, ion signals with mass-to-charge ratio (m/e) of 46, 35, 30 and 16 were detected at various detector angles. These ion signals were attributed to NO_2^+, Cl^+, NO^+ and O^+ ions. The ion signals with m/e = 65 ($NOCl^+$) and 51 (ClO^+) were sought but not detected.

m/e = 46

The Time-of-Flight spectra were recorded for ion signals with m/e = 46, which correspond to NO_2^+, at the following angles of detection (with respect to the molecular beam path). At 10° detection, ion signals with low signal-to-noise ratio of about 2 to 1 are observed to arrive at the detector between ~ 80 and 140 micro seconds after photolysis (Fig.3.20(a)). Although the signal level is low, two partially overlapped peaks with average arrival times of ~ 90 and ~120 micro seconds can be distinguished. At 20° detection, two partially overlapped ion signals are observed to arrive at the detector with similar time of arrival as in 10° detection (Fig.3.20(b)). At 30° detection, two partially overlapped peaks in the Time-of-Flight spectrum is again observed (Fig.3.20(c)). The increase in the intensity ratio of fast to slow peak is observed in the TOF spectra as the angle of detection increases. In each TOF spectrum observed, two partially overlapping ion signals with different time of arrival at the detector have been observed.

m/e = 35

The Time-of-Flight spectra were recorded for ion signals with m/e = 35, which correspond to Cl^+, at the following angles of detection. At 10° detection angle, most of ions are observed to arrive at the detector between ~ 60 to 130 micro seconds after the photolysis laser as shown with open circle in Fig. 3.21(a). There is also a long tail of slowly decaying ion signal arriving at the detector between 130 and ~ 300 microsecond, which has not been observed in m/e = 46 TOF spectra. The main peak shows a hint of shoulder in the rising part of the peak, and again in the decaying part of the peak near the maximum. The overall signal-to-noise level in this spectrum is much better than m/e = 46 TOF spectra.

In Fig. 3.21(b), m/e = 35 ion TOF spectrum obtained with the detector angle of 20° is shown in open circles. The shoulders in the main peak, along with slowly decaying tail, are observed also in this angle of detection. At 30° detection of m/e = 35 ion signal, the shoulder near the maximum of main peak in earlier observation (Fig. 3.21 9a-b) is observed now near the middle of decreasing part of the main peak as shown in Fig. 3.21(c). Figure 3.21(d) shows the 40° detection of m/e = 35 ion signal. Due to the decrease in the signal level compared to smaller angle of detection, shoulders in the main peak is not clearly observed. However, the slowly decaying tail in the TOF spectrum is still observed.

In the m/e = 35 ion TOF spectra, large main peak with hints of features is observed to arrive between ~ 60 to 140 micro seconds after the photolysis followed by a long, slowly decaying tail in the spectra at all angles of observation.

m/e = 30

The Time-of-Flight spectra were recorded for ion signals with m/e = 30, which correspond to NO^+, at the following angles of detection. As shown in Fig. 3.22(a), TOF spectrum at 20° shows a main peak arriving at the detector between 80 and ~ 140 micro seconds after photolysis and a slower tail extending to ~ 300 microseconds. Detailed features in the main peak cannot be ascertained in this spectrum due to reduced signal to noise ratio compared to m/e = 35 spectra. At 30° detection as shown in Fig. 3.22(b), main peak with slow tail can be identified. At 40° detection as shown in Fig. 3.22(c), even larger scatter in the spectrum than the 30° detection is observed. The main peak and the slow tail above the noisy baseline can be discerned with difficulty.

In m/e = 30 ion TOF spectra, a fast arriving main peak with a slow tail is observed. Reduced signal level in overall spectra makes it hard to discern any finer features that may be present in the main peak.

m/e = 16

The Time-of-Flight spectra were recorded for ion signals with m/e = 16, which correspond to O^+, at the following angles of detection. In Fig. 3.23(a), TOF spectrum of m/e = 16 ion signal observed at 10° detector angle is shown. There is a fast arriving (40 ~ 60 micro seconds) shoulder near the baseline, followed by a main peak between 70 ~ 140 micro seconds and a decaying shoulder between 140 ~ 260 micro seconds. The TOF spectrum with similar features is observed at 20° detection angle, as shown in Fig. 3.23(b).

TOF Data Analysis

The data analysis consisted of finding the center-of-mass translational energy distribution $P(E_{Trans})$ from the observed laboratory frame Time-of-Flight spectra. The forward convolution method [10] was used for the analysis, which consisted of calculating Time-of-Flight spectra from a guessed $P(E_{Trans})$ distribution. The calculation took into account several instrument averaging factors such as beam velocity and angular dispersion, ionizer length, detector angular resolution, and multichannel scalar channel width. Then, the $P(E_{Trans})$ was modified until satisfactory fit was achieved between calculated TOF fitted the experimental data. The procedure was repeated for each detected ion signal at each angle of detection. The resulting $P(E_{Trans})$ profiles are shown and discussed in detail in the Discussion section below.

DISSCUSSION

(A) NO_2^* Photolysis Induced Fluorescence Analysis

In the PIF analysis of NO2* emission spectrum, two coefficient distribution expressions called A and B were used in representing LIF excitation energy coefficient distribution. The expression A, introduced in Chapter 2 as

$$\text{Expression A} = (M - X)^{\nu} \exp^{(-(M - X)/\rho)} \qquad \text{(Eq. 2.13)}$$

ν = adjustable parameter,
ρ = adjustable parameter,
M = Maximum allowed internal energy in NO_2, and fixed at each photolysis wavelength.

has two adjustable parameters (ν and ρ) and a constant term (M) at each wavelength of photolysis. This expression generates the coefficient distribution which is within the physically accessible range due to the constant term M. The distribution from highly skewed to nearly symmetric may be generated with appropriate choice of adjustable parameters.

The expression B, on the other hand, generates the symmetric Gaussian profile. With the expression introduced in Chapter 2 as

$$\text{Expression B} = \frac{\exp^{-(\mu - X_L)^2/2\sigma^2}}{(2\pi\sigma^2)^{1/2}} \qquad \text{(Eq. 2.14)}$$

μ = adjustable parameter (mean of the coefficient distribution),
σ = adjustable parameter (width of the distribution).

Two adjustable parameters were varied with no limits until satisfactory fit was achieved between experimental and calculated cumulative sum profile was achieved. This often meant generating a coefficient distribution which extends well into physically inaccessible energy region. However, only part of the overall distribution was used in PIF analysis, and this part is the range of observation between 12500 and 25102 cm^{-1}. This was also the reason why symmetric distribution function could fit highly skewed distribution as well as expression A, which has the asymmetry built in.

The equally good fits achieved by expression A and B suggest that both expressions are capable of generating coefficient distributions used for analysis within the observation range of 12500 cm^{-1} and 25102 cm^{-1}. Therefore, no preference is given for either of the expressions.

The error in the PIF method is at least as large as disagreement observed in the $P(E_{int})$ profiles between expression A and B.

A major source of uncertainty in the $P(E_{int})$ is the fluorescence lifetimes of NO_2 as discussed in Chapter 2. The lifetimes extrapolated by linear least squares fitting below the lowest reported literature values of 15000 cm^{-1} as shown in Eq. 2.18 were used for PIF analysis presented here. An example of how different fluorescence lifetime extrapolations affect $P(E_{int})$ profiles is shown in Fig, 3.24. The middle trace is the $P(E_{int})$ shown in Fig.3.8(a), which is the linear least squares fitted lifetime values used for PIF analysis in this chapter. The upper and lower traces correspond to $P(E_{int})$ profiles resulting from two extreme extrapolations representing lower and upper limits of the uncertainty in the fluorescence lifetime (shown in Fig.2.18(a)). The $P(E_{int})$ profile changes somewhat in the curvature as the lifetime expression is varied, but the overall shape of the distributions remain close to one another. The variation of profiles shown in Fig. 3.24 is taken as the uncertainty in $P(E_{int})$ due to uncertainty in fluorescence lifetimes.

The analyzed $P(E_{int})$ profiles of NO_2^* from 248 nm photolysis are compiled as a function of number of collisions in Figure 3.25. Different collision numbers were prepared from the combination of different pressures and observation delays, which resulted in varying amount of fluorescence emission loss in each observation. Therefore, emission loss must be properly estimated and subtracted from the total observed loss in NO_2 energy before the energy lost per collision can be estimated. This step was not taken in preparing the Figure 3.25, which shows overall (collisional + radiative) loss of NO_2^* internal energy. However, Figure 3.25 does show the shift in $P(E_{int})$ profile as a function of collision, and suggests a possible utility of the PIF analysis in studying collision-induced energy transfer.

In Figure 3.26, nascent NO_2^* $P(E_{int})$ profiles as a function of photolysis wavelength are scaled to each NO_2^* emission yield and overlapped for comparison. The shaded region in each $P(E_{int})$ corresponds to the disagreement between the analysis using expressions A and B. The overall shape of the $P(E_{int})$ profile suggests the shift in NO_2^* internal energy as the photolysis energy increases. The accurate estimate of the average NO_2^* internal energy is not possible, since the instrument is not sensitive below 12500 cm^{-1} and internal energy of NO_2^* (electronic + rovibrational) above 25181 cm^{-1} results in predissociation rather than fluorescence [15]. Within the observation energy range, the average internal (electronic + rovibrational) energy of average NO_2^* is estimated to be about 21000 cm^{-1} from 193 and 248 nm photolysis, and about 17000 cm^{-1} from 266 nm photolysis.

(B) Dissociation Dynamics from PIF Study.

266 nm Photolysis

The energy level diagram for 266 nm photolysis of NO_2Cl is shown in Fig.3.27. The 266 nm photodissociation introduces 37590 cm^{-1} total energy into NO_2Cl parent molecule, of which 11866 cm^{-1} is used for dissociation of NO_2Cl into $NO_2(X)$ and Cl fragments. This leaves excess energy of 25724 cm^{-1} for NO_2 + Cl channel. The average NO_2^* energy was estimated to be ~17000 cm^{-1} from PIF study, which consist of electronic and rovibrational excitation. This leaves ~ 8720 cm^{-1} for translational energy and the internal excitation of spin-orbit electronic states of Cl atom ($^2P_{3/2-1/2}$ = 881 cm^{-1}, [xx]). For the ease of discussion, it is assumed that no internal excitation of Cl atom took place. It is also assumed that NO_2^* was formed in its first excited electronic state (A^2B_2). This is only for the convenience of discussion. This means 9753 cm^{-1} for electronic excitation in NO_2^*, leaving 9247 cm^{-1} for the rovibrational excitation of NO_2^* from the first excited state. This is summarized as

	E_{Trans}	E_{Rovib}	E_{Elect}
NO_2Cl + 266nm --> $NO_2^*(A) + Cl(^2P_{3/2})$	8720cm^{-1}	7250cm^{-1}	9750cm^{-1}
	(0.34)	(0.28)	(0.38)

The extent of Cl population in the spin-orbit excited state is not known. The initial state in which NO_2^* is formed from photolysis is not determined either.

The estimated NO_2^* emission yield of 0.9±0.5 suggest that production of NO_2^* + Cl is a major channel at this wavelength of photolysis. The P(E_{int}) profile also suggests very little dissociation of NO_2^* into NO + O with its skewed distribution toward the low internal energy, where NO + O dissociation limit is 643 cm^{-1} below the total available excess energy.

248 nm Photolysis

The energy level diagram pertinent to 248 nm photolysis of NO_2Cl is shown in Fig.3.28. With 40240 cm^{-1} total energy supplied by 248 nm excitation, 11866 cm^{-1} is taken up for dissociation into NO and Cl which leaves total available excess energy of 28374 cm^{-1}. With the estimated average NO_2^* energy of 21000 cm^{-1}, 7370 cm^{-1} is left for translational and the Cl atom excitation. With the assumptions made in 266 nm case, where ground state Cl atom and $NO_2(A)$ products are considered, following summary can be made.

	E_{Trans}	E_{Rovib}	E_{Elect}
NO_2Cl + 248nm --> $NO_2^*(A) + Cl(^2P_{3/2})$	7370 cm^{-1}	11250 cm^{-1}	9750 cm^{-1}
	(0.26)	(0.40)	(0.34)

The estimated NO_2^* emission yield of 0.7±0.2 suggest that NO_2^* + Cl formation is a major channel.

The NO + O + Cl threshold is 3293 cm^{-1} below the total available excess energy, and considerably more dissociation of NO_2^* into NO and O is suggested based on the NO_2^* $P(E_{int})$ profile from PIF analysis, which shows skewed distribution toward high energy with sharp cut-off at the dissociation limit of internal energy. The estimated energy partitioning and the $P(E_{int})$ profile will be compared with the TOF results.

193 nm Photolysis

The energy level diagram for 193 nm photolysis is shown in Fig. 3.29. With 51813 cm-1 total energy supplied by 193 nm absorption, 11866 cm-1 is used for dissociation into NO2 and Cl which leaves 39947 cm^{-1} as the net available excess energy. With the estimated average NO_2^* energy of 21000 cm^{-1}, 18947 cm^{-1} is left for translational and the Cl atom excitation. With the assumptions made in 266 and 248 nm cases, following summary can be made.

	E_{Trans}	E_{Rovib}	E_{Elect}
NO_2Cl + 193 nm --> $NO_2^*(A) + Cl(^2P_{3/2})$	18947 cm^{-1}	11247 cm^{-1}	9753 cm^{-1}
	(0.47)	(0.28)	(0.25)

However, the estimated NO_2^* emission yield of 0.03±0.03 suggests that NO_2^* + Cl formation is a minor channel. Based on the overall shapes of NO_2^* $P(E_{int})$ profiles normalized to emission yields, which was shown in Fig.3.26, it is suggested that the major channel may be the NO + O + Cl formation. This may be further supported by the observation of NO* emission from 193 nm photolysis. The initially formed NO fragment may absorb an additional UV photon to form NO*. However, the concerted two photon absorption by parent NO_2Cl to produce NO* + O + Cl cannot be ruled out as the source of NO*.

Based on the discussion to now, the following photolysis channels are supported to be available when NO_2Cl is photolyzed at 193, 2248 and 266 nm.

$$NO_2Cl + h\nu \dashrightarrow NO_2^*(A,B) + Cl \qquad \text{(Equation 3.8)}$$

$$NO(X) + O + Cl \qquad \text{(Equation 3.9)}$$

At 266 and 248 nm, Eq.3.8 is a major channel. At 193 nm, it is suggested that Eq.3.9 is a major channel. As the photolysis energy increases from 266 to 193 nm, Equation 3.9 is believed to become more important while contribution from Equation 3.8 decreases.

(C) $P(E_{Trans})$ from TOF/MS Analysis

$P(E_{Trans})$ for m/e = 46

Although the signal levels were low in the m/e = 46 TOF spectra, two partially overlapped peaks observed at each angle of detection were well reproduced by the two peaks in the the probability profile of translational energy ($P(E_{Trans})$) shown in Fig. 3.30. The open circles in Fig.3.30 correspond to fast arriving NO2 which is shown as broken lines in the fit to the TOF spectra (Fig.3.20(a-c)). The filled circles in the Fig.3.30 correspond to the slowly arriving NO_2 component which is represented as a solid line in Fig.3.20(a-c). The achieved fit between experimental and the total calculated (shown as solid lines in Fig.3.20(a-c)) TOF spectra are acceptable, considering low signal to noise ratio in the spectra.

The most probable kinetic energies of the fast and slow peaks in the $P(E_{Trans})$ profile were estimated to be 63 and 24 Kcal/mole, respectively. The maximum kinetic energy release, estimated to be 81± 1 Kcal/mole, is in agreement with the estimates of 81.4 Kcal/mole as the maximum excess energy in the $NO_2(X)$ + Cl channel (Table 3.5, Fig. 3.28).

$P(E_{Trans})$ for m/e = 35, 30 and 16

Unlike the m/e = 46 ion signal, m/e = 35 (Cl^+) cannot uniquely be attributed to Cl neutral fragments. The possible photofragments from NO_2Cl, such as ClO or NOCl, which undergo cracking in the ionizer and give rise to the Cl^+ ion signals, had to be considered as well. Also, other detected ion signals (NO+ and O+) could result from cracking of heavier fragments in the ionizer. Therefore, TOF spectra from m/e = 35, 30 and 16 were analyzed together for consistency.

The analysis of m/e = 46 (NO_2^+) suggested that two types of NO_2 (thus, two types of momentum matched Cl atoms) are produced from photolysis. Therefore, the m/e = 35 (Cl^+) TOF spectra were fitted with a $P(E_{Trans})$ distribution which had similar features as in m/e = 46 $P(E_{Trans})$ distribution. This $P(E_{Trans})$ is shown in Figure 3.31. The peak of fast distribution curve (shown in open circles in Fig.3.31) corresponds to about 60 Kcal/mole. The slower distribution curve has two partially overlapped peaks located at about 30 and 18 Kcal/mole translational energy each. The gap between two peaks (12 Kcal/mole) in the slower $P(E_{Trans})$ is similar to the energy gap of two electronic excited states (A and B) in NO_2^*, which is 14.5 Kcal/mole (5080 cm^{-1}). However, no other direct evidences are available to substantiate this speculation.

The fast $P(E_{Trans})$ curve (shown in open circles) in Fig.3.31 resulted in the indicated fit to the fast Cl^+ ion signal in TOF spectra (shown as a broken line in Figure 3.21(b,c,d) and as a broken line with a dot in Fig.3.21(a)). The filled circles in Fig.3.31 resulted in the indicated fit to the slower Cl^+ ion signal in TOF spectra (shown as broken line in Figures

3.21(a), and shown as solid lines in Fig.3.21(b,c,d)). The x's correspond to the P(E_{Trans}) of NOCl + O channel (Equation 3.5), which was fitted to the slow tail of the Cl^+ TOF spectra (broken line with three dots in Figures 3.21(a), and as broken lines in Fig.3.21(b,c,d)). The NOCl fragment, which was not detected as $NOCl^+$, was thought to undergo cracking in the ionizer to give NO^+ and Cl^+ ions. More direct evidence of this channel is shown below at m/e = 16 (O^+) TOF spectra. Good agreement is observed overall between experimental and the total calculated TOF spectra (shown as solid line in Fig.3.21(a-d)). Some mismatches are observed at 40° detection of m/e = 35, and this is discussed later.

The fast peak and the slow tail in the m/e = 30 TOF spectra (Fig.3.22(a-c)) were fairly well fitted by the same P(E_{Trans}) shown in Fig.3.31, which fitted m/e = 35 TOF spectra (as discussed above). The open circles in Fig.3.31 represent the fast arriving NO+ ion signal (shown as broken line with one dot in Fig.3.22(a-c)), and the filled circles give the main part of the peak (shown as dotted lines in Fig.3.22(a-c)). The x's in the P(E_{Trans}) profile in Fig.3.31 correspond to the slow tail of the TOF spectra (shown as broken line with three dots in the middle in Fig.3.22(a-c)).The disagreements between the total calculated (shown as solid lines in Fig.3.22(a-c)) and the experimental spectra begin to appear especially in the slower portion of the TOF spectra in Fig.3.22(a-c).

The m/e = 16 (O^+) TOF spectra were also fitted with the same P(E_{Trans}) profile (Figure 3.31) which fitted m/e = 35 and 30. The open circles in P(E_{Trans}) profile (Fig.3.31) resulted in the fit to the fast part of the main peak (shown as broken line in Fig.3.23(a), and as broken line with single dot in Fig.3.23(b)). The filled circles generated fits to the rest of main peak in the TOF spectra (shown as solid line in Fig.3.23(a), as broken line in Fig.3.23(b)). The fast arriving shoulder was fitted by x's in the P(E_{Trans}) profile (shown as broken line in Fig.3.23(a), and as broken line with three dots in Fig.3.23(b)), which was assigned to NOCl + O channel. The fast arrival of O+ ion signal was interpreted to be due to mass difference between NOCl and O fragments, which results in fast arrival of O+ ion in the detector. The resulting fit (shown as thick solid line in Fig.3.23(a-b)) matches part of the TOF spectra, but much of the features in the slow arriving portion is not matched at all.

The remaining mismatches, which are observed in the low kinetic energy region, are attributed to the lack of NO + O + Cl channel in the data analysis. The available total excess energy after the dissociation into three fragments (NO + O + Cl) is about 10 Kcal mole^{-1} (Table.3.5), and the corresponding P(E_{Trans}) should occur between 0 and 10 Kcal mole^{-1} translational energy region in Fig.3.31. The P(E_{Trans}) in Fig.3.30, which fitted m/e = 46, is not be affected by the lack of NO + O + Cl channel.

P(E_{Trans}) from m/e = 46 and m/e = 35,30 and 16

The P(E_{Trans}) from m/e = 46 TOF data analysis (Figure 3.30) and from m/e = 35,30 and 16 TOF analysis (Figure 3.31) are overlapped on one another and shown in Figure 3.32. The P(E_{Trans}) of NO_2 should agree with that from Cl within experimental uncertainty. The disagreement between the two P(E_{Trans}) profiles down to ~10 Kcal/mole can be safely assumed to be due to experimental uncertainties. Below 10 Kcal/mole in translational energy scale, NO_2 fragments contain enough internal excitation to undergo dissociation into NO + O and is not expected to appear as NO_2^+ signal. Furthermore, NO_2 fragments with more internal excitations are less likely to survive the ionization and be detected as NO_2^+ signal. Therefore, mismatch is expected between the P(E_{Trans}) for m/e = 46 and m/e = 35 TOF spectra in the low translational energy region of 10 and about 20 Kcal/mole.

The overall profiles of both P(E_{Trans}) are fairly well matched in the high kinetic energy region, with some disagreements in the low kinetic energy region stemming from above mentioned uncertainties.

The obtained P(E_{Trans}) profiles indicated the following photolytic channels at 248 nm photolysis of NO_2Cl.

NO_2Cl + hv -->	$NO_2^*(A,B) + Cl$	(Eq. 3.8)
	$NO_2(X) + Cl$	(Eq. 3.10)
	NOCl + O	(Eq. 3.11)
	$(NO + O + Cl)^*$	(Eq.3.9)

Of the channels shown above, the Eq. 3.8 was also observed from PIF analysis while Eq.3.9 was inferred from P(E_{int}) profile obtained by PIF analysis. In the P(E_{Trans}) obtained from m/e = 35,30 and 16 TOF analysis (Fig.3.31), NO(X) + O + Cl channel (Eq. 3.9) was not included in the analysis.

The average translational energy into $NO_2(X)$ + Cl channel is about 60 Kcal/mole (21000 cm^{-1}) based on the P(E_{Trans}) from m/e = 46 (Fig.3.30) analysis and from P(E_{Trans}) for m/e = 35,30,16 (Fig.3.31), leaving 20 Kcal/mole (7000 cm^{-1}) for internal excitation of NO_2 and Cl spin-orbit excited states. If an average of 1000 cm^{-1} vibrational energy is assumed for NO_2 oscillator, this internal energy corresponds to 7 quanta of average NO_2 vibrational excitation. For the $NO_2(A,B)$ + Cl channel, about 25 Kcal/mole (8750 cm^{-1}) of translational energy is released based on the P(E_{Trans}) for m/e = 35,30,16 (Fig.3.31) leaving about 56 Kcal/mole (19600 cm^{-1}) for NO_2 internal excitation. Assuming that $NO_2(A)$ state is initially populated, approximately 28 Kcal/mole (9800 cm^{-1}) is taken up for the electronic excitation which leaves 28 Kcal/mole (9800 cm^{-1}) for internal excitation of NO_2 and Cl. This corresponds to about 10 quanta of average NO_2 vibrational excitations in the $NO_2(A)$ state. For the NOCl + O channel, average kinetic energy release is estimated to be 13 Kcal/mole out of 46 Kcal/mole available excess energy leaving about 33 Kcal/mole for internal excitation of NOCl. It takes 36.8 Kcal/mole to break the NOCl into NO(X) + Cl (Table 3.5), which implies high internal excitation of NOCl fragment. This may be the reason why m/e = 65 ($NOCl^+$) ion signal was not directly detected.

This is summarized as follows, where energy is in Kcal/mole and fraction of excess energy is shown in parenthesis.The low kinetic energy energy channel, NO + O + Cl, is not shown here for the reason described earlier.

			E_{Trans}	E_{int}	$E_{Elect.}$
NO_2Cl + hv -->	$NO_2^*(A)$ +	Cl	25 (0.30)	28 (0.35)	28 (0.35)
	$NO_2(X)$ +	Cl	60 (0.75)	20 (0.25)	
	NOCl(X) +	$O(^3P)$	13 (0.28)	33 (0.72)	

The observed photolysis channels from PIF study and from the translational energy release spectroscopy may be understood in terms of the tentative UV absorption assignment made earlier. At 248 and 266 nm , UV absorption appears to involve n -> π^* transition while 193 nm involve π -> π^* transition. As was discussed in nitromethane photolysis by Butler et al. [16], this transition involves initial electronic excitation of the parent molecule which is localized in NO_2 moiety. This electronic excitation must be predissociated by another electronic state which is repulsive in Cl-N bond in order for the NO_2Cl to undergo dissociation into NO_2 and Cl. The lack of sharp features in the UV absorption may be an indication of predissociation. This point was discussed by Harris [5] where low lying electronic states of NO_2X molecules were calculated and discussed in relation to the dissociation mechanism. This excitation mechanism puts much of the excess energy into the NO_2 fragment, and the increase in excess energy would result in further dissociation of NO_2 into NO and O for those fragments with internal energy above the dissociation limit.

(D) Comparison of NO_2^* PIF Results to TOF/MS Results.

In Figure 3.22, the $P(E_{Trans})$ from analysis of m/e = 35, 30 and 16 TOF spectra are overlapped against the inferred distribution of kinetic energy based on the $P(E_{int})$ of NO_2^* from PIF analysis.

The inferred distribution of kinetic energy was obtained by subtracting internal energy distribution ($P(E_{int})$) of NO_2^* from the total available excess energy of 81 Kcal/mole. The observed population of reaction products by PIF is restricted to those NO_2^* molecules that fluoresce, and this must be considered in comparing PIF and TOF/MS results. The lower horizontal scale corresponds to the kinetic energy, while NO_2^* internal energy scale is shown on the upper horizontal scale.The inferred distribution of kinetic energy profile shown in shade was adjusted to match the area under the second, slower $P(E_{Trans})$ curve, which corresponded to excited NO_2 fragments. The error bars in the shaded distribution are based on the different NO_2^* fluorescence lifetime extrapolations as discussed earlier, where upper and lower limits of the error bar correspond to estimated upper and lower limit of fluorescence lifetime uncertainties. The difference in the $P(E_{int})$ from expression A and B also fall within this error bars.

The overall $P(E_{Trans})$ profile is estimated by adding the overlapped part of the distributions, and representing the added region with a dotted line in Fig.3.33. The uncertainty in the added overall $P(E_{Trans})$ profile is estimated from the disagreements observed in overlapped $P(E_{Trans})$ profiles in Fig.3.32. However, expected disagreements between the two $P(E_{Trans})$ profiles in the low kinetic energy region are due to (1) internally excited NO_2 cracking in the ionizer giving rise to smaller observed NO_2^+ ion signals in m/e = 46 TOF spectra, and (2) absence of low kinetic energy channel (NO + O + Cl) in the $P(E_{Trans})$ profile (Fig.3.31). These present difficulties in quantitative error estimate in $P(E_{Trans})$ profile in the low kinetic energy region of 0 to about 25 Kcal/mole.

The comparison between $P(E_{Trans})$ and inferred kinetic energy distribution from $P(E_{int})$ shows agreement in the observed overall shape of the distribution, which is skewed toward low kinetic (thus, higher internal) energy. However, mismatches in the curvatures are observed in the high kinetic energy region (about 25 to 40 Kcal/mole), where uncertainty in NO_2 fluorescence lifetime used for PIF analysis increases. In this kinetic energy region, uncertainty in $P(E_{Trans})$ profile is expected to be within the error bars shown. Mismatches in the lower kinetic energy side between the two profiles are attributed to the unaccounted low kinetic energy channel of NO + O + Cl in $P(E_{Trans})$ profile, which is expected to add more to the $P(E_{Trans})$ between 0 and 10 Kcal/mole of translational energy region, and to the excessive dissociation of highly internally excited NO2 in the electron bombardment ionizer.

The fraction of excess energy in the products in the photolysis channel producing NO_2^* was estimated from PIF analysis with the estimated average internal energy of NO_2^* fragment. The same quantity was also estimated from $P(E_{Trans})$ profile obtained by TOF/MS analysis. The estimated fraction of excess energy from each analysis is compared below.

For NO_2Cl + 248nm --> $NO_2^*(A) + Cl(^2P_{3/2})$ channel,

E_{Trans}	E_{Rovib}	$E_{Elect.}$	
0.30	0.35	0.35	from TOF/MS,
0.26	0.40	0.34	from PIF,

where the first excited state of NO_2 was used to estimate the electronic energy in NO_2^*, and no excitation in spin-orbit excited state of Cl atom was assumed. If no assumptions are made in regard to the originating electronic state for NO_2^* fluorescence,

E_{Trans}	E_{int}	
0.30	0.70	from TOF/MS,
0.26	0.74	from PIF.

This shows an good agreement between the two methods in estimating the partitioned excess energy in the products.

Based on the comparison between $P(E_{Trans})$ profile from TOF/MS data and the inferred kinetic energy distribution from $P(E_{int})$ profile, it is concluded that $P(E_{int})$ distribution of NO_2^* from PIF analysis shows good overall match to the $P(E_{Trans})$ profile obtained from a complimentary experiment within the estimated uncertainties of each experimental results. The estimated average internal energy of NO2* from PIF analysis matches the estimated average translational energy of NO_2^*, resulting in agreement in estimated fraction of excess energy in the products.

In addition, experiments are in progress in this laboratory to determine fluorescence lifetime of NO_2 LIF emission especially in the low energy of excitation and to reduce the uncertainty in the $P(E_{int})$ distribution of NO_2^*. Also in progress are PIF study of other NO_2-X molecules, where X = F, CH_3, NO_2, OH, etc. In some of these efforts, molecular beam expansion is used to cool the internal excitation of parent molecules.

CONCLUSION

The Photolysis Induced Fluorescence (PIF) of nitryl chloride (NO_2Cl) was studied at 266, 248 and 193 nm. This method gives an estimate of the distribution of internal energy in the product NO_2 which fluoresce, $P(E_{int})$; and this investigation demonstrates how the internal energy distribution of reaction products changes with the energy of photolysis laser. This study also demonstrates the change in the nascent $P(E_{int})$ profile as the NO_2^* fragment undergoes a controlled number of collisions.

Translational Energy Release Spectroscopy of the photochemical reaction was performed in the Y.T. Lee group's molecular beam machine. This method gives the distribution of translational energies of the product molecules, and it is complimentary to and more detailed than the PIF method.

Combining the experimental results from both studies, following photolytic channels were identified.

	PIF	TOF/MS
NO_2Cl + 248 --> $NO_2(X)$ + Cl		observed
$NO_2^*(A,B)$ + Cl	observed	observed
NO + O + Cl	inferred	inferred
NOCl + O		observed

From PIF study, the average NO_2^* internal energy from 266, 248 and 193 nm was estimated to be 17000 cm^{-1}, 21000 cm^{-1} and 21000 cm^{-1} each. The emission yield of NO_2^* at these photolyses was estimated to be 0.9±0.5, 0.7±0.2 and 0.03±0.03, respectively.

Comparison of $P(E_{Trans})$ distribution from TOF/MS analysis and $P(E_{int})$ from PIF analysis at 248 nm resulted in fair matching of the distribution profiles within the uncertainties of each method.With refinements in the fluorescence lifetime of NO2 for PIF analysis, and addition of low kinetic energy release channel in the TOF/MS analysis, even better matching between the two profiles are expected. The estimated average internal energy of NO_2^* from PIF was well matched by estimated average translational energy of NO_2^* fragment from TOF/MS analysis.

Based on the experimental evidence observed from two complimentary experiments, it is thought that UV photodissociation of NO_2Cl involve highly localized initial excitation in NO_2 group, followed by predissociation of Cl-N bond where much of the excess energy remain in the NO_2 fragment. This is manifested by NO_2^* emission, and the inferred dissociation into NO + O when sufficient excess energy exists

ACKNOWLEDGEMENTS

In developing and refining the PIF analysis method, a need to verify this analysis method with a complimentary experiment was great. Therefore, it is a great pleasure to acknowledge the support by Prof. Y.T.Lee and his coworkers in carrying out the Translational Energy Release Spectroscopy on NO_2Cl. Mike Covinsky and Floyd Davis are two graduate students who have been responsible for most of the effort in performing experiments, analyzing the data, and teaching the author how to analyze the data.

This work at the University of California and the Lawrence Berkeley Laboratory was supported by the Director, Office of Energy Research, Office of Basic Energy Research, Chemical Science Division of the U.S. Department of Energy under Contract No. DE-AC03-76SF00098.

REFERENCES

1. A.J. Illis and G.A. Takacs, J. Photochem. 6 (1976/77) 35.
2. H.H. Nelson and H.S. Johnston, J. Phys. Chem., 85 (1981) 3891.
3. C.E. Moore, Atomic Energy Levels, National Bureau of Standards Circular 467.
4. L. E. Harris, J. Chem. Phys. 58 (1973) 5615.
5. D. A. Kleier and M. A. Lipton, J. Mol. Struct. (Theochem.) 109 (1984) 39.
6. K. Endo, Nippon Kagaku Kaishi 9 (1979) 1129.
7. D.L. Baulch, R.A. Cox, R.F. Hampson Jr., J.A. Ken, J. Troe and R. T. Watson, J. Phys. Chem. Ref. Data 9 (1980) 295 - 471.
8. G.E. Busch and K.R. Wilson, J. Chem. Phys. 56 (1972) 3626.
9. Y.T. Lee, J.D. McDonald, P.R. LeBreton and D.R. Herschbach, Rev. Sci. Instrum. 40 (1969) 1402.
10. A.M. Wodtke and Y.T. Lee, J. Phys. Chem. 89 (1985) 4744.
11. M. Volpe and H.S. Johnston, J. Am. Chem. Soc. 78 (1956) 3903.
12. H. Dunnwald, E. Siegel, W. Urban, J.W. Rich, G.F. Homicz and M.J. Williams, Chemical Physics 94 (1985) 195.
13. K.P. Huber and G. Hertzberg, Constants of Diatomic Molecules, Volume IV ,Van Nostrand Reinhold Co. 1979, N.Y., N.Y.
14. (a) V. M. Donnelly and F. Kaufman, J. Chem. Phys. 66 (1977) 4100; (b) V. M. Donnelly and F. Kaufman, J. Chem. Phys. 69 (1978) 1456; (c) V. M. Donnelly, D. G. Keil and F. Kaufman, J. Chem. Phys. 71 (1979) 659.
15. D. L. Hsu, D. L. Mounts and R. N. Zare, Spectral Atlas of Nitrogen Dioxide , (New York: Academic Press, 1978).
16. L.J. Butler, D. Krajnovich, Y.T. Lee, G. Ondrey and R. Bersohn, J. Chem. Phys. 79 (1983) 1708.
17. K.E.J. Hallin and A.J. Merer, J. Mol. Spec. 65 (1977) 163.
18. J.C.D. Brand and P.H. Chiu, J. Mol. Spec. 75 (1979) 1.

19. A.W. Adamson, Physical Chemistry, 3rd ed., (Academic Press, 1986).
20. J.O. Hirschfelder, C.F. Curtiss and R.B. Bird, Molecular Theory of Gases and Liquids, corrected ed., (Wiley, New York, 1964).

TABLE 3.1 UV absorption cross section of NO_2Cl.

λ (nm)	Absorption (cm^2)
190	2.69e-17
195	1.13e-17
197.5	7.13e-18
200	4.55e-18
205	3.22e-18
210	3.39e-18
215	3.56e-18
220	3.42e-18
225	2.95e-18
230	2.36e-18
235	1.8e-18
240	1.4e-18
250	9.85e-19
260	6.37e-19
270	3.73e-19
280	2.31e-19
290	1.8e-19
300	1.54e-19
310	1.25e-19
320	8.7e-20
330	5.58e-20
340	3.33e-20
350	1.78e-20
360	1.14e-20
370	7.2e-21

* The value between 190 nm and 270 nm are from Illis et.al. [1], while 270 nm to 370 nm were obtained from Nelson et.al. [2].

TABLE 3.2. NO_2Cl Structural Parameters.(Adopted from Endo [6])
Rotational Constants (MHz)

	A	B	C
$^{15}NO_2{}^{35}Cl$	13298	5156.83	3709.76
$^{15}NO_2{}^{37}Cl$	13266	5001.2	3628.6

r_0 (N-O) = 1.198 ± 0.002 Å
r_0 (N-Cl) = 1.843 ± 0.004 Å
< O-N-O = 130.9° ± 0.5

TABLE 3.3. NO_2Cl PIF experimental condition.

λ (nm)	File#	P (mtorr)	E (mj)	PMT (V)	σ (*10^{-20} cm^2)(a)	Gate Delay /width(ns)	Collision number(b)
193	DOD74WB	20	0.2	-1500	1700	30/30	0.014
	DOD74YA	20	0.3	-1450		30/30	
248	DOD42YA	5	9.0	-1300	98.5	10/30	0.002
	DOD42YB	5	9.0	-1300		10/30	
	DOD42YC	5	7.6	-1300		10/30	
	DOD42YD	5	7.5	-1300		10/30	
	DOD36YA	5	0.36	-1450		10/30	
	DOD36YB	5	0.33	-1450		10/30	
	DOD36YC	5	0.28	-1450		10/30	
	DOD36YD	5	0.22	-1450		10/30	
	DOD37WA	5	0.41	-1450		10/30	
	DOD43WB	50	6.0	-1200		2400/30	1.4
	DOD41YA	200	0.4	-1350		6000/30	14.2
266	DOC281A	10	0.44	-1500	48	30/60	0.011
	DOC282B	10	0.4	-1500		30/60	
	DOC283A	10	0.56	-1400		30/60	

(a) NO_2Cl absorption cross section is from Reference [1,2]

(b) The number of collision (hard sphere) was estimated as follows.

For hard sphere model,
collision onto NO_2^* by NO_2Cl can be estimated by expression [19]

$$Z_1(2) = 2\sqrt{2}\,\sigma_{12}^2\,(\pi kT / \mu)^{1/2}\,n2$$

where $Z_1(2)$ = collision frequency experienced by 1 in the presence of 2,

$\sigma_{12} = (\sigma_1+\sigma_2) / 2$ = average hard sphere diameter,

$\mu = (m_1\ m_2 / m_1 + m_2)$ = reduced mass,

n_2 = concentration of 2.

With $1 = NO_2^*$ and $2 = NO_2Cl$,
and estimated $\sigma_1 \cong 4Å$ and $\sigma_2 \cong 6Å$, and so $\sigma_{12} \cong 5Å$ [20]
an example of 200 mtorr NO_2Cl colliding with NO_2^* gives
4.242 E−7 second per collision, or 424 ns per collision.

TABLE 3.4(A) PIF fitting parameters with coefficient Expression A.

λ(nm)	File#	$\nu^{(1)}$	$\rho^{(2)}$	M	# of collision$^{(3)}$
193	DOD74WB	0.9	3.25E3	3.995E4	0.014
	DOD74YA	0.9	3.25E3		
248	DOD42YA	1.0	2.9E3	2.846E4	0.002
	DOD42YB	1.0	2.9E3		
	DOD42YC	1.0	2.9E3		
	DOD42YD	1.0	2.9E3		
	DOD36YA	1.0	2.9E3		
	DOD36YB	1.0	2.9E3		
	DOD36YC	1.0	2.9E3		
	DOD36YD	1.0	2.9E3		
	DOD37WA	1.0	2.9E3		
	DOD43WB	1.0	6.2E3	2.846E4	1.4
	DOD41YA	4.0	1.25E4	2.846E4	14.2
266	DOC281A	1.0	8.0E3	2.573E4	0.011
	DOC282B	1.0	8.0E3		
	DOC283A	1.0	5.0E3		

(1) ν = Variable parameter.

(2) ρ = Variable parameter.

(3) For collision number calculation, see Table 3.3.

TABLE 3.4(B) PIF fitting parameters with coefficient Expression B.

λ(nm)	File#	$\mu^{(1)}$	$\sigma^{(2)}$	# of collision$^{(3)}$
193	DOD74WB	2.5E4	4.0E3	0.014
	DOD74YA	2.5E4	4.0E3	
248	DOD42YA	4.1E4	9.8E3	0.002
	DOD42YB	4.1E4	9.8E3	
	DOD42YC	4.1E4	9.8E3	
	DOD42YD	4.1E4	9.8E3	
	DOD36YA	4.1E4	9.8E3	
	DOD36YB	4.1E4	9.8E3	
	DOD36YC	4.1E4	9.8E3	
	DOD36YD	4.1E4	9.8E3	
	DOD37WA	4.1E4	9.8E3	
	DOD43WB	2.1E4	7.0E3	1.4
	DOD41YA	5.0E3	6.3E3	14.2
266	DOC281A	1.6E4	6.0E3	0.011
	DOC282B	1.6E4	6.0E3	
	DOC283A	1.6E4	5.0E3	

(1) μ = Variable parameter (Mean of the Gaussian distribution).

(2) σ = Variable parameter (width of the Gaussian distribution).

(3) For collision number calculation, see Table 3.3.

TABLE 3.5. Thermochemical Data for Product formation.

	ΔH^o_f(298 K)*	
$NO_2Cl(X)$	12.5	KJ mole^{-1}
$NOCl(X)$	51.7	
$Cl(^2P_{3/2})$	121.3	
$Cl(^2P_{1/2})^{(a)}$	132.8	
$NO(X^2\Pi)$	90.25	
$NO_2(X^2A_1)$	33.2	
$NO_2(A^2B_2)^{(b)}$	149.9	
$NO_2(B^2B_1)^{(c)}$	210.7	
$O(^3P)$	249.17	
$ClO(X)$	102.0	

	ΔH^o_f(298°K)		
	KJ mole-1	cm-1	Kcal mole-1
$NO_2Cl(X) \rightarrow NO_2(X^2A_1) + Cl(^2P_{3/2})$	142.0	11866	33.9
$NO_2(X^2A_1) + Cl(^2P_{1/2})$	153.5	12827	36.7
$NO(X^2\Pi) + ClO(X)$	179.75	15021	43.0
$NO_2(A^2B_2) + Cl(^2P_{3/2})$	258.7	21619	61.8
$NOCl(X) + O(^3P)$	288.4	24098	68.9
$NO_2(B^2B_1) + Cl(^2P_{3/2})$	319.5	26700	76.4
$NO(X^2\Pi) + O(^3P) + Cl(^2P_{3/2})$	448.32	37456	107.1

* The Enthalpy data were taken from Reference[7].

(a) The spin-orbit state difference of 881cm^{-1} was used for $Cl(^2P_{3/2})$ <-> $Cl(^2P_{1/2})$ [3].

(b) $NO_2(A^2B_2)$ of 9750 cm^{-1} [17] above the ground state is used.

(c) $NO_2(B^2B_1)$ of 14830 cm^{-1} [18] above the ground state is used.

TABLE 3.6. NO_2^* emission yields from NO_2 LIF and NO_2Cl PIF.

NO_2 LIF

λ(nm)	File #	Normalized Intensity* (arb.unit)	
410.29	DOD88WB	5.45E-3	
	DOD88WC	3.62E-3	
	DOD88WD	2.71E-3	
415.76	DOD90YC	7.97E-3	
	DOD90YD	4.14E-3	
	DOD91WA	7.16E-3	
421.0	DOD90WA	5.98E-3	
	DOD90WC	5.12E-3	
	DOD90WD	4.09E-3	
	DOD90YA	7.82E-3	Avg. = (5.4± 3.4**)E-3
			Ratio = 1 ± 0.63((2σ)

NO_2Cl PIF

λ(nm)	File #	Normalized Intensity* (arb.unit)	
193	DOD74YB	1.28E-4	
	DOD74WA	2.81E-4	
	DOD74WB	1.60E-4	
	DOD75WA	0.86E-4	
			Avg. = (1.6±1.6)E-4
			Ratio ~0.03±0.03(2σ)
248	DOD42YA	3.48E-3	
	DOD42YB	3.10E-3	
	DOD42YC	3.45E-3	
	DOD42YD	4.00E-3	
			Avg. = (3.5±0.8)E-3
			Ratio ~ 0.7±0.2(2σ)
266	DOC281A	5.09E-3	
	DOC282B	6.39E-3	
	DOC283A	3.66E-3	
			Avg. = (5.05±2.74)E3
			Ratio ~ 0.9±0.5(2σ)

* Normalized for sample pressures, absorption cross scetions, instrument settings, and laser fluence normalized to the per photon basis.

** The range of uncertainty reflects 2σ (2 standard deviations).

TABLE 3.7. Raw P(E_{Trans}) of Detected fragments from 248 nm NO_2Cl Photolysis.

K.E.(Kcal)	P(E_{Trans}) m/e=46		P(E_{Trans}) m/e=35,30,16		
0	0		0		65
1	0		1		64
2	0		3		63
3	0		5		62
4	0		8		61
5	0		12		60
6	0		18		59
7	0		24		58
8	6		33		57
9	12		42		56
10	18		51		55
11	24		60		54
12	29		67		53
13	35		73		52
14	40		77		51
15	45		80		50
16	50		82		49
17	55		83		48
18	60		84		46
19	65		83		44
20	70		81		42
21	74		78		40
22	77		75		38
23	79		72		36
24	80		70		34
25	79		69		32
26	78		69		30
27	76		70		28
28	73		72		26
29	70		74	0	24
30	67		75	2	22
31	64		74	4	20
32	61		72	7	18
33	58		70	10	16
34	54	0	67	13	15
35	51	1	63	17	14
36	47	3	59	21	13
37	43	5	56	25	12
38	39	8	53	29	11
39	36	11	50	33	10
40	33	14	46	37	9
41	30	18	42	42	8
42	27	22	38	47	7
43	24	26	34	52	6
44	21	30	30	57	5
45	18	34	26	62	4

46	14	38	22	67	3
47	10	42	18	72	2
48	7	46	14	78	1
49	4	51	10	84	0
50	2	56	6	89	
51	0	61	2	93	
52	0	66	0	97	
53	0	71	0	101	
54	0	76	0	104	
55	0	80	0	106	
56	0	84	0	107	
57	0	87	0	108	
58	0	90	0	108	
59	0	93	0	107	
60	0	95	0	106	
61	0	97	0	104	
62	0	98	0	101	
63	0	97	0	98	
64	0	95	0	95	
65	0	92	0	92	
66	0	88	0	88	
67	0	83	0	83	
68	0	77	0	77	
69	0	70	0	70	
70		62		62	
71		54		54	
72		46		46	
73		39		39	
74		31		31	
75		25		25	
76		19		19	
77		13		13	
78		8		8	
79		4		4	

FIGURE CAPTIONS

Figure 3.1: UV absorption curve of NO_2Cl is smooth and continuous, with a few absorption features [1,2]. Although no assignments have been made on NO_2Cl absorption features, tentative assignments are made on the strong absorption feature near 190 nm as $\pi \rightarrow \pi^*$ transition, weaker feature around 220 nm as $n \rightarrow \pi^*$ transition, and a much weaker feature around 300 nm as $\sigma \rightarrow \pi^*$ transition. See Table 3.1 for the numerical values of the absorption cross sections.

Figure 3.2: The structural parameters of NO_2Cl are shown, based on the microwave spectroscopy study reported by Endo [6]. The molecule is planer with C_{2v} symmetry. Reported rotational constants are: A = 13298 Mhz, B = 5156.83 Mhz, C = 3709.76 Mhz for $^{15}NO_2{}^{35}Cl$, and A = 13266 Mhz, B = 5001.2 Mhz, C = 3628.6 Mhz for $^{15}NO_2{}^{37}Cl$, respectively. The N-O bond length of 1.198 ± 0.002Å, N-Cl bond length of 1.843 ± 0.004Å, and the bond angle <O-N-O of $130.9^\circ \pm 0.5$ are also calculated from these spectra.

Figure 3.3: Experimental apparatus of Time-of-Flight Mass Spectrometry for measuring translational energy release. After the laser pulse photodissociates NO_2Cl in the molecular beam, resulting photofragments travel 20.8 cm before being ionized by electron bombardment. After ion mass selection via quadrupole mass spectrometer, ions are counted with Daly type ion counter. The ion flight times are recorded with a multichannel scaler operating at 1 microsecond per channel time resolution.

Figure 3.4(a): The NO_2^* emission from NO_2Cl photodissociation at 266 nm, analyzed with coefficient expression A. The experimental emission spectrum, overlapped by calculated emission curve, is shown in the left-hand side. The experimental cumulative sum profile, overlapped by fitted cumulative sum curve, is shown on the right-hand side. Another curve in the left-hand side shows the internal energy distribution ($P(E_{int})$) of NO_2^* obtained from analysis. The Mu and Sigma should read ν and ρ in the body of text, including Tables. These are variable fitting parameters, which were varied independently for least-squares optimum fit. The M represents the maximum excess energy available for NO_2 fragment at this wavelength of photolysis, and is fixed throughout the analysis. The B represents scaling factor to match experimental and fitted cumulative sum profiles. See Results for more detail.

Figure 3.4(b): The coefficient distribution of LIF excitation energy (X_L), obtained from PIF analysis with expression A (Eq. 2.13). Two vertical bars mark the lower and upper limits of the detected NO_2^* emission, and therefore the range of analysis as well.

Figure 3.5(a): Same data as shown in Fig. 3.4(a), except PIF analysis was carried out with coefficient expression B (Eq. 2.14).In expression B, Mu and Sigma are variable fitting parameters, while B represents the scaling factor.

Figure 3.5(b): The coefficient distribution, generated with expression B, used for analysis in Figure 3.5(a). Two vertical bars mark the lower and upper limits of the detected NO_2^* emission and the analysis.

Figure 3.6: The $P(E_{int})$ of NO_2^* from 266 nm photolysis with coefficient expression A and B.

Figure 3.7(a): Same as Fig. 3.4(a) except data are from 248 nm photolysis of NO_2Cl.

Figure 3.7(b): The coefficient distribution from analysis in Figure 3.7(a).

Figure 3.8(a): Same data as in Fig. 3.7(a), but analyzed with expression B.

Figure 3.8(b): The coefficient distribution from Figure 3.8(a).

Figure 3.9: The $P(E_{int})$ of NO_2^* from 248 nm photolysis analyzed with expression A and B.

Figure 3.10(a): Same as 3.4(a), except data are from 193 nm photolysis of NO_2Cl.

Figure 3.10(b) The coefficient distribution used for analysis in Figure 3.10(a).

Figure 3.11(a): Same data as in Fig. 3.10(a), except analyzed with expression B.

Figure 3.11(b): The coefficient distribution used for analysis in Figure 3.11(a).

Figure 3.12: The $P(E_{int})$ of NO_2^* from 193 nm photolysis with coefficient expression A and B overlapped for comparison.

Figure 3.13(a): Same as in Fig. 3.4(a), except data are from 248 nm photolysis of NO_2Cl, observed after 1.4 hard sphere collision on NO_2^*.

Figure 3.13(b): The coefficient distribution used for analysis in Figure 3.13(a).

Figure 3.14(a): Same data as in Fig. 3.13(a), but analyzed with expression B.

Figure 3.14(b): The coefficient distribution used to generate the $P(E_{int})$ in Figure 3.14(a).

Figure 3.15: The $P(E_{int})$ of NO_2^* from 248 nm photolysis of NO_2Cl, after 1.4 collision, from expression A and B in PIF analysis are overlapped for comparison.

Figure 3.16(a): Same as in Fig. 3.4(a) except data is from 248 nm photolysis of NO_2Cl observed after NO_2^* had undergone 14.2 hard sphere collisions on the average.

Figure 3.16(b): The coefficient distribution used to generate the $P(E_{int})$ of NO_2^* in Fig. 3.16(a).

Figure 3.17(a): Same data as in Fig. 3.16(a), but analyzed with expression B.

Figure 3.17(b): The coefficient distribution used to generate the $P(E_{int})$ of NO_2^* in Fig. 3.17(a).

Figure 3.18: The $P(E_{int})$ of NO_2^* after 248 nm photolysis of NO_2Cl, which had undergone 14.4 hard sphere collisions before detection, obtained from PIF analysis with coefficient expression A and B.

Figure 3.19: The dispersed NO* emission observed in second order diffraction from 193 nm photodissociation of NO_2Cl under high laser fluence (focused laser beam). No vibrational band assignment was carried out, but range of emission wavelength suggest NO A -> X (γ - band) and B -> X (β - band) transition [12,13]. Energetics require at least 2 photons to produce $NO^*(A)$ at 193 nm photodissociation of NO_2Cl.

Figure 3.20(a): Time of flight spectrum of ion m/e = 46 observed at 10° with respect to the direction of molecular beam. The open circles represent the arrival time (with respect to the laser pulse) of photofragments which were ionized to produce m/e=46. This ion mass is thought to correspond to NO_2^+ ions, which would have come from initial NO_2 photofragment. Two peaks in this TOF spectrum suggest two types of NO_2 fragments are produced with different translational energies. Thick solid line represents overall calculated TOF, while thin line and broken lines represent internally excited (thus lower kinetic energy) NO_2 and the ground state NO_2 respectively. See the text for more discussions and the details.

Figure 3.20(b): Time of flight spectrum of ion m/e = 46 observed at 20° with respect to the direction of molecular beam.

Figure 3.20(c): Time of flight spectrum of ion m/e = 46 observed at 30° with respect to the direction of molecular beam.

Figure 3.21(a): Time of flight spectrum of ion m/e = 35 observed at 10° with respect to the direction of molecular beam. This ion mass is thought to correspond to Cl^+ ion. See the inserted legend for explanation of various curves.

Figure 3.21(b): Time of flight spectrum of ion m/e = 35 observed at 20° with respect to the direction of molecular beam.

Figure 3.21(c): Time of flight spectrum of ion m/e = 35 observed at 30° with respect to the direction of molecular beam.

Figure 3.21(d): Time of flight spectrum of ion m/e = 35 observed at 40° with respect to the direction of molecular beam.

Figure 3.22(a): Time of flight spectrum of ion m/e = 30 observed at 20° with respect to the direction of molecular beam. This ion mass is thought to correspond to NO^+ ion. See the inserted legend for more detail on various fitted curves.

Figure 3.22(b): Time of flight spectrum of ion m/e = 30 observed at 30° with respect to the direction of molecular beam.

Figure 3.22(c): Time of flight spectrum of ion m/e = 30 observed at 40° with respect to the direction of molecular beam.

Figure 3.23(a): Time of flight spectrum of ion m/e = 16 observed at 10° with respect to the direction of molecular beam. This ion mass correspond to O^+ ion. See the inserted legend for more detail on various fitted curves.

Figure 3.23(b): Time of flight spectrum of ion m/e = 16 observed at 20° with respect to the direction of molecular beam.

Figure 3.24. P(Eint) profile of NO2* from 248 nm photolysis is analyzed with expression B in PIF method, and shown in the middle trace. Upper and lower traces resulted from fluorescence lifetimes extrapolated to the upper and lower limits, as shown in Fig.2.28(b).

Figure 3.25. The NO_2^* $P(E_{int})$ profiles, which traces the average of the $P(E_{int})$ from expression A and B, as a function of collision are shown after 248 nm photolysis of NO_2Cl. The maximum of each $P(E_{int})$ curve was normalized to an arbitrary unit.

Figure 3.26: Nascent NO_2^* $P(E_{int})$ profiles from 266, 248 and 193 nm photodissociation of NO_2Cl are shown with area under the profile approximately scaled to each NO_2^* emission yield. The fluorescence emission yields of 0.9, 0.7 and 0.03 are estimated in Table 3.6. The darkened region represents the differences in NO_2^* $P(E_{int})$ profiles from PIF analysis with coefficient distribution expression A and B.

Figure 3.27: Energy level diagram of NO_2Cl photodissociation at 266 nm. The thermodynamic thresholds of various photolysis channels were estimated in the Table 3.5.

Figure 3.28: Energy level diagram of NO_2Cl photodissociation at 248 nm.

Figure 3.29: Energy level diagram of NO_2Cl photodissociation at 193 nm.

Figure 3.30: The $P(E_{Trans})$ profile used to fit the experimental TOF spectrum of m/e = 46.

Figure 3.31: The $P(E_{Trans})$ profile used to fit experimental TOF spectra of m/e = 35, 30 and 16 at various angle of detections.

Figure 3.32: The $P(E_{Trans})$ distribution profile obtained from m/e = 46 data (Fig.3.30) is overlapped to that of m/e = 35, 30, and 16 (Fig.3.31).

Figure 3.33. The NO_2^* $P(E_{int})$ from PIF analysis of 248 nm photodissociation is overlapped against the $P(E_{Trans})$ distribution profile from m/e = 35,30 and 16 TOF/MS analysis.

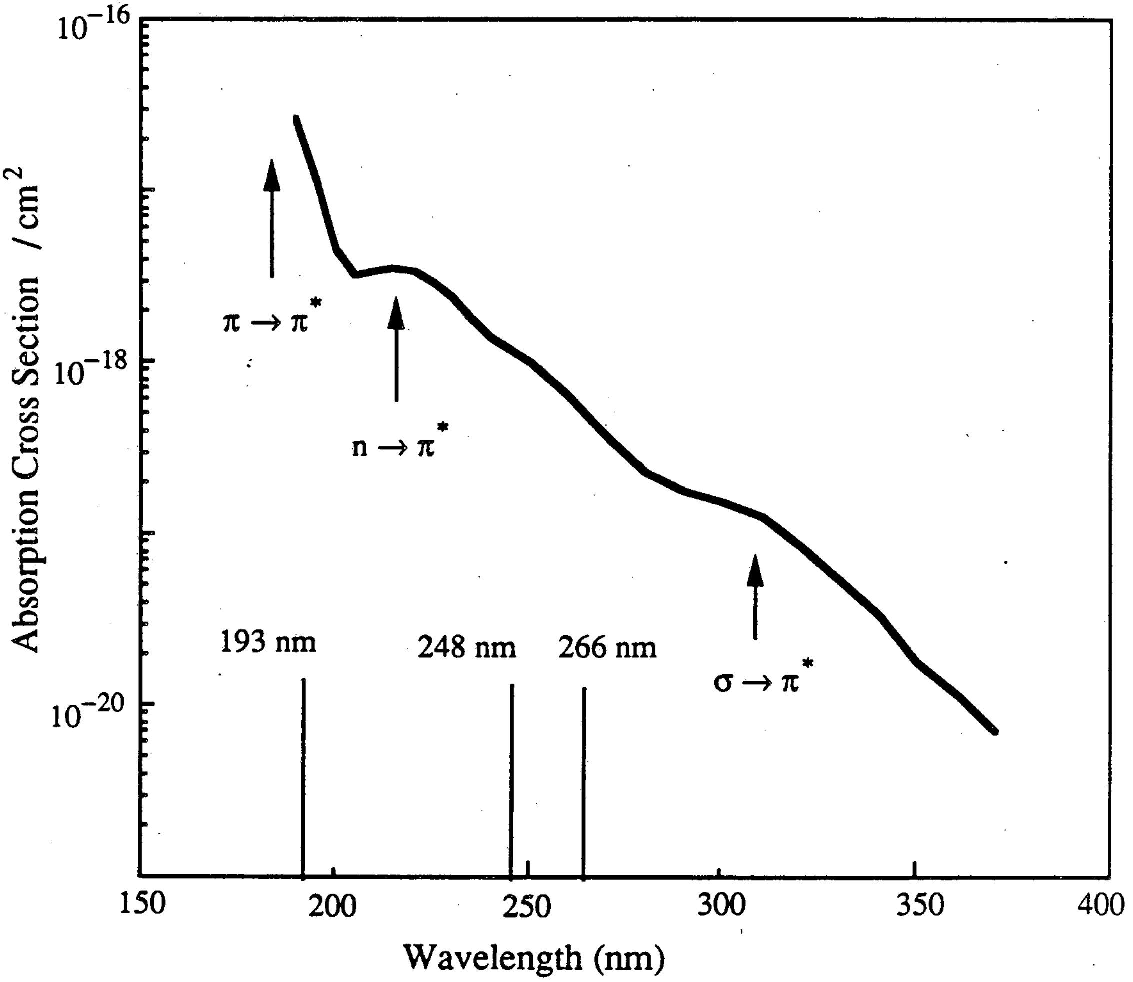
10^{-16}
10^{-18}
10^{-20}
Absorption Cross Section / cm^2
$\pi \rightarrow \pi^*$
$n \rightarrow \pi^*$
$\sigma \rightarrow \pi^*$
193 nm
248 nm
266 nm
150
200
250
300
350
400
Wavelength (nm)

Figure 3.1

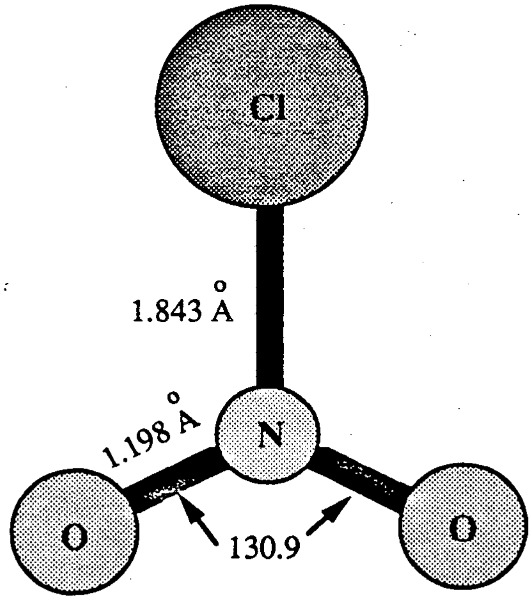

Figure 3.2

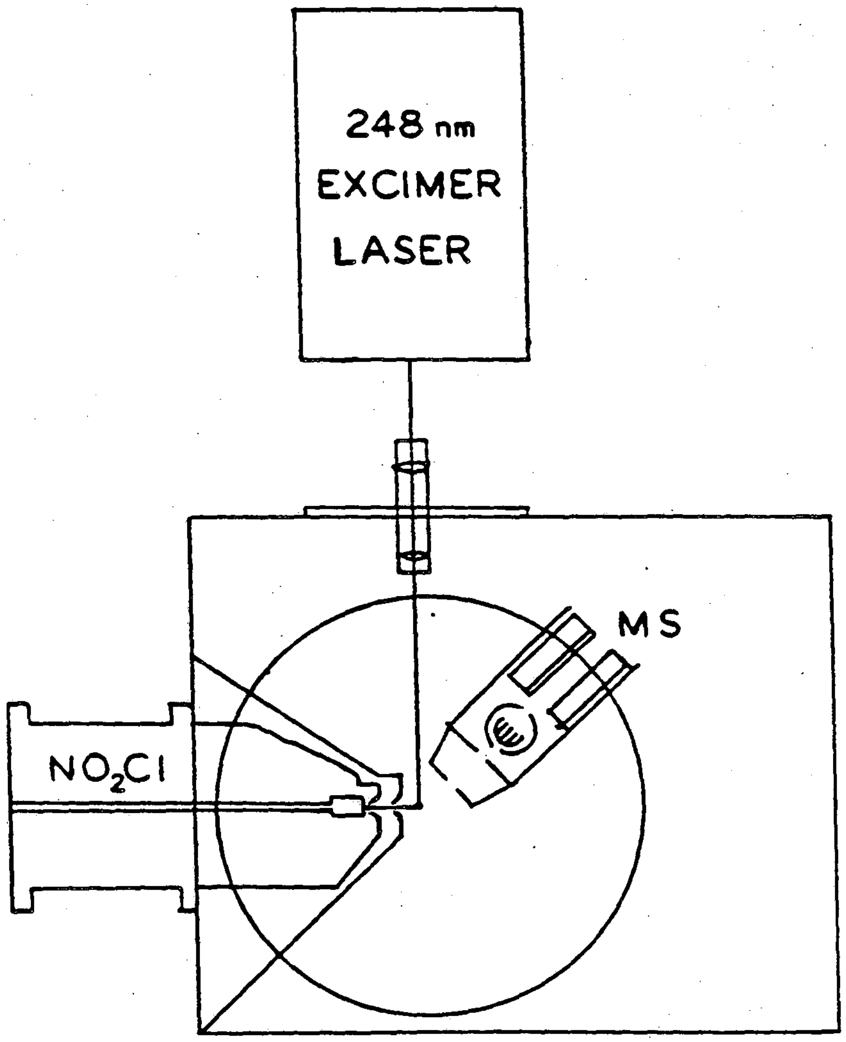

Figure 3.3

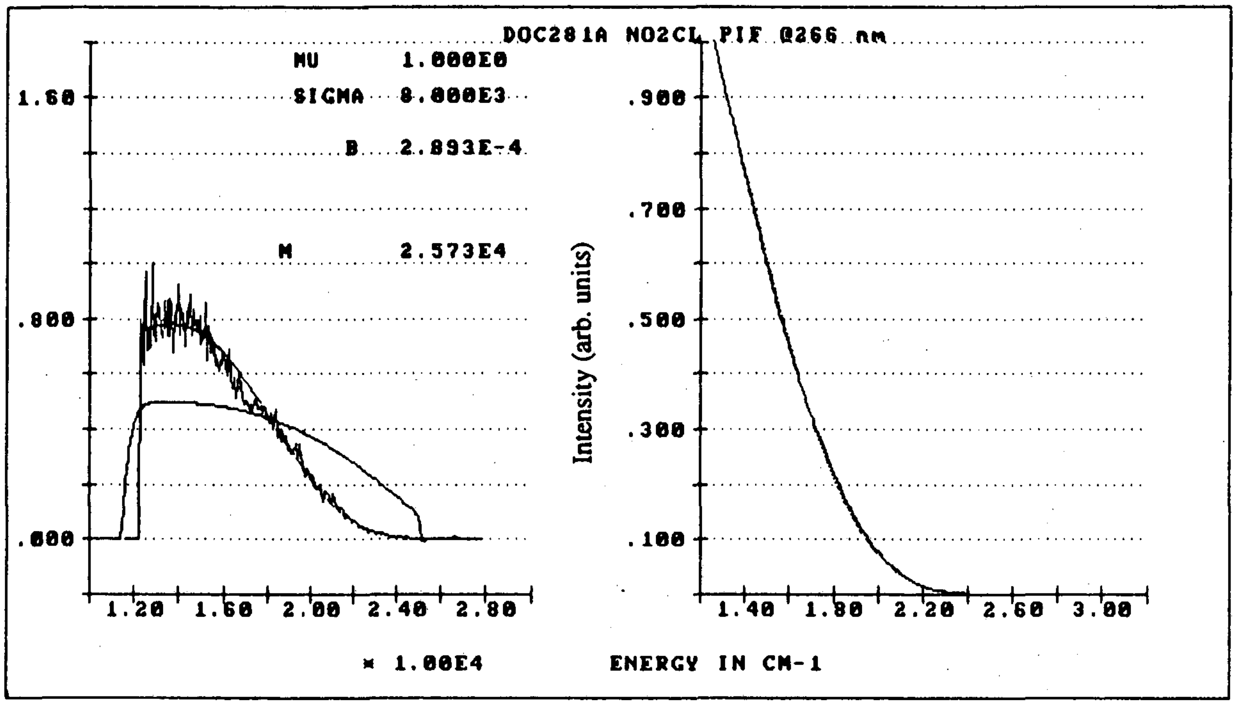
DOC281A NO2CL PIF @266 nm
MU 1.000E0
SIGMA 8.000E3
B 2.893E-4
M 2.573E4
1.60
.800
.000
.900
.700
.500
.300
.100
Intensity (arb. units)
1.20
1.60
2.00
2.40
2.80
1.40
1.80
2.20
2.60
3.00
* 1.00E4
ENERGY IN CM-1

Figure 3.4(a)

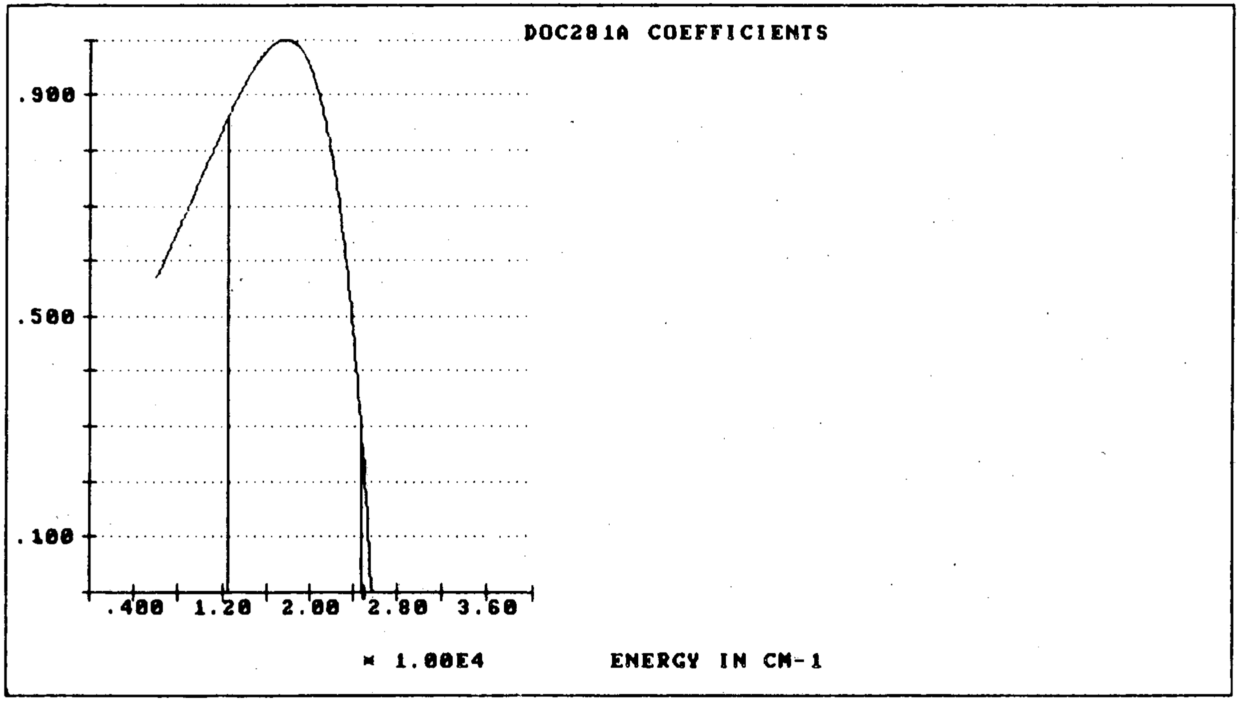
DOC281A COEFFICIENTS
.900
.500
.100
.400
1.20
2.00
2.80
3.60
× 1.00E4
ENERGY IN CM-1

Figure 3.4(b)

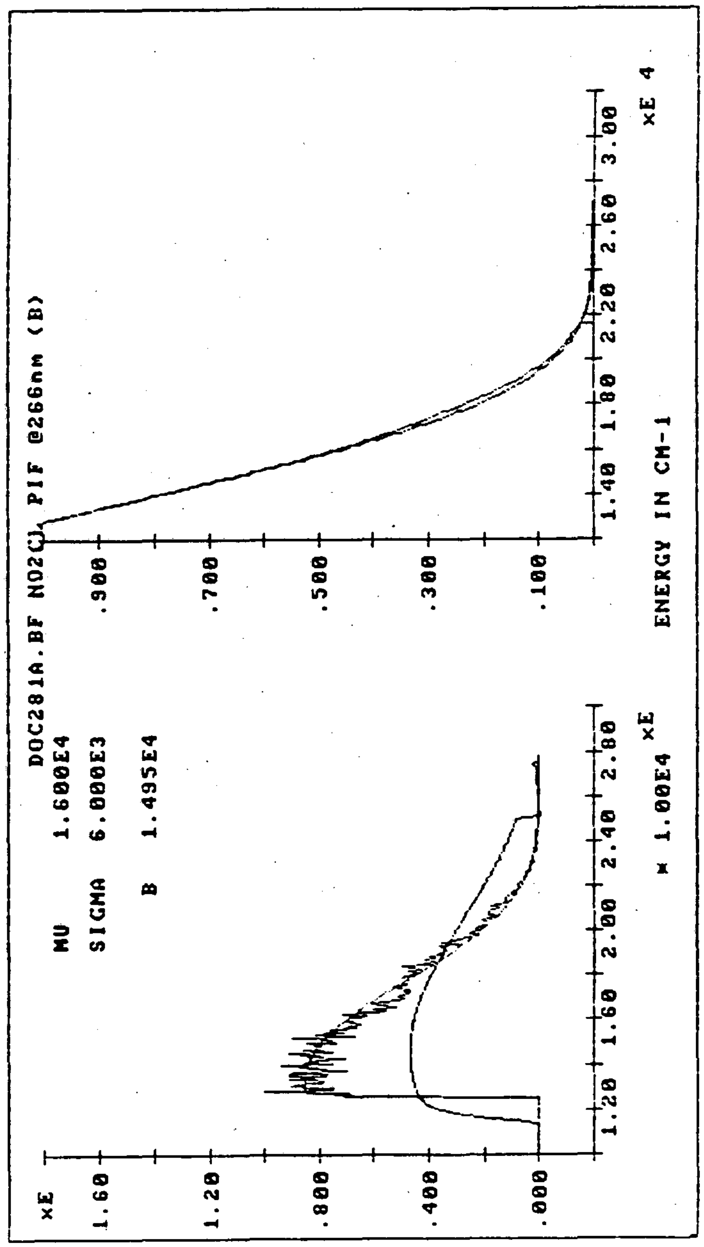
DOC281A.BF NO2(J) PIF @266nm (B)
MU 1.600E4
SIGMA 6.000E3
B 1.495E4
×E
1.60
1.20
.800
.400
.000
1.20
1.60
2.00
2.40
2.80
× 1.00E4 ×E
.900
.700
.500
.300
.100
1.40
1.80
2.20
2.60
3.00
×E 4
ENERGY IN CM-1

Figure 3.5(a)

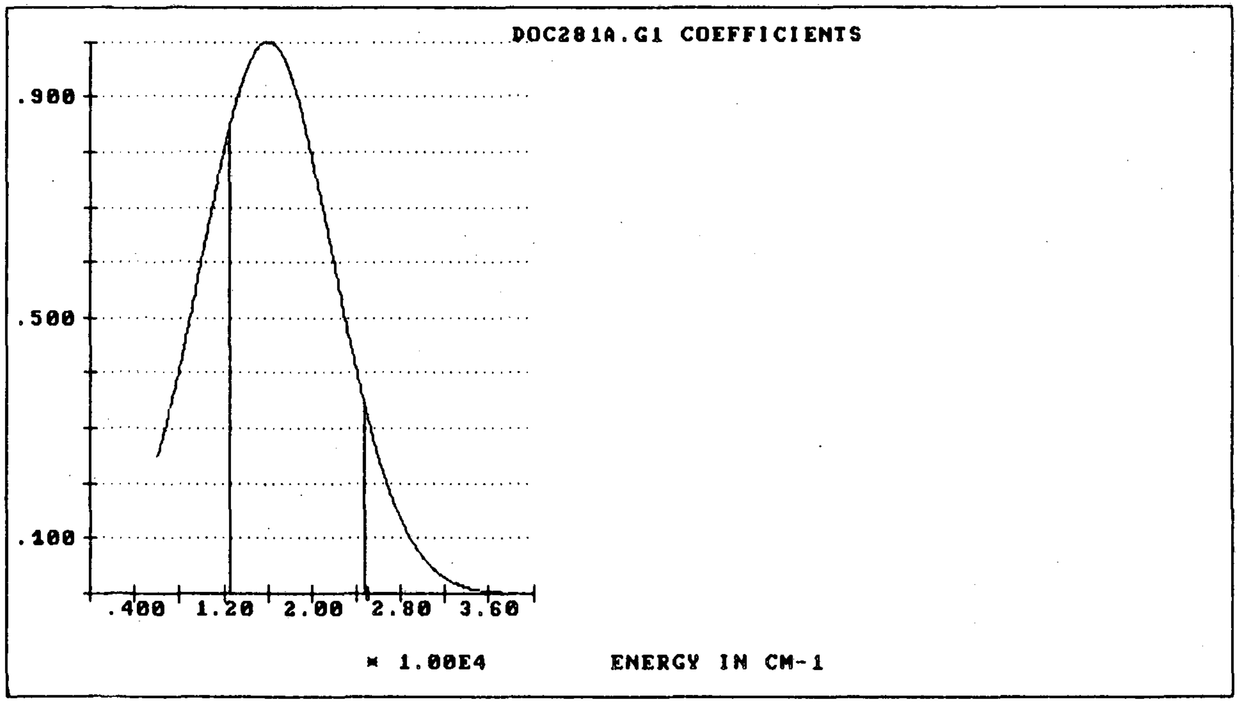
DOC281A.G1 COEFFICIENTS
.900
.500
.100
.400
1.20
2.00
2.80
3.60
× 1.00E4
ENERGY IN CM-1

Figure 3.5(b)

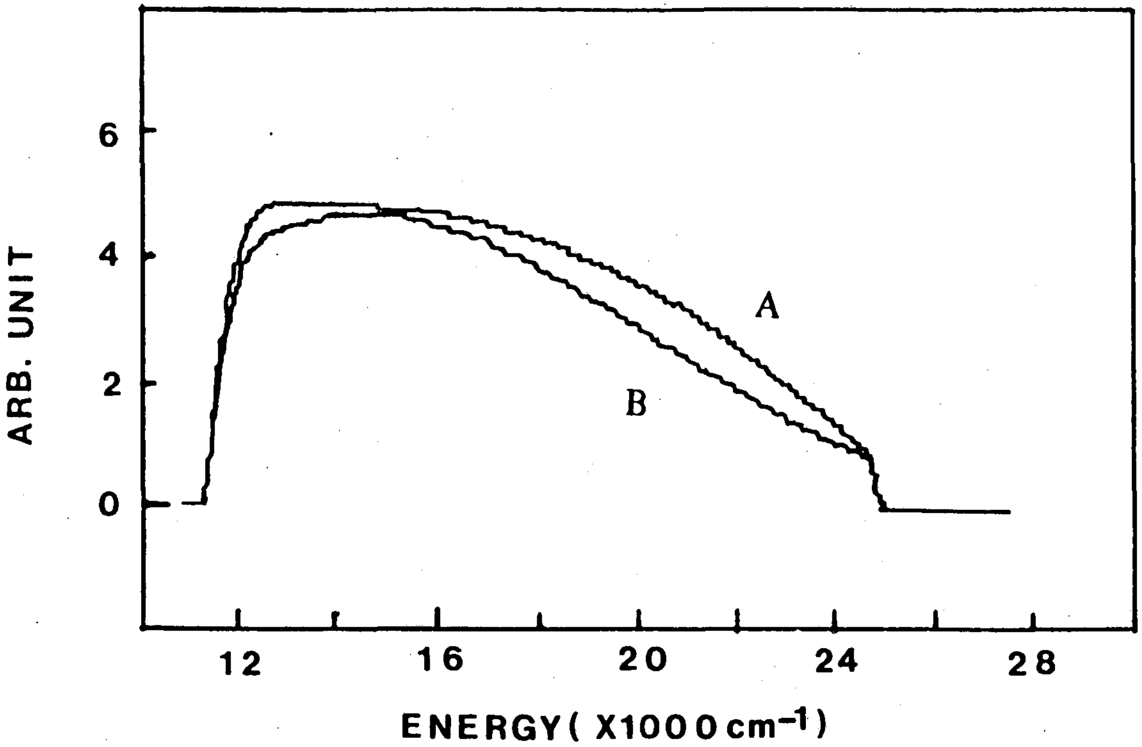

Figure 3.6

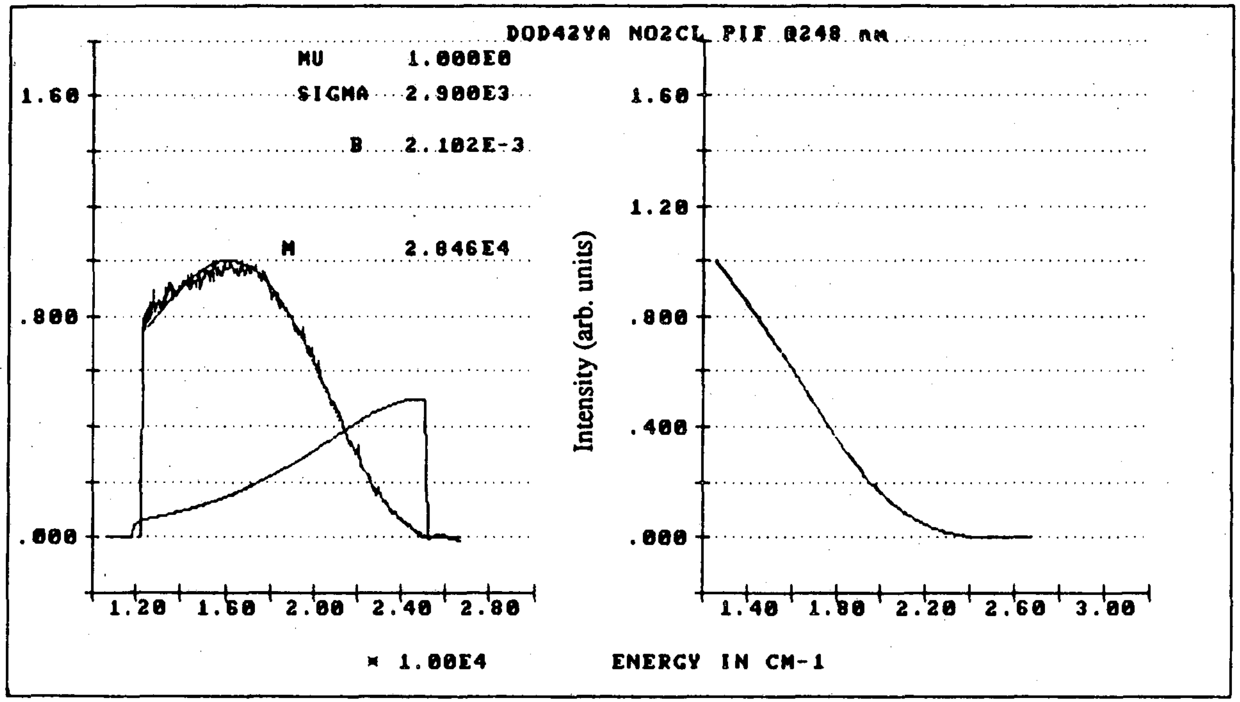
DOD42YA NO2CL PIF @248 nm
MU 1.000E0
SIGMA 2.900E3
B 2.102E-3
M 2.046E4
1.60
.800
.000
1.20
1.60
2.00
2.40
2.80
Intensity (arb. units)
1.60
1.20
.800
.400
.000
1.40
1.80
2.20
2.60
3.00
× 1.00E4
ENERGY IN CM-1

Figure 3.7(a)

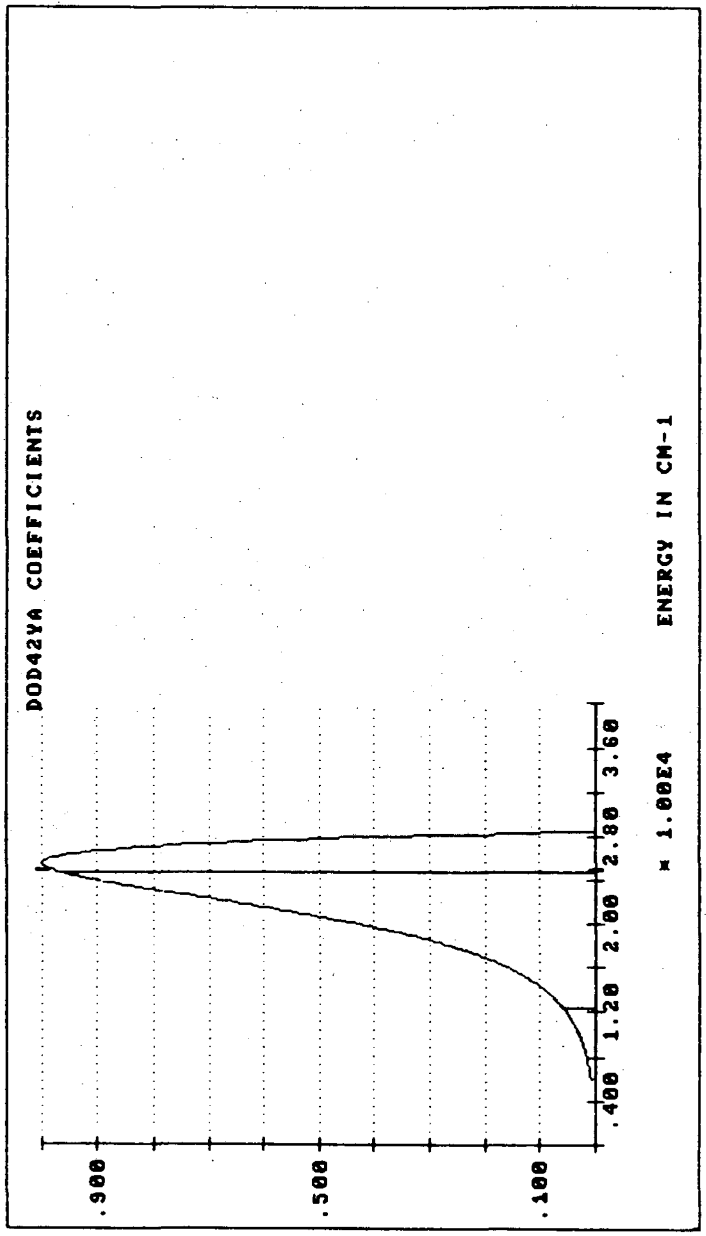
DOD42YA COEFFICIENTS
.900
.500
.100
.400
1.20
2.00
2.80
3.60
x 1.00E4
ENERGY IN CM-1

Figure 3.7(b)

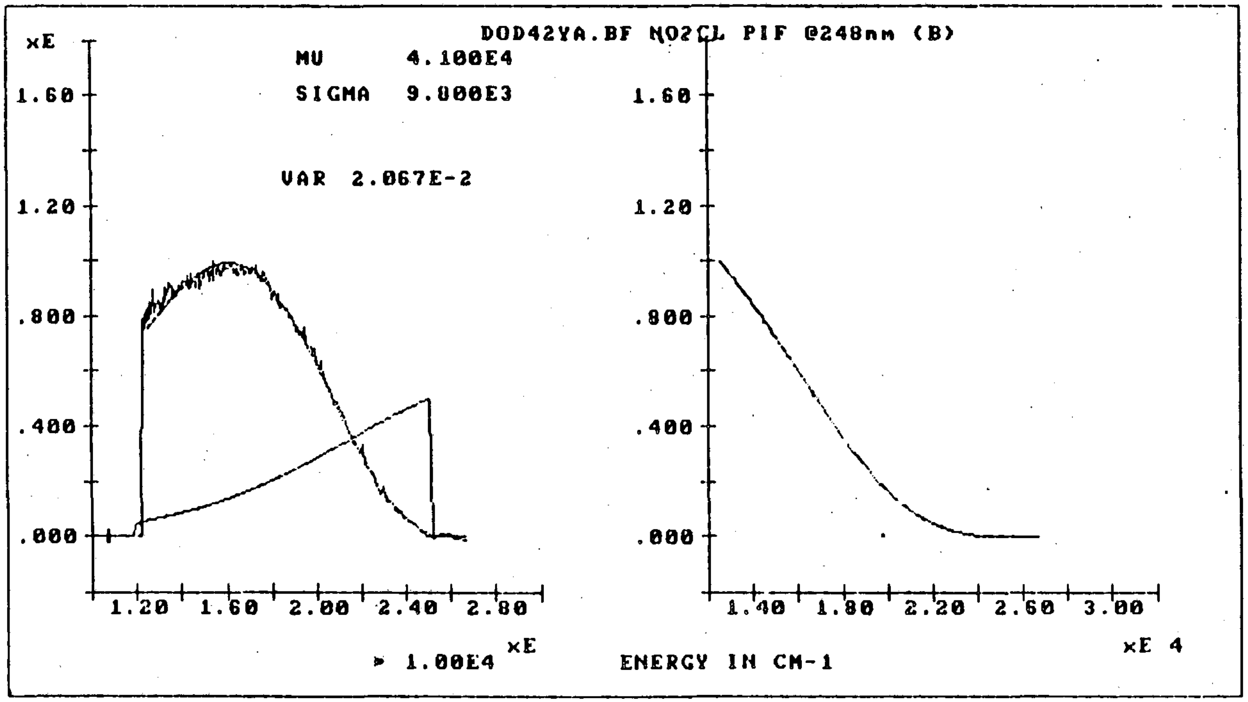
DOD42YA.BF NO2CL PIF @248nm (B)
xE
MU 4.100E4
SIGMA 9.000E3
VAR 2.067E-2
1.60
1.20
.800
.400
.000
1.20
1.60
2.00
2.40
2.80
* 1.00E4 xE
1.40
1.80
2.20
2.60
3.00
xE 4
ENERGY IN CM-1

Figure 3.8(a)

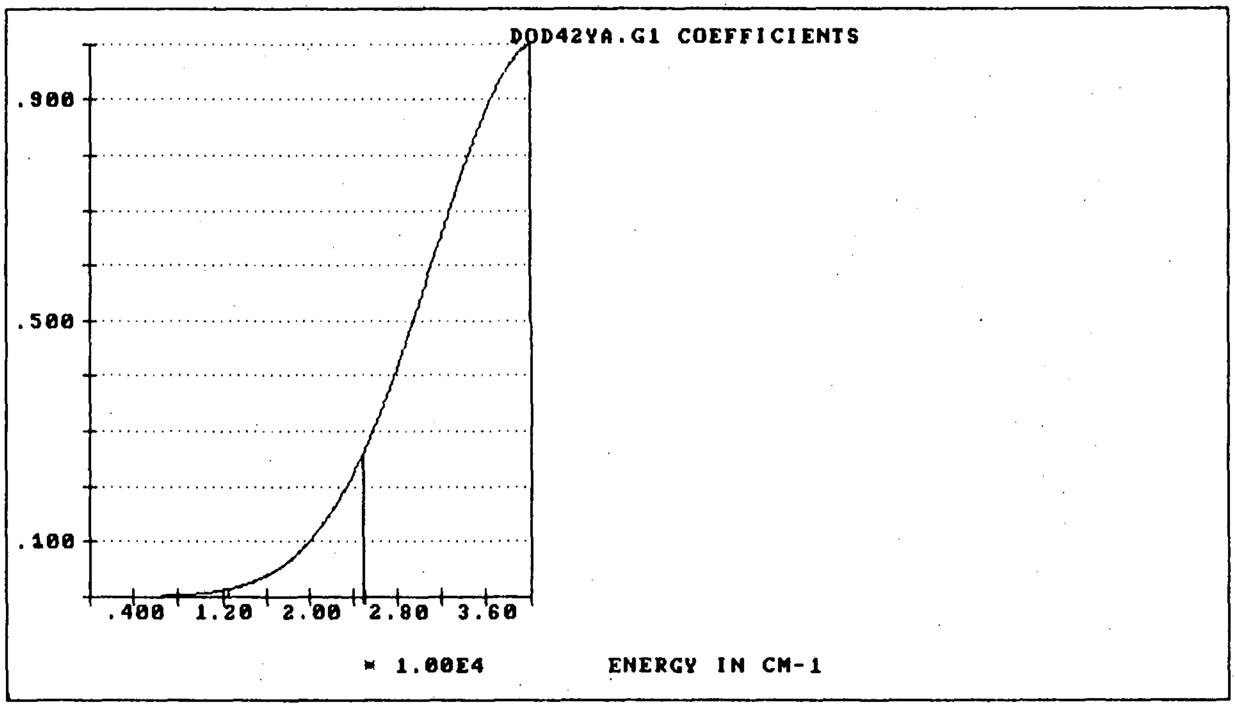
DOD42YA.G1 COEFFICIENTS
.900
.500
.100
.400
1.20
2.00
2.80
3.60
* 1.00E4
ENERGY IN CM-1

Figure 3.8(b)

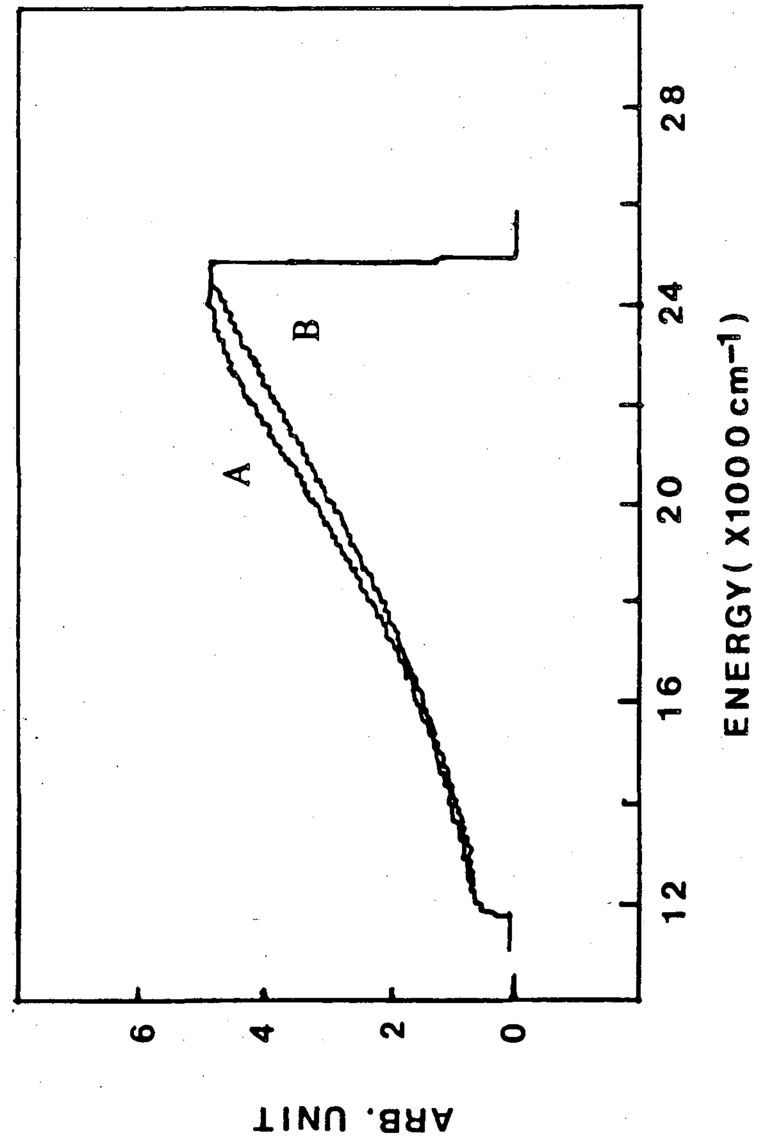

Figure 3.9

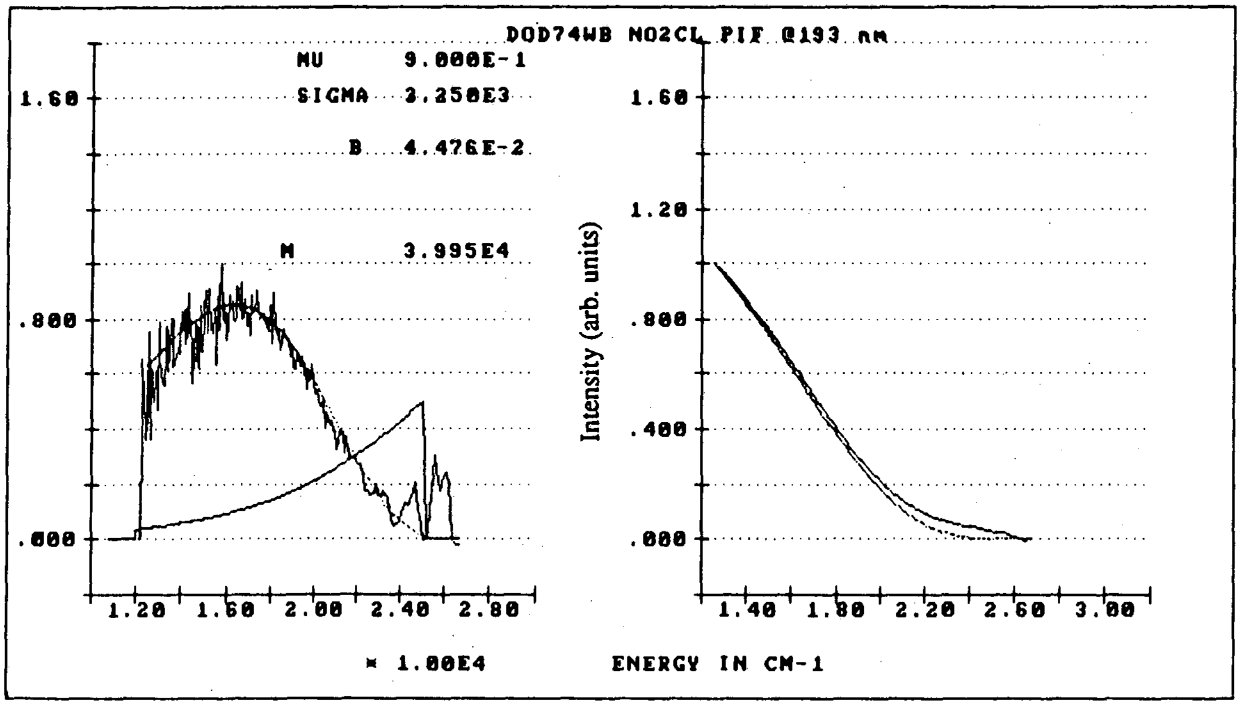
DOD74WB NO2CL PIF @193 nm
MU 9.000E-1
SIGMA 3.250E3
B 4.476E-2
M 3.995E4
1.60
.800
.000
1.20
1.60
2.00
2.40
2.80
Intensity (arb. units)
1.60
1.20
.800
.400
.000
1.40
1.80
2.20
2.60
3.00
* 1.00E4
ENERGY IN CM-1

Figure 3.10(a)

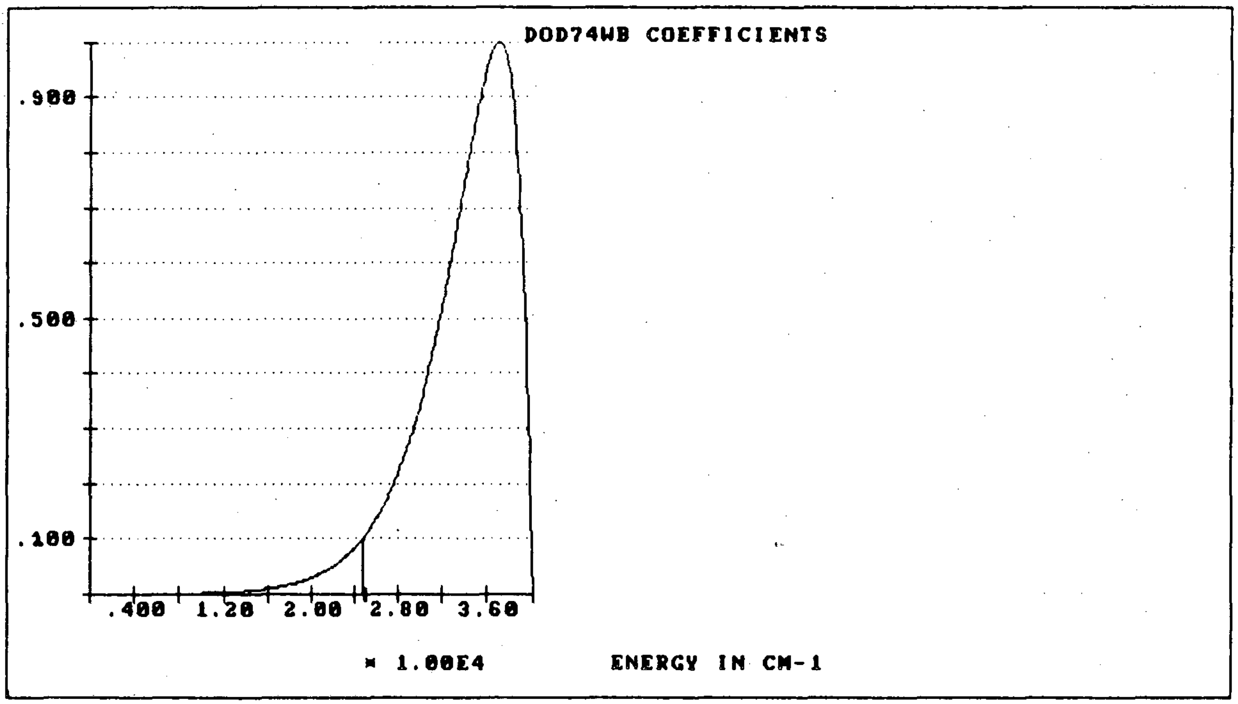
DOD74WB COEFFICIENTS
.900
.500
.100
.400
1.20
2.00
2.80
3.60
× 1.00E4
ENERGY IN CM-1

Figure 3.10(b)

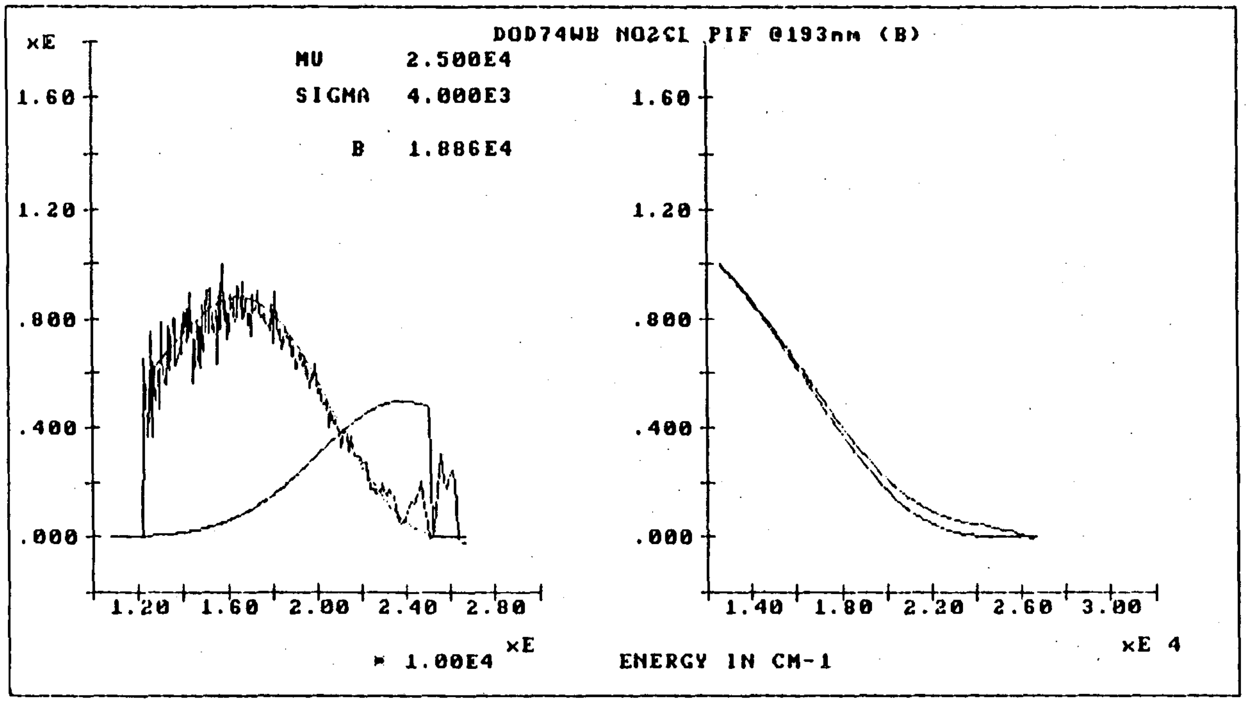
DOD74WB NO2CL PIF @193nm (B)
MU 2.500E4
SIGMA 4.000E3
B 1.886E4
xE
1.60
1.20
.800
.400
.000
1.20
1.60
2.00
2.40
2.80
xE
* 1.00E4
1.60
1.20
.800
.400
.000
1.40
1.80
2.20
2.60
3.00
xE 4
ENERGY IN CM-1

Figure 3.11(a)

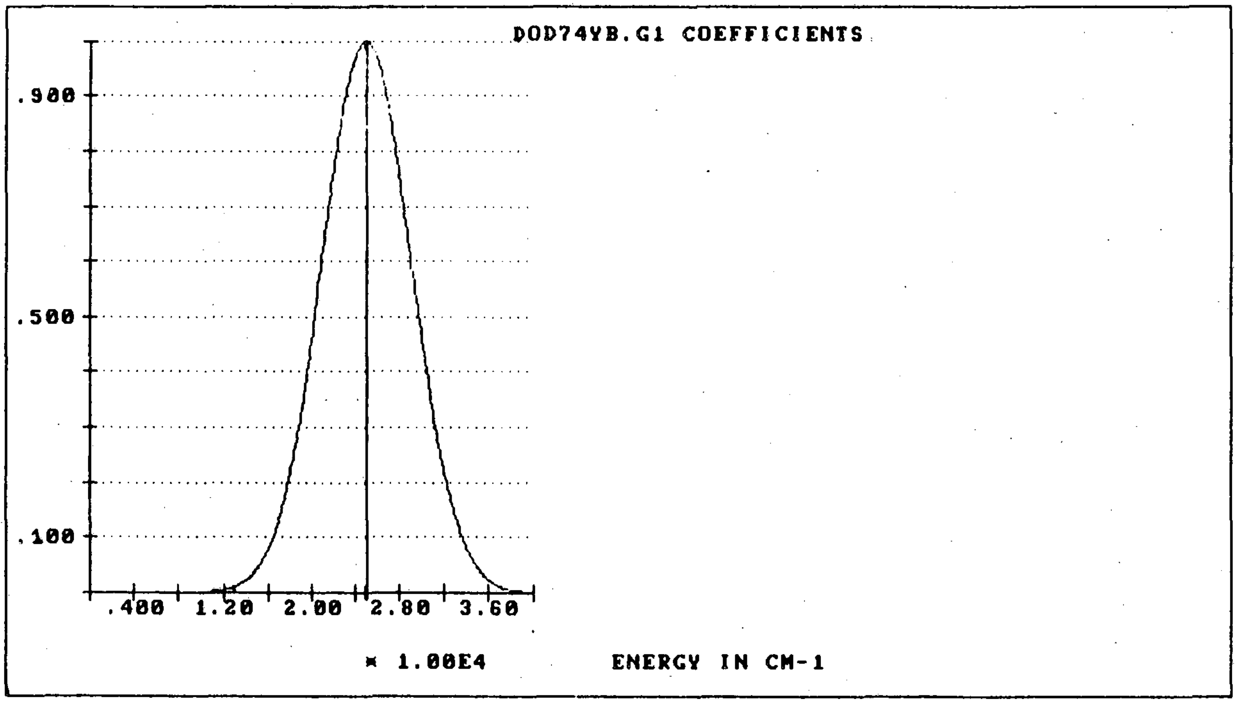
DOD74YB.G1 COEFFICIENTS
.900
.500
.100
.400
1.20
2.00
2.80
3.60
* 1.00E4
ENERGY IN CM-1

Figure 3.11(b)

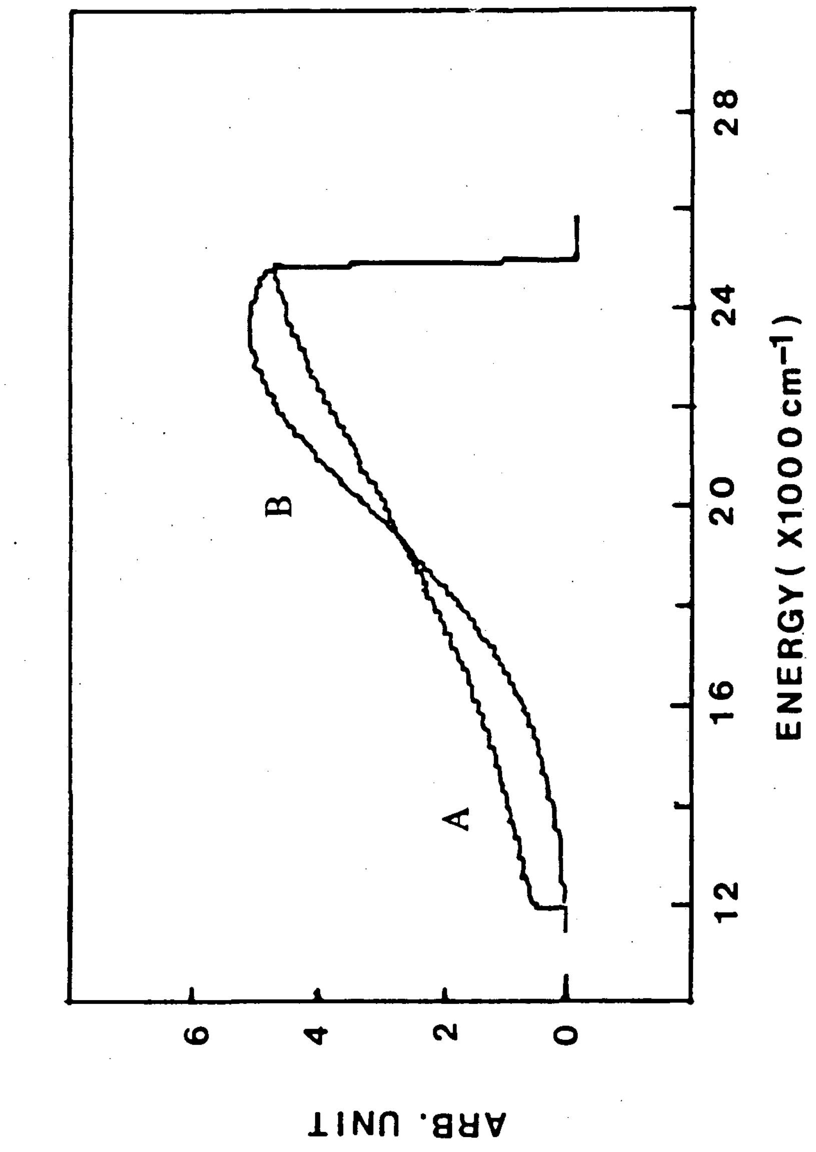

Figure 3.12

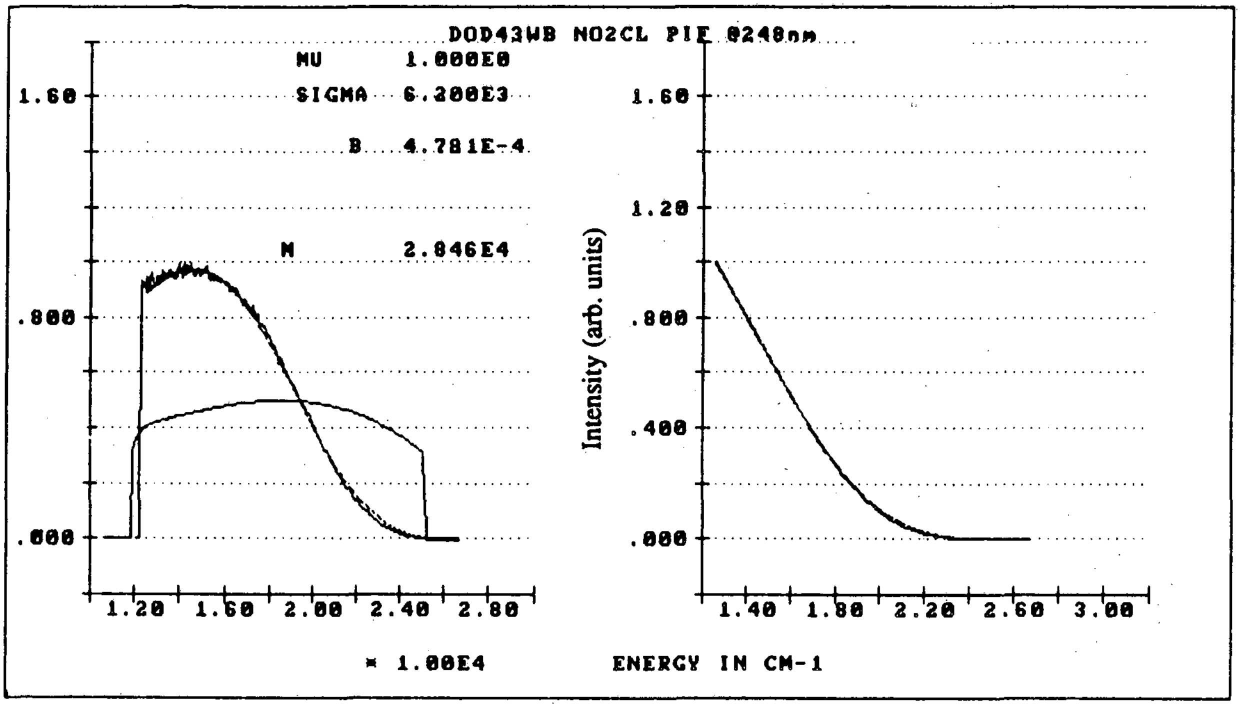
DOD43WB NO2CL PIE @248nm
MU 1.000E0
SIGMA 6.200E3
B 4.781E-4
M 2.846E4
1.60
.800
.000
1.20
.400
Intensity (arb. units)
1.20
1.60
2.00
2.40
2.80
1.40
1.80
2.20
2.60
3.00
* 1.00E4
ENERGY IN CM-1

Figure 3.13(a)

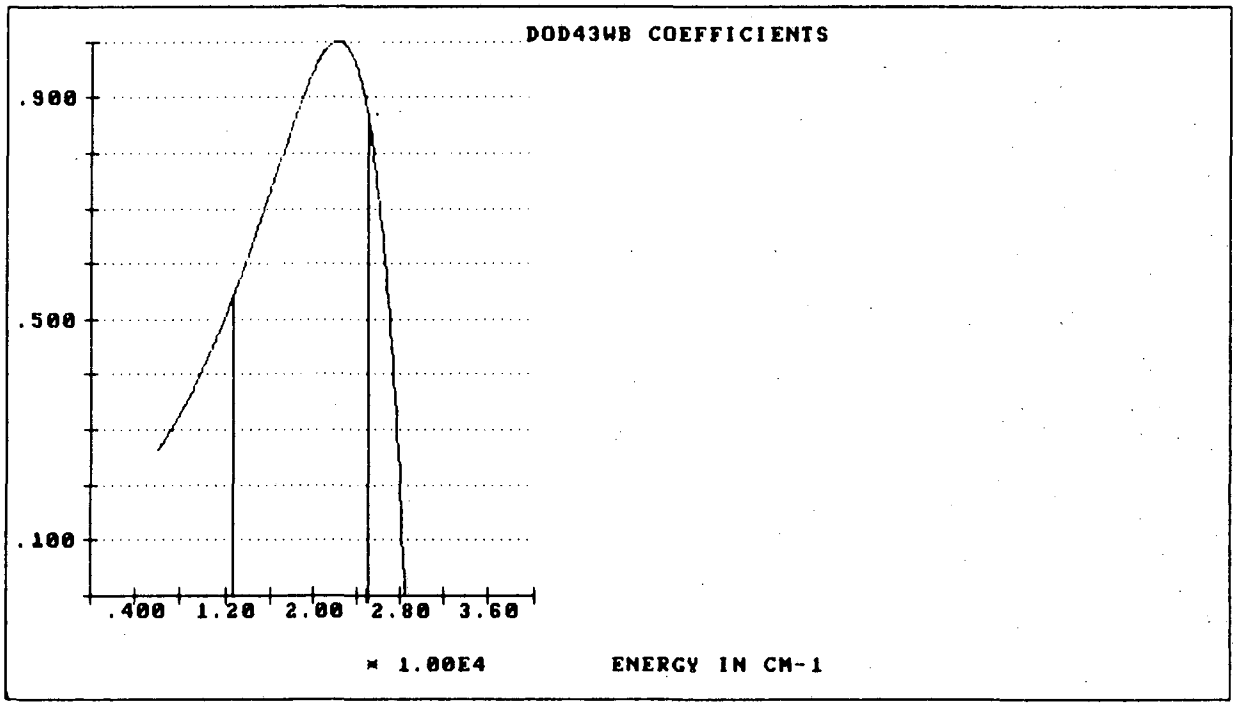
DOD43WB COEFFICIENTS
.900
.500
.100
.400
1.20
2.00
2.80
3.60
* 1.00E4
ENERGY IN CM-1

Figure 3.13(b)

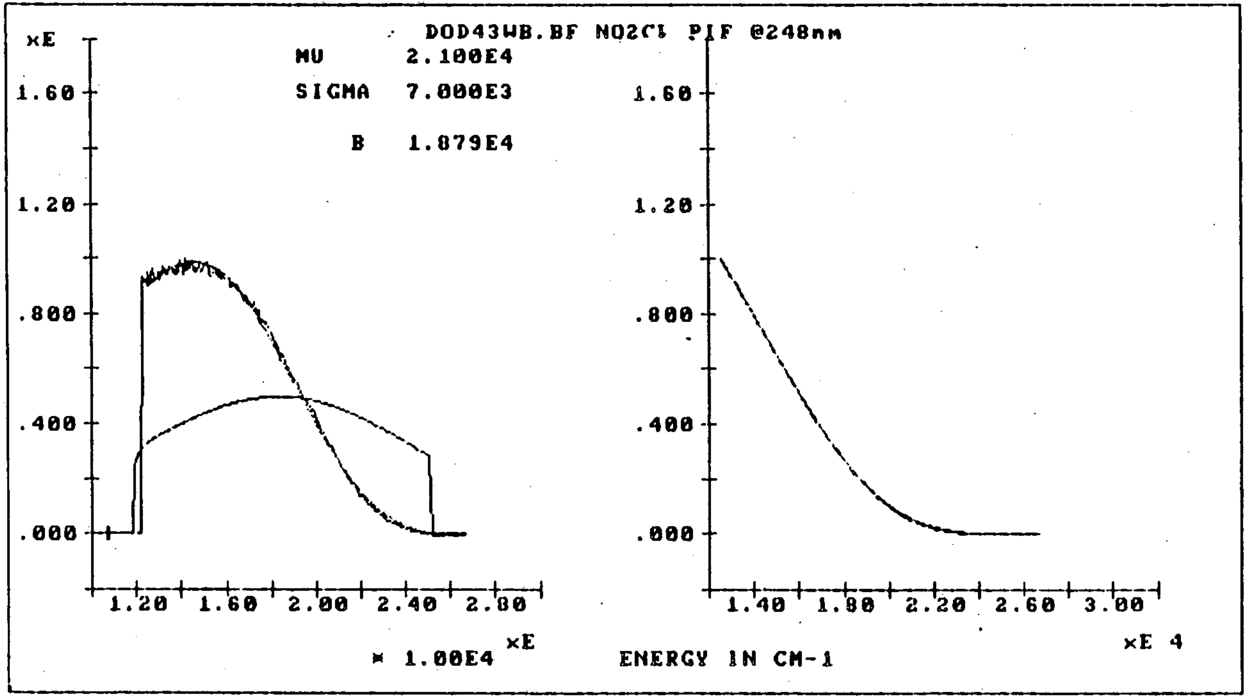
DOD43WB.BF NO2Cl PIF @248nm
MU 2.100E4
SIGMA 7.000E3
B 1.879E4
xE
1.60
1.20
.800
.400
.000
1.20
1.60
2.00
2.40
2.80
* 1.00E4
xE
1.60
1.20
.800
.400
.000
1.40
1.80
2.20
2.60
3.00
xE 4
ENERGY IN CM-1

Figure 3.14(a)

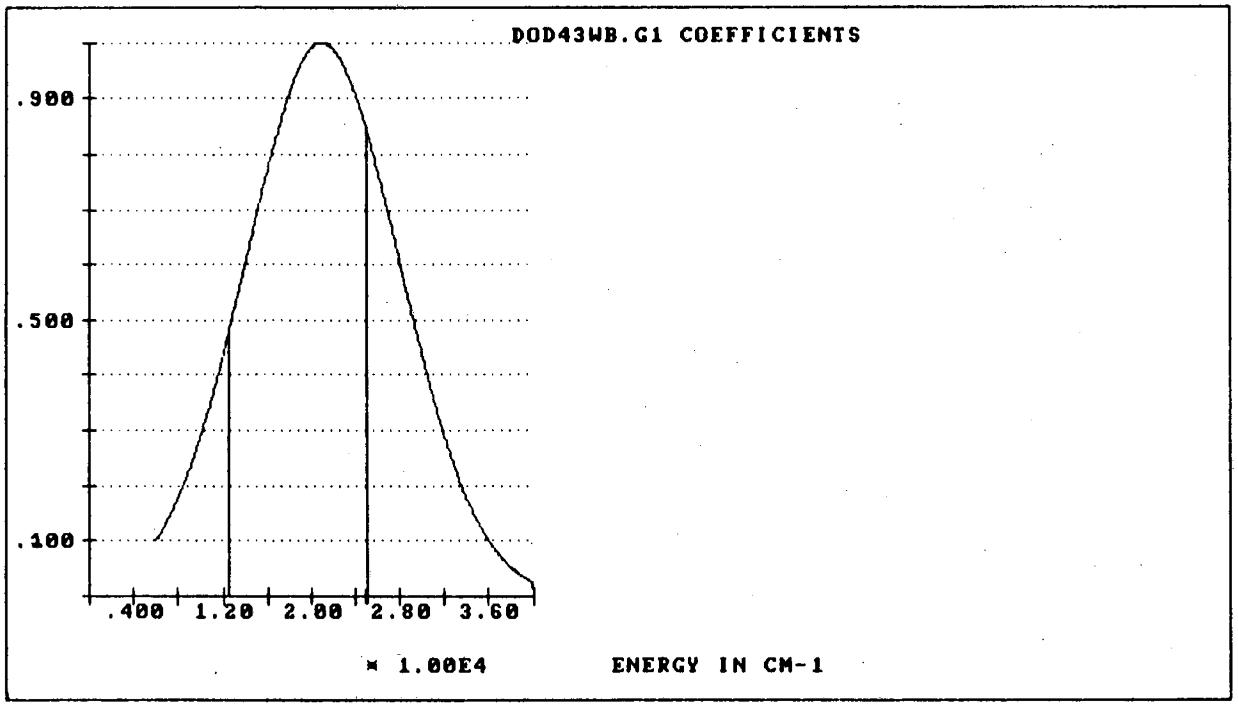
DOD43WB.G1 COEFFICIENTS
.900
.500
.100
.400
1.20
2.00
2.80
3.60
* 1.00E4
ENERGY IN CM-1

Figure 3.14(b)

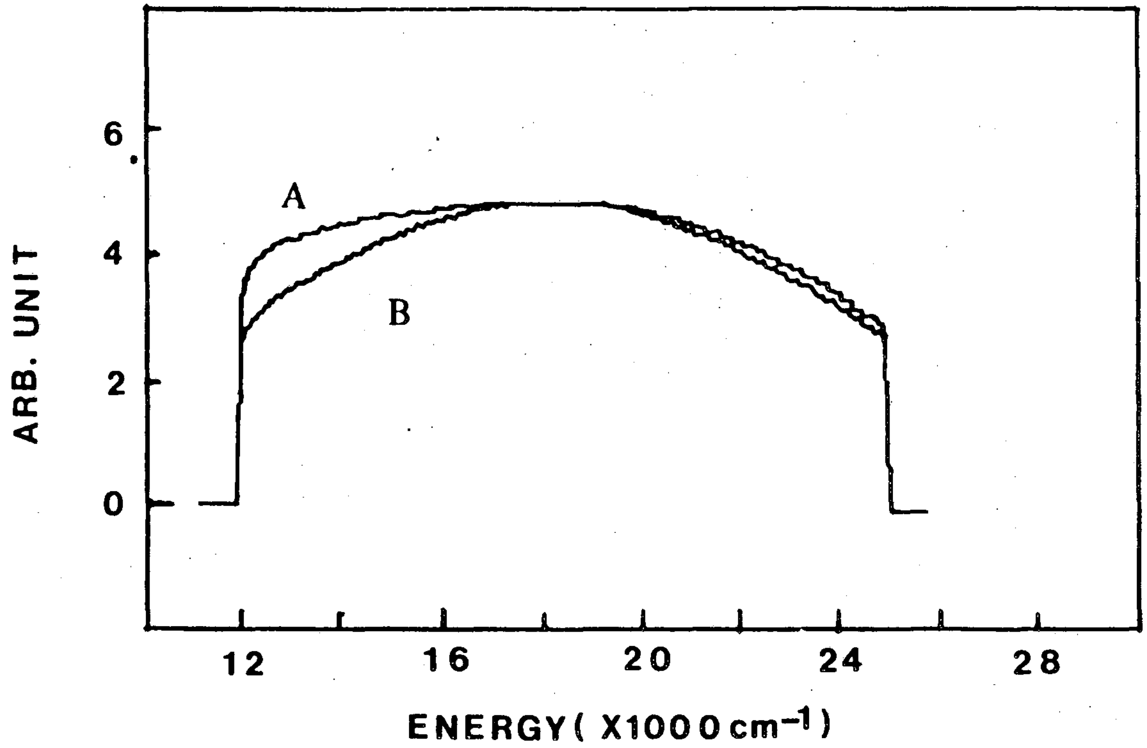

Figure 3.15

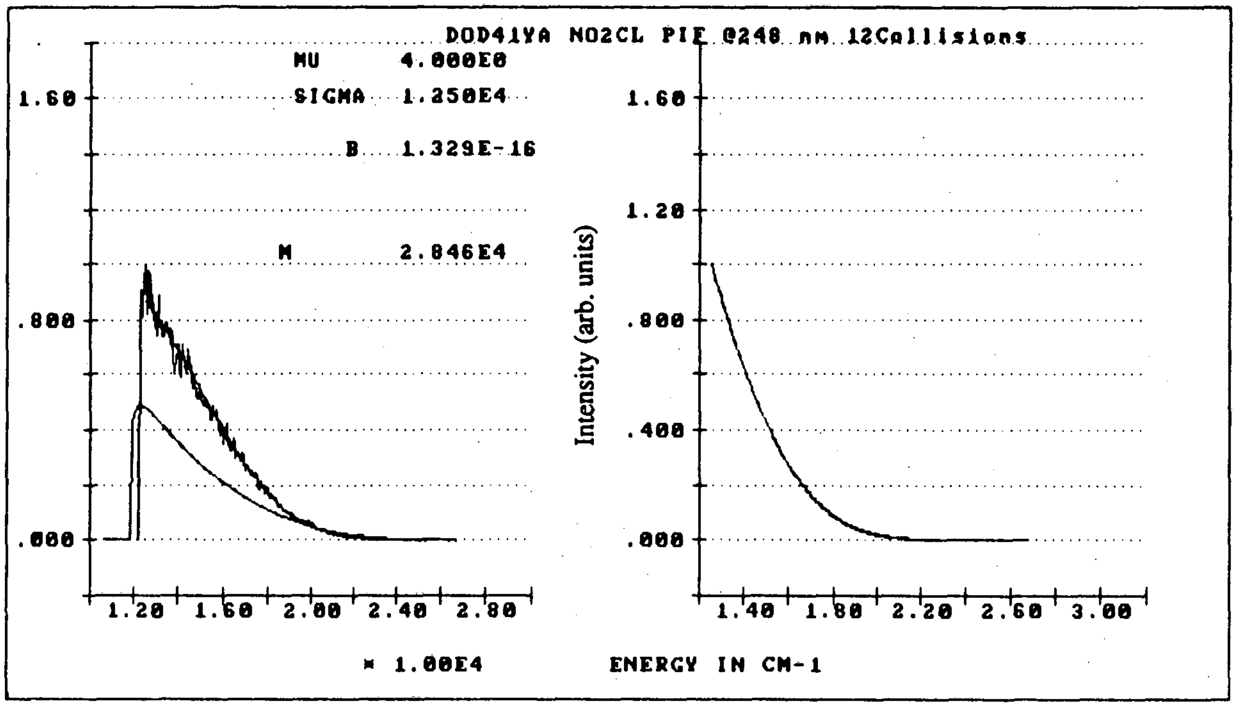
DOD41YA NO2CL PIE @248 nm 12Collisions
MU 4.000E0
SIGMA 1.250E4
B 1.329E-16
M 2.846E4
1.60
.800
.000
1.20
1.60
2.00
2.40
2.80
Intensity (arb. units)
1.60
1.20
.800
.400
.000
1.40
1.80
2.20
2.60
3.00
* 1.00E4
ENERGY IN CM-1

Figure 3.16(a)

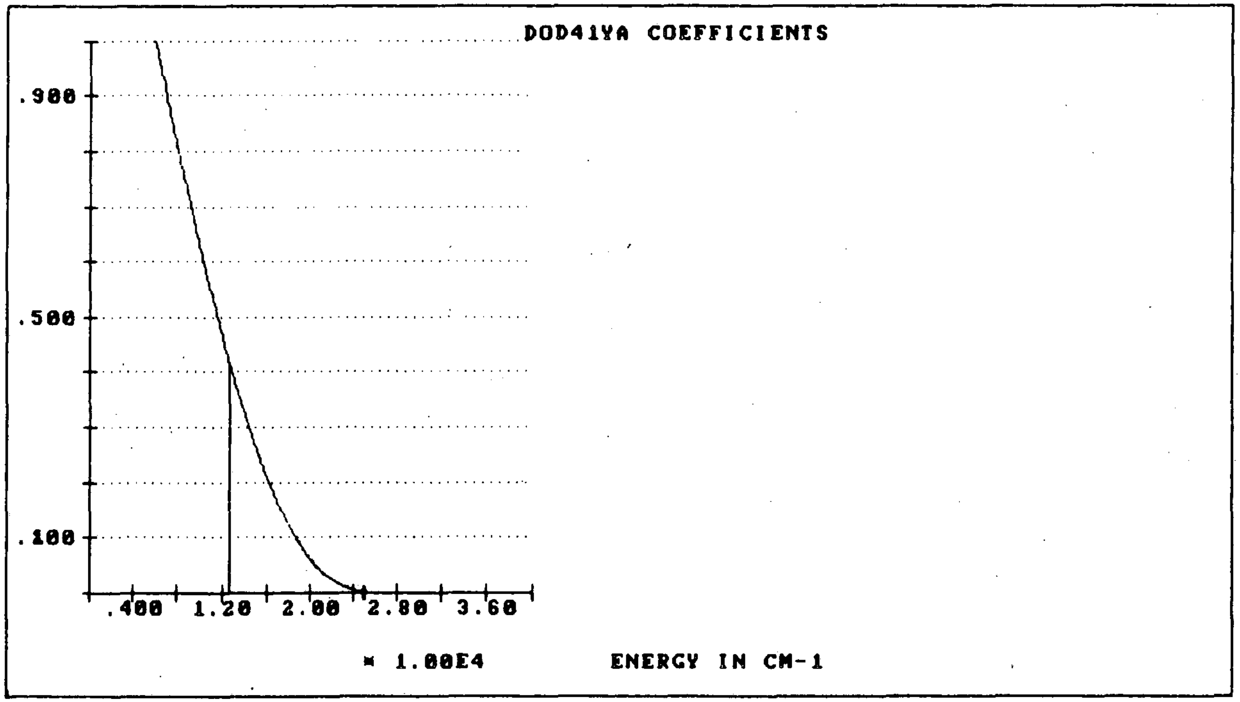
DOD41YA COEFFICIENTS
.900
.500
.100
.400
1.20
2.00
2.80
3.60
* 1.00E4
ENERGY IN CM-1

Figure 3.16(b)

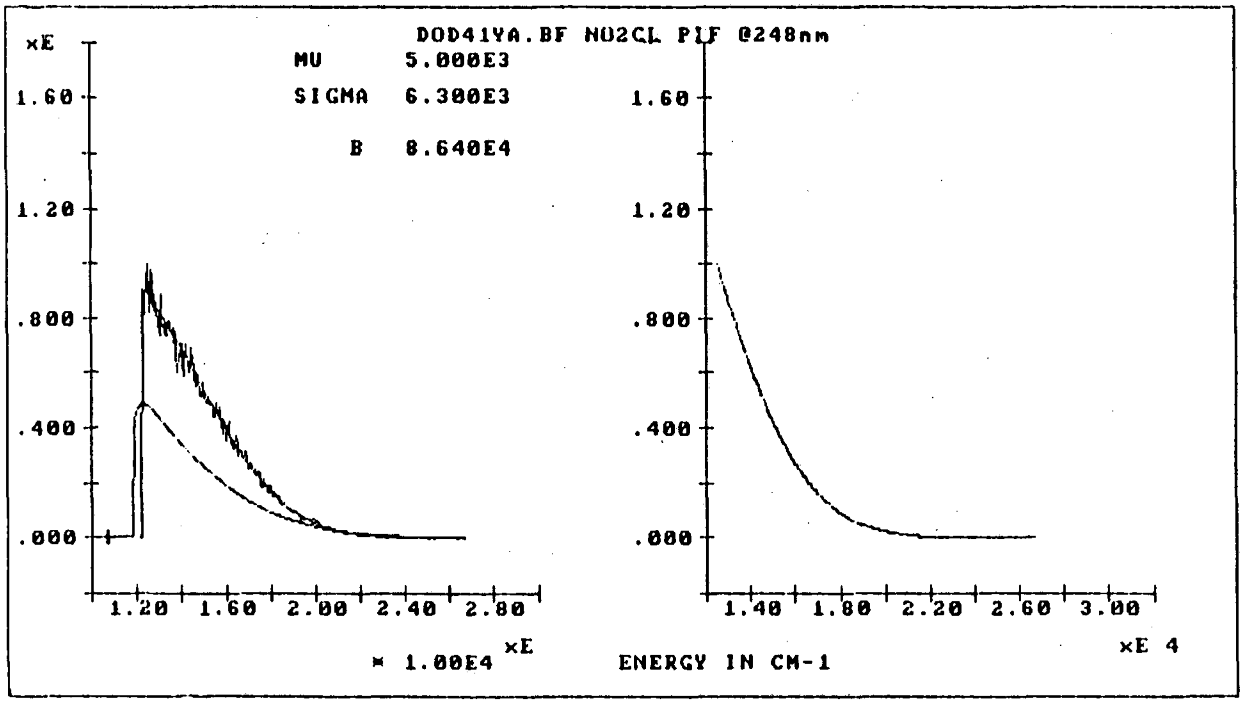
DOD41YA.BF NO2CL PIF @248nm
MU 5.000E3
SIGMA 6.300E3
B 8.640E4
xE
1.60
1.20
.800
.400
.000
1.20
1.60
2.00
2.40
2.80
* 1.00E4
xE
ENERGY IN CM-1
1.60
1.20
.800
.400
.000
1.40
1.80
2.20
2.60
3.00
xE 4

Figure 3.17(a)

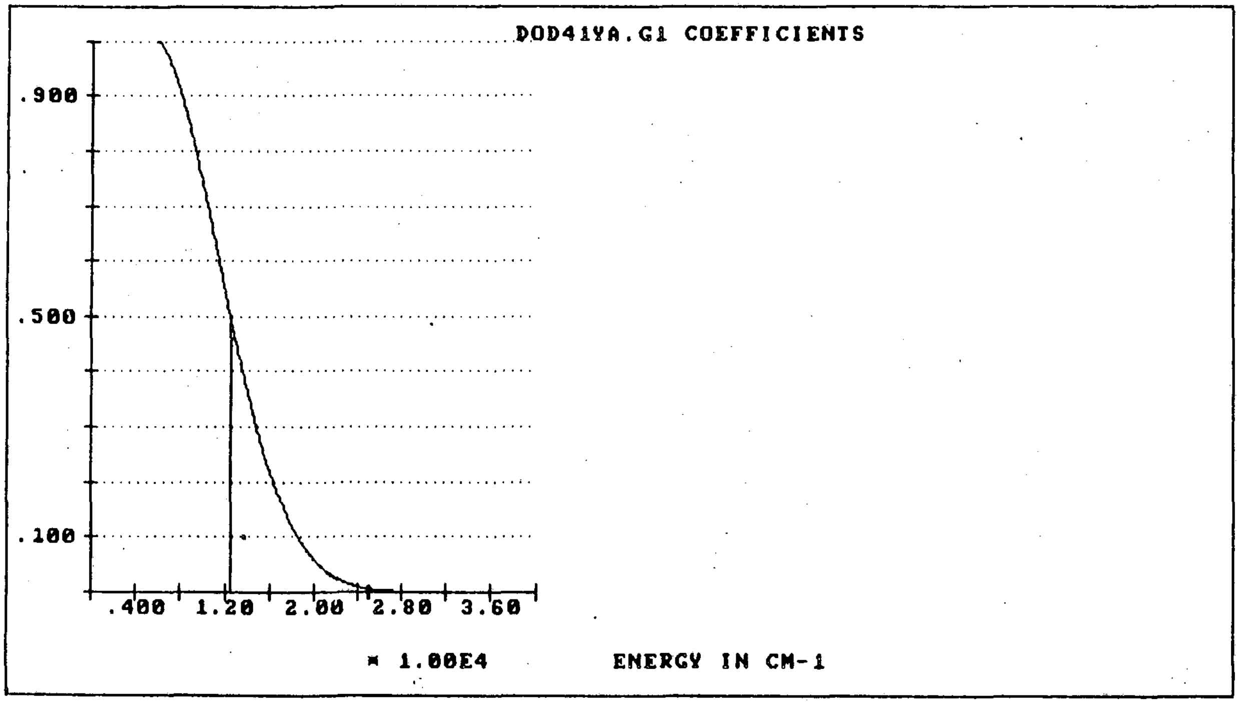
DOD41YA.G1 COEFFICIENTS
.900
.500
.100
.400
1.20
2.00
2.80
3.60
* 1.00E4
ENERGY IN CM-1

Figure 3.17(b)

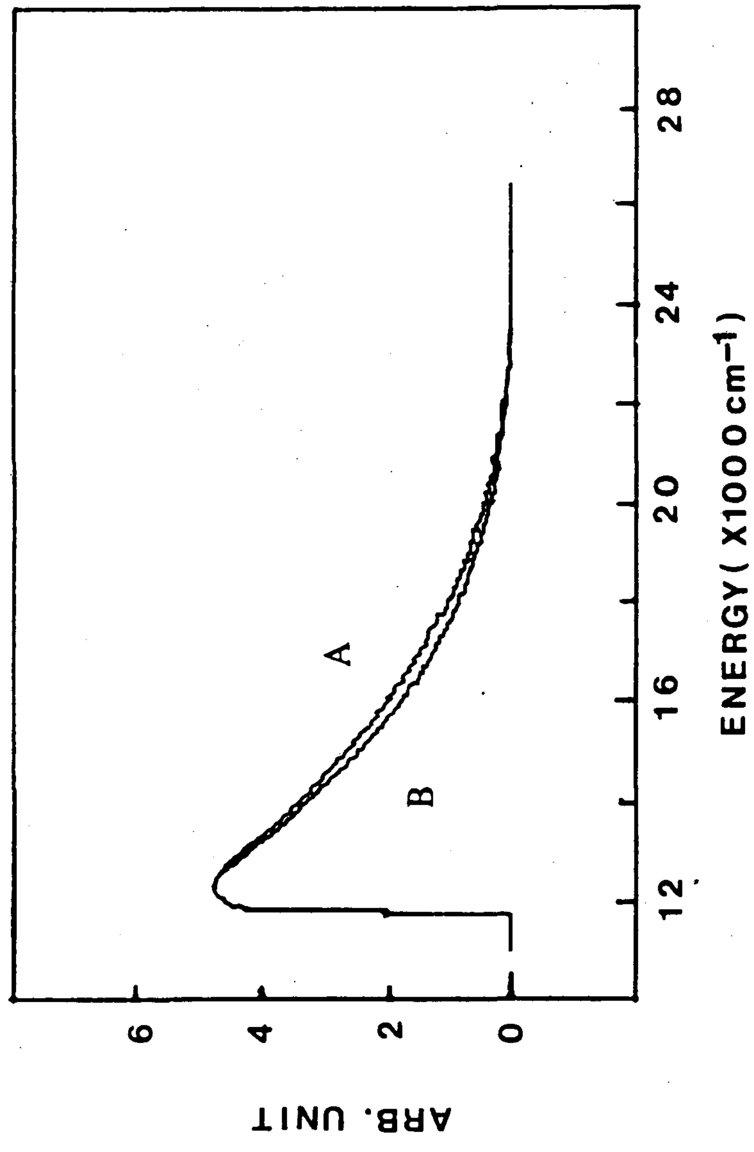

Figure 3.18

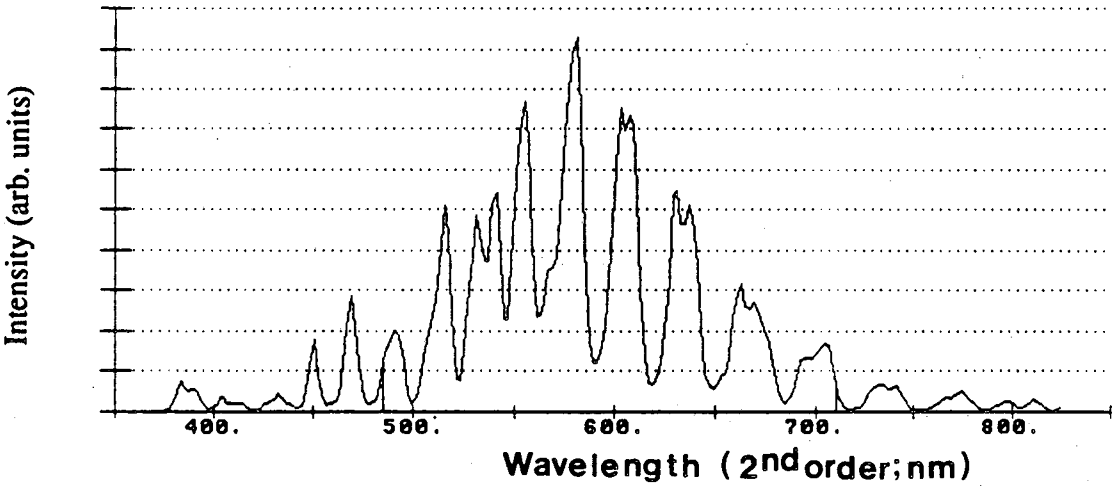
Intensity (arb. units)
400.
500.
600.
700.
800.
Wavelength (2nd order; nm)

Figure 3.19

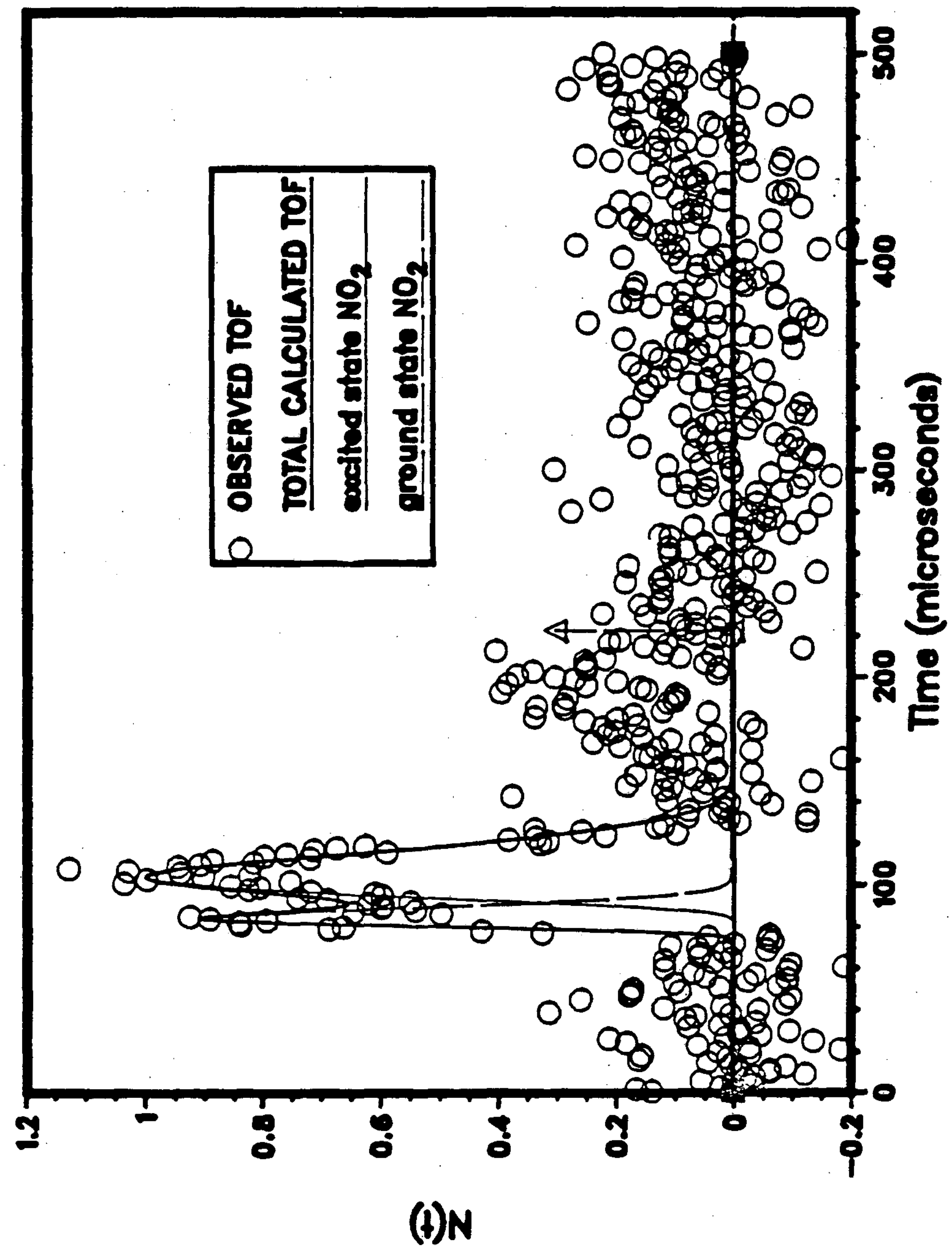
N(t)
1.2
1
0.8
0.6
0.4
0.2
0
−0.2
0
100
200
300
400
500
Time (microseconds)
OBSERVED TOF
TOTAL CALCULATED TOF
excited state NO_2
ground state NO_2

Figure 3.20(a)

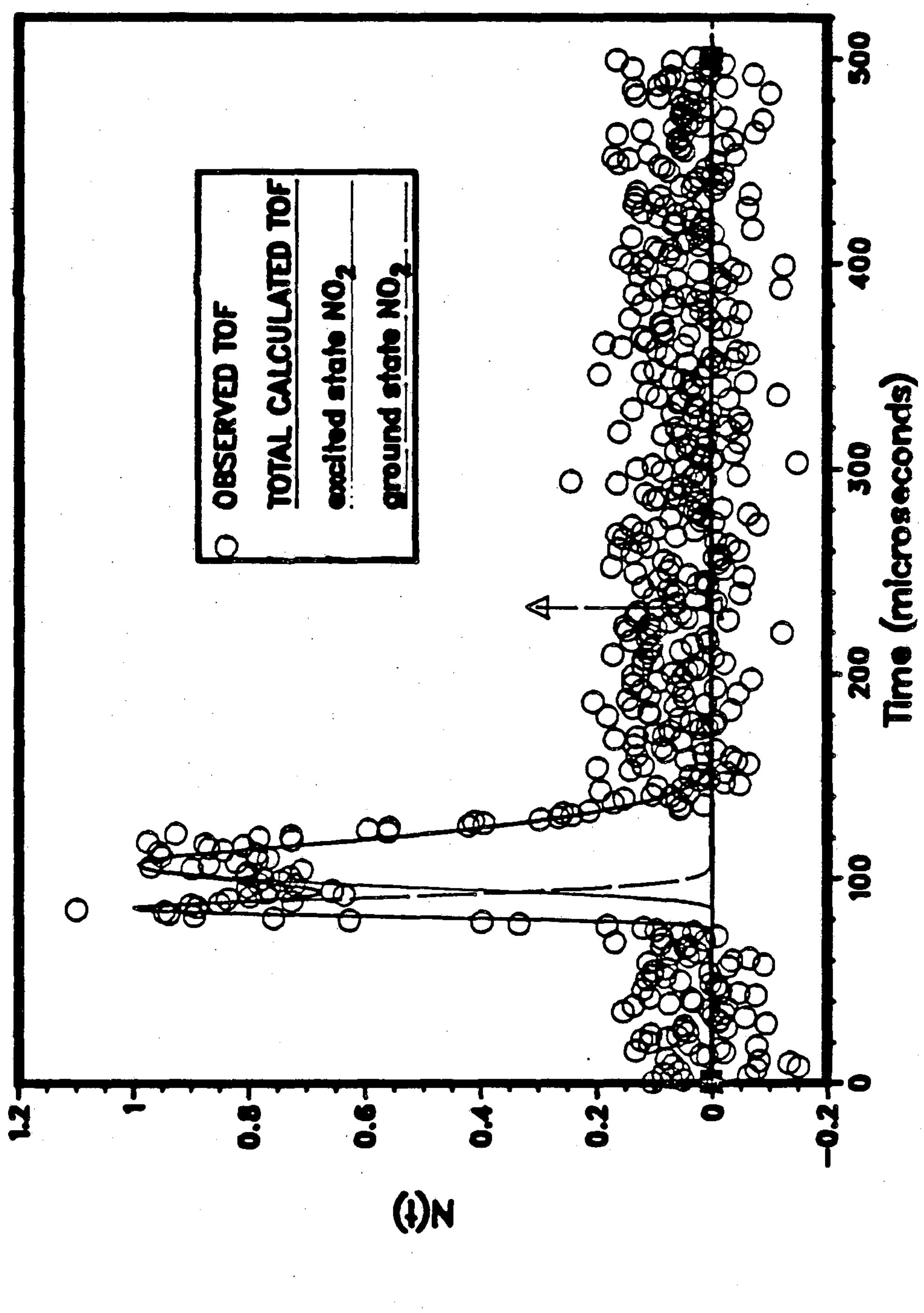
OBSERVED TOF
TOTAL CALCULATED TOF
excited state NO_2
ground state NO_2
N(t)
1.2
1
0.8
0.6
0.4
0.2
0
-0.2
0
100
200
300
400
500
Time (microseconds)

Figure 3.20(b)

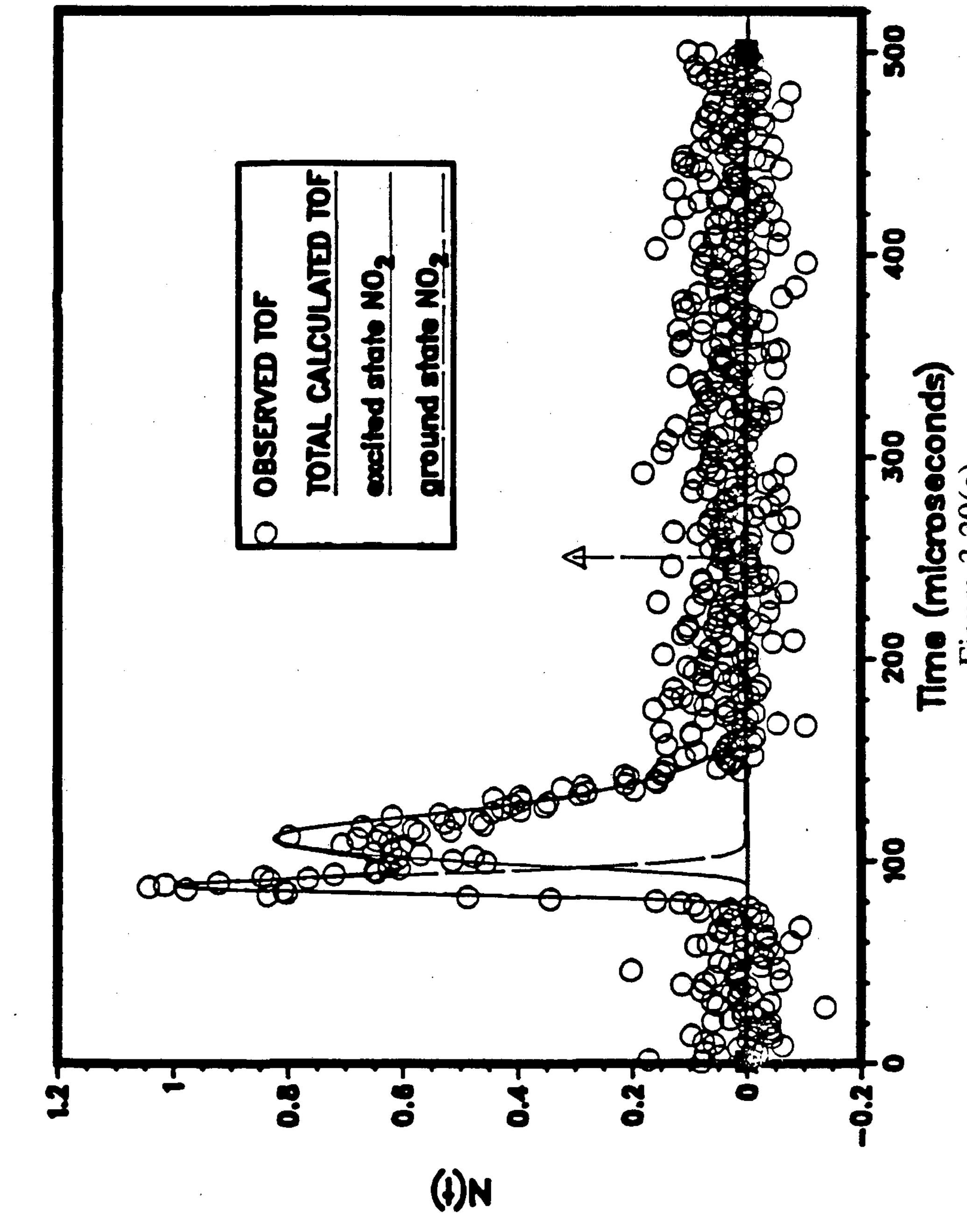
OBSERVED TOF
TOTAL CALCULATED TOF
excited state NO_2
ground state NO_2
N(t)
1.2
1
0.8
0.6
0.4
0.2
0
-0.2
0
100
200
300
400
500
Time (microseconds)

Figure 3.20(c)

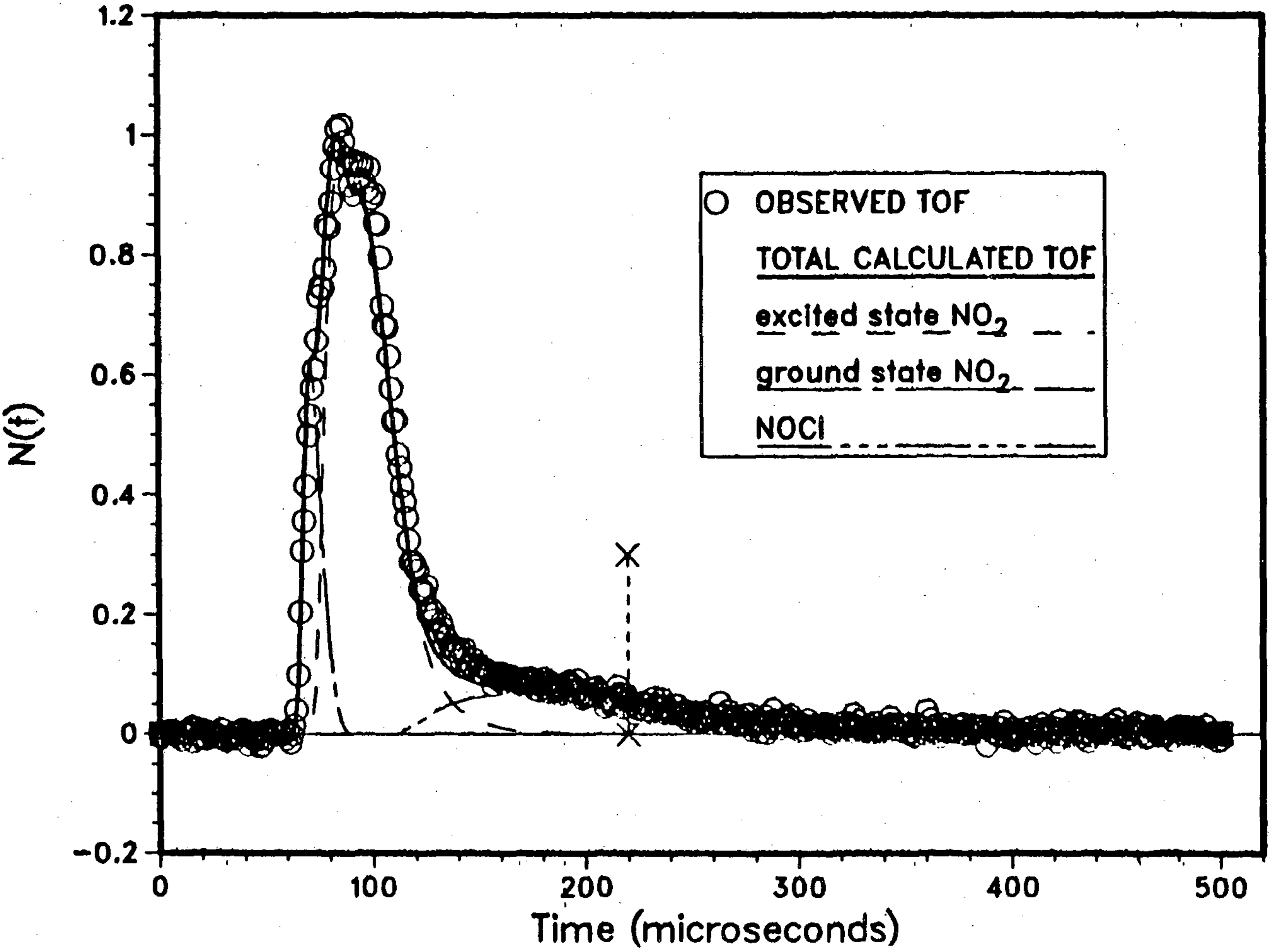
1.2
1
0.8
0.6
0.4
0.2
0
−0.2
N(t)
0
100
200
300
400
500
Time (microseconds)
OBSERVED TOF
TOTAL CALCULATED TOF
excited state NO_2
ground state NO_2
NOCl

Figure 3.21(a)

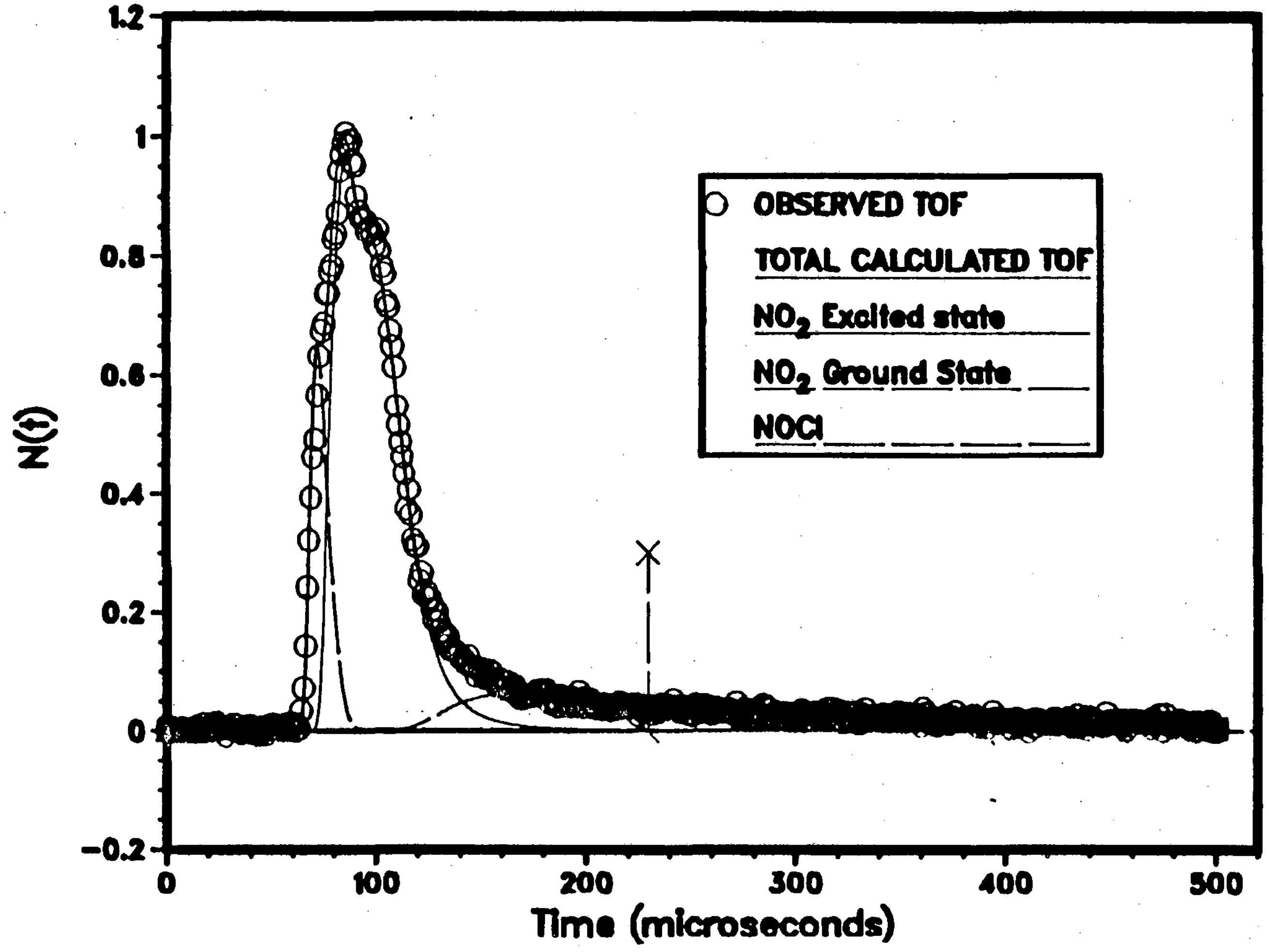
OBSERVED TOF
TOTAL CALCULATED TOF
NO_2 Excited state
NO_2 Ground State
NOCl
N(t)
1.2
1
0.8
0.6
0.4
0.2
0
−0.2
0
100
200
300
400
500
Time (microseconds)

Figure 3.21(b)

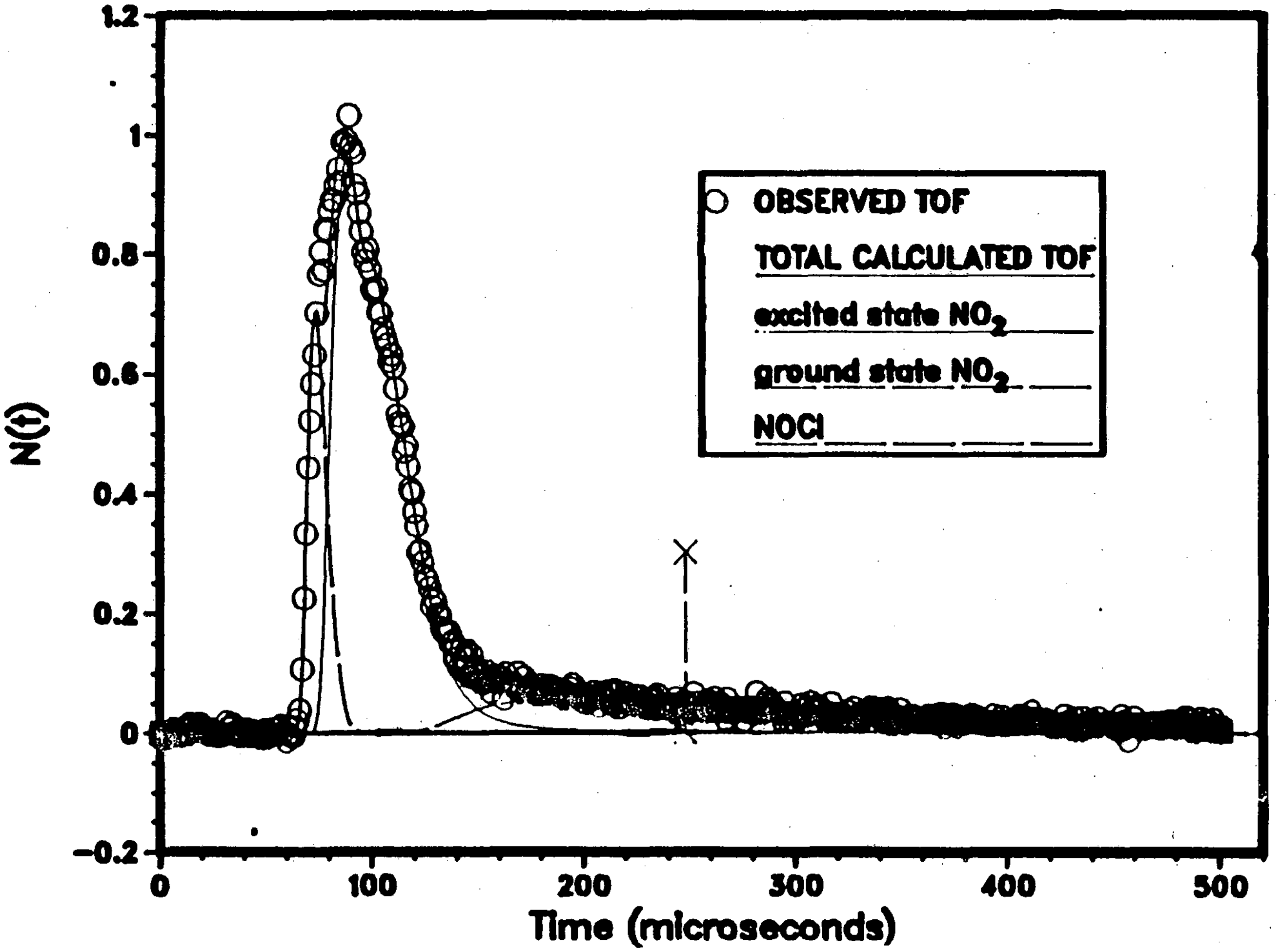
OBSERVED TOF
TOTAL CALCULATED TOF
excited state NO_2
ground state NO_2
NOCl
N(t)
1.2
1
0.8
0.6
0.4
0.2
0
−0.2
0
100
200
300
400
500
Time (microseconds)

Figure 3.21(c)

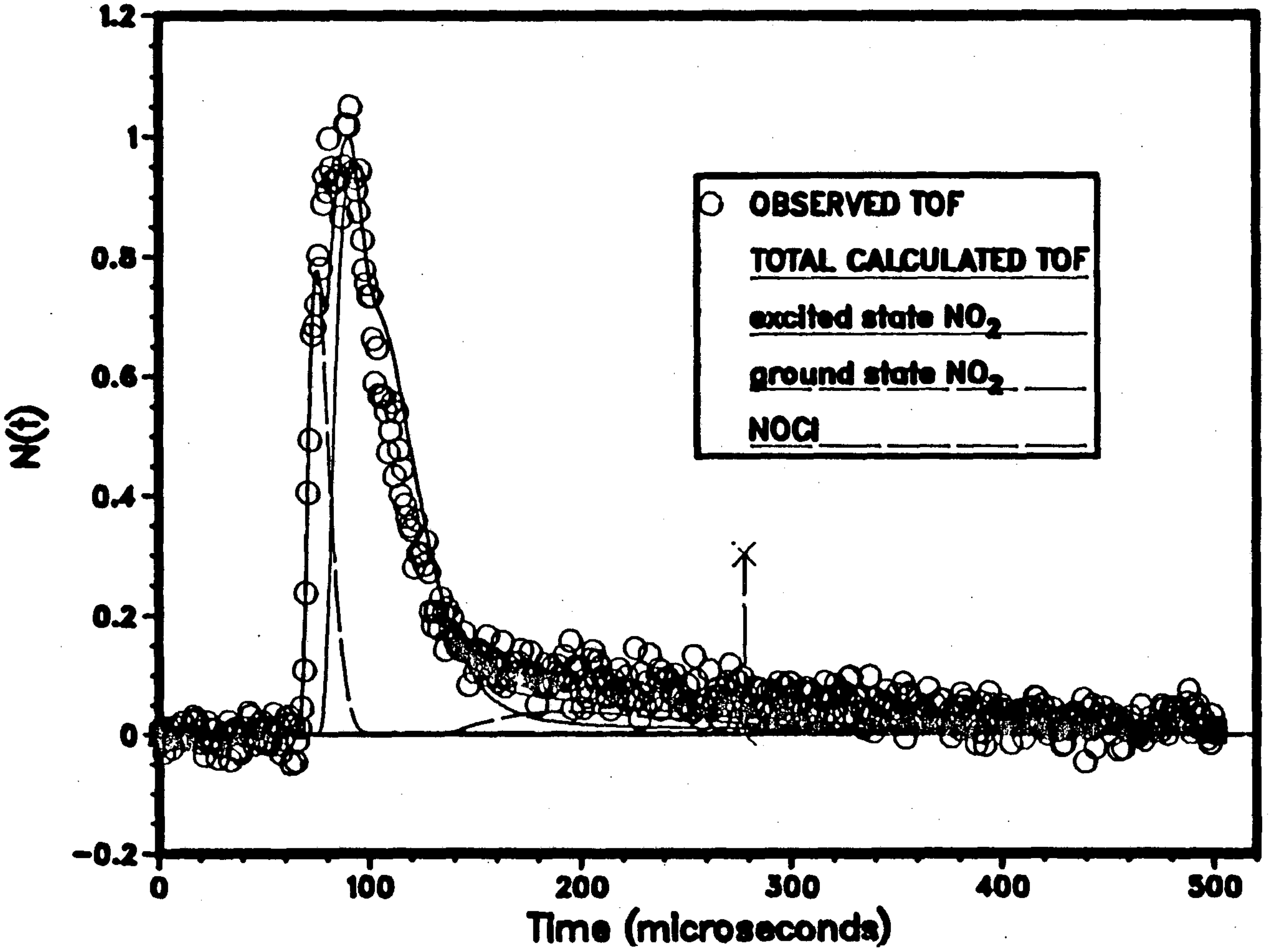
OBSERVED TOF
TOTAL CALCULATED TOF
excited state NO_2
ground state NO_2
NOCl
N(t)
1.2
1
0.8
0.6
0.4
0.2
0
−0.2
0
100
200
300
400
500
Time (microseconds)

Figure 3.21(d)

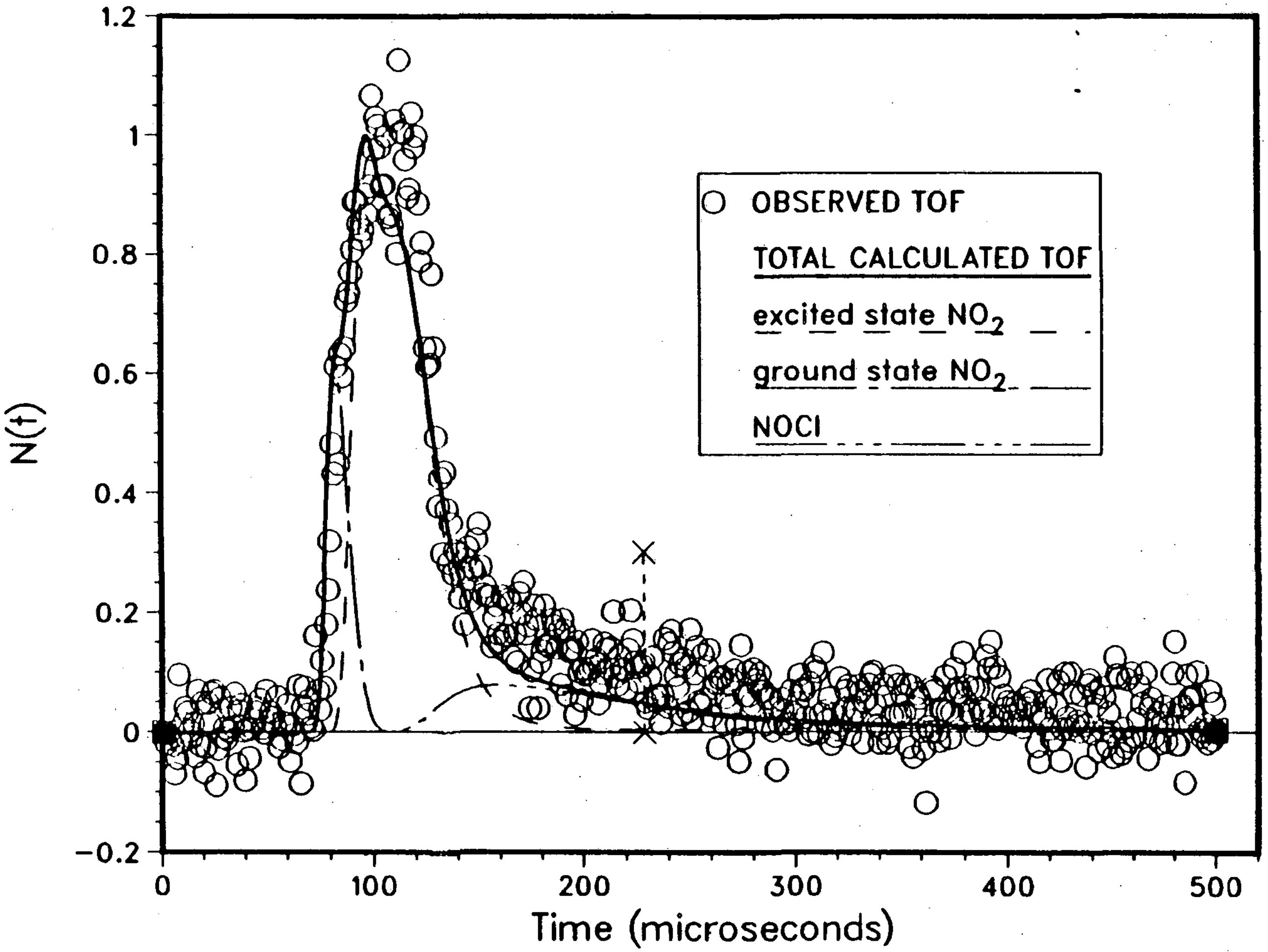
1.2
1
0.8
0.6
0.4
0.2
0
−0.2
N(t)
0
100
200
300
400
500
Time (microseconds)
○ OBSERVED TOF
TOTAL CALCULATED TOF
excited state NO_2
ground state NO_2
NOCl

Figure 3.22(a)

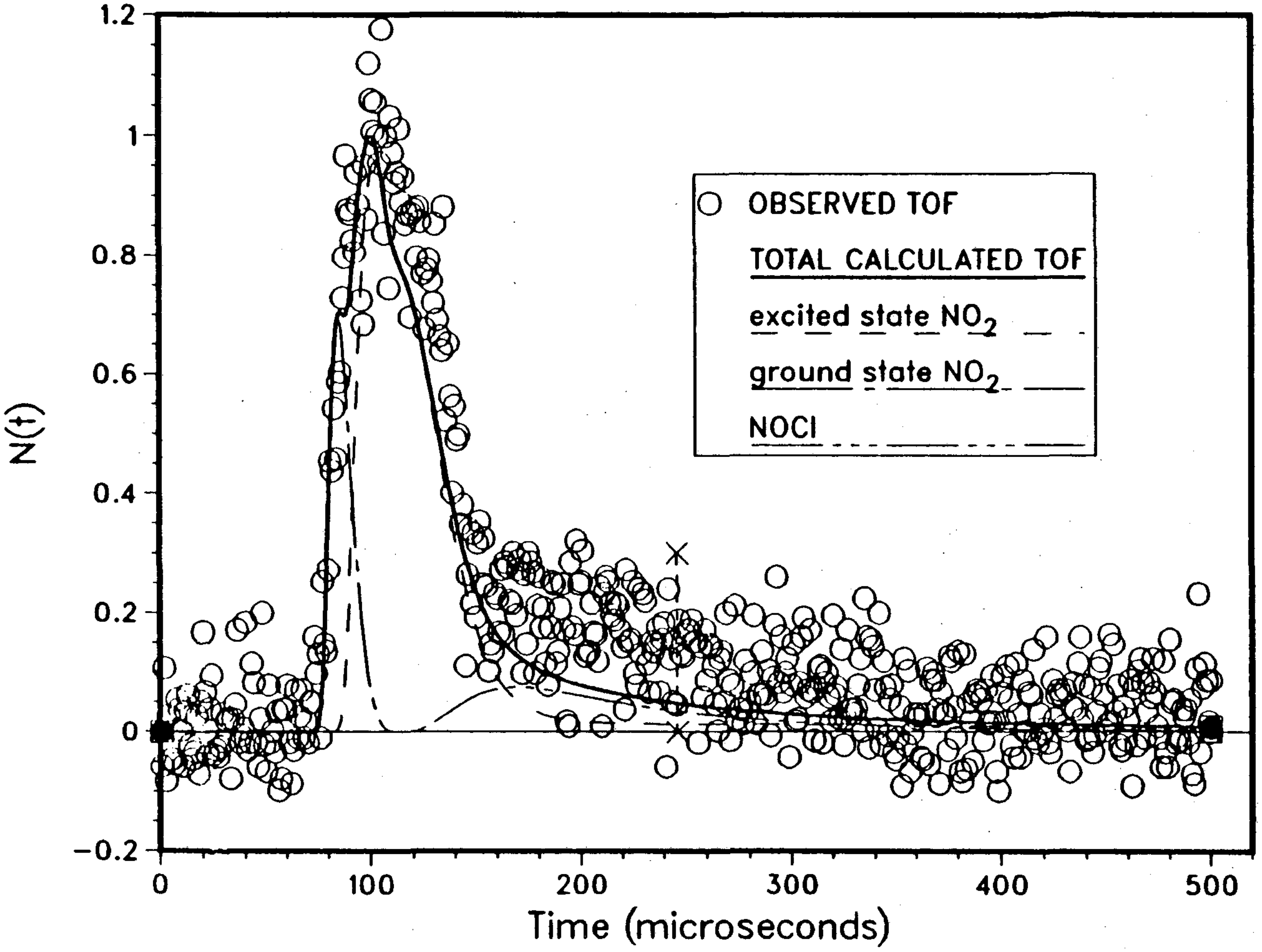
1.2
1
0.8
0.6
0.4
0.2
0
−0.2
N(t)
0
100
200
300
400
500
Time (microseconds)
OBSERVED TOF
TOTAL CALCULATED TOF
excited state NO2
ground state NO2
NOCl

Figure 3.22(b)

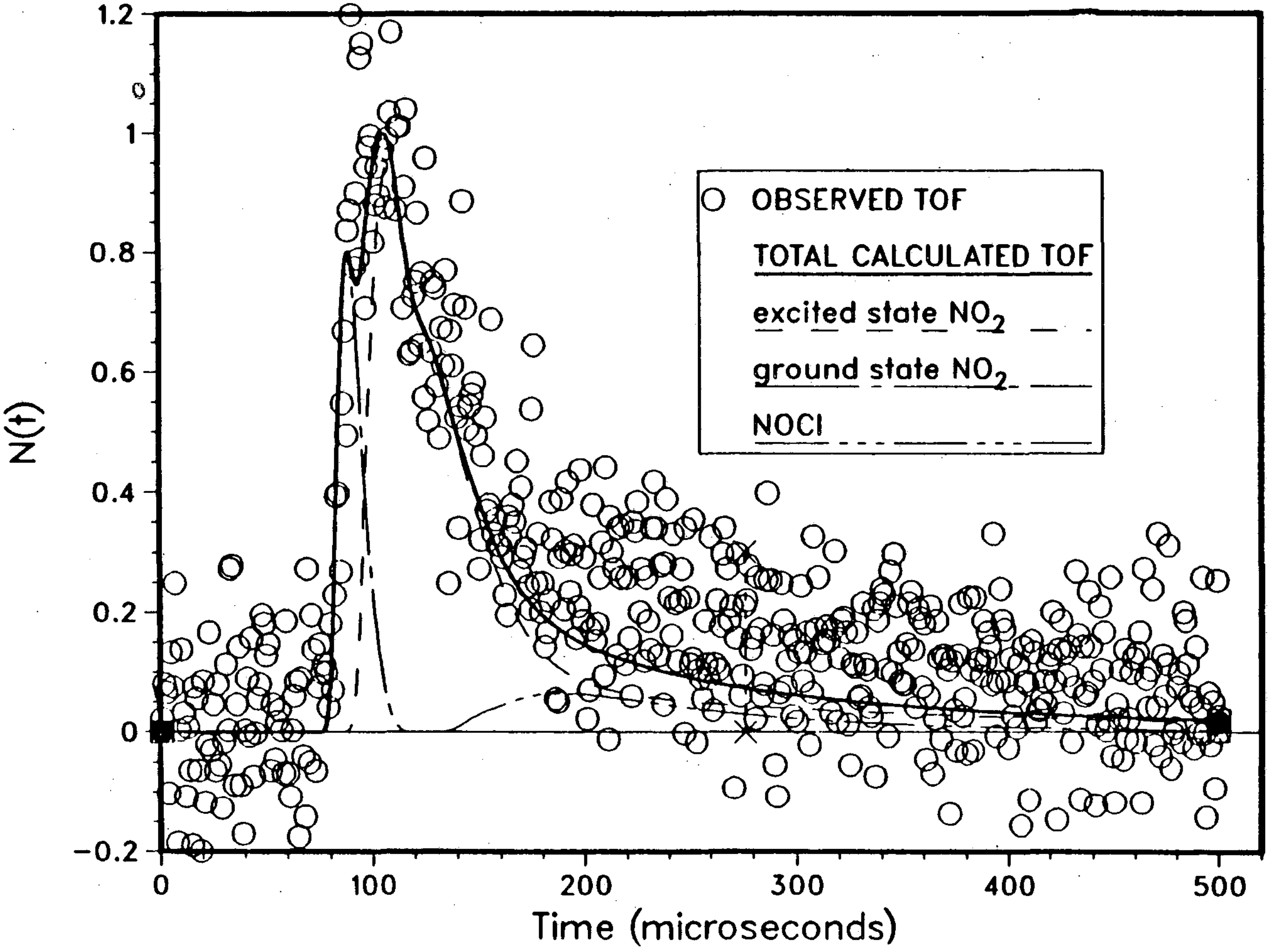
1.2
1
0.8
0.6
0.4
0.2
0
−0.2
N(t)
0
100
200
300
400
500
Time (microseconds)
OBSERVED TOF
TOTAL CALCULATED TOF
excited state NO_2
ground state NO_2
NOCl

Figure 3.22(c)

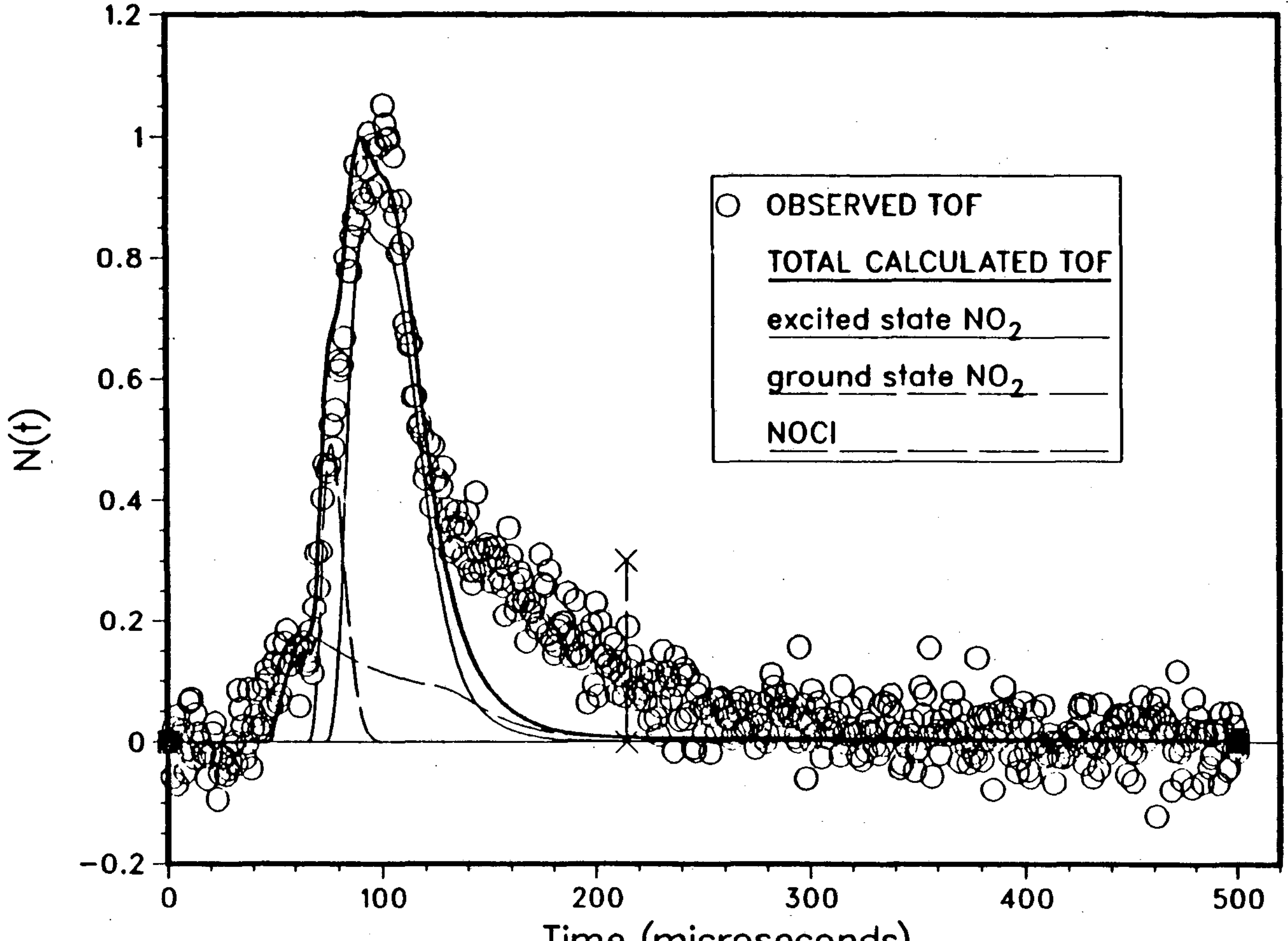
1.2
1
0.8
0.6
0.4
0.2
0
−0.2
N(t)
0
100
200
300
400
500
Time (microseconds)
OBSERVED TOF
TOTAL CALCULATED TOF
excited state NO_2
ground state NO_2
NOCl

Figure 3.23(a)

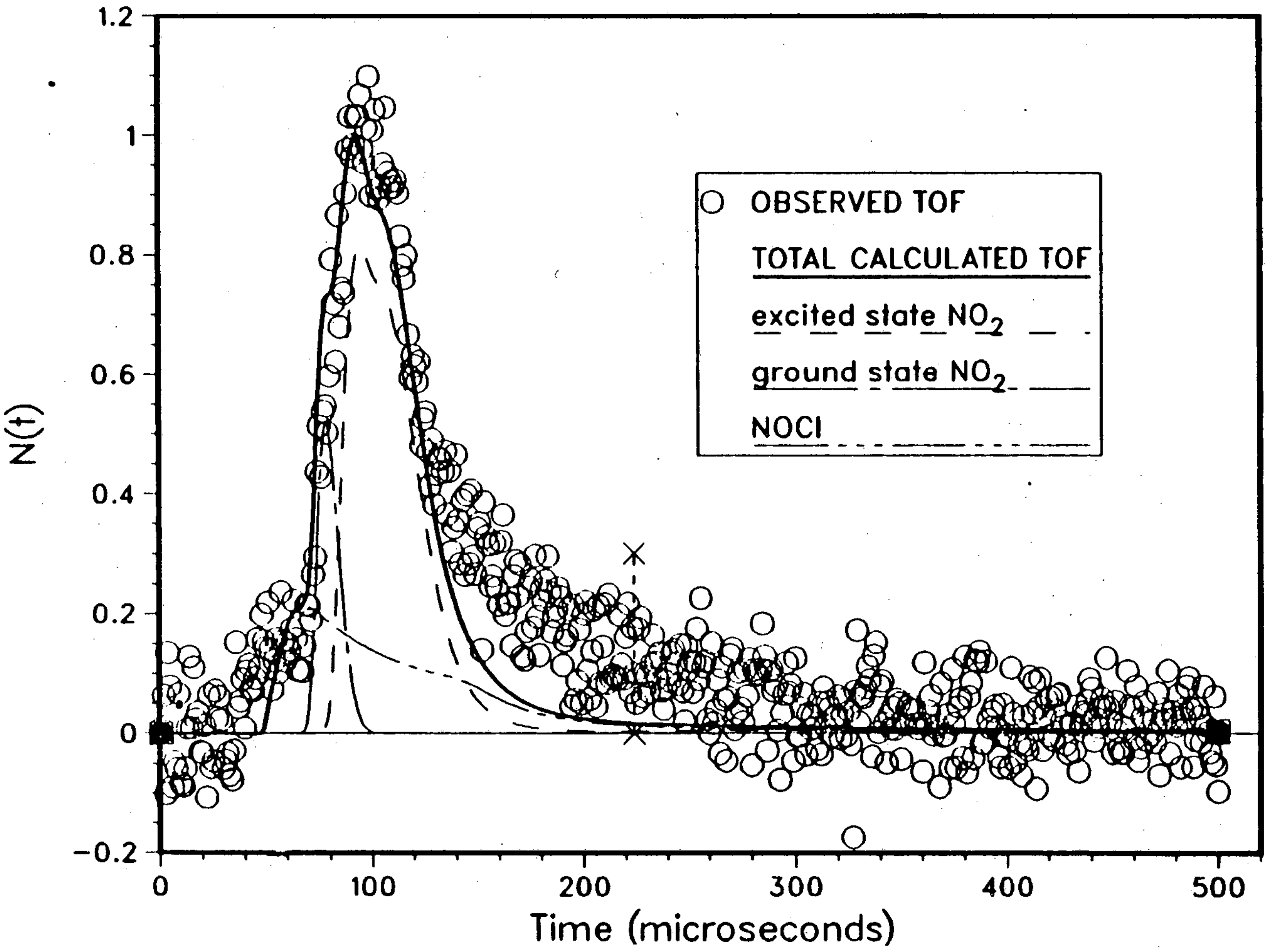
1.2
1
0.8
0.6
0.4
0.2
0
−0.2
N(t)
0
100
200
300
400
500
Time (microseconds)
OBSERVED TOF
TOTAL CALCULATED TOF
excited state NO2
ground state NO2
NOCl

Figure 3.23(b)

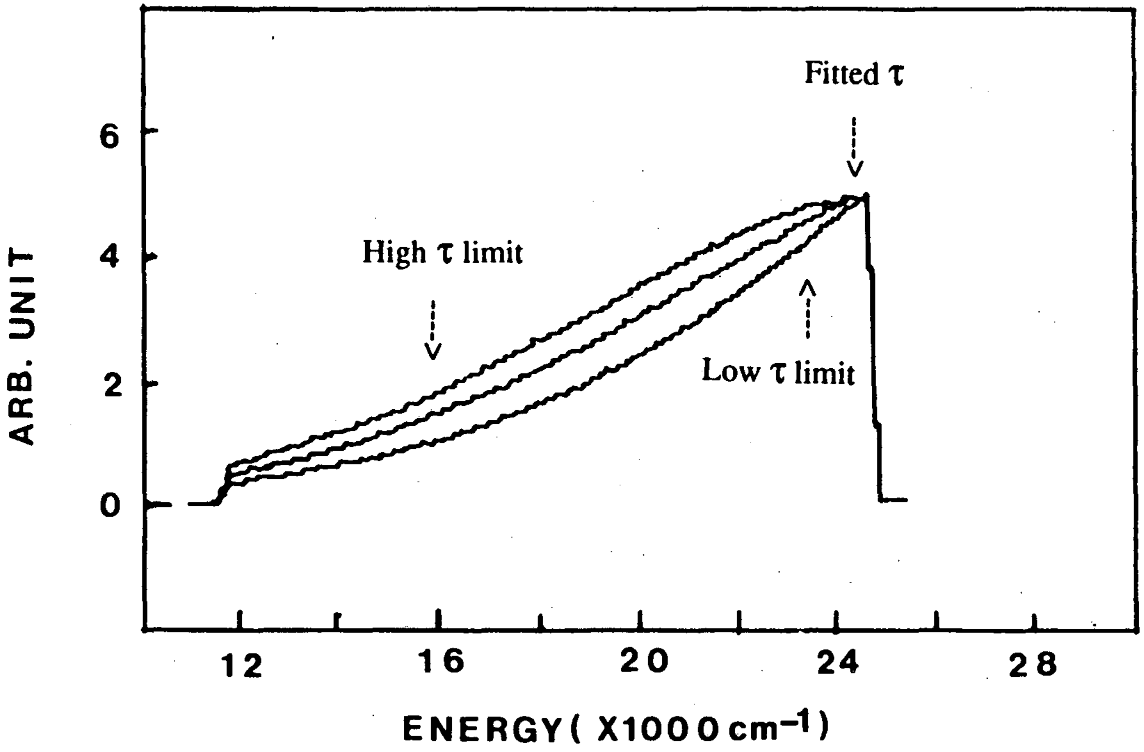
Fitted τ
High τ limit
Low τ limit
ARB. UNIT
6
4
2
0
12
16
20
24
28
ENERGY(X1000 cm-1)

Figure 3.24

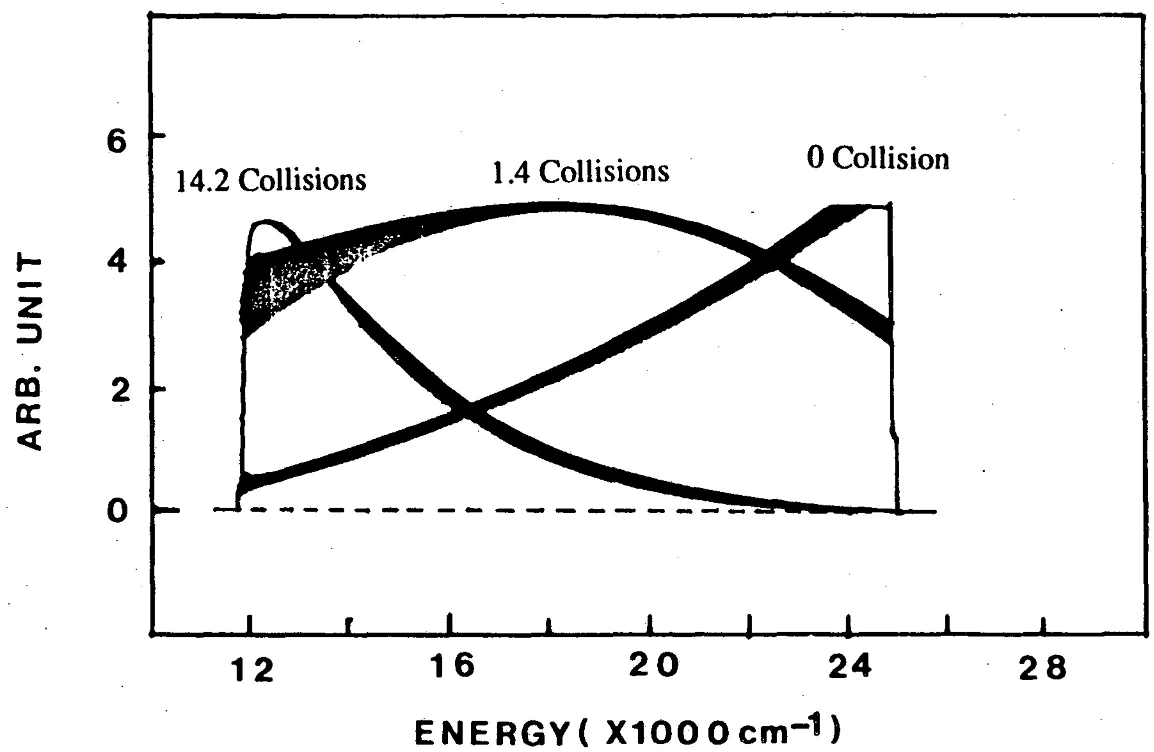

14.2 Collisions
1.4 Collisions
0 Collision
ARB. UNIT
6
4
2
0
12
16
20
24
28
ENERGY(X1000 cm⁻¹)

Figure 3.25

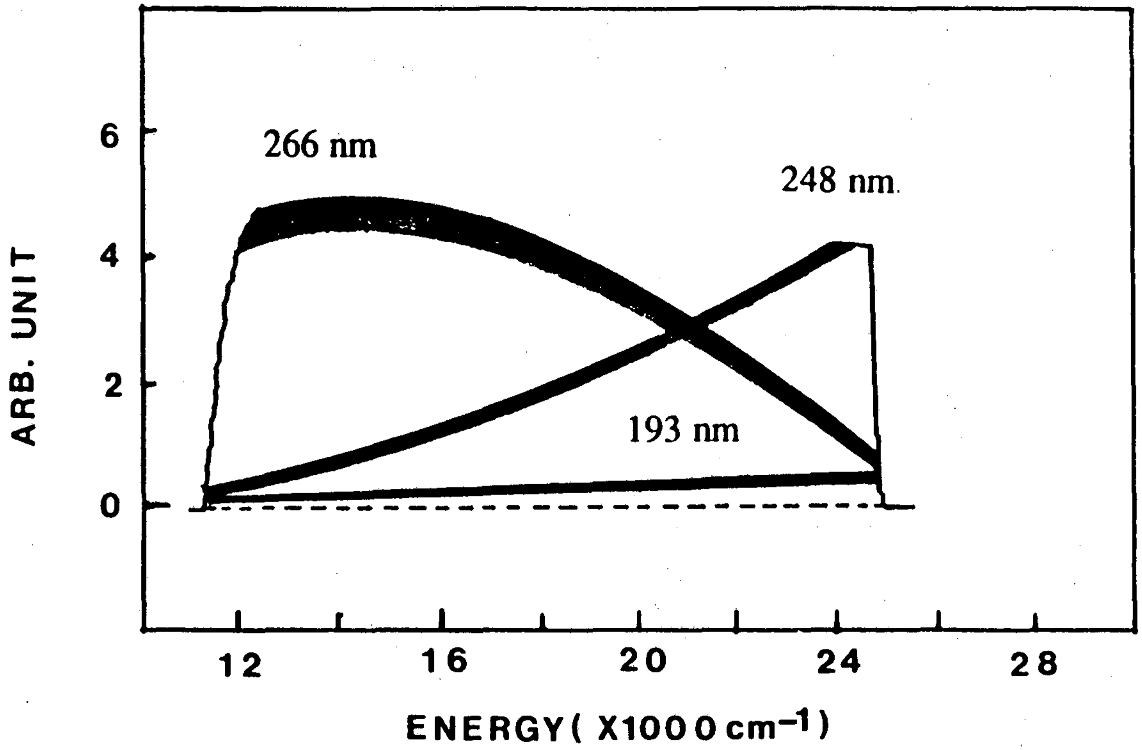
6
4
2
0
ARB. UNIT
266 nm
248 nm
193 nm
12
16
20
24
28
ENERGY(X1000 cm^{-1})

Figure 3.26

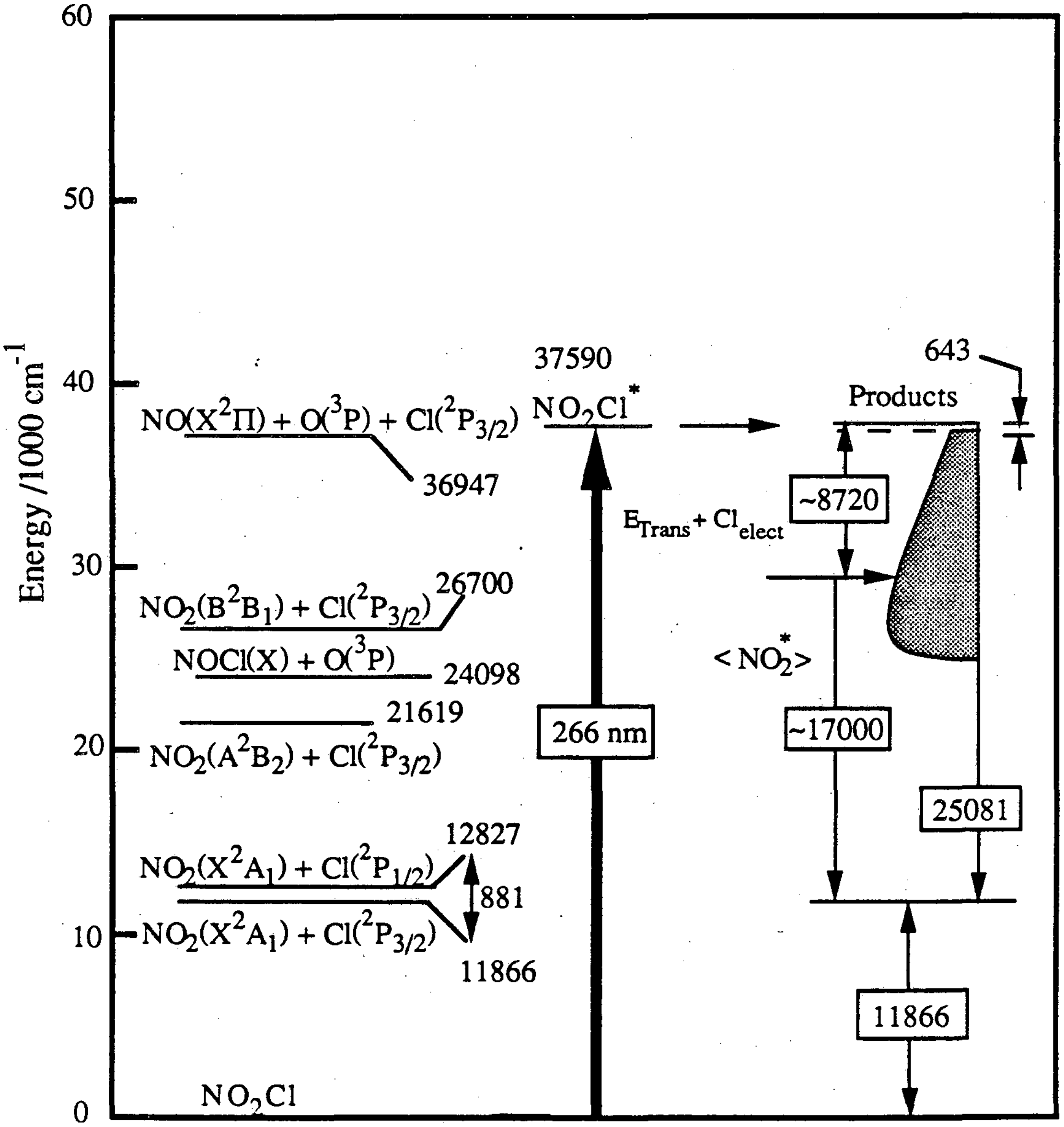
60
50
40
30
20
10
0
Energy /1000 cm^{-1}
37590
643
NO_2Cl^*
Products
$NO(X^2\Pi) + O(^3P) + Cl(^2P_{3/2})$
36947
~8720
$E_{Trans} + Cl_{elect}$
$NO_2(B^2B_1) + Cl(^2P_{3/2})$
26700
$NOCl(X) + O(^3P)$
24098
$<NO_2^*>$
21619
$NO_2(A^2B_2) + Cl(^2P_{3/2})$
266 nm
~17000
25081
12827
$NO_2(X^2A_1) + Cl(^2P_{1/2})$
881
$NO_2(X^2A_1) + Cl(^2P_{3/2})$
11866
11866
NO_2Cl

Figure 3.27

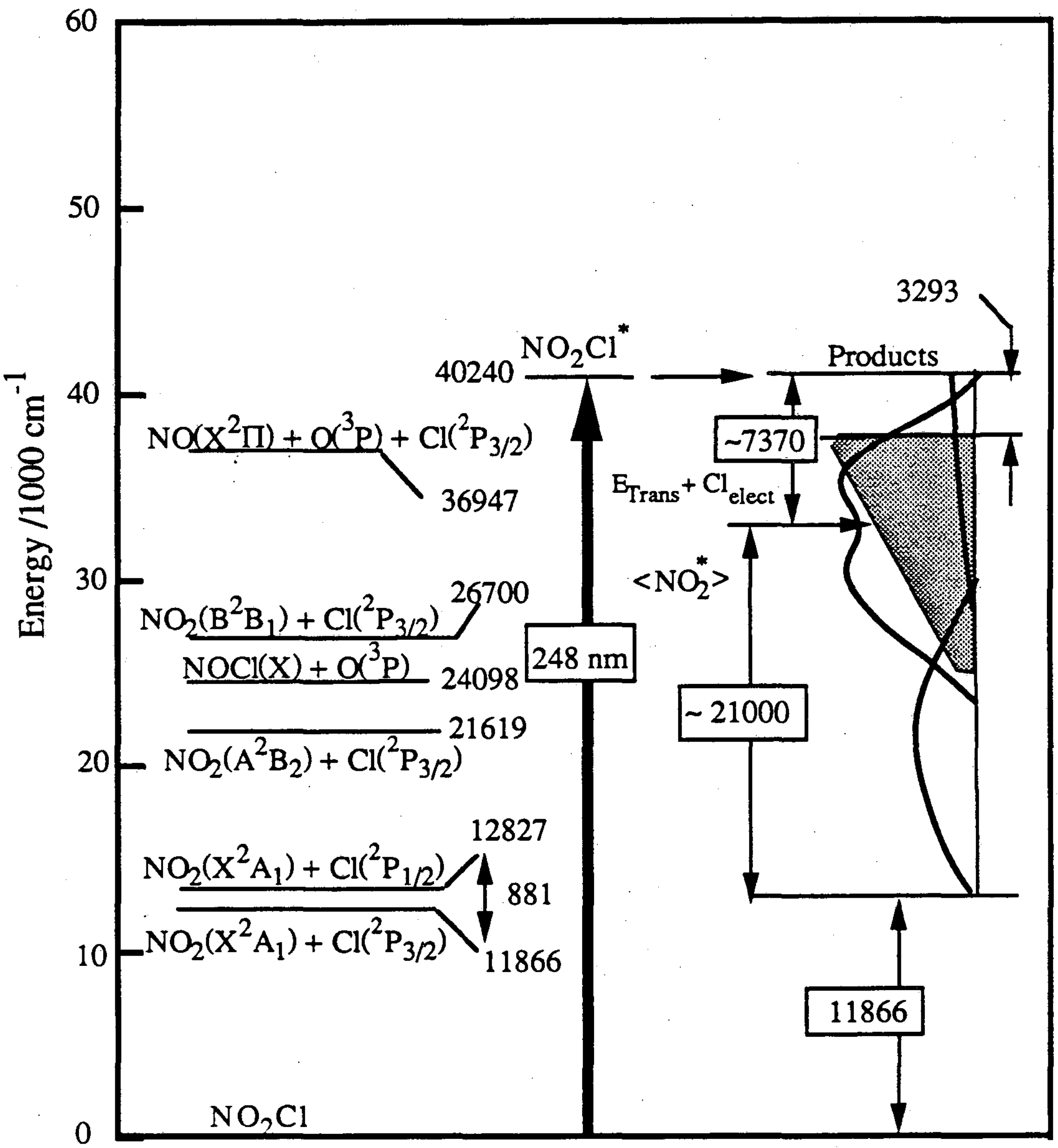
60
50
40
30
20
10
0
Energy /1000 cm^{-1}
NO$_2$Cl*
40240
NO(X$^2\Pi$) + O(^{3}P) + Cl(^{2}P$_{3/2}$)
36947
26700
NO$_2$(B^{2}B$_1$) + Cl(^{2}P$_{3/2}$)
NOCl(X) + O(^{3}P)
24098
21619
NO$_2$(A^{2}B$_2$) + Cl(^{2}P$_{3/2}$)
12827
NO$_2$(X^{2}A$_1$) + Cl(^{2}P$_{1/2}$)
881
NO$_2$(X^{2}A$_1$) + Cl(^{2}P$_{3/2}$)
11866
NO$_2$Cl
248 nm
3293
Products
~7370
E$_{Trans}$ + Cl$_{elect}$
<NO$_2^*$>
~ 21000
11866

Figure 3.28

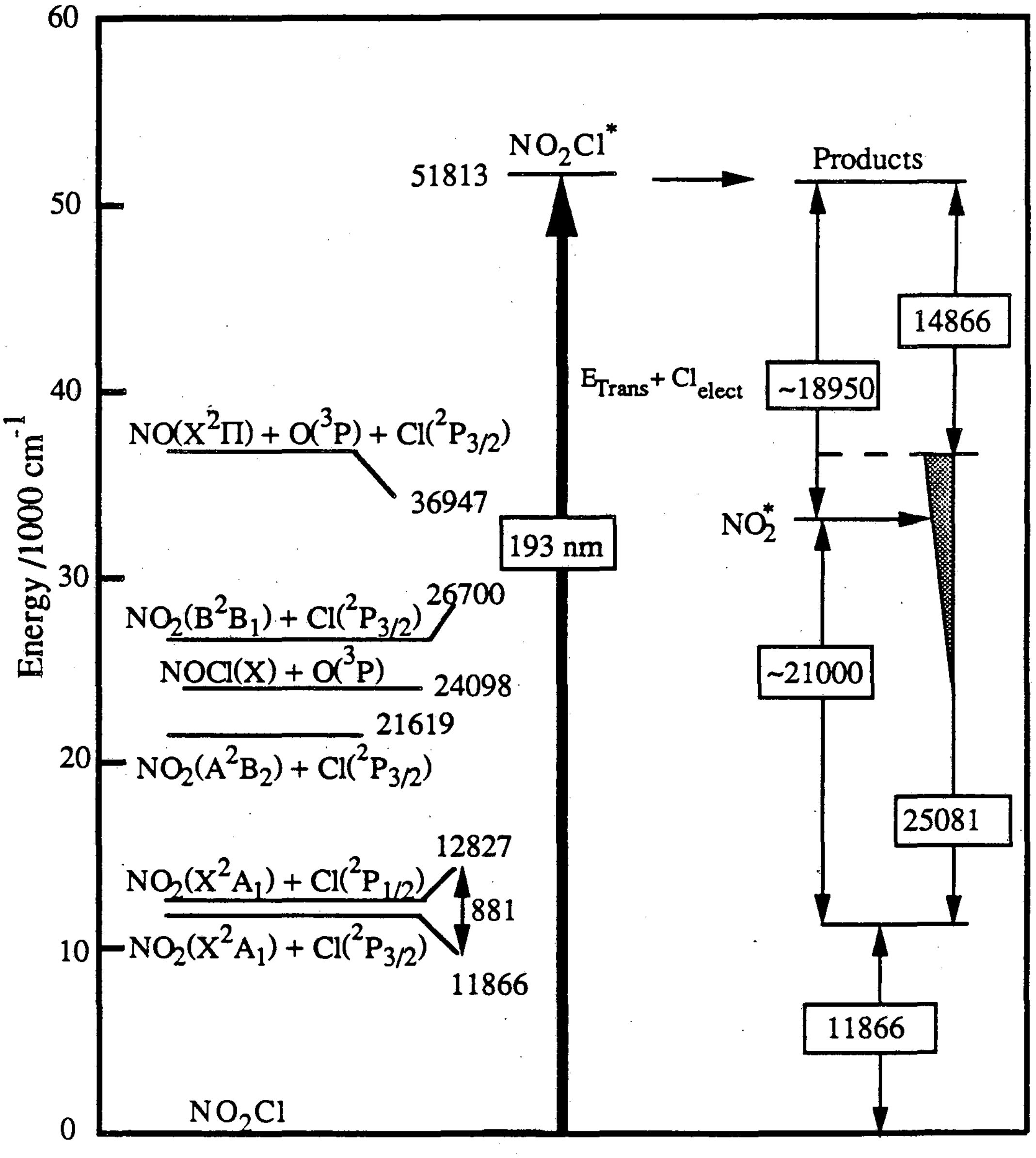
60
50
40
30
20
10
0
Energy /1000 cm^{-1}
NO_2Cl^*
51813
Products
14866
~18950
$E_{Trans} + Cl_{elect}$
$NO(X^2\Pi) + O(^3P) + Cl(^2P_{3/2})$
36947
NO_2^*
193 nm
$NO_2(B^2B_1) + Cl(^2P_{3/2})$
26700
~21000
$NOCl(X) + O(^3P)$
24098
21619
$NO_2(A^2B_2) + Cl(^2P_{3/2})$
25081
12827
$NO_2(X^2A_1) + Cl(^2P_{1/2})$
881
$NO_2(X^2A_1) + Cl(^2P_{3/2})$
11866
11866
NO_2Cl

Figure 3.29

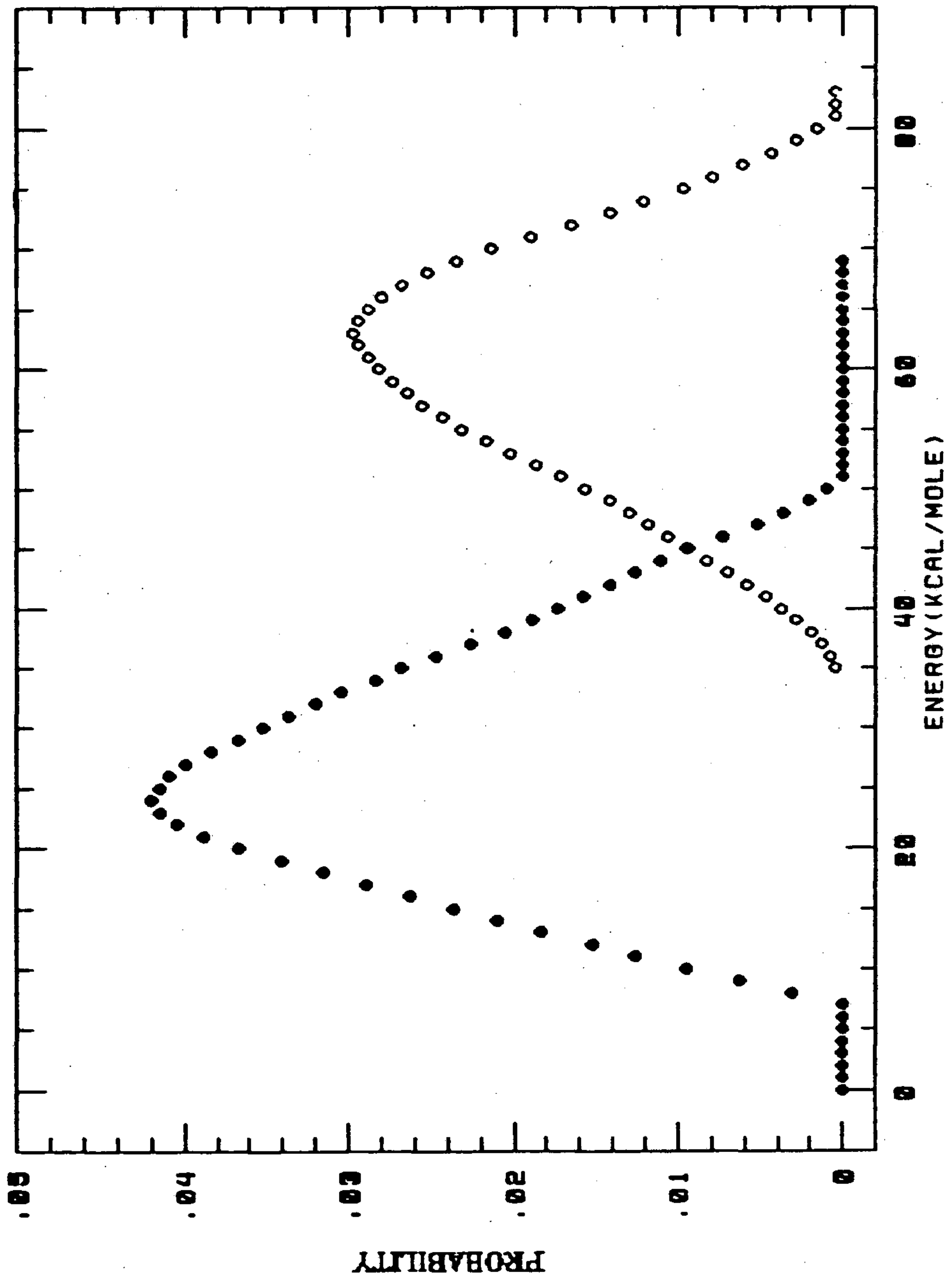

Figure 3.30

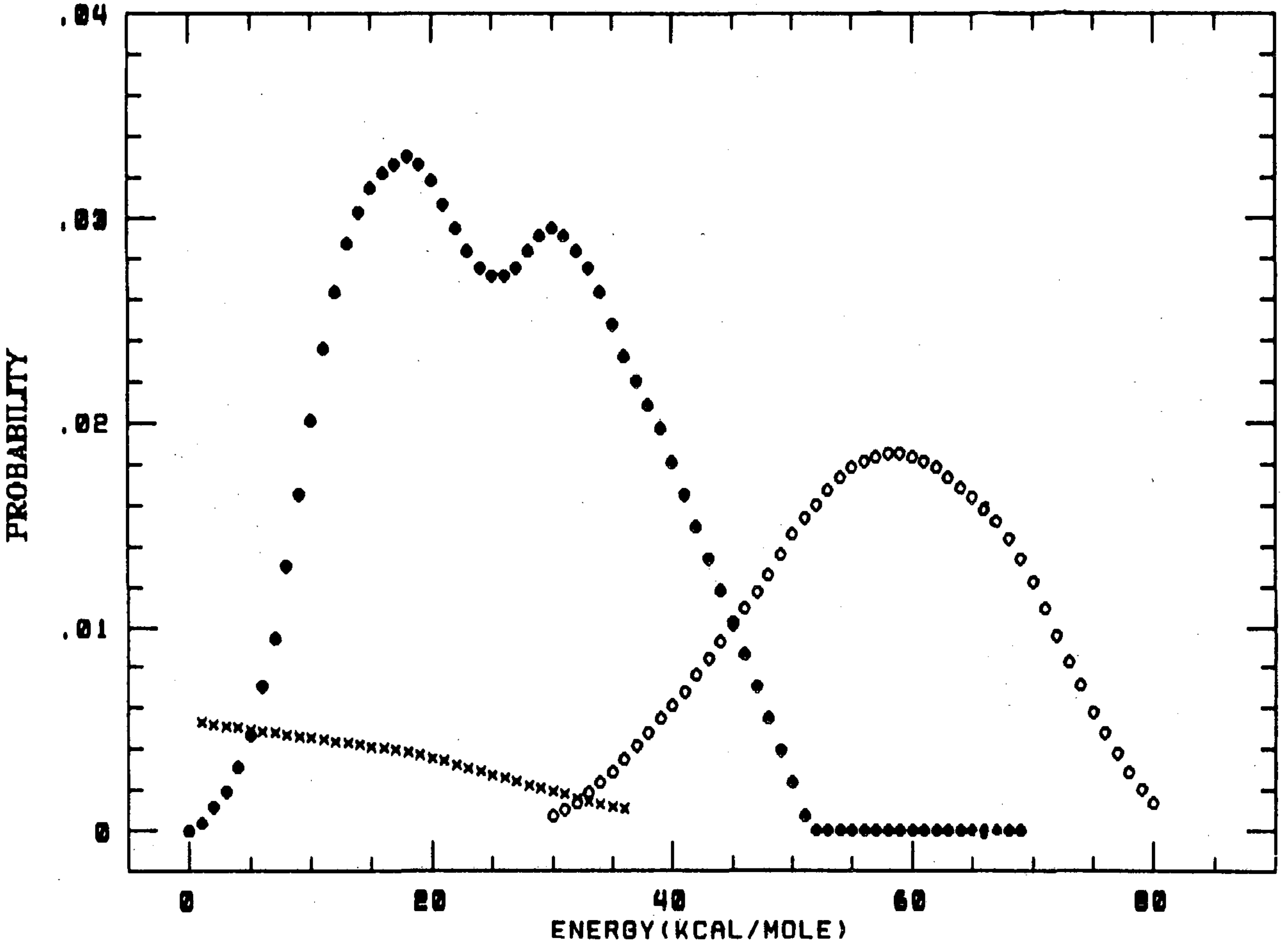

Figure 3.31

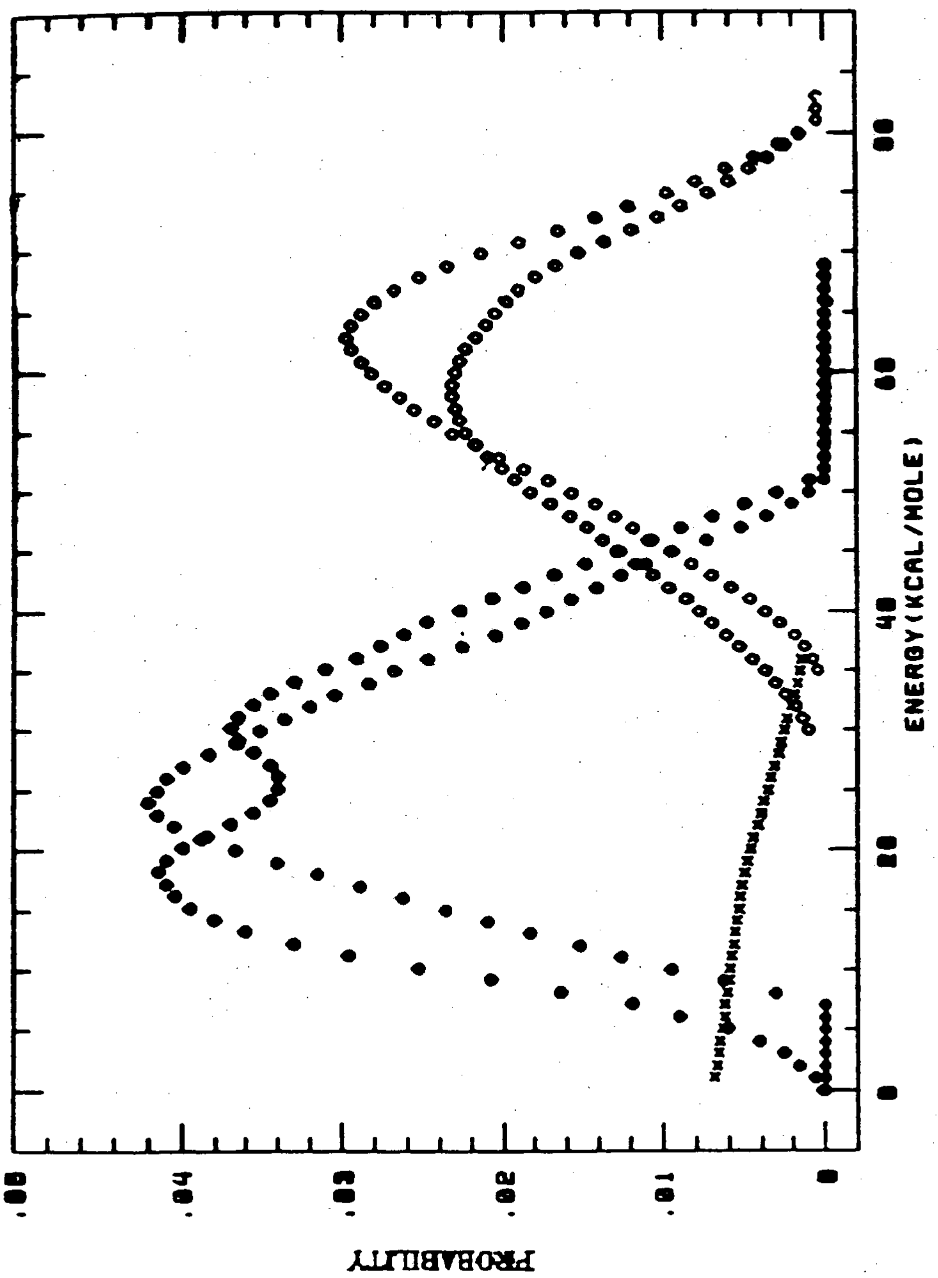

Figure 3.32

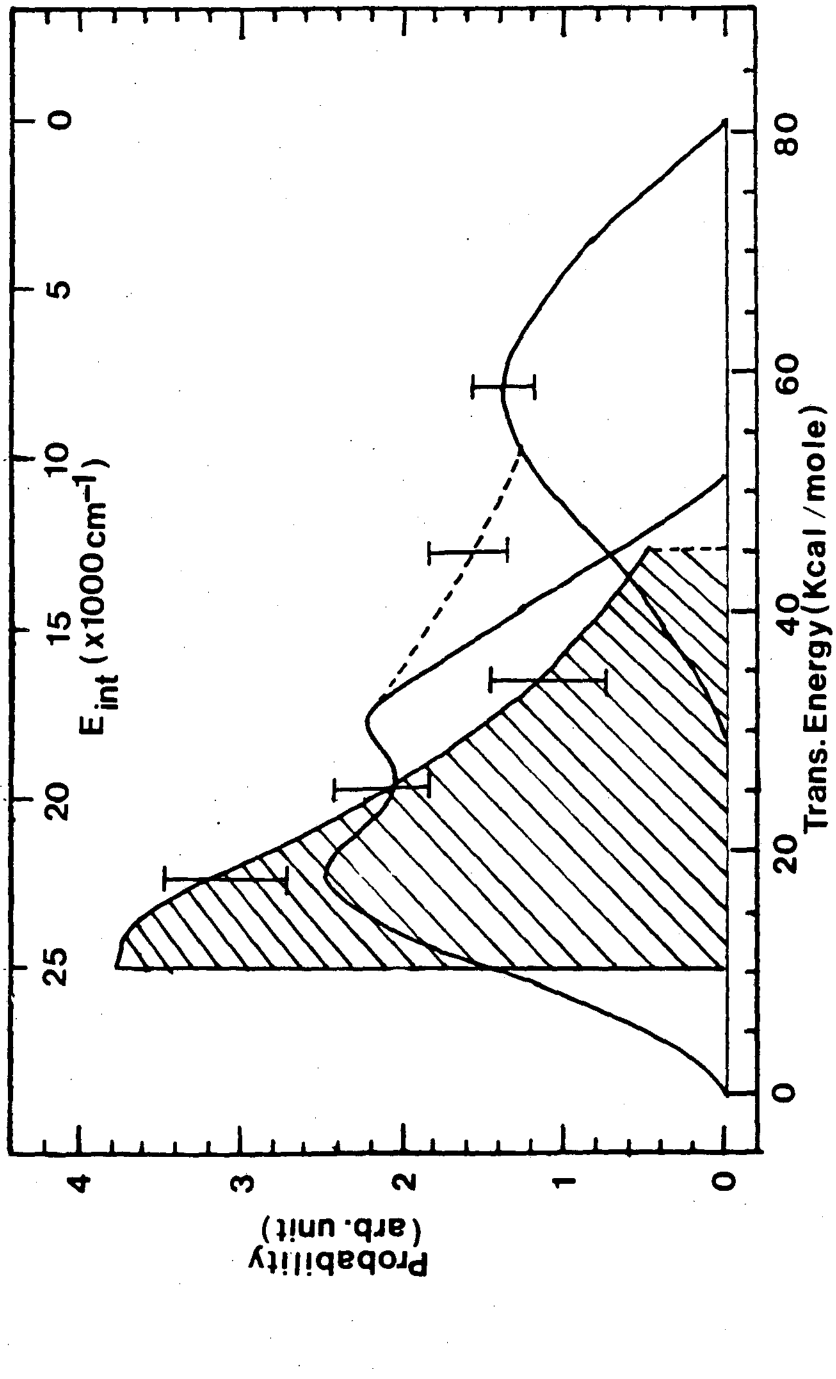
Probability
(arb. unit)
0
1
2
3
4
E_{int} (x1000cm^{-1})
25
20
15
10
5
0
Trans. Energy (Kcal/mole)
0
20
40
60
80

Figure 3.33

LAWRENCE BERKELEY LABORATORY
TECHNICAL INFORMATION DEPARTMENT
1 CYCLOTRON ROAD
BERKELEY, CALIFORNIA 94720